1975

Inelastic analysis of beam-slab bridges, July 1975

William S. Peterson

Celal N. Kostem

Recommended Citation

Peterson, William S. and Kostem, Celal N., "Inelastic analysis of beam-slab bridges, July 1975" (1975). *Fritz Laboratory Reports*. Paper 484.
http://preserve.lehigh.edu/engr-civil-environmental-fritz-lab-reports/484

LEHIGH UNIVERSITY

OFFICE
OF
RESEARCH

THE INELASTIC ANALYSIS OF BEAM-SLAB BRIDGES

by

William S. Peterson
Celal N. Kostem

Fritz Engineering Laboratory Report No. 400.20

THE INELASTIC ANALYSIS
OF
BEAM-SLAB BRIDGES

by

William S. Peterson
Celal N. Kostem

Fritz Engineering Laboratory
Department of Civil Engineering
Lehigh University
Bethlehem, Pennsylvania

July 1975

Fritz Engineering Laboratory Report No. 400.20

Parts of this work were sponsored by the Pennsylvania Department of Transportation and the United States Department of Transportation, Federal Highway Administration.

The contents of this report reflect the views of the authors, who are responsible for the facts and the accuracy of the data presented herein. The contents do not necessarily reflect the official view or policies of the Pennsylvania Department of Transportation or the Federal Highway Administration. This report does not constitute a standard, specification, or regulation.

TABLE OF CONTENTS

ABSTRACT

This dissertation describes an analysis scheme to predict the overload response of simple-span, right or skewed, beam-slab type highway bridge superstructures with a reinforced concrete deck slab and reinforced or prestressed concrete beams. As a subset of the overall investigation, analytic models for both the individual beam and slab components of the bridge superstructure are presented. The analysis scheme employs the finite element displacement method. The bridge superstructure is discretized into beam and slab finite elements. These finite elements are allowed to deform in both bending and in-plane displacement modes.

To allow for the initiation and propagation of material nonlinearity during overloading, the beam and slab finite elements are divided into a series of layers through their depth. Nonlinear stress-strain laws are employed on a layer by layer basis. Each layer is assumed to be in the plane state-of-stress. Beam concrete, prestressing steel, and beam and slab mild steel reinforcement are assumed to be stressed uniaxially. A biaxial stress field is used for the slab concrete. In addition to the inelastic stress-strain behavior, nonlinearities including cracking and crushing of the concrete and yielding of the steel are also considered. In order to solve for the nonlinear overload response of the bridge superstructure a piece-wise linear incremental-iterative tangent stiffness approximation is employed. The iteration procedure used within each load step gives a solution which satisfies convergence criteria. The total force-displacement response is obtained by adding the values corresponding to each load increment.

The method is verified through comparisons with laboratory and field overload tests of seven reinforced concrete slabs, five full-scale bridge superstructures, and numerous beams. The phase concerned with the overload analysis of reinforced and prestressed concrete bridge beams has been previously verified and reported in the literature.

This report is based on the doctoral research of the first author.

Overloading of the superstructure may cause cracking and crushing of the concrete and yielding of the steel. These material nonlinearities, including the inelastic stress-strain behavior for both steel and concrete, are permitted in the analysis. Thus, structural damage caused by the overload vehicle can be assessed. In order to facilitate the inclusion of the material nonlinearities, the beam and slab finite elements are divided into a series of layers as shown in Fig. 2. The extent of damage, including cracking and crushing of the concrete and yielding of the steel, is monitored on a layer by layer basis throughout the superstructure.

Inclusion of material nonlinearities necessitates adoption of a particular solution scheme other than that used for linearly elastic problems. Thus a tangent stiffness approach has been chosen where the solution is obtained by solving for the response in a series of piecewise-linear steps. Iterations may take place within each step so as to ensure convergence of the solution.

The accuracy of the method is illustrated by several comparisons between experimental and analytical results. Satisfactory agreement is obtained for all test cases. Thus the analytic model and solution technique are verified.

Superstructures built with a skew have also been successfully analyzed (see Chapter 4). Comparisons of experimental and analytical load-deflection histories indicate that a marked improvement in the results can be obtained by including the skew angle. However, correlative studies on the overload behavior of isolated skewed slabe were not carried out. The effect of particular boundary conditions, element geometries, and loadings for the slab model in the inelastic range was not evaluated. Thus, the accuracy of the model, as applied to skewed slabs, in determining local effects such as crack patterns could not be ascertained.

1.1 Problem Statement

The overloading of beam-slab type highway bridges is becoming a very common occurrence due to the increasing use of large capacity vehicles. An overload vehicle is defined as one which exceeds in some way the design vehicle weight for which the superstructure was proportioned. Overloading of bridge superstructures can result: (1) from the transport of heavy industrial loads, construction equipment, and National Defense Equipment, (2) from the legal across-the-board increase in vehicular weight limits, and (3) from additional permit overloads.

If the highway bridge superstructure does not have sufficient reserve capacity to carry the overload vehicle, then the excessive load may cause detrimental effects to the superstructure. The applied overload may produce a response in the elastic region or in the inelastic, i.e. nonlinear, region. The nonlinear region lies between the elastic region and the ultimate capacity. An elastic analysis and/or ultimate strength analysis will not allow for the assessment of damage to the superstructure for a load level between the elastic and ultimate loads. Therefore, a nonlinear analysis, which allows for the assessment of damage in the inelastic region, is required in the overload analysis scheme.

Currently there does not exist, with the exception of the method presented herein, an analytic scheme to realistically predict the structural behavior and associated structural damage, if any, that would occur to the bridge superstructure when subjected to an overload vehicle.

1.2 Purpose and Scope of the Research

The purpose of the overall research program is to develop an analytic model and solution technique to predict the full-range overload response of beam-slab type highway bridge superstructures (Ref. 24). Due to the complexity of the problem, the overall research is divided into three phases:

1. The development of an inelastic analysis technique for prestressed and reinforced concrete beams (Refs. 27,28,31,32).
2. The development of an inelastic analysis technique for reinforced concrete slabs (Ref. 43).
3. Interfacing the separate beam and slab analysis techniques, which were developed and verified in phases 1 and 2, so as to formulate a consistent analysis technique for prestressed and reinforced concrete highway bridge superstructures (Refs. 45,46,47).

Phase 1 of the overall research had been previously developed and verified. This phase is presented in Refs. 26-30 and 32. Therefore, since this phase was not part of the particular research being reported, only major concepts concerning Phase 1 will be given.

This report deals primarily with Phases 2 and 3 and has included the following subtopics:

For the slabs:

1. Analytic modeling of reinforced concrete slabs (see Chapter 3)
2. Analytic modeling of the complete stress-strain behavior for the biaxially stressed concrete including cracking and crushing (see Chapter 2).
3. Analytic modeling of the stress-strain behavior for the uniaxially stressed steel including yielding (see Chapter 2).
4. Verification of the slab analysis technique by comparing analytic results to experimental tests (see Chapter 4).

For the bridge:

1. Analytic modeling of right and skewed highway bridge superstructures (see Chapter 3).
2. Verification of the analytic model and solution technique by comapring analytic results to experimental tests (see Chapter 4).

1.3 Previous Studies

The end product of this research is to determine the overload response of beam-slab superstructures. Therefore, only those studies applicable to this problem will be reviewed.

Very few techniques applicable to the overload analysis of beam-slab type highway bridge superstructures have been reported in the literature. Analytic techniques that have been developed for possible application to the overload problem are the finite element method, the finite difference technique, and the lumped parameter technique.

The finite difference technique has been applied to the inelastic analysis of plates by relatively few researchers (e.g. Ref. 6). This has been due to the complexities in establishing either the appropriate nonlinear differential equation or the assignment of proper stiffness properties in a piecewise-linear incremental solution. Furthermore, the manual algebraic operations required in the coding of these operations for computer based solutions have always been discouraging. This approach is further complicated in bridge overload problems by the necessity to solve coupled in-plane and out-of-plane differential equations which is discussed in Section 1.4. This aspect alone necessitates the adoption of a solution technique other than finite differences.

Some of the complexities involved in the finite difference technique have been eliminated through the use of the lumped parameter technique. Lopez and Ang (Ref. 38) applied this method to mild steel plates. However, its applicability to reinforced concrete slabs and especially to a bridge overload analysis presents a major problem. Its accuracy, generality, and ease of usage have not been demonstrated as yet.

The finite element method enjoys a history of application to complex problems involving material nonlinearities, various boundary conditions, and loadings. This method has been used extensively in both the analysis of steel, reinforced concrete, and prestressed concrete beams (e.g. Refs. 14,27,29,30,31,32,42,56,58,59) and reinforced concrete slabs (e.g. Refs. 5,14,16,22,23,35).

Wegmuller and Kostem (Ref. 59) have developed an analysis technique and computer program to predict the elastic-plastic behavior of plates and eccentrically stiffened plate systems. The technique employed the finite element method which used the rectangular plate bending element with twelve degrees of freedom developed by Adini and Clough and independently by Melosh (Ref. 1). In-plane displacement fields reported by Clough (Ref. 9) were also employed in the analysis technique. The beam and slab elements were divided into a series of layers through the depth so that the spread of yielding through the eccentrically stiffened plate system could be simulated. In this analysis a material obeying von Mises yield condition was assumed.

Kulicki and Kostem (Refs. 26,32) developed a technique based on the finite element method for the inelastic analysis of plates composite with eccentrically placed reinforced or prestressed concrete beams. In this analysis the von Mises yield criterion was employed for the plate as was previously done by Wegmuller and Kostem (Ref. 59). However, reinforced and prestressed concrete beams were realistically modeled. Cracking and crushing of the concrete and yielding of the steel in the beams were considered. Separate stress-strain curves for the individual concrete layers and steel layers were also employed.

The above applications have demonstrated that the finite element method is an efficient tool that can be applied to the inelastic analysis of eccentrically stiffened slab systems. Complexities in the stress-strain behavior of the material or materials can be incorporated directly into the analysis scheme.

1.4 The Analytic Model

The characteristics of the analytic model, i.e. the analytic representation of the real structure, must be chosen to adequately describe the physical model. In the current context it is desired to describe the response of prestressed and reinforced concrete highway bridge superstructures subjected to a vehicular overload. In order to adequately reflect the inelastic behavior of eccentrically stiffened beam-slab highway bridge superstructures, the following must be considered:

1. The out-of-plane response
2. The in-plane response
3. The interaction between the in-plane and out-of-plane responses.

When the superstructure is subjected to wheel loads, both longitudinal and transverse bending develops in the deck slab while longitudinal bending is predominant in the beams. Thus, the out-of-plane response is primarily described by the flexure behavior of the superstructure. Also, beams and slabs with dimensions similar to those encountered in bridge design primarily deform in a flexure mode when subjected to out-of-plane loading.

The deck slab and beams are considered to act compositely. For illustration purposes, the deck slab can be thought of as the compression flange of a composite beam where the eccentricity of the beams may induce in-plane stresses which are of the same order of magnitude or even greater than the bending stresses. The bending and inplane responses are interdependent for the class of problems considered in this report. This interdependency, which is commonly referred to as coupling, is manifested in the following response characteristic: application of an out-of-plane (or in-plane) force causes both out-of-plane and in-plane deformations in both the deck slab and the beams. This interdependency arises from an unsymmetric distribution of stiffness properties about a reference axis (Ref. 44). This unsymmetric distribution of stiffness properties is (1) due to the geometry of the superstructure, e.g. the eccentric placement of the beams, and (2) due to the nonlinearities inherent in the stress-strain behavior of the materials. Terms describing the in-plane and out-of-plane responses and the associated coupling are explicitly presented in Chapter 3.

Material nonlinearities affect the in-plane, bending, and coupling terms and have a significant effect on the behavior of the superstructure. The realistic representation of material behavior is a key factor in the analysis scheme. Material response modes appropriate to the analysis of beam-slab type highway bridge superstructures include:

For the beam:

1. Concrete, mild steel reinforcing, and prestressing steel subjected to uniaxial stress states

For the slab:

1. Concrete subjected to biaxial stress states
2. Mild steel reinforcing subjected to uniaxial stress states

Since inelastic response due to overloading is expected, the nonlinearities inherent in the stress-strain behavior of the specific materials mentioned above must be considered. These nonlinearities include cracking and crushing of the concrete under both uniaxial and biaxial stress fields and yielding of the steel.

The basic stress-strain relationships for concrete (Refs. 4, 13,19,20,27,28,30,33,36,37,40,48,50) and for both mild steel reinforcing bars and prestressing strands (Refs. 27,28,30,49) have been previously defined both experimentally and analytically. These basic stress-strain relationships must be utilized in the stiffness formulation for the various finite elements employed in the analysis scheme. The nonlinearities inherent in the stress-strain relations have profound affect on the stiffness properties of the elements and, consequently, on the analytical response of the bridge superstructure. To account for the variation of material properties through the depth of the slab and the beams, whose aggregation is used to model the superstructure, the finite elements are divided into a series of layers through their depth. Each layer is assumed to be in a state of plane stress (see Fig. 2). By defining the stress-strain relation on a layer by layer basis, the penetration of cracking, crushing, and yielding can be monitored throughout the structure. Excellent agreement has been noted in previous investigations that utilized the layer approach (Refs. 3,15,16,27,32,35,57,59,61).

Structural phenomena that have significant effect on the behavior of bridge superstructures have been reviewed in the previous paragraphs. A consistent set of assumptions is made which simplify the requirements that may be placed on the analytic model but still permit the simulation of the basic structural response of the bridge superstructure.

The beams under consideration are assumed:

1. To be prismatic
2. To be simply supported
3. To be made of reinforced or prestressed concrete
4. To have only strong axis bending (minor axis bending and torsional stiffnesses are neglected)

5. To have perfect bond between steel and concrete
6. To fail in a flexural mode.

The slabs under consideration are assumed:

1. To lie in one plane, i.e. be planar
2. To have a constant thickness
3. To have arbitrary rhomboidal boundaries
4. To have tension and compression reinforcement placed at arbitrary angles and depths within the slab
5. To be subjected to vertical concentrated and patch loads, concentrated in-plane loads, and moments
6. To have perfect bond between the steel and concrete
7. To fail in a flexural mode

The beam-slab superstructures under consideration are assumed:

1. To be simply supported
2. To be subjected to static loading
3. To be under small strain and small deformation fields
4. To have full or no composite action between the beams and the deck slab
5. To fail in a flexural mode

Thus, the development of the analytic model has been based on the premise that the inelastic response and the progressive collapse of the slab, beams, and therefore, the bridge superstructure is primarily due to the flexural response and its associated in-plane and coupling behavior.

The geometry and loading for the class of problems being considered in this investigation permit exclusion of several important structural effects. These include:

1. Local buckling and lateral torsional buckling:

   The geometry of the deck slab and reinforced or prestressed concrete bridge beams excludes the possibility of local or lateral-torsional buckling.

2. Torsional stiffness of the beams:

   Torsional stiffness of the beams has a minor effect on the behavior of right angle beam-slab bridges and therefore, it can be neglected (Refs. 26,32,58). Torsion becomes more important in the case of skewed superstructures. A limited number of analyses carried out on the effect of torsion in right angle superstructures seem to indicate that results will be on the conservative side if torsion is neglected (Ref. 26).

3. Shear punch failure of the slab:

   Loads are transmitted to the bridge superstructure through the tires of the vehicle. As the vehicular loads are increased, more wheels are used which will distribute the load over a greater area. Also, the tires will flatten out as the load is increased and will cause an additional distribution of load. Since a substantial area is involved, shear punch failure is not likely to occur (Ref. 23).

4. Dynamic effects and impact:

Static loading was assumed since the speed of an overload vehicle would be slow so as not to produce dynamic effects and impact during its passage over the bridge superstructures.

Highway bridge superstructures may be constructed with superelevation, diaphragms, and permanent metal deck forms. These items have not been included in the analysis for the following reasons: (1) by neglecting the diaphragms and metal deck forms a conservative result will be obtained, and (2) the magnitude of the superelevation is usually so small that it can be neglected with little error in the result.

This report is based on the doctoral research of the first author (Ref. 67).

2. MATERIAL BEHAVIOR

This chapter presents the stress-strain relationships employed in the reported analysis scheme. The material stress-strain relations are defined for the steel reinforcing bars, prestress strands, and the concrete. These relations are later used in the definition of the stiffness properties of the bridge components.

The behavior of concrete is very much dependent on the particular stress state, i.e. tension or compression, and whether the stress field is uniaxial, biaxial, or triaxial. A beam may be idealized as a one dimensional structural element in which bending in the longitudinal direction produces a uniaxial state of stress (Ref. 27). A slab on the other hand could be considered as a two dimensional structural element in which bending in both the longitudinal and the transverse directions produce a biaxial state of stress. Thus the beam concrete is assumed to be subjected to uniaxial states of stress while the slab concrete is assumed to be subjected to biaxial states of stress (Ref. 43).

The inelastic biaxial and uniaxial behavior of concrete is analytically described by empirical formulae. These empirical formulae are based on experimental observations and are characterized by:

1. The utilization of a linear or nonlinear stress-strain curve (see Sections 2.1.1 and 2.1.2)

2. The utilization of a biaxial failure envelope which defines the onset of concrete failure at the peak stress (see Section 2.1.3)
3. The assignment of a particular strain value (peak strain) which occurs at the peak stress (see Section 2.1.4)
4. The assignment of a particular slope (peak slope) which occurs at the peak stress (see Section 2.1.5)
5. The assignment, after concrete failure, of a downward slope to the stress-strain curve for the purpose of redistributing the stress (see Section 2.1.8).

The analytic stress-strain equations are differentiated so as to obtain an expression for the slope, i.e. tangent modulus, of the stress-strain curve. The tangent modulus is used to formulate the elasticity matrix, [D], which relates the stress increment to the strain increment:

$$\{\dot{\sigma}\} = [D]\{\dot{\varepsilon}\} \tag{2.1}$$

The elasticity matrix is utilized in formulating the stiffness properties of the beam and slab finite elements (see Chapter 3).

The stress-strain relations discussed in this chapter will sometimes involve both total stresses and strains and incremental stresses and strains. Incremental quantities are distinguished by a dot over the appropriate symbol, e.g. Eq. 2.1.

2.1 Biaxial Stress-Strain Relationships

A limited number of experimental investigations of concrete behavior in the biaxial stress state have been carried out (Refs. 33, 36,37,40). These studies have covered the entire biaxial principal stress space consisting of the compression-compression region, the tension-tension region, and the compression-tension (or, conversely tension-compression) region. These regions are shown in Fig. 3.

Analytical expressions for the biaxial principal stress-strain relations for the compression-compression region have been adopted from Liu (Refs. 36,37). Similar formulation is developed, based on the reported experiments, to cover the nonlinear compression-tension and tension-tension regions. The idealized biaxial stress-strain curves have two basic forms: the nonlinear form and the linear form. The nonlinear equation is used for biaxial stress states where compression is dominant while the linear expression is used for biaxial stress states where tension is dominant. Figure 4 shows the approximate regions in the biaxial stress space where the nonlinear and linear equations are applicable. E_p in the figure designates the peak slope.

2.1.1 Nonlinear Stress-Strain Equation for Concrete

The nonlinear stress-strain curve for concrete was assumed to have the following form (Refs. 36,37);

$$\sigma = \frac{A + B\varepsilon \; E_c}{(1 - \nu\alpha) \; (1 + C\varepsilon + D\varepsilon^2)} \qquad (2.2)$$

Where: σ = the principal stress in the direction of interest

ε = the strain in direction of interest

ν = Poisson's ratio (taken to be 0.2 but other choices are also permissible)

α = the ratio of the principal stress in the orthogonal direction to the principal stress in the direction of interest, e.g. $\alpha_1 = \sigma_2/\sigma_1$

E_c = Initial tangent modulus in uniaxial loading. E_c can be obtained by performing a standard compression cylinder test or through an accepted formula such as the ACI equation (Ref. 65), the Jensen equation (Ref. 21), the Hognestad equation (Ref. 30), or the Saenz equation (Ref. 50).

A,B,C,D = Curve parameters to be determined

A positive stress from Eq. 2.2 denotes compression, and likewise a positive strain denotes contraction. The parameters A,B,C,D are determined by considering the basic shape of the nonlinear stress-strain curve: the stress-strain curve must pass through the zero stress-zero strain point at a slope of E_c and must also pass through the peak stress-peak strain point at a slope of E_p. Enforcing these curve characteristics leads to the following;

$$A = 0$$

$$B = 1$$

$$C = \frac{E_c}{\sigma_p\ (1 - \nu\alpha)} - \frac{2}{\varepsilon_p} + \frac{E_p\ E_c\ \varepsilon_p}{(1 - \nu\alpha)\ \sigma_p^2} \tag{2.3}$$

$$D = \frac{1}{\varepsilon_p^2} - \frac{E_p\ E_c}{(1 - \nu\alpha)\ \sigma_p^2}$$

where: σ_p is the peak stress

ε_p is the strain at the peak stress

E_p is the slope of the stress-strain curve at the peak stress

The instantaneous slope of the stress-strain curve may be obtained by differentiating Eq. 2.2 resulting in

$$\frac{d\sigma}{d\varepsilon} = \frac{E_c\ (1 - D\varepsilon^2)}{(1 - \nu\alpha)\ (1 + C\varepsilon + D\varepsilon^2)^2} \tag{2.4}$$

Where: $A = 0$

$B = 1$

The instantaneous slope of the stress-strain curve, given in Eq. 2.4, can be used to relate the incremental stress in a principal direction to the incremental strain in that same direction. Thus the instantaneous slopes of the stress-strain curves for the two principal directions can be expressed as:

$$E_{1b} = \frac{d\sigma_1}{d\varepsilon_1} = \frac{E_c}{(1 - \nu\alpha_1)} \; \frac{(1 - D_1\varepsilon_1^2)}{(1 + C_1\varepsilon_1 + D_1\varepsilon_1^2)^2} \qquad (2.5a)$$

$$E_{2b} = \frac{d\sigma_2}{d\varepsilon_{\varepsilon}} = \frac{E_c}{(1 - \nu\alpha_2)} \; \frac{(1 - D_2\varepsilon_2^2)}{(1 + C_2\varepsilon_2 + D_2\varepsilon_2^2)^2} \qquad (2.5b)$$

Where: E_{1b} and E_{2b} are the tangent moduli in the two principal directions 1 and 2 respectively

$\alpha_1 = \sigma_2/\sigma_1$

$\alpha_2 = \sigma_1/\sigma_2$

D_1 and C_1 are the D and C curve parameters evaluated for the "1" principal direction using Eq. 2.3

D_2 and C_2 are the D and C curve parameters evlauated for the "2" principal direction using Eq. 2.3

Thus the incremental stress-incremental strain relation can be defined as:

$$\dot{\sigma}_1 = E_{1b}\,\dot{\varepsilon}_1$$
$$\dot{\sigma}_2 = E_{2b}\,\dot{\varepsilon}_2 \qquad (2.6a)$$

or in matrix form:

$$\begin{Bmatrix} \sigma_1 \\ \sigma_2 \end{Bmatrix} = \begin{bmatrix} E_{1b} & 0 \\ 0 & E_{2b} \end{bmatrix} \begin{Bmatrix} \varepsilon_1 \\ \varepsilon_2 \end{Bmatrix} \qquad (2.6b)$$

The curve parameters C and D, which are presented in Eq. 2.3, can be determined if the following quantities are known: E_c, ν, α, σ_p, ε_p, and E_p. The first three quantities, Young's Modulus, Poisson's ratio and the stress ratio have been previously defined in this section. The latter three quantities, i.e. the peak stress, the peak strain, and the peak slope, will be defined in Sections 2.1.3, 2.1.4, and 2.1.5, respectively.

2.1.2 Linear Stress-Strain Equation for Concrete

The linear stress-strain equation for concrete has the general form shown below:

$$\sigma = A + B\,\varepsilon \tag{2.7}$$

The curve parameters, A and B, may be defined by forcing the curve to pass through the zero stress-zero strain point, i.e. the origin, and also through the peak stress-strain point. The curve parameters are thus defined as

$$\begin{aligned} A &= 0 \\ B &= \frac{\sigma_p}{\varepsilon_p} \end{aligned} \tag{2.8}$$

The following stress-strain equation is determined by substituting Eq. 2.8 into Eq. 2.7

$$\sigma = \frac{\sigma_p}{\varepsilon_p}\,\varepsilon \tag{2.9}$$

A tangent modulus, which is constant, is obtained by differentiating the stress-strain equation:

$$\frac{d\sigma}{d\varepsilon} = \frac{\sigma_p}{\varepsilon_p} \tag{2.10}$$

The incremental stress - incremental strain relationship follows from Eq. 2.10 as:

$$\begin{Bmatrix} \dot{\sigma}_1 \\ \dot{\sigma}_2 \end{Bmatrix} = \begin{bmatrix} E_{1b} & 0 \\ 0 & E_{2b} \end{bmatrix} \begin{Bmatrix} \dot{\varepsilon}_1 \\ \dot{\varepsilon}_2 \end{Bmatrix} \tag{2.11a}$$

Where:

$$\begin{aligned} E_{1b} &= \frac{d\sigma_1}{d\varepsilon_1} = \frac{\sigma_{p1}}{\varepsilon_{p1}} \\ E_{2b} &= \frac{d\sigma_2}{d\varepsilon_2} = \frac{\sigma_{p2}}{\varepsilon_{p2}} \end{aligned} \tag{2.11b}$$

σ_{p1} (ε_{p1}) and σ_{p2} (ε_{p2}) denote the peak stress (strain) for the "1" and "2" principal directions, respectively. The linear stress-strain curve can be determined if the peak stress and peak strain values are known.

In the particular case of the tension-tension region the initial slope of $E_c/(1 - \nu\alpha)$, obtained from Hooke's Law, is maintained. Thus, if the peak stress is known, the peak strain in this region can be defined as $\varepsilon_p = \sigma_p (1 - \nu\alpha)/E_c$.

2.1.3 Biaxial Failure Envelope - Definition of σ_p

Non-dimensionsal experimental peak stress envelopes for concrete strengths of 2700 psi and 4450 psi are shown in Fig. 5 (Ref. 33). The close agreement between the two curves indicate that the basic shape of the failure envelope is essentially invariant and only the size of the envelope will change with concrete strength. The true envelope can be approximated by a series of straight lines as shown in Fig. 5. The maximum increase in biaxial compressive strength, as compared to uniaxial strength for the idealized failure envelope is 20%. This corresponds to a value of 1.2 on the non-dimensional plot in Fig. 5.

The characteristic points used to define the idealized peak stress envelope are shown in Fig. 6 and are enumerated in the table below:

Point	σ_{p1}	σ_{p2}
A	f'_c	0.0
B	Rf'_c	$\alpha_B \; Rf'_c$
C	Rf'_c	Rf'_c
D	Rf'_c/α_D	Rf'_c
E	0.0	f'_c
F	σ_{2F}/α_F	σ_{2F}
G	$-f_t$	0.0
H	$-f_t$	$-f_t$
I	0.0	$-f_t$
J	σ_{1J}	$\alpha_J \; \sigma_{1J}$

The terms used in the table above and on Fig. 6 are defined as:

f'_c = uniaxial compressive strength from 6" x 12" cylinder test (28 days)

f_t = direct tensile strength

σ_1 = principal stress in direction 1

σ_2 = principal stress in direction 2

α = σ_2/σ_1

σ_{p1} = peak stress in direction 1

σ_{p2} = peak stress in direction 2

σ_{ij} = stress in direction i at point j

α_j = stress ratio σ_{2j}/σ_{1j}

R = increase in strength due to the biaxial compressive stress state

The following values were used in all test examples included in this report. These values were selected to provide an acceptable approximation to experimentally observed biaxial stress states (Refs. 33,36).

$$R = 1.2$$

$$\alpha_B = \frac{1}{\alpha_D} = \nu = 0.2$$

$$\alpha_F = \frac{1}{\alpha_J} = -19.2$$

$$\sigma_{2F} = \sigma_{1J} = 0.85\ f'_c$$

Equations defining the straight line segments ued in Fig. 6 are expressed in terms of the characteristic points and the stress ratio, α. These equations are explicity presented in Ref. 43.

2.1.4 Peak Strain Envelope - Definition of ε_p

The non-dimensional peak strain envelope, shown in Fig. 7, is idealized as a series of straight lines passing through, or very near to, the experimental peak strain points indicated in the figure (Refs. 33,36). Peak strain is defined as the strain occurring at peak stress. The characteristic points used to define the peak strain envelope are shown in Fig. 8 and are enumerated in the table below:

Point	σ_{p1}	ε_{p1}
A'	f'_c	ε_c
B'	Rf'_c	ε_c
C'	σ_ν	0
D'	0	$-\nu\varepsilon_c$
E'	$-f_t$	$-\varepsilon_c$
F'	0	$\nu\varepsilon_t$
G'	σ_{ct}	ε_{ct}

R, f'_c, ν, and f_t are defined in the previous section. The following additional terms used in the table above are defined as:

σ_ν = peak compressive stress at an $\alpha = 1/\nu$ as obtained from the peak stress envelope

$\sigma_{ct}, \varepsilon_{ct}$ = a peak stress-strain value defining point G'

ε_c = peak strain for uniaxial compression

ε_t = peak strain for uniaxial tension

The following values were used for all test examples in this report. They were selected to provide an acceptable approximation to experimentally observed peak strains in biaxial stress states,

$R = 1.2$

$\nu = 0.2$

$\sigma_{ct} = 0.8 f'_c$

ε_{ct} = 1150 microstrain

ε_c = 2500 microstrain

ε_t = tensile strength divided by Young's modulus

Equations defining the straight line segments used in Fig. 8 are expressed in terms of the characteristic points and the stress ratio, α. These equations are explicity presented in Ref. 43.

2.1.5 Peak Slope - Definition of E_p

The peak slope is defined as the tangent of the non-linear stress-strain curve evaluated at the peak stress. According to experimental observations the peak slope for the compression-compression stress region has a value of zero (Refs. 33,36,40). In the tension-compression region the peak slope may range from a value of zero for stress states near uniaxial compression to a value equal to the σ_p/ε_p for the stress states near uniaxial tension. In this study the ratio of peak slope to initial slope has been assumed to vary linearly with respect to the stress ratio, α. The peak slope ratio has a value of zero for stress states near uniaxial compression and ranges to a value of 1.0 for stress states near uniaxial tension.

Two peak slope ratios, necessary to define the aforementioned linear variation, were scaled from the experimental stress-strain curves, which are designated as A and C in Fig. 11 and are listed below along with the values of α associated with those curves.

Point	α	$\frac{\text{Peak Slope}}{\text{Initial Slope}}$
I	-0.204	1.000
II	-0.052	0.125
I'	-4.900	1.000
II'	-19.200	0.125

Points I and II, located in the compression-tension region, were obtained by measuring the peak slope ratio for curves C and A, respectively. Points I' and II', located in the tension-compression region, were obtained by computing the reciprocals of the values associated with points I and II.

Points I, II, I', and II' and a plot of the ratio of peak slope to initial slope as a function of the stress ratio, α, shown in Fig. 9. The peak slope function is represented as a series of straight line segments. These straight line segments and corresponding biaxial stress plane regions are indicated by the letters A through E in Fig. 9. The corresponding biaxial stress plane regions designate where that particular straight line segment is applicable. The letters C+ and E+ indicate that the curve extends to a stress ratio of plus infinity while the letters C- and E- indicate that the curve extends to negative infinity at the indicated points on the failure envelope. The straight line segments delineated by the points E-, I, II, A and C+ reflect the peak slope ratios for the compression-tension region through the compression-compression region. The straight line segments associated with the points C-, II', I', D and E+ describe the peak slope relationship for the tension-compression region through the tension-tension region.

2.1.6 Biaxial Constitutive Relationships for Concrete

The incremental stress-strain relationship for concrete in terms of principal stresses is represented by Eq. 2.12 in which the subscripts $_1$ and $_2$ identify the principal stress directions and the dots indicate incremental quantities:

$$\begin{Bmatrix} \dot{\sigma}_1 \\ \dot{\sigma}_2 \\ \dot{\tau}_{12} \end{Bmatrix} = [\bar{D}] \begin{Bmatrix} \dot{\varepsilon}_1 \\ \dot{\varepsilon}_2 \\ \dot{\gamma}_{12} \end{Bmatrix} \tag{2.12}$$

Needless to say, the shear stress increment, $\dot{\tau}_{12}$, will be zero but its presence is required in the principal stress vector so as to include the shearing stiffness term in the [D] matrix. This is necessary so that transformation of the [D] matrix from principal axes to global x-y axes results in the proper elasticity relationships. The $[\bar{D}]$ matrix is the constitutive relationship for the principal stress space. The $[\bar{D}]$ matrix for anisotropic materials can be expressed as (Ref. 36).

$$[\bar{D}] = \begin{bmatrix} \dfrac{E'_{1b}}{1 - \nu_1 \nu_2} & \dfrac{\nu_2 E'_{1b}}{1 - \nu_1 \nu_2} & 0 \\ \dfrac{\nu_1 E'_{2b}}{1 - \nu_1 \nu_2} & \dfrac{E'_{2b}}{1 - \nu_1 \nu_2} & 0 \\ 0 & 0 & \dfrac{E'_{1b} E'_{2b}}{E'_{1b} + E'_{2b} + 2\nu_1 E'_{2b}} \end{bmatrix} \tag{2.13}$$

E'_{1b} and E'_{2b} are the tangent moduli in the first and second principal stress directions, respectively, and ν_1 and ν_2 are the Poisson's ratios in the indicated directions. In the equation above it is assumed that $\nu_1/E'_{1b} = \nu_2/E'_{2b}$.

The analytic stress-strain curves of Section 2.1.1 and 2.1.2 relate the stress in a particular principal direction to the strain in that same direction and only that direction. Thus, as indicated by Eq. 2.6a and 2.11a, relationships of the following form are defined:

$$\begin{aligned} \dot{\sigma}_1 &= E_{1b}\,\dot{\varepsilon} \\ \dot{\sigma}_2 &= E_{2b}\,\dot{\varepsilon} \end{aligned} \tag{2.14}$$

Where E_{1b} and E_{2b} are the effective tangent moduli for the principal stress space obtained by differentiating the analytic stress-strain curves of Sections 2.1.1 and 2.1.2. The terms in the $[\bar{D}]$ matrix of Eq. 2.13 must now be related to the known moduli, E_{1b} and E_{2b}.

The unknown terms in the stress-strain relations may be expressed as functions of the known E_{1b} and E_{2b} values by diagonalizing the stress-strain relations of Eq. 2.13. Diagonalized relations may be obtained by eliminating $\dot{\sigma}_1$ and $\dot{\sigma}_2$ from the first and second algebraic equations of matrix equation, Eq. 2.13. This is done by substituting for $\dot{\sigma}_1$ and $\dot{\sigma}_2$ the relations given by

$$\begin{aligned} \dot{\sigma}_2 &= \dot{\sigma}_1\,\alpha_1 \\ \dot{\sigma}_1 &= \dot{\sigma}_2\,\alpha_2 \end{aligned} \tag{2.15}$$

The above substitution leads to

$$\dot{\varepsilon}_1 = \dot{\sigma}_1 \left(\frac{1}{E'_{1b}} - \frac{\nu_2\,\alpha_1}{E'_{2b}} \right) \tag{2.16a}$$

$$\dot{\varepsilon}_2 = \dot{\sigma}_2 \left(\frac{1}{E'_{2b}} - \frac{\nu_1 \alpha_2}{E'_{1b}} \right) \tag{2.16b}$$

The relation $\nu_2/E'_{2b} = \nu_1/E'_{1b}$ allows Eq. 2.16 to be expressed as

$$\dot{\varepsilon}_1 = \frac{\dot{\sigma}_1}{E'_{1b}} \left(1 - \nu_1 \alpha_1\right) \tag{2.17a}$$

$$\dot{\varepsilon}_2 = \frac{\dot{\sigma}_2}{E'_{2b}} \left(1 - \nu_2 \alpha_2\right) \tag{2.17b}$$

Rearranging Eq. 2.17 leads to the diagonalized stress-strain relations given by

$$\dot{\sigma}_1 = \left(\frac{E'_{1b}}{1 - \nu_1 \alpha_1} \right) \dot{\varepsilon}_1 \tag{2.18a}$$

$$\dot{\sigma}_2 = \left(\frac{E'_{2b}}{1 - \nu_2 \alpha_2} \right) \dot{\varepsilon}_2 \tag{2.18b}$$

Comparison of Eq. 2.18 with Eq. 2.14 shows that the tangent moduli relating principal stresses to strains in the corresponding directions are given by

$$E_{1b} = \frac{E'_{1b}}{1 - \nu_1 \alpha_1} \tag{2.19a}$$

$$E_{2b} = \frac{E_{2b}}{1 - \nu_2 \alpha_2} \tag{2.19b}$$

Rearranging Eq. 2.19 leads to Eq. 2.20 which defines the moduli E'_{1b} and E'_{2b} needed in Eq. 2.13:

$$E'_{1b} = E_{1b}\ (1 - \nu_1\alpha_1) \tag{2.20a}$$

$$E'_{2b} = E_{2b}\ (1 - \nu_2\alpha_2) \tag{2.20b}$$

E_{1b} and E_{2b} are defined in Eq. 2.5 for the nonlinear case and in Eq. 2.11b for the linear case. E_{1b} and E_{2b} are computed using the current total stress state. The α's are also based on the current total stress state so as to be consistent with the definition of E_{1b} and E_{2b}. The curve parameters C and D in the aforementioned expressions are given by Eq. 2.3.

ν_1 and ν_2 in Eq. 2.13 must still be obtained. The relation $\nu_2/E'_{2b} = \nu_1/E'_{1b}$ leads to the following equations:

$$\nu_A = \nu \tag{2.21a}$$

$$\nu_B = \cfrac{1}{\cfrac{E_{Ab}\ (1 - \nu_A\alpha_A)}{E_{Bb}\ \nu_B} + \alpha_B} \tag{2.21b}$$

where subscripts (A,B) correspond to directions (1,2) or (2,1) whichever is applicable. Applicability was determined by selecting the combination that resulted in positive values for both ν_1 and ν_2. This investigation has used the value of 0.2 for ν_A. The range of values for ν_B, resulting from the application of Eq. 2.21 for various combinations of cylinder strength, stress ratios and stress levels, was approximately 0.16 to 0.24, or about 80% to 120% of the value assumed for ν_A.

All terms of Eq. 2.13 can thus be defined using Eqs. 2.5, 2.11b, 2.20, and 2.21. The resulting $[\bar{D}]$ matrix is the constitutive relationship for the particular layer expressed in principal stress directions. Before computing the contribution of this layer to the element stiffness matrix, the $[\bar{D}]$ matrix must be transformed into an elasticity matrix [D], relating stress and strain in the x-y coordinate system of the element:

$$\begin{Bmatrix} \dot{\sigma}_x \\ \dot{\sigma}_y \\ \dot{\tau}_{xy} \end{Bmatrix} = [D] \begin{Bmatrix} \dot{\varepsilon}_x \\ \dot{\varepsilon}_y \\ \dot{\gamma}_{xy} \end{Bmatrix} \tag{2.22}$$

This transformation is carried out in the following manner (Refs. 16, 55,64):

$$[D] = [T]\,[\bar{D}]\,[T]^T \tag{2.23}$$

where the transformation matrix, [T] is defined by

$$[T] = \begin{bmatrix} \cos^2\theta & \sin^2\theta & -2\cos\theta\,\sin\theta \\ \sin^2\theta & \cos^2\theta & 2\cos\theta\,\sin\theta \\ \cos\theta\,\sin\theta & -\cos\theta\,\sin\theta & \cos^2\theta - \sin^2\theta \end{bmatrix} \tag{2.24}$$

The angle θ is defined as the angle between the 1 and the x direction. This angle is positive when measured in a clockwise direction from the positive x axis.

Figures 10, 11, and 12 compare the idealized and experimental biaxial stress-strain curves (Ref. 33). Curves A, B, and C in each figure corresponds to the specific stress ratios listed on the figures. Two curves are plotted for each stress ratio. One corresponds to σ_1/σ_0 versus ε_1 and the other to σ_1/σ_0 versus ε_2. σ_1 and σ_2 are the principal stresses as shown in the inset of each figure while σ_0 is the uniaxial compressive strength. ε_1 and ε_2 are the strains in the first and second principal stress directions, respectively.

2.1.7 Concrete Failure Modes

Concrete exhibits different types of failure modes which are dependent upon the applied stress ratio as shown in Fig. 13A. Figures 13A and 13B each show one-half of a symmetric region. The four physically distinct failure modes can be described as follows (Ref. 44):

TYPE I. In the tension-tension region and up to a tensile stress/compressive stress ratio of -1/30 failure occurs by the formation of one crack perpendicular to the largest tensile stress and perpendicular to the free plane, i.e. unloaded plane, of the specimen. For a stress ratio of equal tension in both directions there is no preferred crack direction (Ref. 33).

TYPE II. For stress ratios between -1/30 and -1/100 numerous cracks are formed instead of just a single crack as was the case for the previous region. These cracks are also perpendicular to the tensile stress and the free plane of the specimen.

TYPE III. From a stress ratio of -1/100 in the compression-tension region to a stress ratio of 3/10 in the compression-compression region, cracks are not only formed perpendicular to the applied tensile stress and free surface of the specimen but also cleavage planes occur parallel the free surface of the specimen.

TYPE IV. For stress ratios between 3/10 and 1/1 in the compression-compression region only cleavage cracks parallel to the free plane of the specimen occur.

Kupfer, Hildsorf, and Rusch (Ref. 33) report two general types of failure modes. They are a Type IV crushing failure for stress ratios occurring between 1/1 and -1/15 (-1/30 according to Ref. 40) and a Type I cracking failure for stress ratios from -1/15 to -1/-1.

The idealized failure modes used in this report are depicted in Fig. 13B. A cracking failure mode is assumed to occur from the tension-tension region to a stress ratio of -1/15. The direction of the crack(s) is assumed to be perpendicular to the largest tensile stress and to the free surface of the specimen. From the compression-compression region to the stress ratio of -1/15, a crushing failure mode is assumed to occur. The direction of crushing is assumed to be perpendicular to the largest compressive stress and perpendicular to the free surface of the specimen.

The method presented in this study can define cracked regions and not individual cracks which may occur in the superstructure. Within the context of the scope and purpose of this investigation, it is not necessary to obtain the exact or even an approximate number of the individual cleavage and tension cracks. However, it is required that regions of cracking or crushing be defined. Also, the effect of cracking or crushing on the stiffness of the element and its subsequent effect on the rest of the superstructure must be approximated.

2.1.8 Cracked or Crushed Concrete

Cracking or crushing of the concrete is deemed to occur when the principal stress has exceeded the idealized peak stress as defined in Fig. 6. The direction of cracking or crushing is assumed to be perpendicular to the direction of the corresponding principal tensile or compressive stress, whichever is appropriate. The concrete layer is assumed to have stiffness only in the uncracked or uncrushed direction. For example, the constitutive stress-strain relation for a concrete layer which has experienced a failure caused by the stress in direction 2 would be

$$\begin{Bmatrix} \dot{\sigma}_1 \\ \dot{\sigma}_2 \\ \dot{\tau}_{12} \end{Bmatrix} = \begin{bmatrix} E'_{1b} & 0 & 0 \\ 0 & 0 & 0 \\ 0 & 0 & 0 \end{bmatrix} \cdot \begin{Bmatrix} \dot{\varepsilon}_1 \\ \dot{\varepsilon}_2 \\ \dot{\gamma}_{12} \end{Bmatrix} \qquad (2.25)$$

The first principal direction is still effective in contributing stiffness to the element. The elasticity matrix, $[\bar{D}]$, would then be rotated from the principal stress coordinate axis to the x-y coordinate system for use in the element stiffness formulation.

The shear retention factor, which provides for shearing stiffness of the cracked or crushed concrete, has been used to model aggregate interlock behavior along the crack face (Refs. 15,16,34,35, 51). It has been reported that analytic results for the flexural analysis of slabs are insensitive to the particular value of the shear retention factor chosen (Refs. 15,16,35). In the present study it was assumed that aggregate interlock failure occurs immediately after cracking or crushing, and consequently the third term on the diagonal of Eq. 2.25 has been set to zero.

After cracking or crushing of the concrete layer, the layer will be incapable of sustaining the stress that caused the failure. This stress must be reduced to zero within the layer while still maintaining equilibrium between the external forces and internal stresses. Thus, unloading of the layer stress to zero necessitates the adjustment of the internal stress field of the slab. This adjustment or redistribution is accomplished through the use of fictitious forces which are statically equivalent to the amount of stress to be redistributed within the slab. A solution of the stiffness equations corresponding to these forces will produce the necessary redistribution of stresses.

Experimental evidence indicates that after attainment of peak strength, either tension or compression, the concrete stress-strain curve has a downward, i.e. unloading, leg (Refs. 4,13,19,20,33,36,52). It is assumed that this downward portion is a straight line (Ref. 27). Thus unloading proceeds at some finite rate determined by the slope of the downward portion of the stress-strain curve. This unloading branch can also be used to model the tension stiffening effect due to the gradual transfer of load from the cracked concrete to the steel reinforcing bars (Ref. 35).

2.1.9 Additional Considerations

This section describes for the sake of completeness two additional considerations that are relevant to the material presented herein. These considerations have not been included in the present analysis scheme due to the lack of verification by experimental evidence. One of the considerations, an isotropic stress-strain law, can possibly simplify the presented method. Whereas the other one, a constrained plastic-flow rule, could refine and complicate the presented scheme.

A. An isotropic stress-strain law

An alternative stress-strain formulation for biaxially stressed concrete can be derived by enforcing an isotropic constitutive elasticity relationship rather than an anisotropic relationship (see Eq. 2.13). The isotropic model was not used in the analysis scheme being reported. The isotropic model has the advantage that ν_1 and ν_2 are defined by the computed tangent moduli, E_{1b} and E_{2b}, and the stress ratio, α. Thus it eliminates the assumption of a value for either ν_1 or ν_2 and then making a subsequent check on the assumption, as was done in Section 2.1.6.

The assumption of an isotropic material will lead to the following basic relations:

$$E'_{1b} = E'_{2b} \tag{2.26a}$$

$$\nu_1 = \nu_2 = \frac{E_{2b} - E_{1b}}{E_{2b}\,\alpha_2 - E_{1b}\,\alpha_1} \tag{2.26b}$$

In addition to the above equations, the isotropic model requires the relation for peak strain,

$$\varepsilon_p = \frac{\sigma_p}{E_c}(1 - \nu\alpha) \tag{2.27}$$

to be satisfied for all portions of the stress space where the linear form of the concrete stress-strain curve is applicable. It must be noted that within constraints of present knowledge and accuracy of experimental measurements, the isotropic and anisotropic models, as presented in this report, are equally valid mathematical approximations to the observed concrete stress-strain behavior in the biaxial stress space. However, agreement of the isotropic model to experimental stress-strain curves is not as good as that for the anisotropic model. This lack of agreement, though small, is due to the additional constraint placed on the peak strain by Eq. 2.27. This is in contrast to the anisotropic model which allows one the freedom of obtaining a best fit approximation to the experimental peak strain points for a portion of this region.

B. Constrained plastic flow

When concrete crushes, plastic flow may take place. This flow may be constrained to follow a certain path depending upon the state of stress existing within the crushed concrete. A constrained plastic flow must satisfy a specified flow rule and yield surface criteria. Analytic models employing such formulation have been developed and have been used in slab analysis procedures (Refs. 15,35). Previous analytic studies have indicated that for regions of limited plastic flow, as would be the practical case in a reinforced concrete slab, there is a negligible difference between results based on the constrained and unconstrained formulations (Ref. 35). Therefore, since there is a negligible difference between the results, the present study employs the computationally more efficient unconstrained plastic flow concept.

2.2 Uniaxial Stress-Strain Relationships

The steel reinforcing bars and the beam concrete are considered to be in a uniaxial state of stress. The uniaxial stress-strain curve is assumed to follow the Ramberg-Osgood formulation (Refs. 27, 32,49) given by:

$$\varepsilon = \frac{\sigma}{E_i} + \left(\frac{1 - m}{m}\right) \frac{\sigma_s}{E_i} \left(\frac{\sigma}{\sigma_s}\right)^n \tag{2.28}$$

Where: σ = stress

ε = strain

E_i = initial modulus of elasticity

σ_s = secant yield strength equal to the ordinate of the intersection of the stress-strain curve and a line of slope $(m) \cdot (E_i)$

m = a dimensionless constant defining a line of slope $(m) \cdot (E_i)$ on the stress-strain curve

n = a dimensionless constant

The tangent modulus can be found by differentiating the stress-strain equation as follows:

$$\frac{d\sigma_1}{d\varepsilon_1} = \frac{E_i}{1 + n \left(\frac{1 - m}{m}\right)\left(\frac{\sigma_1}{\sigma_s}\right)^{n-1}} \tag{2.29}$$

The constitutive relation between the stress and strain increments is:

$$\begin{Bmatrix} \dot{\sigma}_1 \\ \dot{\sigma}_2 \\ \dot{\tau}_{12} \end{Bmatrix} = \begin{bmatrix} \bar{D}_{11} & 0 & 0 \\ 0 & 0 & 0 \\ 0 & 0 & 0 \end{bmatrix} \begin{Bmatrix} \dot{\varepsilon}_1 \\ \dot{\varepsilon}_2 \\ \dot{\gamma}_{12} \end{Bmatrix} \tag{2.30}$$

Where: $\bar{D}_{11} = d\sigma_1/d\varepsilon_1$ as defined in Eq. 2.29.

Subscript "$_1$" refers to the principal stress direction.

2.2.1 Beam Concrete

The complete stress-strain curve for uniaxial compressed concrete is approximated by the combination of three mathematically distinct curves (Refs. 27,32):

1. A nonlinear Ramberg-Osgood curve passing through the point of maximum compressive strength, f'_c, and a strain of $\bar{\varepsilon}$
2. A horizontal straight line passing through points $(f'_c, \bar{\varepsilon})$ to and $(f'_c, \bar{\varepsilon}_m)$
3. A straight downward leg passing through $(f'_c, \bar{\varepsilon}_m)$ to a zero stress level.

This downward slope Ed_c is not employed in the stiffness matrix formulation but is used to determine the fictitious forces resulting from the unloading of concrete layer stresses (see Section 2.1.8).

In steps 2 and 3 above, $\bar{\varepsilon}_m$ and Ed_c are determined from the table below (Refs. 27,32):

f'_c (ksi)	$\bar{\varepsilon}_m$	Ed_c (ksi)
5.60 (or greater)	0.0022	3000.
4.75	0.0022	1800.
3.90	0.0023	1250.
3.00 (or less)	0.0024	700.

Optimum empirical Ramberg-Osgood curve parameters were obtained by comparing numerous experimental and corresponding analytical stress-strain curves. These parameters were found to be (Ref. 27, 28,32):

$\sigma_s = f'_c$, 6" x 12" cylinder strength

$E_i = E_c$, initial Young's modulus for concrete (see Section 2.1.1)

$\bar{\varepsilon} = 0.0020$ in./in. for normal weight concrete

$n = 9$

$m = f'_c/(\bar{\varepsilon}\ E_i)$

The concrete tensile stress-strain curve is assumed to be linear with slope E_c up to the tensile strength of the concrete. Then a linear downward leg at a slope of Ed_t is continued to the zero stress level. The optimum Ramberg-Osgood curve parameters were found to be (Refs. 27,28,32):

$\sigma_s = f_t$, tensile strength

$E_i = E_c$

$n = 9$

$m = 1.0$ which forces the curve to be linear

$Ed_t = 800$ ksi

2.2.2 Beam and Slab Steel

Stress-strain relations for both mild steel reinforcing and prestressing strands are approximated with Ramberg-Osgood curves (Eq. 2.28). Curve parameters for the mild steel are listed as follows:

$\sigma_s = f_y$, yield strength of the steel

$E_i = E_s$, Young's modulus for steel which may be taken to equal to 29000 ksi

$n = 100.0$

$m = 0.70$

Mathematical distinction between yielded and non-yielded steel need not be made since the Ramberg-Osgood formulation provides a continuous stress-strain curve. Proper selection of the curve parameters can produce an almost perfectly plastic plateau in the case for mild steel. This plateau will have some finite slope but its value will be so small that for all practical purposes its effect on the structural behavior can be considered negligible.

Ramberg-Osgood parameters for the prestressing strands can be determined by a trial and error process of fitting various analytic stress-strain curves to the corresponding experimental curves. Very close agreement between the experimental and analytic curves is possible as shown in Fig. 35. In Fig. 35 the following values were used to generate the curve:

σ_s = 250. ksi,

E_i = 27000 ksi,

n = 0.67, and

m = 25.0

Special consideration must be made when the slab reinforcement is placed at an angle with respect to the longitudinal x-axis of the bridge. In this case, the principal stress direction, "1", does not coincide with the x-direction. Since the stress-strain relation must be expressed in the x-y coordinate system, a transformation is needed. The $[\bar{D}]$ matrix is transformed from the principal stress direction, which corresponds to the direction of the reinforcing bars, to the x-y axes. This transformation is shown in Eq. 2.28 where [T] is as previously defined by Eq. 2.24. The angle θ is the angle between the x-axis and the longitudinal direction of the reinforcing bars measured in a clockwise direction.

As can be seen in Eq. 2.30, the shearing stiffness of the reinforcing bars in the slab is not considered. Experimental studies on dowel action of reinforcing bars has been carried out and is available in the literature (Ref. 39). These experiments were concerned with investigating dowel action caused by the shearing deformation of the reinforcing bars in the plane of the slab. The dowel action discussed here should not be confused with the type of dowel action considered when discussing shear perpendicular to the plane of the slab. It was concluded from these studies that after a flexural type of failure in a reinforced concrete slab, the reinforcing bars do not distort across the cracks. This implies that the reinforcing bars do not carry excessive shearing forces. Thus for the analysis procedure reported herein, it was assumed that the steel reinforcing bars have a shearing stiffness of zero. Furthermore, it should be noted that this assumption is consistent with the assumption regarding the stress fields of the reinforcing bars, i.e. uniaxial stressing.

3. FINITE ELEMENT ANALYSIS

3.1 Introduction

The analysis procedure being reported is based on the finite element method. A complete treatment of the finite element method can be found in numerous books on the subject (e.g. Refs. 55, 64). Therefore, only the major concepts and necessary steps related to this research will be presented.

Assumptions and their implications concerning the finite element model are first discussed. A brief review of the finite element method is presented. Basic equations which help to introduce the notation used in later sections are given in this review section. The finite element method as applied to reinforced concrete slabs, reinforced and prestressed concrete beams (Refs. 19, 27 - 32), and reinforced and prestressed concrete highway bridges (Refs. 45,46,47) is discussed. Finally the solution procedure is outlined.

3.2 Assumptions

Several assumptions are employed in the development of the analytic model. The assumptions and associated implications will be discussed in the following paragraphs.

1. Geometry Restrictions:

   Bridge superstructures which are rectangular in plan, i.e. right bridges, and rhomboidal in plan, i.e. skewed bridges, are considered. The formulation presented in Sections 3.3 through 3.7 is applicable to right bridges. Section 3.8 extends the formulation so that skewed superstructures can be analyzed.

2. Assumptions Regarding Strain Distribution:

   Kirchoff's assumption that plane sections normal to the middle surface of the plate before deformation remain plane and normal after deformation is employed. Correspondingly, the Bernoulli beam theory, which applies the plane section assumption to beam bending analysis is used. Application of Kirchoff's and Bernoulli's assumptions are a usual practice in bending solutions for thin plates and beams. A thin plate is defined as a plate whose length and width dimensions are considerably greater than its thickness. It is also assumed that the slab and beams do not change thickness due to the applied forces. Thus the strains and stresses normal to the plane of the slab and beams are neglected. Application of Kirchoff's and Bernoulli's assumptions and the elimination of the normal strain offered the following simplifications:

   A. The reduction of a three-dimensional continuum problem requiring six stress components to define the state of stress at a point to a two-dimensional plate bending problem involving only three stress components (σ_x, σ_y, τ_{xy}) and a one-dimensional beam bending problem involving only one stress component (σ_x).

B. The strains at any depth in the plate or beam can be computed from the displacements of the reference plane.

The assumed strain distribution does not permit the inclusion of the bond failure phenomena where slippage between the reinforcing bars and the surrounding concrete takes place. A possible way of including bond-slip is briefly outlined in Ref. 43.

3. Small Deformations:

   The inplane and bending displacements are assumed to be small in comparison to the dimension of the slab. This implies that the geometry of the finite elements will not substantially change after deformation. Thus the geometry of the element need not be updated as the analysis proceeds.

4. Small Strains:

   The reinforced concrete slabs and highway bridge superstructures are assumed to be subjected to small strains. Thus the usual linear strain-displacement relations can be used as opposed to the more involved nonlinear equations necessary for the large strain formulation.

5. Layering:

   The inclusion of material nonlinearities will cause the stiffness properties of the beam and slab finite elements to vary with depth. These material nonlinearities, including cracking and crushing of the concrete and yielding of the steel, are inherent in the stress-strain relations. The existence of both steel and concrete in the same finite element also causes a variation of stiffness through the depth of the element. To facilitate the computation of the element stiffness, the finite element will be divided into a series of layers through the depth (Figs. 2,14,15). The total stiffness of the element will then be obtained by a summation of the stiffness properties of these individual layers. The stresses within a particular layer will be assumed to be constant within the layer for the purpose of computing the stiffness of each layer. Thus the stress field through the depth of the slab and beam will vary in a step-like manner. Increasing the number of layers will improve the representation of the stress field and consequently the accuracy.

3.3 Review of the Finite Element Method

The finite element method requires that the continuum be divided into an assemblage of subunits called finite elements. The elements are considered to be interconnected at discrete points called node points. In this context the continuum is a highway bridge superstructure (Fig. 1). The stiffness properties of the elements can be found using the principles of the finite element method. The result is a set of equilibrium equations relating node point forces to node point displacements:

$$\{F^e\} = [k^e]\ \{\delta^e\} \tag{3.1}$$

Where: $\{F^e\}$ = a vector of applied nodal forces on the element

$[k^e]$ = the element stiffness matrix

$\{\delta^e\}$ = a vector of nodal displacements for the element

Assembly of the elements to form the entire structural system results in a set of nodal equilibrium equations:

$$\{F\} = [K]\ \{\delta\} \tag{3.2}$$

Where: $\{F\}$ = a vector of the forces applied to the structure at the nodes

$[K]$ = the assembled stiffness matrix

$\{\delta\}$ = a vector of node point displacements

The unknown node point displacements, $\{\delta\}$, are obtained by solving this set of simultaneous equations.

It can be shown that the element stiffness matrix can be evaluated using either Eq. 3.3a or Eq. 3.3b (Refs. 55,64):

$$[k^e] = [C]^{-1^{T}} \int_v [Q]^T\ [D]\ [Q]\ dv\ [C]^{-1} \tag{3.3a}$$

$$[k^e] = \int_v [B]^T\ [D]\ [B]\ dv \tag{3.3b}$$

where v is the volume of the element.

This presentation will be restricted to an explanation of the matrices in Eq. 3.3 rather than their derivation. A two-dimensional approach employing the coordinates (x,y) will be used. The overall scheme is equally valid for a one-dimensional system, i.e. beam, where only a single coordinate position is needed.

The stress-strain relationships for a layer can be expressed by an elasticity matrix, [D], as shown in Eq. 3.4:

$$\{\sigma\} = [D]\ \{\varepsilon\} \tag{3.4}$$

The displacements within an element are assumed to be adequately described by a polynomial function of position within the element and initially unknown constants. This combination of functions and constants will be called a displacement function. Thus it is possible to define the displacements at any point within the element as:

$$\{\Delta(x,y)\} = [P(x,y)]\ \{\alpha\} \tag{3.5}$$

in which: $\{\Delta(x,y)\}$ = displacements at any position within the element defined by the coordinates (x,y)

$[P(x,y)]$ = particular functions of x and y, or their derivatives, used to describe the displacement fields

$\{\alpha\}$ = constant coefficients of the displacement functions

The individual $\{\alpha\}$ are evaluated using the boundary conditions given by the displacements at the node points of the element:

$$\{\delta^e\} = [C]\ \{\alpha\} \tag{3.6}$$

[C] is populated by substituting the coordinates of each node point, (x_n,y_n), into Eq. 3.5 where:

$$\{\delta^e\} = \{\Delta(x_n, y_n)\}$$

$$[C] = [P(x_n, y_n)] \tag{3.7}$$

Solving Eq. 3.6 for the constant coefficients lead to

$$\{\alpha\} = [C]^{-1} \{\delta^e\} \tag{3.8}$$

The differential operators necessary to define the strains (see Eq. 3.4) in terms of the displacement fields (see Eq. 3.5) will be called $[\Gamma]$. Thus

$$\{\varepsilon\} = [\Gamma] \{\Delta(x,y)\} \tag{3.9a}$$

Substitution of Eq. 3.5 into Eq. 3.9a gives:

$$\{\varepsilon\} = [\Gamma] [P(x,y)] \{\alpha\} = [Q] \{\alpha\} \tag{3.9b}$$

$[Q]$ is a connection matrix relating $\{\varepsilon\}$ to $\{\alpha\}$ within the element. Substitution of Eq. 3.8 yields

$$\{\varepsilon\} = [Q] [C]^{-1} \{\delta^e\} = [B] \{\delta^e\} \tag{3.9c}$$

Matrix [B] relates the strains within the element to the nodal point displacements.

A summary of the necessary steps in the finite element method to formulate the elemental stiffness matrix is as follows;

1. Choose displacement functions and formulate the displacement field (Eq. 3.5).

2. Express the node point displacements in terms of the constant coefficients by substituting the known nodal point locations into step 1 (Eq. 3.6).
3. Solve for $\{\alpha\}$ (Eq. 3.8).
4. Substitute $\{\alpha\}$ into step 1 (Eq. 3.5).
5. Identify the strain-displacement relations and perform the required differentiation of the displacement function (Eq. 3.9).
6. Find the stress-strain relationship [D] (Eq. 3.4).
7. Substitute the necessary matrices into Eq. 3.3 and perform the indicated integration. The result will be the element stiffness matrix.

3.4 The Layered Slab Model

The necessary steps in the formulation of the stiffness matrix by the finite element method were discussed, abstractly, in Section 3.3. These steps will be discussed in detail with respect to the nonlinear analysis of reinforced concrete slabs in the following sections. Explicit expressions for the matrices used in the layered slab model can be found in Appendix A.

3.4.1 Plate Bending and Inplane Displacement Functions

The purpose of this section is to present the displacement functions and describe the displacement field, $\{\Delta(x,y)\}$.

Displacement functions are chosen so that the deformation of the finite element can be adequately described. These displacement functions are polynomial expressions in terms of the (x,y) in-plane coordinate locations and unknown constants. As stated in Chapter 1 both the inplane and bending displacements must be considered.

The bending deformation of a plate can be fully described by the vertical displacement of the middle plane of the plate via assumptions presented in Section 3.2. The bending deformation will consist of the vertical displacement, W, the rotation about the x-axis, θ_x, and the rotation about the y-axis, θ_y. The rotations may be obtained by differentiating the vertical displacement. Thus the displacement field which describes the bending deformations can be expressed in vector form as

$$\begin{Bmatrix} W \\ \theta_x \\ \theta_y \end{Bmatrix} = \begin{Bmatrix} W \\ \frac{\partial W}{\partial y} \\ -\frac{\partial W}{\partial x} \end{Bmatrix} \tag{3.10}$$

The ACM-Adini, Clough, Melosh (Ref. 1) plate bending finite element will be used in this study. A review of the finite element displacement functions and the resulting stiffness matrices for the analysis of plate bending has been given by Clough and Tocher (Ref. 10), Wegmuller and Kostem (Refs. 57,58,59) and Kostem (Ref. 25). They concluded that the ACM rectangular finite element gives very satisfactory results. By increasing the number of ACM finite elements used to model a particular continuum an apparent convergence to classical solutions has been demonstrated for several example problems (Refs. 10,58). The ACM displacement function expresses the vertical displacement, W, as a twelve term polynomial (Refs. 1,10,55,64):

$$W(x,y) = A_1 + A_2x + A_3y + A_4x^2 + A_5xy + A_6y^2 + A_7x^3 + A_8x^2y + A_9xy^2 + A_{10}y^3 + A_{11}x^3y + A_{12}xy^3 \quad (3.11)$$

The inplane deformation is characterized by two displacement functions U and V. U is defined as the in-plane displacement directed along the x-axis and V is defined as the in-plane displacement directed along the y-axis. The in-plane displacement polynomials shown below have been presented by Clough (Ref. 9):

$$\begin{aligned} U(x,y) &= B_1 + B_2x + B_3y + B_4xy \\ V(x,y) &= B_5 + B_6x + B_7y + B_8xy \end{aligned} \quad (3.12)$$

Previous studies using these in-plane displacement polynomials have been successfully carried out (Refs. 58,59). The coefficients, A_i's in Eq. 3.11 and B_i's in Eq. 3.12, correspond to the constant coefficients of the displacement functions, $\{\alpha\}$, used in Eq. 3.5.

Nodal points are considered to be located at the four corners of the rectangular finite element positioned on the reference plane in the middle of the plate. Nodal points are designated by the letters, I, J, K, L as indicated in Fig. 14. Thus all nodal point displacements refer to reference plane deformations. The terms "reference plane" and "middle plane" are considered to be interchangeable in this report.

The displacement vector is described in terms of five displacements for each nodal point, i.e. two in-plane displacements and three bending displacements. The total number of displacements per finite element is twenty, i.e. four nodes at the corners with five degrees of freedom per node.

The displacement functions W(x,y), V(x,y), and U(x,y) can be used to define the displacement field $\{\Delta(x,y)\}$ for any location given by the coordinates (x,y):

$$\{\Delta(x,y)\} = \left\{\begin{matrix} U \\ V \\ W \\ \theta_x \\ \theta_y \end{matrix}\right\} = \left\{\begin{matrix} U \\ V \\ W \\ \frac{\partial W}{\partial y} \\ -\frac{\partial W}{\partial x} \end{matrix}\right\} \tag{3.13}$$

Thus Eq. 3.5 can be established once the displacement functions have been chosen.

The displacement field $\{\Delta(x,y)\}$, can be partitioned by separating it into those involving only in-plane displacements and those involving only bending displacements:

$$\{\Delta(x,y)\} = \left\{\begin{matrix} \Delta_u(x,y) \\ \text{-------} \\ \Delta_\phi(x,y) \end{matrix}\right\} = \left\{\begin{matrix} U(x,y) \\ V(x,y) \\ \text{------} \\ W(x,y) \\ \theta_x(x,y) \\ \theta_y(x,y) \end{matrix}\right\} \tag{3.14}$$

This will simplify further discussion of the stiffness matrices in the following sections. The subscripts u and ϕ refer to the in-plane displacements and the bending displacements respectively. Substituting the displacement functions (Eqs. 3.11 and 3.12) into the right-hand side of the above equation leads to

$$\{\Delta(x,y)\} = \left\{\begin{array}{c} \Delta_u(x,y) \\ \hline \Delta_\phi(x,y) \end{array}\right\} = \left[\begin{array}{c|c} P_u(x,y) & 0 \\ \hline 0 & P_\phi(x,y) \end{array}\right] \left\{\begin{array}{c} B \\ \hline A \end{array}\right\} \tag{3.15}$$

where $[P_u(x,y)]$ and $[P_\phi(x,y)]$ correspond to the in-plane and bending polynomial terms, respectively. The vector $\left\{\begin{array}{c} B \\ \hline A \end{array}\right\}$ is the partitioned $\{\alpha\}$ vector while the matrix $\left[\begin{array}{c|c} P_u(x,y) & 0 \\ \hline 0 & P_\phi(x,y) \end{array}\right]$ is the partitioned $[P(x,y)]$ matrix.

3.4.2 Strain-Displacement Relations

The strain-displacement relations are derived using the thin-plate small-deflection theory as mentioned in Section 3.2. The strain-displacement relationships for a point at a distance z from the reference plane are

$$(\varepsilon_x)_z = \frac{\partial U_z}{\partial x} \tag{3.16a}$$

$$(\varepsilon_y)_z = \frac{\partial V_z}{\partial y} \tag{3.16b}$$

$$(\gamma_{xy})_z = \frac{\partial U_z}{\partial y} + \frac{\partial V_z}{\partial x} \qquad (3.16c)$$

where: z = Distance of point under consideration from the reference plane

U_z = Displacement in the x-direction at any depth z

V_z = Displacement in the y-direction at any depth z

$(\varepsilon_x)_z$ = Strain in the x-direction at any depth z

$(\varepsilon_y)_z$ = Strain in the y-direction at any depth z

$(\gamma_{xy})_z$ = Shear strain at any depth z

The prescribed displacement functions correspond to reference plane displacements. The displacements U_z and V_z must be expressed in terms of these middle plane displacements. Kirchoff's assumption of plane sections permits the displacement for a point located at any distance, z, away from the reference plane to be expressed in terms of the inplane displacements of the reference plane plus the product of the rotations about the reference plane and the distance z as shown by Eq. 3.17:

$$U_z = U - z \frac{\partial W}{\partial x} \qquad (3.17a)$$

$$V_z = V - z \frac{\partial W}{\partial y} \qquad (3.17b)$$

$$W_z = W$$

Substituting Eq. 3.17 into Eq. 3.16 leads to Eq. 3.18 in which $\{\varepsilon\}_z$ represents the strain at depth z:

$$\{\varepsilon\}_z = \begin{Bmatrix} \varepsilon_x \\ \varepsilon_y \\ \gamma_{xy} \end{Bmatrix}_z = \begin{Bmatrix} \frac{\partial U}{\partial x} \\ \frac{\partial V}{\partial y} \\ \frac{\partial U}{\partial y} + \frac{\partial V}{\partial x} \end{Bmatrix} + z \begin{Bmatrix} \frac{-\partial^2 W}{\partial x^2} \\ \frac{-\partial^2 W}{\partial y^2} \\ -2 \frac{\partial^2 W}{\partial x \partial y} \end{Bmatrix} \qquad (3.18)$$

In the equation above, the strain vector $\{\varepsilon\}_z$ is separated into in-plane and bending contributions. Identifying the required differentials of Eq. 3.18 to be $[\Gamma_u]$ and $[\Gamma_\phi]$, corresponding to the in-plane and bending functions respectively, leads to

$$\{\varepsilon\}_z = [\Gamma_u]\ [P_u(x,y)]\ \{B\} + z\ [\Gamma_\phi]\ [P_\phi(x,y)]\ \{A\} \qquad (3.19)$$

Performing the differentiation results in the following equation:

$$\{\varepsilon\}_z = [Q_u]\ \{B\} + z\ [Q_\phi]\ \{A\} \qquad (3.20)$$

where: $[Q_u] = [\Gamma_u]\ [P_u(x,y)]$

$[Q_\phi] = [\Gamma_\phi]\ [P_\phi(x,y)]$

The strains are now expressed in terms of the matrices $[Q_u]$ and $[Q_\phi]$, which are obtained by differentiating the functions $[P_u(x,y)]$, $[P_\phi(x,y)]$, and multiplying by the associated constant terms $\{B\}$ and $\{A\}$.

As indicated by Eq. 3.8, the unknown polynomial coefficients in Eq. 3.20 can be related to the nodal point displacement vector $\{\delta^e\}$. The inplane and bending displacement fields have been previously defined as $\{\Delta_u(x,y)\}$ and $\{\Delta_\phi(x,y)\}$, respectively. Substitution of the nodal point coordinates (x_n,y_n) into the above displacement fields result in the following expressions:

$$\{\delta^e_u\} = \{\Delta_u(x_n,y_n)\} = [C_u]\ \{B\} \tag{3.21a}$$

$$\{\delta^e_\phi\} = \{\Delta_\phi(x_n,y_n)\} = [C_\phi]\ \{A\} \tag{3.21b}$$

where: $[C_u] = [P_u(x_n,y_n)]$

$[C_\phi] = [P_\phi(x_n,y_n)]$

$\{\delta^e_u\}$ and $\{\delta^e_\phi\}$ are the in-plane and bending nodal point displacements. Solving for the vectors $\{A\}$ and $\{B\}$ gives

$$\{A\} = [C_\phi]^{-1}\ \{\delta^e_\phi\} \tag{3.22a}$$

$$\{B\} = [C_u]^{-1}\ \{\delta^e_u\} \tag{3.22b}$$

Substituting Eq. 3.22 into the strain-displacement relation of 3.20 yields

$$\{\varepsilon\}_z = [Q_u]\ [C_u]^{-1}\ \{\delta^e_u\} + z\ [Q_\phi]\ [C_\phi]^{-1}\ \{\delta^e_\phi\} \tag{3.23}$$

Equation 3.23 is analogus to Eq. 3.9c and represents the strain displacement equation relating the strains at a distance z from the middle plane to the basic set of unknowns, i.e. the nodal point displacements.

For convenience, the $[B_u]$ and $[B_\phi]$ matrices, defined by Eqs. 3.24a and b, are substituted into Eq. 3.23. This results in an expression for the strain given by Eq. 3.24c:

$$[B_u] = [Q_u]\,[C_u]^{-1} \tag{3.24a}$$

$$[B_\phi] = [Q_\phi]\,[C_\phi]^{-1} \tag{3.24b}$$

$$\{\varepsilon\}_z = [B_u]\,\{\delta_u^e\} + z\,[B_\phi]\,\{\delta_\phi^e\} \tag{3.24c}$$

3.4.3 Layering

Multiaxial bending of the slab in both the longitudinal and transverse directions causes a continuously varying biaxial stress field within the concrete. The elasticity matrix, [D], for a nonlinear material depends on the stress level, and, therefore, will also vary throughout the finite element. In order to evaluate the volume integral of Eq. 3.3, [D] must be defined over the volume of the element. Since the explicit definition of the elasticity matrix for reinforced concrete under biaxial stress is prohibitevely complex for solution purposes, this stiffness matrix is evaluated by a combination of explicit integration and numerical integration. The numerical integration is performed using a summation process, as explained in the following paragraphs.

A slab finite element will be divided into a series of layers as shown in Fig. 14. This idealization facilitates inclusion of material nonlinearities through the depth, i.e. layer to layer, and through the plane of the slab, i.e. element to element. Each layer can have its own elasticity relation, $[D_i]$, which is dependent upon the representative state of stress existing within that layer, $\{\bar{\sigma}_i\}$. This implies that there is a constant state of stress and stiffness within any particular layer and that there is a step-like variation of stress and stiffness properties through the depth of the finite element. A state of plane stress is assumed to exist within each layer.

The representative state of stress in a layer is taken to be equal to the integrated average stress for the mid-plane of that particular layer. The location of the mid-plane of layer-i is defined by the distance $\bar{z}_i$ from the reference plane of the slab. The integrated average stress can be expressed in terms of the integrated average strain, $\{\bar{\varepsilon}\}_{\bar{z}_i}$, using Eq. 3.25:

$$\{\bar{\sigma}_i\} = [D_i]\ \{\bar{\varepsilon}\}_{\bar{z}_i} \tag{3.25}$$

By employing Eq. 2.24c, the integrated average strain may be defined as

$$\{\bar{\varepsilon}\}_{\bar{z}_i} = \frac{1}{\text{AREA}} \iint \left[[B_u] \;\middle|\; \bar{z}_i\ [B_\phi] \right] dxdy \left\{ \begin{array}{c} \delta^e_u \\ \hline \delta^e_\phi \end{array} \right\} \tag{3.26a}$$

where: $$\text{AREA} = \int_{-b}^{b} \int_{-a}^{a} dxdy = 4ab \tag{3.26b}$$

Substitution of Eq. 2.26a into Eq. 2.25 results in an equation defining the integrated average stress:

$$\{\bar{\sigma}_i\} = \frac{1}{\text{AREA}} [D_i] \iint \left[[B_u] \;\middle|\; \bar{z}_i\ [B_\phi] \right] dxdy \begin{Bmatrix} \delta_u^e \\ \hline \delta_\phi^e \end{Bmatrix} \tag{3.27}$$

Once the representative state of stress, given by $\{\bar{\sigma}_i\}$, is known the elasticity matrix, $[D_i]$, can be determined for various layers. Numerical integration can then be performed and the stiffness matrix can be evaluated. The elasticity matrix is a function of $\{\bar{\sigma}_i\}$ which is, in turn, dependent on the elasticity matrix. Thus the stiffness matrix is stress-dependent and a step-by-step solution scheme is required. This will be discussed in Section 3.9.

Reinforcing bars are treated just the same as any other layer in the integration process but of course a uniaxial elasticity relationship is used. A separate steel layer is assumed for each set of reinforcing bars placed at a particular depth and at a particular angle to the x-axis. Idealizing the reinforcing bars as a layer and not as individual entities requires the computation of an equivalent steel layer thickness. The equivalent thickness of a steel layer must be such that the total area of steel in a cross-section perpendicular to the bar direction remains the same. The equivalent thickness for a steel layer can be represented by Eq. 3.28:

$$T_s = \frac{A_s}{b_s} \tag{3.28}$$

where A_s indicates the area of a reinforcing bar and b_s is the bar spacing. This approach to modeling steel reinforcement allows consideration of reinforcing systems which have variable bar spacing and size from element to element and are placed in arbitrary directions and depths within the slab.

Progressive cracking and crushing of the concrete and yielding of the steel through the depth of the slab during loading can be monitored by obtaining the stress history for each layer. The angle of crushing or cracking of a particular concrete layer is not predefined by previous cracking or crushing and may vary from layer to layer through the depth of the slab.

3.4.4 Element Stiffness Matrix

Eq. 3.3b defines the element stiffness matrix

$$[k^e] = \int_V [B]^T \, [D] \, [B] \, dv \qquad (3.3b)$$

in which matrix [B] relates the strains to the nodal point displacements. Comparison of Eqs. 3.9c and 3.24c shows that Eq. 3.3b can be rewritten, in this context, as

$$[k^e] = \int_V \begin{bmatrix} [B_u]^T \\ z[B_\phi]^T \end{bmatrix} [D] \begin{bmatrix} [B_u] & z[B_\phi] \end{bmatrix} dv \qquad (3.29a)$$

Performing the indicated matrix multiplication results in

$$[k^e] = \int_v \begin{bmatrix} [B_u]^T [D] [B_u] & [B_u]^T [D] z [B_\phi] \\ [B_\phi]^T [D] z [B_u] & [B_\phi]^T [D] z^2 [B_\phi] \end{bmatrix} dv \qquad (3.29b)$$

The submatrices of Eq. 3.29b will be defined as shown below for convenience:

$$[k^e_{uu}] = \int_v [B_u]^T [D] [B_u] \, dv \qquad (3.30a)$$

$$[k^e_{u\phi}] = \int_v [B_u]^T [D] z [B_\phi] \, dv \qquad (3.30b)$$

$$[k^e_{\phi\phi}] = \int_v [B_\phi]^T [D] z^2 [B_\phi] \, dv \qquad (3.30c)$$

This will result in the following definition of the element stiffness matrix:

$$[k^e] = \begin{bmatrix} [k^e_{uu}] & [k^e_{u\phi}] \\ [k^e_{\phi u}] & [k^e_{\phi\phi}] \end{bmatrix} \qquad (3.30d)$$

where $[k^e_{\phi u}] = [k^e_{u\phi}]^T$

$[k^e_{uu}]$ is the inplane stiffness matrix relating the in-plane force to the in-plane displacements. $[k^e_{\phi\phi}]$ is the bending stiffness matrix relating bending forces to bending displacements. The off diagonal submatrices, $[k^e_{u\phi}]$ and $[k^e_{\phi u}]$ are the coupling stiffness matrices which interrelate the bending and in-plane actions (Ref. 44). The importance of the coupling stiffness terms has been discussed in Chapter 1.

As was noted in the discussion of layering in Section 3.4.3, the state of stress, and hence the terms of the elasticity matrix, are assumed to be constant throughout a particular layer. Therefore, [D] is not dependent on x or y coordinates. Likewise, since the displacement functions were independent of the coordinate z, $[B_u]$ and $[B_\phi]$ are also independent of z. Thus the integrations indicated in Eqs. 3.30 may be separated as shown below:

$$[k^e_{uu}] = \int_y \int_x [B_u]^T \left(\int_z [D] \, dz \right) [B_u] \, dxdy \qquad (3.31a)$$

$$[k^e_{u\phi}] = \int_y \int_x [B_u]^T \left(\int_z [D] \, zdz \right) [B_\phi] \, dxdy \qquad (3.31b)$$

$$[k^e_{\phi\phi}] = \int_y \int_x [B_\phi]^T \left(\int_z [D] \, z^2 dz \right) [B_\phi] \, dxdy \qquad (3.31c)$$

As also mentioned in Section 3.4.3, a summation process will be used to approximate the integration over z. This will be done by integrating over each layer and then summing the results and storing them in the appropriate $[D_{uu}]$, $[D_{u\phi}]$, or $[D_{\phi\phi}]$ matrix. Thus the terms $[D_{uu}]$, $[D_{u\phi}]$, and $[D_{\phi\phi}]$ may be defined as

$$[D_{uu}] = \int_z [D] \, dz = \sum_{i=1}^{L} [D_i] \, (Z_{i+1} - Z_i) \qquad (3.32a)$$

$$[D_{u\phi}] = \int_z [D]\, z dz = \frac{1}{2} \sum_{i=1}^{L} [D_i]\, (Z_{i+1}^2 - Z_i^2) \qquad (3.32b)$$

$$[D_{\phi\phi}] = \int_z [D]\, z^2 dz = \frac{1}{3} \sum_{i=1}^{L} [D_i]\, (Z_{i+1}^3 - Z_i^3) \qquad (3.32c)$$

Z_{i+1} and Z_i delineate the boundaries of layer-i. L is the total number of layers. $[D_{uu}]$, $[D_{u\phi}]$, and $[D_{\phi\phi}]$ are often called, respectively, the in-plane rigidity, the coupling rigidity, and the bending rigidity.

Substitution of Eqs. 3.32 into Eqs. 3.31 results in the following expressions which can be explicity integrated over the area of the elements:

$$[k_{uu}^e] = \int_y \int_x [B_u]^T\, [D_{uu}]\, [B_u]\, dxdy \qquad (3.33a)$$

$$[k_{u\phi}^e] = \int_y \int_x [B_u]^T\, [D_{u\phi}]\, [B_\phi]\, dxdy \qquad (3.33b)$$

$$[k_{\phi\phi}^e] = \int_y \int_x [B_\phi]^T\, [D_{\phi\phi}]\, [B_\phi]\, dxdy \qquad (3.33c)$$

This integration leads to the force-displacement relations for the finite element given by

$$\left\{ \begin{array}{c} F_u^e \\ \hline F_\phi^e \end{array} \right\} = \left[\begin{array}{c|c} [k_{uu}^e] & [k_{u\phi}^e] \\ \hline [k_{u\phi}^e]^T & [k_{\phi\phi}^e] \end{array} \right] \left\{ \begin{array}{c} \delta_u^e \\ \hline \delta_\phi^e \end{array} \right\} \qquad (3.34)$$

$\{F_u^e\}$ and $\{F_\phi^e\}$ are, respectively, the inplane and bending forces applied to the nodes of the element. $\{\delta_u^e\}$ and $\{\delta_\phi^e\}$ are, respectively, the resulting inplane and bending displacements at the nodes of the element.

3.5 Review of the Layered Beam Model

Theoretical development of the finite element analysis technique as applied to reinforced and prestressed concrete beams is presented in detail in Refs. 27 and 32. Also in the above references, the developed methodology is verified through numerous comparisons between analytic and experimental results. Since the major emphasis of this is on the layered slab and bridge models, only a brief review of the layered beam model will be presented for the sake of completeness. Explicit expressions for the matrices used in the layered beam model can be found in Appendix B.

Both inplane and bending displacement polynomials are prescribed for the beam element:

$$U(x) = B_1 + B_2 x \tag{3.35a}$$

$$W(x) = A_1 + A_2 x + A_3 x^2 + A_4 x^3 \tag{3.35b}$$

U(x) is the axial in-plane displacement of the beam while W(x) is the vertical bending displacement of the beam. The displacement expressions of Eq. 3.35 are a function of only the coordinate position (x) and not (x,y) as was the case for the slab. Because of this, the beam element can be considered as a one-dimensional structrual element. The displacement functions chosen for the beam are consistent with those chosen for the slab (see Eq. 3.11 and 3.12). The beam displacement field is defined by U(x), W(x), and $\theta_y(x)$ [i.e. $-\partial W(x)/\partial x$]. These three quantities can be obtained from Eq. 3.35.

Nodal points, designated by letters I and K, are located at the two ends of the beam element and are positioned on the reference plane as shown in Fig. 15. Thus there are six nodal point displacements for a beam, that is horizontal and vertical displacements and rotations at each end.

The remaining equations necessary to formulate the beam element stiffness matrix are analogous to those employed for the layered slab in Section 3.4 and will be briefly summarized below:

1. Strain-Displacement

$$(\varepsilon_x)_z = \partial U_z/\partial x \qquad (3.36)$$

$$U_z = U - z\ \partial W/\partial x \qquad (3.37)$$

$$(\varepsilon_x)_z = \partial U/\partial x - z\ \partial^2 W/\partial x^2 \qquad (3.38)$$

$$(\varepsilon_x)_z = [B_u]\ \{\delta_u^e\} + z\ [B_\phi]\ \{\delta_\phi^e\} \qquad (3.39a)$$

where

$$\begin{aligned}[B_u] &= [Q_u]\ [C_u]^{-1} \\ [B_\phi] &= [Q_\phi]\ [C_\phi]^{-1}\end{aligned} \qquad (3.39b)$$

2. Stress-Strain

$$(\bar{\sigma}_x)_i = (D_i)\,(\bar{\varepsilon}_x)_{\bar{z}i} \qquad (3.40)$$

where stress, strain, and the elasticity relationship are defined at the centroid of the layer

3. Layer Rigidities

$$(D_{uu}) = \sum_{i=1}^{L} (D_i)\,(Z_{i+1} - Z_i)\,(T_i) \qquad (3.41a)$$

$$(D_{u\phi}) = \frac{1}{2}\sum_{i=1}^{L} (D_i)\,(Z^2_{i+1} - Z^2_i)\,(T_i) \qquad (3.41b)$$

$$(D_{\phi\phi}) = \frac{1}{3}\sum_{i=1}^{L} (D_i)\,(Z^3_{i+1} - Z^3_i)\,(T_i) \qquad (3.41c)$$

(T_i) is defined as the layer width measured in the y-direction. Expressions for the layer ridigities (Eq. 3.41) can be further simplified by noting the following equivalent expressions

$(Z_{i+1} - Z_i)\,(T_i) = (A_i)$, layer area (3.42)

$\frac{1}{2}\,(Z^2_{i+1} - Z^2_i)\,(T_i) = (A_i\,\bar{Z}_i)$, statical moment for layer i (3.43)

$\frac{1}{3}\,(Z^3_{i+1} - Z^3_i)\,(T_i) = (A_i\,\bar{Z}^2_i + I_i)$, moment of inertia for layer i about the reference plane (3.44)

After the summations in Eqs. 3.41 are carried out, descriptive labels, as used in Ref. 27, of equivalent area, equivalent statical moment, and equivalent moment of inertia can be used in lieu of the more intangible labels of in-plane, coupling, and bending rigidities, respectively.

4. Element-Stiffness Matrix is the same as Eq. 3.30d, and the submatrices are defined as

$$[k^e_{uu}] = \int_x [B_u]^T (D_{uu}) [B_u] \, dx \tag{3.45a}$$

$$[k^e_{u\phi}] = \int_x [B_u]^T (D_{u\phi}) [B_\phi] \, dx \tag{3.45b}$$

$$[k^e_{\phi\phi}] = \int_x [B_\phi]^T (D_{\phi\phi}) [B_\phi] \, dx \tag{3.45c}$$

3.6 Unloading of Cracked or Crushed Concrete Layers

As stated in Section 2.1.8 a concrete layer that has cracked or crushed will be incapable of sustaining the stress that caused the failure. The stress within the layer must be reduced to zero by adjusting the internal stress field of the damaged layer. At the same time the internal stress field is adjusted, a statically equivalent force vector, referred to as a fictitious force vector, is applied to the structure so as to maintain equilibrium between the externally applied forces and the internal stress field (Refs. 27,32).

The fictitious force vector can be computed using

$$\{F^e_c\} = \int_v \Big[[B_u] \quad z[B_\phi] \Big]^T \{\dot{\sigma}_r\} \, dv \tag{3.46}$$

where the vector $\{\dot{\sigma}_r\}$ is the increment of stress in the x-y coordinate system to be redistributed and $\{F^e_c\}$ is the resulting vector of fictitious forces. The fictitious force vector can be separated into terms involving only in-plane fictitious forces, $\{F^e_{uc}\}$, and terms involving bending fictitious forces, $\{F^e_{\phi c}\}$, as shown below:

$$\left\{\begin{array}{c} F^e_{uc} \\ \hline F^e_{\phi c} \end{array}\right\} = \left\{\begin{array}{c} \int_v [B_u]^T \{\dot{\sigma}_r\}\, dv \\ \hline \int_v [B_\phi]^T \{\dot{\sigma}_r\}\, z dv \end{array}\right\} \tag{3.47}$$

If it is assumed that the stress to be unloaded is constant through the thickness of a layer, the integration of Eq. 3.47 over the thickness of the layer results in

$$\{F^e_{uc}\} = \left(\int_y \int_x [B_u]^T\, dx\, dy\right) \{\dot{\sigma}_r\} (Z_{i+1} - Z_i) \tag{3.48a}$$

$$\{F^e_{\phi c}\} = \left(\int_y \int_x [B_\phi]^T\, dx\, dy\right) \{\dot{\sigma}_r\} (Z^2_{i+1} - Z^2_i)/2 \tag{3.48b}$$

The amount of stress to be redistributed, $\{\dot{\sigma}_r\}$, for a particular load cycle can be computed in the principal stress space by multiplying the unloading modulus by the appropriate integrated average strain increment. Transformation of the stress vector from the principal to the x-y global coordinate system is necessary before substituting into Eqs. 3.48.

3.7 The Layered Bridge Model

3.7.1 Model Characteristics

The bridge superstructure is divided up into a series of beam and deck slab finite elements as shown in Fig. 1. The beams and deck slab are further divided up into a series of layers as shown in Fig. 2. The beam and slab models were combined so as to formulate the bridge model. Thus comments made for the layered beam model described in Section 3.5 and the layered slab model described in Section 3.4 are applicable to the layered bridge model and will not be repeated here.

The layered beam model was developed using an arbitrary reference plane. This reference plane is located, for convenience, at the mid-plane of the deck slab. The consideration of an arbitrary reference plane in the beam formulation enabled the eccentricity of the bridge beams to be included in the bridge formulation (Refs. 27,32,58, 59). Thus a realistic approach to modeling the structural behavior of the eccentric beam-slab system could be made. Layer coordinates and stiffness properties of the beam elements reflect this eccentricity and are computed using the mid-plane of the slab as the reference plane (see Eq. 3.41).

The displacement field of the bridge superstructure is defined by the in-plane, U and V, and bending, W, displacements of the reference plane. Compatibility between beam and slab displacements is maintained for points that are located at the beam-slab interface. Thus composite action between the beams and the deck slab is maintained.

3.7.2 Assembly of the Force-Displacement Equations

As stated previously in Section 3.3, the element stiffness matrix relates nodal point forces of the element to the nodal displacements of the element. This relationship is expressed in Eq. 3.1. The individual element stiffness matrices, including all beam and slab finite elements, are assembled to form the global stiffness matrix of the entire structure. These individual element stiffness matrices are generated as previously stated in Sections 3.4 and 3.5.

The global stiffness matrix relates the forces at the node points of the structure to the displacements of those node points. The process of assembly entails addition of the slab and beam element stiffness terms which contribute to the same force-displacement location in the global stiffness matrix. The total force at a particular node is determined by adding up the contributing forces from the individual elements for that particular node. Thus after incorporating subscript locations in Eq. 3.2, the force-displacement relationship for the entire bridge superstructure can be expressed as

$$\{F_i\} = [K_{ij}]\,\{\delta_j\} \qquad (3.49)$$

where i and j correspond to the various degrees of freedom at the node points. The subscript i indicates row positions in the force vector and stiffness matrix and j indicates row positions in the displacement vector and column locations in the stiffness matrix. Assembly procedures require that

$$\{F_i\} = \sum_e \{F_i^e\} \qquad (3.50a)$$

$$[K_{ij}] = \sum_e [k_{ij}^e] \qquad (3.50b)$$

where the summation is carried out over all individual slab and beam elements. The stiffness term k_{ij}^e in the above equation relates the force at node i to the displacement at node j for element e. Summing up the contributing stiffness terms from all elements as indicated in Eq. 3.50b gives the term K_{ij} which populates the (i,j) location in the global stiffness matrix. The assembly procedure guarantees displacement compatibility at the node points and results in Eq. 3.2. This equation is then solved for the nodal point displacements. The layer strains and stresses can then be computed by substituting the nodal point displacements into appropriate relationships (see Eqs. 3.26, 3.27 and 3.39a, 3.40).

3.8 Extension to Skewed Highway Bridge Superstructures

Skewed highway bridge superstructures are commonly encountered in the field. In these types of bridges the plan view has the shape of a parallelogram. The presented method can be extended to consider those cases in which the highway bridge is constructed with a skew angle.

For the case of skewed superstructures, the deck slab is divided into a mesh of rombiodal, i.e. parallelogram, finite elements rather than rectangular finite elements as was done for right bridge superstuctures. These parallelogram elements have the same skew angle as the bridge superstructure. Displacement functions used for the parallelogram finite element are expressed in skew coordinates rather than Cartesian coordinates and have the same form as used for the rectangular finite element (Refs. 11,64). The previously developed expressions in Sections 3.3 through 3.4 that used these displacement functions are therefore considered to be applicable in a skew coordinate system. It is only necessary to apply a series of transformations so as to obtain the required expressions in the cartesian coordinate system. A transformation to Cartesian coordinates is necessary since

1. Boundary conditions for the bridge superstructure are usually defined in the Cartesian system
2. The stress-strain relationships of Chapter 2 are evaluated using Cartesian stresses and strains
3. Relationships that define structural damage and serviceability criteria are evaluated using quantities defined in the Cartesian system.

Quantities in the skew coordinate system will be denoted with a prime while unprimed quantities will refer to the Cartesian coordinate system. The following transformations will be needed:

$$\{\delta\} = [T\delta]\,\{\delta'\} \quad \text{displacement} \tag{3.51a}$$

$$\{F\} = [TF]\,\{F'\} \quad \text{force} \tag{3.51b}$$

$$\{\varepsilon\} = [T\varepsilon]\,\{\varepsilon'\} \quad \text{strain} \tag{3.51c}$$

$$\{\sigma\} = [T\sigma]\,\{\sigma'\} \quad \text{stress} \tag{3.51d}$$

These transformations have been previously presented by Argyris (Ref. 2) and will only be reviewed in the following sections.

The beam elements are considered to already be in the Cartesian coordinate system and need not be transformed. These beams are assumed to be parallel to the coordinate axis that is common for both the Cartesian and the skewed coordinates, i.e. x-axis. Should they have been parallel to the other coordinate axis that is not common for both coordinate systems then a transformation would have been needed. Therefore, beam finite elements are treated as before. Only transformations for the skewed deck slab need be considered.

3.8.1 Transformation of Displacement

The polynomial displacement functions describing the bending and in-plane displacement fields for the parallelogram finite element can be obtained by writing Eqs. 3.11 and 3.12 in a skew coordinate system:

$$W' = W(x',y') \tag{3.52a}$$

$$U' = U(x',y') \tag{3.52b}$$

$$V' = V(x',y') \tag{3.52c}$$

where W', U', and V' are the displacements in the skew coordinate system shown in Fig. 16A. W' is in the same direction as W shown in Figs. 2 and 14. The rotations in the skew coordinate system, θ'_x and θ'_y, are obtained by differentiating W'.

The corresponding displacements in the Cartesian coordinate system are defined by

$$\begin{Bmatrix} \delta_u \\ \delta_\phi \end{Bmatrix} = \begin{bmatrix} T\delta_u & 0 \\ 0 & T\delta_\phi \end{bmatrix} \begin{Bmatrix} \delta'_u \\ \delta'_\phi \end{Bmatrix} \tag{3.53}$$

where $[T\delta_u]$ and $[T\delta_\phi]$ are the appropriate in-plane and bending transformation matrices respectively. Transformation matrix $[T\delta_u]$ can be obtained by considering the covariant components of an arbitrary in-plane displacement vector shown in Fig. 16b. Therefore from geometry relationships

$$[T\delta_u] = \begin{bmatrix} 1 & 0 \\ -1/\tan\beta & 1/\sin\beta \end{bmatrix} \tag{3.54}$$

Terms in the transformation matrix $[T\delta_\phi]$ are obtained by employing the chain rule for partial differentiation:

$$\begin{Bmatrix} W \\ \theta_x \\ \theta_y \end{Bmatrix} = \begin{bmatrix} 1 & 0 & 0 \\ 0 & \partial y'/\partial y & -\partial x'/\partial y \\ 0 & -\partial y'/\partial x & \partial x'/\partial x \end{bmatrix} \begin{Bmatrix} W' \\ \theta'_x \\ \theta'_y \end{Bmatrix} \tag{3.55}$$

From geometry the skew coordinate position (x',y') is given by

$$x' = x - y/\tan\beta \tag{3.56a}$$

$$y' = y/\sin\beta \tag{3.56b}$$

Thus,

$$[T\delta_\phi] = \begin{bmatrix} 1 & 0 & 0 \\ 0 & 1/\sin\beta & 1/\tan\beta \\ 0 & 0 & 1 \end{bmatrix} \tag{3.57}$$

3.8.2 Transformation of Forces

The in-plane and bending force transformations are $[TF_u]$ and $[TF_\phi]$ respectively and relate the forces in the skew system to the forces in the Cartesian system:

$$\begin{Bmatrix} F_u \\ F_\phi \end{Bmatrix} = \begin{bmatrix} TF_u & 0 \\ 0 & TF_\phi \end{bmatrix} \begin{Bmatrix} F'_u \\ F'_\phi \end{Bmatrix} \tag{3.58}$$

The force transformations can be determined by considering the contravariant components of the force vectors shown in Figs. 17a and 17b. From geometry considerations the following relationships can be determined:

$$[TF_u] = \begin{bmatrix} 1 & \cos\beta \\ 0 & \sin\beta \end{bmatrix} \tag{3.59a}$$

$$[TF_\phi] = \begin{bmatrix} 1 & 0 & 0 \\ 0 & \sin\beta & 0 \\ 0 & -\cos\beta & 1 \end{bmatrix} \tag{3.59b}$$

3.8.3 Transformation of Strain

Transformation of strain can be accomplished by employing the chain rule for partial differentiation:

$$(\varepsilon_x)_z = \partial U_z/\partial x = (\partial U_z/\partial x')\ (\partial x'/\partial x) + (\partial U_z/\partial y')\ (\partial y'/\partial x) \qquad (3.60a)$$

$$(\varepsilon_y)_z = \partial V_z/\partial y = (\partial V_z/\partial x')\ (\partial x'/\partial y) + (\partial V_z/\partial y')\ (\partial y'/\partial y) \qquad (3.60b)$$

$$(\gamma_{xy})_z = (\partial U_z/\partial y + \partial V_z/\partial x) = (\partial U_z/\partial y')\ (\partial y'/\partial y) + (\partial U_z/\partial x')\ (\partial x'/\partial y)$$

$$+ (\partial V_z/\partial y')\ (\partial y'/\partial x) + (\partial V_z/\partial x')\ (\partial x'/\partial x) \qquad (3.60c)$$

Substitution of Eqs. 3.53 and 3.56 into Eq. 3.60 will lead to

$$\begin{Bmatrix} \varepsilon_x \\ \varepsilon_y \\ \gamma_{xy} \end{Bmatrix} = \begin{bmatrix} 1 & 0 & 0 \\ 1/\tan^2\beta & 1/\sin\beta & -\cos\beta/\sin^2\beta \\ -2/\tan^2\beta & 0 & 1/\sin^2\beta \end{bmatrix} \begin{Bmatrix} \varepsilon'_x \\ \varepsilon'_y \\ \gamma'_{xy} \end{Bmatrix} \qquad (3.61)$$

where the skew strains are defined as

$$(\varepsilon'_x)_z = \partial U'_z/\partial x' \qquad (3.62a)$$

$$(\varepsilon'_y)_z = \partial V'_z/\partial y' \qquad (3.62b)$$

$$(\gamma'_{xy})_z = \partial U'_z/\partial y' + \partial V'_z/\partial x' \qquad (3.62c)$$

Equation 3.61 will be written as

$$\{\varepsilon\} = [T\varepsilon]\ \{\varepsilon'\} \qquad (3.63)$$

where $[T\varepsilon]$ is the strain transformation matrix.

3.8.4 Interrelationships Between the Transformation Matrices

The invariance of external and internal work is used to define relationships between the various transformation matrices. Utilization of these relationships can lead to an efficient procedure in extending the previously developed method for right angle highway bridge superstructures to one in which the skew angle is considered.

The invariance of external work in the Cartesian and skew coordinate systems can be expressed as

$$\{\delta\}^T \{F\} = \{\delta'\}^T \{F'\} \tag{3.64}$$

Substitution of the displacement and force transformation leads to

$$\{\delta'\}^T [T\delta]^T [TF] \{F'\} = \{\delta'\}^T \{F'\} \tag{3.65}$$

which establishes the relationship

$$[T\delta]^T = [TF]^{-1} \tag{3.66}$$

The invariance of internal work in the Cartesian and skew coordinate systems can be expressed as

$$\{\varepsilon\}^T \{\sigma\} = \{\varepsilon'\}^T \{\sigma'\} \tag{3.67}$$

Substitution of the strain and stress transformation matrices leads to

$$\{\varepsilon'\}^T [T\varepsilon]^T [T\sigma] \{\sigma'\} = \{\varepsilon'\}^T \{\sigma'\} \tag{3.68}$$

which establishes the relationship

$$[T\varepsilon]^T = [T\sigma]^{-1} \tag{3.69}$$

3.8.5 Modification of the Right Bridge Formulation to Consider Skew Bridges

Equation 3.9c will now express the strain in the skew coordinate system:

$$\{\varepsilon'\} = [B]\,\{\delta'\} \tag{3.70}$$

Transformation from the skew to the Cartesian coordinate system gives

$$\{\varepsilon\} = [T\varepsilon]\,[B]\,[T\delta]^{-1}\,\{\delta\} \tag{3.71}$$

Equating external and internal work leads to

$$\{\delta\}^T\,\{F\} = \{\delta\}^T\,[T\delta]^{-1\,T}\int_{v'}[B]^T\,[T\varepsilon]^T\,[D]\,[T\varepsilon]\,[B]\,dv'\,[T\delta]^{-1}\,\{\delta\} \tag{3.72}$$

After substituting Eq. 3.66, the stiffness matrix can be expressed as

$$[k^e] = [TF]\,[k_s^e]\,[TF]^T \tag{3.73}$$

where $[k_s^e]$ is the stiffness matrix in the skew coordinate system

$$[k_s^e] = \int_{v'}[B]^T\,[T\varepsilon]^T\,[D]\,[T\varepsilon]\,[B]\,dv' \tag{3.74}$$

The integration is carried out over the volume of the finite element which is expressed in the skew coordinate system:

$$dv' = dx'\,dy'\,dz\,\sin\beta \tag{3.75}$$

where

$$\sin\beta = \begin{vmatrix} 1 & -1/\tan\beta \\ 0 & \sin\beta \end{vmatrix} \qquad (3.76)$$

and is obtained from the coordinate relationships of Eq. 3.56.

Equation 3.46, used in determing the fictitious force vector, must also be modified to reflect the change in coordinate systems. Employing Eq. 3.72 and using the following definition,

$$\{\dot{\sigma}'_r\} = [T\varepsilon]^T [D] [T\varepsilon] [B] [T\delta]^{-1} \{\delta'\} \qquad (3.77)$$

gives

$$F^e_c = [TF] \int_{v'} [B]^T dv' \{\dot{\sigma}'_r\} \qquad (3.78)$$

where $\{\dot{\sigma}'_r\}$ is the stress to be redistributed expressed in the skew coordinate system and is considered to be constant throughout the volumn of the layer.

3.8.6 Application of Boundary Conditions

Boundary conditions may be imposed in the skew or Cartesian coordinate systems. Only boundary conditions which will prevent displacements and rotations will be considered.

Boundary conditions specified for the skew coordinate system will be applied to the skew stiffness matrix $[k^e_s]$ at the element level rather than at the global level. The particular procedure adopted does not require the reordering and deletion of equations. The procedure involves setting the row and column of the skew stiffness matrix, which corresponds to the fixed displacements, to zero. The diagonal element of the stiffness matrix is set equal to one. The corresponding position in the skew force vector is then set to zero.

Enforcement of boundary conditions specified in the Cartesian coordinate system is carried out on the global stiffness matrix expressed in Cartesian coordinates. The diagonal element of the stiffness matrix, which corresponds to the fixed displacment, is multiplied by a comparatively large number. The associated term of the force vector in the Cartesian system is set to zero.

3.9 Solution Scheme

The solution process can be divided up into four main phases:

1. Problem definition
2. Dead load and/or prestress solutions
3. Scaling procedure
4. Overload solution procedure

The detailed explanation of the computer program based on the reported analysis scheme including the required input and the generated output are contained in Refs. 46 and 47. A brief explanation of the above phases are contained in the following paragraphs:

1. Problem Definition

This phase defines the particular problem that will be solved. The following topics must be specified:

A. Bridge superstructure geometry -

Geometry for the beam and slab finite elements must be defined. This includes specifying concrete, mild steel reinforcing bar, and Prestress strand layer thicknesses, widths, and locations.

B. Material Properties -

Material properties for the concrete, mild steel reinforcing, and prestress strands must be defined. In particular, parameters used in defining the stress-strain relationships of Chapter 2 must be given. These include the compressive and tensile strengths, Young's moduli, and Ramberg-Osgood constants (Refs. 27,45).

C. Loading -

The loads on the superstructures must be defined. These loads may include dead loads, prestress forces, or live loads. The live loads are considered to be static in nature. Thus multiple solutions investigating several critical vehicle load positions may be desired.

D. Boundary Conditions -

Displacement boundary conditions for the node points are considered to be either fixed or free and must be specified. Advantage may be taken of situations where a line of symmetry exists. In such cases the size of the problem and correspondingly the solution time can be reduced if the appropriate boundary conditions for that line of symmetry are employed.

2. Dead Load and/or Prestress Solutions

Since the analytic technique considers material nonlinearities which are stress dependent, the initial stress state, i.e. the stress state occurring prior to overload, must be included in the solution procedure. Due to the nonlinear nature of the problem the initial stress state solution cannot be directly superimposed on a separate overload solution. Thus, the appropriate stress field must reflect not only those stresses due to the overload vehicle but also the initial stress state. Therefore an initial dead load and/or prestress solution may be performed to obtain the response and initial stress states of individual beams subjected to dead loads and/or prestressing. Also a dead load solution in which the entire bridge superstructure is considered may be performed. This solution is applicable when there is composite action between the deck slab and the beams under dead load and produces an initial stress state in both the beam and slab. The dead load solution procedure for the entire bridge superstructure would be desired in monolithic shored construction.

Nonlinear material behavior is considered in the dead load and prestress solutions. Thus iterations and the application of fictitious forces, which result from layer cracking or crushing, are performed.

3. Scaling Procedure

The scaling procedure prevents an excessive number of live load solutions from being conducted on essentially an elastic structure. Scaling of the prescribed live load forces takes place prior to the incremental overload solution procedure and following the dead load and/or prestress solution procedures. This procedure scales the initial live load solution so that the stress field which includes the dead load stress state is within specified tolerances of first cracking, crushing, or yielding whichever governs. Thus solution time is not wasted and an elastic solution is obtained in one load increment rather than in many load increments.

4. Overload Solution Procedure

The structural response to an overload vehicle is obtained by solving the set of global force-displacement equations in Section 3.7. The force vector is considered to be the increment of nodal point forces applied to the structure. The displacement vector is considered to be the displacement increment resulting from the applied force increment. Total forces and displacements are obtained by addition of the various increments.

The global stiffness matrix, which relates the force increment to the displacement increment, reflects the instantaneous stiffness of the bridge superstructure. An incremental approach is necessary because the global stiffness matrix which reflects the nonlinear material behavior is dependent upon the state of stress existing within the material and changes during the loading process. The state of stress is in turn dependent upon the displacement solution which is dependent upon the global stiffness matrix. Symbolically the above dependency relationship can be written in equation form as

$$\{\dot{F}\} = [K\ (\sigma + \dot{\sigma})\ ]\ \{\dot{\delta}\} \tag{3.79}$$

where [K] is shown as being dependent upon the current total stress plus the unknown stress increment. In the above equation $\{\dot{F}\}$ is the applied force increment and $\{\dot{\delta}\}$ is the resulting displacement increment. Thus it can be seen that the system of equations to be solved is nonlinear and cannot be solved with the usual techniques employed for a linear equation system. Thus, the formulation was modified to permit piecewise - linearization of the nonlinear phenomenon (Eq. 3.79). Two schemes were employed for the solution of the piecewise - linearized problem. These schemes will be explained in the following paragraphs.

The analytic results for the overload response are generated by solving a linear system of equations for a given load increment. The system of equations reflects the global stiffness of the structure at the time the load increment is applied. The tangent to the stress-strain curve for that particular layer is used in computing the element stiffness and finally the global stiffness matrix. Since the element stiffness and global stiffness matrices depend on the current state of stress, the stiffness matrix is recomputed for each load step. Also, iteration within each load step or load increment is performed until convergence of the solution for that load increment has been obtained. Solution of the displacement equations and updating of the global stiffness matrix occurs for each iteration. Load increments are scaled down or up so that an optimum load step is applied. This load step will ensure that the critical stress will be within some specified tolerance of the failure stress. When iteration within each load step is employed the procedure will be referred to as the "incremental-iterative" method. An approximation to the process of iterating within each load step is to update the stiffness matrix only at the start of each load increment. When iteration within each load step is not performed the term "incremental" method will be used.

The advantage of the incremental solution procedure over the incremental-iterative procedure lies in the fact that less solution time is needed for the former than the latter. The disadvantage of the incremental solution procedure is that judgment and experience must be used in selection of the size of the fixed load increment. If an excessively large load increment is selected then the incremental approach although being faster with respect to solution time, would overshoot the true analytic result. This is because a fixed load increment may cause a layer to overstress in which the stress within the layer may exceed the specified failure stress. Thus the incremental mode produces a load-deflection history that will appear stiffer and lie above a load-deflection history produced using the incremental-iterative mode. As the size of the fixed load increment is reduced the incremental solution will approach that of the incremental-iterative solution. When using the incremental mode, the load at which specific structural phenomena (e.g. cracking, crushing, or yielding) occurs can only be determined to lie within a specific load increment and not at a specific load as would be the case for the incremental-iterative approach. Therefore when damage (e.g. cracking, crushing, or yielding) occurs within a load increment, the reported load will be the load after the increment is applied.

Flow charts describing the basic operations for both the incremental and the incremental-iterative solution schemes are presented in Fig. 18. The following corresponds to a more elaborate explanation of several key steps used in the incremental method:

1. Formulate the element stiffness matrices based on the current total stress level.
2. Form the global stiffness matrix by assembling the element stiffness matrices.
3. Solve for the displacement increment using the global stiffness matrix and the force increment. Next compute the strain and the stress increments.
4. Unload the excess layer stresses and compute the corresponding fictitious force vector if applicable.

5. If the current total stress level has exceeded the lower tolerance on the failure envelope set the codes for newly cracked or crushed concrete layers and newly yielded steel layers.

6. Compute the total stress, strain, displacement, and force vectors by adding together the old totals and the current increments.

7. Apply a new force increment and go to Step 1.

An initial stress and displacement increment of zero is chosen for each load step. Thus the first iteration within a load step uses an elasticity matrix based on the stress level of the previous load cycle.

The following corresponds to a more elaborate explanation of several key steps used in the incremental-iterative method:

1. Formulate the element stiffness matrices based on the current total stress level.

2. Form the global stiffness matrix by assembling the element stiffness matrices.

3. Solve for the displacement increment using the global stiffness matrix and the force increment. Next compute the strain and the stress increments.

4. If the displacement increment has converged to a specified tolerance go to Step 7, otherwise continue.

5. If the stress state falls outside the upper tolerance set on the failure envelope then scale down the applied force

increment such that the total stress is between the upper and lower tolerances.

6. If the maximum number of iteration cycles has been reached go to Step 7; otherwise go to Step 1.
7. Unload the excess layer stresses and compute the corresponding fictitious force vector if applicable.
8. If the current total stress level has exceeded the lower tolerance on the failure envelope set the codes for newly cracked or crushed concrete layers and newly yielded steel layers.
9. Compute the total stress, strain, displacement, and forces vectors by adding together the old totals and the current increments.
10. Apply a new force increment and go to Step 1.

An initial stress and displacement increment of zero is chosen for each load step. Thus the first iteration within a load step uses an elasticity matrix based on the stress level of the previous load cycle.

Allowable limits on deflections, live loads, stresses, strains, number of cracked, crushed, or yielded layers, and crack widths can be specified for both the deck slab and beams to define serviceability limits for the bridge superstructure (Refs. 46,47). These checks can be used to terminate the overload solution procedure if a specific serviceability limit is exceeded. Thus an efficient solution procedure is developed, which will meet the requirements of the analyst.

4. CORRELATION WITH EXPERIMENTAL TESTS

This chapter contains comparisons of experimental and analytical studies on reinforced concrete slabs, and on reinforced and prestressed concrete highway bridge superstructures. These comparisons were made so as to provide a basis for the verification of the developed method. The experimental studies were obtained from the available literature and were not conducted as part of reported investigation.

The analytic studies were carried out using the method reported herein. A total of seven reinforced concrete slabs and five highway bridge superstructures were analyzed. To prevent repetition, two of the seven slabs along with three of the five bridges will be discussed in this chapter. Another bridge example is presented in Chapter 5 which presents a limited parametric study. Thus a total of four bridges are discussed. Detailed presentation of the slab examples can be found in Ref. 43, while the bridge examples can be found in Ref. 45. Within the scope of the reported investigation, satisfactory agreements for all slab and bridge examples were observed.

Development of the layered beam model was not part of this dissertation. The layered beam model had been previously verified and numerous test cases can be found in Refs 27 and 32.

4.1 Reinforced Concrete Slabs

A comparison of experimental and analytical results are presented in this section to verify that the developed analytical model accurately represents reinforced concrete slabs. Comparisons for the seven test cases listed below have been made. The reference which is listed along with the example, indicates where the experimental test is reported:

No. 1: A simply supported reinforced concrete beam (Ref. 66).

No. 2: A rectangular slab simply supported on two opposite sides and free on the other sides (Ref. 8).

No. 3: A corner supported square slab (Ref. 22).

No. 4: A simply supported square slab with orthogonal reinforcement (Ref. 53).

No. 5: A simply supported square slab with diagonal reinforcement (Ref. 53).

No. 6: A rectangular slab fixed on two opposite sides and free on the other two (Ref. 54).

No. 7: A square slab fixed on all edges (Ref. 54).

Only No. 2 and No. 7 in the above list will be presented in this report and will be referred to as the "Simple-Free Slab" and the "Fixed-Fixed Slab", respectively. Details of all examples can be found in Ref. 43.

The material properties of the test specimens in units of ksi are listed below:

Material Property	Simple-Free Slab	Fixed-Fixed Slab
f'_c-4"	----	5.06*
f'_c	5.150*	4.20
f_t	0.502	0.375
E_c	4330.	3100.*
f_y	50.0*	44.6*
E_s	30000.*	30000.

* Given

where: f'_c-4" = 4" x 4" x 4" cube strength
f'_c = 6" x 12" cylinder strength
f_t = direct tensile strength
E_c = Young's modulus for concrete
f_y = yield strength for steel
E_s = Young's modulus for steel

As noted in the above table, not all material properties needed in the analysis scheme were reported or obtained by the experimenters. In all examples either the 6" x 12" cylinder strength, f'_c, or the 4" x 4" x 4" cube strength, f'_c-4", was reported. If the concrete properties f_t and E_c were not experimentally obtained, they were computed from f'_c or f'_c-4" in the following manner:

1. If the cube strength is readily available then it can be converted to cylinder strength by any acceptable relationship such as the equation below (Refs. 4,41):

$$f'_c = 0.83\ (f'_c - 4'')$$

2. Young's modulus, E_c, was obtained using an acceptable formula such as those mentioned in Section 2.1.1. For example, in the case of the Simple-Free Slab, E_c was computed using Jensen's equation (Ref. 21).

3. The direct tensile strength, f_t, can be obtained from Ref. 41 which gives relationships between the cylinder strength and the direct tensile strength. The tensile strength used for the Simple-Free Slab is taken as a value previously used by other investigators (Ref. 8).

The following material properties were assumed for all test cases:

Poisson's ratio, $\nu = 0.2$
Compression unloading modulus = 1000 ksi (Ref. 27)
Tension unloading modulus = 800 ksi (Ref. 27)

Material properties needed for steel are the yield strength, Young's modulus, and the Ramberg-Osgood parameters (see Section 2.2.2). Young's modulus was assumed to be 30×10^3 ksi if it was not given.

4.1.1 Simple-Free Slab

This 54" x 40.5" x 4.14" slab (Slab B7 of Ref. 8) was loaded by a uniformly distributed moment along two opposite sides as shown in Fig. 19A. The constant moment region was idealized as one finite element. This is an adequate idealization because the stress field does not, theoretically, vary with position in the plane of the plate. The distributed moment was applied on the short sides which were considered as simply supported. The long sides of the slab were free to displace. Reinforcement consisted of 1/4" diameter deformed bars placed at ±45° to the slab edges. The bars closest to the surface of the slab were spaced at 1.5" with a minimum cover of 3/8". The bars in the next layer were spaced at 1.375" with a cover of 5/8".

The slab was divided into ten concrete layers and two steel layers as shown in Fig. 19B. T_s in Fig. 19B indicates the steel layer thickness and θ_x indicates the reinforcing bar angle measured from the x-axis. The location of the steel layers in the model corresponds to the centroidal location of the steel reinforcing bars in the test specimen. The experimental and analytical distributed moment versus curvature histories are presented in Fig. 20. The agreement between the experimental and analytic results is quite good with respect to the formation of the collapse mechanism and the ultimate load. Figures 21 and 22 show the applied moment versus concrete compressive strain and the moment versus average steel strain (tension side) histories, respectively, for both the experimental and analytic models. It can be noted that there is scatter of experimental strain readings about their average values for some levels of applied moment. The overall agreement between the experimental and analytic results is quite satisfactory.

4.1.2 Fixed-Fixed Slab

Two almost identical 6' x 6' x 4" square slabs were tested as part of the experimental study contained in Ref. 54. The slabs were fixed on all four sides and loaded by a concentrated center point load applied through a 9" x 9" steel plate. Reinforcing consisted of 1/4" and 3/8" diameter mild steel bars placed orthogonal to the slab edges. Both top and bottom tension reinforcements were used since tensile stresses are developed on both the top and the bottom surfaces of the slab due to the boundary conditions. Although the distribution of reinforcing varied throughout the slab, it is believed that an adequate model was developed by using a constant thickness for each steel layer. There is, however, no analytic difficulty in extending this formulation to consider a steel layer whose thickness varies from element to element.

The analytic model was developed using the material properties of the first experimental slab of this pair. These properties have been previously listed in Section 4.1. A quarter of the slab was discretized into sixteen finite elements as shown in Fig. 23. The depth was divided into six concrete layers and four steel layers as indicated in Fig. 24.

The load-deflection histories for the two experimental slabs and the analytic model are shown in Fig. 25. A shear punch failure occurred during the experimental tests and caused a premature collapse of the slabs before their full flexural capacity could be developed. Since the model considers only the flexural action, the shear punch type of failure could not be obtained analytically. The possibility of a shear punch failure can be examined through the use of appropriate design formulas. Enlarged portions of experimental and analytic load-deflection histories up to the occurrence of the shear punch failure are shown in Fig. 26. The figure indicates that when flexural action is dominant a close agreement between experimental and computed results is obtained. The slight difference between the analytic and experimental load-deflection histories may be attributed to the lack of total fixity observed by the experimenters. It was estimated that the fixed edge supports were 90% effective. The analytic work assumes full restraint along the edges in question. Thus, as indicated, the analytic model produced a load-deflection history which is stiffer than that obtained experimentally.

The analytic and experimental crack patterns for the top surface of the quarter slab are shown in Figs. 27A and 27B, respectively. The experimental crack pattern was not perfectly symmetric but it had essentially the same general form for all quadrants of the slab. The top surface cracks in both the experimental and analytic cases developed into concentric circle-like patterns around the center of the slab. The bottom surface crack patterns are shown in Figs. 28A and 28B. The center portion of the slab exhibited extensive cracking due to the shear punch failure. As would be expected, the analytic model did not reflect those cracks due to the shear punch failure. Good agreement was obtained between the experimental and analytic crack patterns that were primarily caused by the flexural action in the slab.

Both the analytic and experimental bottom surface cracks developed into fan-shape patterns radiating from the center point.

The fact that these experimental slabs failed by shear punch action does not reduce the value of the flexural analysis presented herein when applied to the bridge overload problem. Work currently underway (Ref. 23) substantiates former conclusions that punching shear failures are very unlikely in bridge decks subjected to vehicular loadings.

4.1.3 Observations

From the comparisons presented in Sections 4.1.1 and 4.1.2 and the additional comparisons contained in Ref. 43, several observations can be made for the developed analytic model. These observations include:

1. The inelastic flexural behavior of reinforced concrete beams up to collapse, can be obtained (Slab No. 1 of Ref. 43).
2. The inelastic flexural behavior of reinforced concrete slabs up to collapse, can be obtained (Slab No. 3 - 5, of Ref. 43 and simple-free slab of Section 4.1.1).
3. A variety of complex support conditions and loadings can be handled.
4. An increase in the number of concrete layers used to model the continuum improves the analytic approximation to the actual behavior (Slab No. 1 of Ref. 43).

5. Steel reinforcing bars placed at different angles and depths within the slab can be modeled as a system of uniaxially stressed layers.

6. In-plane boundary conditions and loadings have a pronounced effect on the behavior of reinforced concrete slabs (Slab Nos. 4 and 5 of Ref. 43).

7. If the primary response of the slab is due to flexure but the failure is due to punching shear, then the method can accurately predict the load-deflection behavior up to the initiation of the shear punch failure (Slab No. 6 of Ref. 43 and Fixed-Fixed Slab of Section 4.1.2).

8. Gross crack patterns can be simulated (Slab No. 6 of Ref. 43 and Fixed-Fixed Slab of Section 4.1.2).

4.2 Reinforced and Prestressed Concrete Beam-Slab Highway Bridge Superstructures

A comparison of experimental and analytical results will be presented in this section to verify that the developed analytic model accurately represents beam-slab bridge superstructures. Comparisons for the five test cases listed below have been made:

No. 1: A simply supported bridge at a skew of 75° with a span length of 65' and a width of 28' having four prestressed concrete beams (Bridge No. 2 Test-2500 of Refs. 7,12).

No. 2: A simply supported bridge at a skew of 60° with a span length of 50' and a width of 24' having four reinforced concrete beams (Bridge No. 3, Test-3300 of Refs. 7,12).

No. 3: A simply supported right bridge with a span length of 50' and a width of 15' having three prestressed concrete beams (Bridge 6A of Refs. 17,18).

No. 4: A simply supported right bridge with a span length of 50' and a width of 15' having three prestressed concrete beams (Bridge 6B of Refs. 17,18).

No. 5: A simply supported right bridge with a span length of 50' and a width of 15' having three reinforced concrete beams (Bridge 8B of Refs. 17,18).

Three of the above bridges are included in this chapter. They are Bridges Nos. 1, 5, and 2, and are referred to as Examples 1, 2, and 3, respectively, within context of this report. Results for Bridge No. 3 are presented in Chapter 5 as part of the parametric study. Detailed presentation of all bridges, i.e. No. 1 through No. 5 can be found in Ref. 45.

4.2.1 Example No. 1

A. Geometry:

This bridge was designed using the AASHO HS-20 design loading and was constructed in 1963. The overload test was conducted in 1970.

This bridge consisted of four prestressed precast AASHO Type III I-beams composite with a concrete deck. The deck had an average thickness of 7 inches. The actual bridge cross-section is shown in Fig. 29A while the idealized cross-section used for analysis purposes is depicted in Fig. 29B. In these figures only half of the cross-section is shown since the cross-section is symmetric about the longitudinal centerline.

The curb portion of the superstructure was considered to be in the same plane and of the same thickness as the slab. The roadway of this bridge was placed on a 4-1/2 percent grade and was superelevated to accommodate a 4-1/2° horizontal curve. The superstructure was built with a skew angle of 75° (90° designates a right bridge). The grade and superelevation were not considered in this analysis.

A plan view of the superstructure is shown in Fig. 30A. The length of the bridge was 65 ft. centerline of bearing to centerline of bearing. The four beams were placed at a center-to-center spacing of 8.9 ft.

Loads were applied to the bridge deck by 200 kip center hole jacks resting on bearing grills. The bearing grills were constructed from two 14 in. wide flange beams 46 in. long and spaced 30 in. from center-to-center. The bearing grills rested on concrete pads which were poured directly on the bridge deck. These pads created a horizontal loading surface and also prevented a punching shear failure from occurring. The location of the loaded areas are indicated by the cross-hatched rectangles in Fig. 30A. Eight loading jacks were used and each jack applied an equal increment of load.

Figure 30B shows the idealized superstructure. The idealized loads are indicated by the cross-hatched areas. The actual loaded areas positioned on line "A" in Fig. 30A have been extended to the centerline of the structure. Also the lengths of the loaded areas in the transverse direction have been extended to cover the distance between the beams. These modifications of the actual loaded areas while not necessary, permitted a discretization which results in a more efficient analysis. The loaded areas in Fig. 30B correspond to jacks and are designated by the letter "Q" and numbered from one to four. The values of the distributed loads have been chosen in such a manner that equal force is applied by each individual jack. The necessary ratios of the distributed loads, Q_1 through Q_4, which are inversely proportional to the areas that they cover, are listed in Fig. 30B. The loading devices are depicted in Fig. 31. The photograph clearly shows the jacks, bearing grills, and concrete pads.

The discretized superstructure is shown in Fig. 32. Thirty-six finite elements were used in the discretization. This resulted in a model having 49 node points with a total of 245 degrees of freedom. Node points and element numberings, dimensions, and loadings are indicated in the figure.

The beam discretization is shown in Fig. 33C. The finite elements used for modeling the beam have lengths that are equal to those used for the corresponding slab elements along the length of the bridge superstructure. The reference plane is shown as the mid-plane of the deck slab. Figure 33A shows the actual beam cross-section while Fig. 33B shows the idealized layered cross-section with appropriate dimension. The trapezoidal portions of the I-beam cross-section are approximated as rectangular sections.

Prestressing steel is also modeled as a layer or set of layers. In this example only the centerline eccentricity and total area of the draped strand were reported. The area was 4.792 sq. in. per beam and the centerline eccentricity was 6.45 in. from the bottom of the beam. An end eccentricity which produced no tension at release was computed and used in lieu of more precise information. One point draping was also assumed resulting in an analytic strand profile whose centroid varied linearly from 6.45 in. from the bottom of the cross-section at the centerline to 10.75 in. at the ends. The prestressing steel is shown as a dashed line in Fig. 33B. The location of the steel is that for a cross-section at midspan. The assumed strand profile is shown as the dashed line in Fig. 33C.

The prestress tension of the strands was calculated in Refs. 7 and 12. The computed value before release of the strands was found to be 173.5 ksi. The calculated steel stress at the time of the test was 127.5 ksi. The theoretical method presented herein requires that all losses except the initial elastic loss at transfer be deducted from the prestressing force, since the elastic loss is automatically calculated by the computer program. A prestress of 140.11 ksi was specified as input to the program. This gave a final prestress of 133.2 ksi after the elastic loss which is within 5% of that computed in Refs. 7 and 12.

The reinforced concrete deck slab was divided into six equal concrete layers and four steel layers. The layering and associated dimensions are given in Fig. 34. The quantities "T_s" and "θ_x" in the table below the figure designate the layer thickness and direction of reinforcement with respect to the x-axis. The exact reinforcement distribution in the slab was not specified and was selected using current design practices.

B. Material Properties

A "certified load-strain" curve for the prestressing strand used in the bridge was presented in Refs. 7 and 12. This stress-strain plot is shown as the dashed curve, designated as "B", in Fig. 35. The idealized Ramberg-Osgood stress-strain curve for the prestress strand is designated as "A" and is shown as the solid curve in Fig. 35. The arrow on the end of curve "A" implies that the analytic curve will extend beyond what is shown. The values needed to define the analytic curve are: Yield Stress, f_y = 250 ksi; Young's Modulus, E_s = 27,000 ksi; a Ramberg-Osgood "m" value m_s = 0.67 and a Ramberg-Osgood "n" value, n_s = 25.0.

The stress-strain curve for the steel reinforcement in the slab is shown in Fig. 36. A steel with a 36 ksi yield stress and a Young's modulus of 30,000 ksi was assumed. Ramberg-Osgood "m" and "n" values of 0.7 and 100.0 were chosen so that the analytic stress-strain curve would approximate that for mild steel.

Concrete strengths were determined by performing compression tests on cores taken from the deck slab and beams (Refs. 7,12). The cores taken from the slab had a maximum, minimum, and average compressive strength of 6.28 ksi, 4.58 ksi, and 5.50 ksi, respectively. Cores taken from the beams showed maximum, minimum, and average compressive strengths of 10.3 ksi, 7.5 ksi, and 8.7 ksi, respectively. Figs. 37 and 38 depict the uniaxial analytic Ramberg-Osgood compressive and tensile concrete stress-strain curves for the prestressed concrete beams. Beam concrete properties include: cylinder strength, $f'_c = 8.7$ ksi; direct tensile strength, $f_t = 0.609$ ksi; Young's modulus, $E_c = 5374$ ksi; downward compressive modulus, $Ed_c = 3000$ ksi; downward tensile modulus, $Ed_t = 800$ ksi; Ramberg-Osgood "m" value, $m_c = 0.8094$; Ramberg-Osgood "n" value, $n_c = 9.0$. Slab concrete properties include: $f'_c = 5.5$ ksi, $f_t = 0.44$ ksi, $E_c = 4273$ ksi, $Ed_c = 1000$ ksi, $Ed_t = 800$ ksi.

C. Results:

Bridge 2 was described as being "structurally sound" before the experimental tests were conducted (Refs. 7,12). The average traffic volume was approximately 2000 vehicles per day (counts made in 1968). This bridge had been in service for approximately five years. Load tests prior to the ultimate load test included lateral load-distribution studies and dynamic response studies to both rolling loads and vibratory loading. References 7 and 12 contain load-deflection histories for various points on the bridge superstructure. Deflection diagrams of the midspan cross-section for various load levels are presented. Photographs showing the mode of failure are also included.

Figure 39 shows the experimental and analytical load-deflection histories for node 18. A load increment of 37.8 kips was used in the analysis. This node point, which can be located in Fig. 32, corresponds to the midspan of the interior beam. The experimental points are plotted as open circles while the computed results are shown as solid lines. Curve "A" corresponds to an analysis which considers the skew angle of 75° while curve "B" corresponds to an analysis which does not consider the skew. The computed curves are shown with an arrow drawn on the end to indicate that they will extend further.

The numbers along the side of the load-deflection history correspond to load levels at which significant response phenomena occurs. The analytical response phenomena can be noted by observing the stress histories of the individual layers along with annotated printer plots generated by the program. The numbers along the curve correspond to the following response histogram:

1. At a load of 433 kips first cracking occurred in the beams. This was experimentally determined by using pulse velocity tests. The load at first cracking was computed by the method presented herein to be 382 kips.

2. At this load level three concrete layers in the interior beam have been predicted to crack. Figure 33B shows that these three concrete layers comprise 32% of the depth of the beam and that the analytic cracked region would extend past the center of gravity of the strand. Also at this load level a cracked region has been predicted to occur in the first concrete layer of the slab. The first concrete layer has a thickness of 1-1/6 in. (see Fig. 34) which corresponds to 16.5% of the slab thickness.
3. At a load of 521 kips visible cracking of the interior girders occurred.
4. At a load of 533 kips analytic results indicate that a predicted cracked region has penetrated to a maximum depth of four concrete layers in the interior girder corresponding to a depth of 53% of the total beam depth. Also a predicted cracked region has penetrated to a maximum depth of three concrete layers in the deck slab. This corresponds to 50% of the slab thickness.
5. At a load of 685 kips cracking of the bottom concrete layer of the exterior beam is predicted.
6. At a load of 760 kips the analytic cracked region has penetrated through seven concrete layers in the beam. This corresponds to a distance of 41-1/2 in. or 92% of the beam depth. Also at this load a predicted cracked region has progressed to a depth of 67% of the slab thickness.

7. At a load of 950 kips composite action of the interior girders with the deck slab was lost (Refs. 7,12). The vertical stirrups crossing the interface between the girder and the deck slab were sheared. A maximum interface shear of 0.375 ksi was predicted at a load of 950 kips. Also at this load level predicted cracked regions have penetrated completely through the interior beams.

8. At a load of 1025 kips yielding of the prestress strand in the interior girder was predicted.

9. The measured ultimate load was 1140 kips. At this load the interior girders were observed to fail after the formation of diagonal tension cracks. The computed ultimate load was 1139 kips. At this load crushing of the concrete in the deck slab was indicated by the analytic results.

10. The predicted ultimate load from Refs. 7 and 12 was 1267 kips.

Figure 40 shows a photograph of one of the prestressed concrete I-beams after the ultimate load had been reached. Extensive cracking is evident in the girder at the time of failure. This is in agreement to that predicted by the analytic model. The concrete diaphragms cracked at a relative early stage of loading and were found by the experimenters to have no measurable effect on the load-deflection behavior of the bridge superstructure (Refs. 7,12).

It is possible to obtain the load-deflection histories of all node points used in the discretization (Fig. 32). Figure 41 shows the load-deflection history for node point 18, which was previously presented in Fig. 39, plus additional node points that lie on the midspan node line, 4-11-18-25. As expected node point 25, which is located at the center point of the bridge superstructure, is seen to have the largest deflection for any given load.

Figure 42 shows the deflected shape of the midspan cross-section for various load levels. The dashed line and solid line correspond to the experimental and analytic results respectively. The bridge superstructure is seen to be experiencing considerable dishing in the transverse direction. This dishing was also noted in the experimental test. The unsymmetrical behavior indicated by the experimental results is due to geometric variables such as the skew and superelevation of the bridge superstructure. Also undetermined material property variations throughout the superstructure may contribute to the unsymmetrical deflected shape of the cross-section.

Figures 43 and 44 show the progression of analytic cracked regions on the bottom face of the deck slab and through the depth of the interior girder, respectively. These figures were constructed with the aid of the stress histories and printer plots generated by the computer program. Load levels of 420 kips, 723 kips, and 1108 kips are represented. Figure 43 is a plan view of the bottom surface of the deck slab divided into finite elements. The directions of the cracks are indicated by the dashed lines. Cracking is considered to occur throughout a layer of a given element and is represented symbolically by the single line in the figure. At a load level of 420 kips cracks have developed in the deck slab between the two interior beams. These cracks have been caused by the principal stress in the direction perpendicular to the given crack directions. At a load level of 723 kips cracked regions have developed over most of the bottom surface of the deck slab. From 723 kips to 1108 kips very little increase in the spread of the predicted cracked regions over the bottom surface is seen to occur. Therefore at 723 kips the bottom surface crack pattern is fully developed. Due to high twisting moments near the simple supports of the bridge superstructure, the cracks are seen to occur at a larger angle to the longitudinal direction than those cracks that occur near midspan. Crack depth within the slab can also be monitored. For the analyst's convenience crack depth is indicated on the printer plots of the program output.

The crack depth within the interior beam is shown in Fig. 44. The dotted line in the figure represents the assumed prestress profile. The predicted crack depth, designated by the cross-hatching, can be seen to progress through the entire depth of the girder as the ultimate load is approached. Experimental results corresponding to Figs. 43 and 44 are not included in the report since the data was not available (Refs. 7,12).

4.2.2 Example No. 2

A. Geometry:

This bridge was a reinforced concrete beam bridge and was designed using loading "B", as referred to in Refs. 17 and 18 shown in

Fig. 45. The bridge was constructed in 1958 and tested in 1970. Bridge 8B was a right bridge and had a length of 50 ft. center-to-center of bearing. The deck slab for the bridge had cross-sectional dimensions of 6.5 in. by 15 ft. Three rectangular reinforced concrete beams composite with the deck slab were used. Figures 46A, 46B, and 46C show the shape of the cross-section including dimensions and reinforcement details. The total weight of the bridge superstructure was 103.3 kips, which included an average beam weight of 204.9 kips/ft., a slab weight of 83.7 lbs./sq. ft. and a wood timber guard of 40 lbs./ft.

Loads were applied to the superstructures by a moving overload vehicle. The overload vehicle is shown in Fig. 47. Axle spacing of the overload vehicle is indicated in Fig. 45. The loading procedure consisted of placing weights on the overload vehicle which would then travel across the bridge usually thirty times. Figure 45 also indicates the range of axle weights used during the overload test. During the loading process deflections at the midspan position of each beam were measured. The load was then increased and another set of runs were made. This procedure was continued until the bridge superstructure collapsed onto the safety crib.

In the AASHO Road Tests the overload moved across the bridge rather than having the overload applied in a static manner by fixed devices as was done for Example Bridge 1. The moment envelope produced by the passage of the overload vehicle is of interest since the behavior of the bridge superstructure is primarily governed by the flexure action. A series of concentrated loads must be defined so that this moment envelope is approximated (Ref. 48). Figure 48 shows the plan view for the bridge superstructure. The beam locations are indicated in the figure. The small squares indicate where the assumed concentrated forces are placed.

Figure 49 shows the superstructure discretized into a series of finite elements. The node points, element numbering, and element dimensions are indicated in the figure. Since the structure was assumed to be symmetric in geometry and loading, one-quarter of the structure was analyzed. Fifteen slab finite elements were used in the discretization. The concentrated nodal point loads are indicated by the cross-hatched squares. The beam locations are indicated in the finite element discretization. It should be noted that the interior beam lies on a line of symmetry and only one-half of the cross-section is to be included in the model.

The actual beam cross-section and corresponding layered idealization is shown in Fig. 50. The layer dimensions and centroidal locations of the steel layers, indicated by the dashed lines, are presented in the above figure. The top row of steel reinforcing bars had an area of 2.66 sq. in. while the bottom row had an area of 4.57 sq. in.

Layering for the deck slab is indicated in Fig. 51. Six equal concrete layers and four steel layers were used. The table below the figure indicates the direction, thickness, and bar size/spacing for the various reinforcing bar layers.

B. Material Properties:

Figure 52 shows the idealized and experimental stress-strain curves for the mild steel reinforcement. Close agreement between the experimental and the idealized curves is evident. Material properties for the beam and slab steel include: $f_y = 50.4$ ksi, $E_s = 28800$ ksi, $m_s = 0.7$, $n_s = 100.0$. An average yield strength of 50.4 ksi was specified for the reinforcing bars placed in the concrete beams and slab. The range of yield strengths for the various sizes of reinforcing bars used in beams and slab was considered to be marginal. Thus no differentiation of the yield strengths was made.

Figures 53 and 54 show the idealized beam concrete compressive and tensile stress-strain curves, respectively. Slab and beam concrete material properties include: $f'_c = 4.88$ ksi, $f_t = 0.40$ ksi, $E_c = 5700.$, $Ed_c = 1800.$ ksi, $Ed_t = 800.$ ksi, $m_c = 0.77$, $n_c = 9.0$.

C. Results:

The AASHO Road Tests included (Ref 18): (1) a regular test traffic program of 500,000 trips, (2) dynamic load tests, and (3) increasing load tests, i.e. overload tests. Therefore, before the increasing load tests, the bridge was subjected to a variety of loading programs. The testing programs prior to overloading produced structural changes within the bridge superstructure. Tension cracks were found in all beams of the bridge immediately after removal of the forms and extensive tensile cracking in the reinforced concrete beams was observed following the regular test traffic program. The maximum crack width exceeded 0.01 in. Cracks were spaced between 6 in. and 8 in. Figure 55A shows cracks which were observed in the field after the removal of the forms. Analytic crack regions were formed after the dead load solution was performed by the computer. These regions designated by the cross-hatching are shown in Fig. 55B. The analytic cracked region shows very good overall agreement to those actually measured. Figure 55C indicates the extent of cracking measured after the regular test traffic. Cracks are seen to have penetrated into the deck slab.

The bridge failed in a flexure mode. Reference 18 presents the overload behavior of the bridge in terms of displacement history plots. The plots show the maximum static moment at midspan caused by the overload truck versus the average displacement at midspan of the three beams. The maximum static moment is computed from the known axle weights and spacings. The deflections reported on the plots were caused by the overload vehicle. Usually the overload vehicle made thirty trips with the same load. The load was then increased and the vehicle would make another thirty trips. If thirty trips were not made, the number of trips would then be indicated and circled on the moment-displacement history plots.

Figure 56 shows the midspan moment-displacement history for the bridge. The experimental and analytic results are indicated by the dashed and solid lines, respectively. A load increment of 140 kip-ft. was used in the analysis. Five vehicle load increments were used in the experimental test. The vehicle speed during the first

124 trips ranged from 30 to 35 mph. During the last three trips a speed of 15 mph was maintained. The dots on the experimental curve indicate load levels where permanent changes in the structure did not occur. The horizontal portions of the experimental load-deflection history indicate that permanent changes have occurred in the bridge superstructure. These permanent changes reflect material nonlinear phenomena such as cracking or crushing of the concrete and yielding of the steel. Only the live load moment caused by the truck is reported in Fig. 56. The total moment at midspan can be obtained by adding a dead load moment of 653 kips-ft. to the moment values used in Fig. 56 (Ref. 18). During the seventh trip of the last load increment, crushing of the top portion of the deck slab was observed.

The load levels numbered in Fig. 56 have the following significance in a response histogram:

1. A maximum midspan moment of 503 kip-ft. was caused by the regular test vehicle.
5. At a moment level of 1171 kip-ft. first yielding of the reinforcing steel placed in the beams was predicted in Ref. 18.
6. At a moment level of 1205 kip-ft. first yielding in the steel reinforcing was predicted by the method presented in this report.
7. At a moment level of 1390 kip-ft. first yielding of the reinforcing steel was measured.

8. An ultimate moment capacity of 1457 kips-ft. was predicted in Ref. 18.

9. The ultimate moment capacity was measured at 1550 kips-ft.

10. The computed ultimate moment capacity using the presented method was found to be 1680 kips-ft.

The analytic model and the experimental test both predicted crushing of the deck slab at the ultimate load. Figure 57A shows the bridge superstructure after failure. A photograph showing the reinforced concrete beams of the bridge at failure was not presented in Ref. 18. But instead a photograph of a beam of an "identical" bridge (Bridge 8A of Refs. 17 and 18) was presented. Bridges 8A and 8B showed very similar structural response. Therefore this photograph will be used in lieu of a photograph of the reported bridge example. Fig. 57B shows the crack depth in one of the reinforced concrete beams of Bridge 8A. Crack depth was predicted to penetrate through the reinforced concrete beams and into the deck slab as observed in the experimental test.

4.2.3 Example No. 3

A. Geometry:

This bridge will be presented as a last example and will be used to primarily demonstrate the effect of skew on the analysis. Figures 58A and 58B show the actual and idealized cross-sections, respectively. As can be noted, the curb section is included in the analysis.

Figures 59A and 59B show the actual and idealized plan views. The superstructure was built with a 60° skew. Two analyses will be presented: one considering the bridge as an "equivalent" right bridge and one considering the bridge as skewed. Figure 59B gives the finite element discretization employed in the analysis. The cross-hatched squares show where the static loading devices were placed. These devices are similar to those described for Example No. 1 in Section 4.2.1. The idealized loads are indicated in Fig. 59B by the solid dots which represent concentrated vertical forces. Experimental and analytical load-displacement results are given for the positons marked with an "X" in Fig. 59B.

Figures 60A and 60B show the actual and idealized beam cross-sections employed in the analysis. Eight concrete layers and three steel layers which are indicated by the dashed lines, were used. As can be seen the curb and parapet have been included in the modeling of the exterior beams and are assumed to be fully effective.

The slab layering is shown in Fig. 61. Four concrete and four steel layers were used. The table below the figure indicates the assumed size and spacing of the reinforcement in the slab.

It should be noted that the following assumptions were made due to the incompleteness of the information on the bridge (Refs. 7,12):

1. The exact distribution of reinforcing steel in the beam was not given and therefore was assumed.
2. The amount and distribution of reinforcing steel in the slab was assumed.

3. The curb and parapet were assumed to act in a fully composite manner with the rest of the superstructure. However, partial composite action may actually exist.

4. The effect of the diaphragms were neglected in the analysis.

B. Material Properties:

Figure 62 shows the analytic and experimental stress-strain curves for the slab and beam steel. The experimental curve for steel was approximated by specifying the following properties: $f_y = 65$ ksi, $E_s = 29000$ ksi, $m_s = 0.15$, $n_s = 5.0$. Beam and slab concrete was approximated by specifying the following properties: $f'_c = 6.5$ ksi, $f_t = 0.67$ ksi, $E_c = 4870$ ksi, $m_c = 0.67$, $n_c = 9.0$, $Ed_c = 3000$ ksi, $Ed_t = 800$ ksi.

C. Results:

Results for the positions marked with an "X" in Fig. 59 are given by: (1) Fig. 63 which shows the load-deflection history for the midspan of the exterior beam, and (2) Fig. 64 which shows the load-deflection history for the centerpoint of the superstructure. The experimental results are indicated by the open circles while the analytic results are indicated by curves marked with an "S" (skew) and an "NS" (no skew). A load step of 90.2 kips was used in the analysis. Several key load levels at which significant structural phenomena occurred are listed below:

1. Load causing first cracking in the slab:

   skew - 383 kips

   no skew - 337 kips

2. Load causing first yield (f_y = 40 ksi)

   experiment - 660 kips (measured from load-deflection history)

   skew - 834 kips

   no skew - 758 kips

   computed - 759 kips (Refs. 7,12)

3. Ultimate load

   experiment - 1580 kips

   skew - 1555 kips

   no skew - 1350 kips

   computed - 1465 kips (Refs. 7,12)

As expected, due to the assumptions made for the analysis (see Section 4.2.3, part A) differences between the computer and experimental load-deflection histories occurred. A significant improvement in the analytic load-deflection history was obtained by including the appropriate skew angle (curve "S" compared to curve "NS" in Figs. 63 and 64). Also the analytic results indicate that the solution which does not include the skew will result in a more flexible superstructure as compared to that which includes the skew.

4.2.4 Observations

From the comparisons presented in Sections 4.2.1, 4.2.2, 4.2.3 and the additional comparisons contained in Ref. 45 several observations can be made for the developed analytic model. These observations include:

1. Satisfactory results were obtained for both prestressed and reinforced concrete bridges.
2. Superstructures built with a skew can be considered.
3. Analytic results obtained using the correct skew angle give an upperbound to an analysis that neglects the skew where dimensions are projected onto a Cartesian coordinate system.
4. Superstructures with a slight superelevation can be considered.
5. Superstructures subjected to previous loadings, which have caused "minor" damage, can be considered.
6. Even though the analysis is based on static loading, the traverse of the vehicle can be approximated as the static loading which produces the moment envelope or which produces the maximum static moment diagram.
7. The incremental solution mode gives an upperbound to the incremental-iterative solution mode.
8. The nonlinear response of the individual beams subject to dead loads and/or prestress can be considered.

9. The nonlinear response of the entire bridge superstructure subjected to dead loads can be considered.

10. The elastic-live load response can be obtained.

11. The inelastic-live load response can be obtained.

12. The progression of cracking and crushing of the concrete and yielding of the steel can be monitored throughout the entire bridge superstructure.

13. Transverse shear in the beam caused by flexural stresses can be determined. Also the interfacial shear between the beam and the deck slab can be approximated.

14. The ultimate capacity of the bridge superstructure can be predicted.

5. PARAMETRIC STUDY

5.1 Introduction

This chapter describes a limited parametric study conducted using the developed analysis scheme and the relevant computer program. The analytic models used in this study are based on Bridge 6A. Bridge 6A was subjected to an overload as part of the AASHO Road Test (Refs. 17,18). Three areas were investigated:

1. The effect of load idealization
2. The effect of material properties
3. The effect of load increment size and solution method

The study on the effect of load idealization involves two analyses: (1) the moment envelope caused by the moving vehicle is approximated using nodal point forces, and (2) where the maximum static moment diagram is approximated by nodal point forces, i.e. positioning the vehicle at midspan to induce the maximum moment condition. This study will provide the analyst with a comparison between results using the simplified maximum moment diagram rather than the computationally involved moment envelope.

The study on the effect of material properties involves two analyses: (1) default values are employed, and (2) the reported test values are employed. Default values are defined as the acceptable approximations for material characteristics. These values are based on various experimental tests and code recommendations. The developed computer program automatically assigns these values unless more precise information is provided (Ref. 46). This study is of importance to the analyst since values for the actual material properties may be inconclusive due to the fact that: (1) the experimental values were not reported, (2) statistical evaluation is unreliable due to the excessive scatter or the limited number of experimental values, or (3) experimental values are inconsistent with past experience. If values for the material properties are inconclusive then the analyst may choose to use the default values. The default values are computed from previously reported formulae that are based on past experimental results. This study will provide the analyst with a comparison between results based on the default values and results based on the reported test values.

The study on the effect of load increment size and solution method involves three analyses which employs: (1) the incremental solution method using a fixed load increment of 150 kip-ft., (2) the incremental solution method using a fixed load increment of 50 kip-ft., and (3) the incremental-iterative solution method using a variable load increment. This study is presented since the analyst can select one of two solution methods (see Section 3.9) which have associated advantages and disadvantages and may affect the results considerably. The analyses are compared to the experimental results. From this comparison the effect of the size of the fixed load increment and the effect of the particular solution method used is illustrated.

It should be noted that this chapter presents a limited parametric study. Results of an overload analysis depend on numerous parameters including bridge geometry, boundary conditions, type of vehicle, load placement, material properties, and solution method. Also just as important, results depend on how the actual bridge and load configurations are idealized so as to be compatible with the finite element method of analysis. Furthermore, the beam and deck slab exhibit complex interactions depending on the aforementioned parameters. Therefore a quantitative extension of the results of this chapter to describe the overload behavior of other bridge and load configurations would be difficult if not impossible. Thus this study is of value to the analyst in a qualitative rather than a quantative manner.

5.2 The Model

Figures 48 and 65 show the plan view and the cross-section for the bridge. The bridge was simply supported and had a length of 50 ft. The deck slab had a thickness of 6.5 in. and a width of 15 ft. Transverse and longitudinal reinforcement in the deck slab consisted of #5 bars at 8 in. and #4 bars at 20 in., respectively. A prestress of 165 ksi was prescribed as input to the computer program.

The compressive strength of the concrete and the yield strength of the steel were the only material properties specified as input to the program. The other parameters needed to define the material behavior were automatically assigned default values by the computer program. Assumptions concerning the default values are presented in Ref. 46. The following material properties were used in the analysis:

For the slab concrete;

f'_c = 5.48 ksi (specified), f_t = 0.438 ksi (Refs. 41,46),

E_c = 4265.37 ksi (ACI Formula, Ref. 65, Ref. 46),

Ed_c = 1000.00 ksi (Refs. 43,46), Ed_t = 800.0 ksi (Refs. 43,46

For the slab steel;

f_y = 50.4 ksi (specified), E_s = 29000.0 ksi (assumed),

m_s = 0.70 (Refs. 43,46), n_s = 100.0 (Refs. 43,46)

For the beam concrete;

f'_c = 9.11 ksi (specified), f_t = 0.638 ksi (Refs. 41,40),

E_c = 5499.52 ksi (ACI Formula, Ref. 65, Ref. 46),

Ed_c = 3000.0 ksi (Refs. 27,46), Ed_t = 800. ksi (Refs. 27,46),

m_c = 0.828 (Refs. 27,40), n_c = 9.0 (Refs. 27,40)

For the beam steel;

f_y = 240. ksi (specified), E_s = 27000. ksi (Ref. 46),

m_s = 0.67 (Ref. 46), n_s = 25.0 (Ref. 46)

Bridge 6A was subjected to a moving overload vehicle. The vehicle made successive runs across the superstructure with increasing loads until the structure collapsed. The small squares shown in Fig. 48 represent concentrated vertical forces of equal magnitude. These nodal point forces are used to simulate the moment envelope caused by the overload vehicle.

The deck slab was divided into six equal concrete layers and four steel layers through the depth. The beams were divided into eight concrete layers and two steel (prestressing steel) layers. The finite element representation of the superstructure is shown in Fig. 49. Symmetry about the longitudinal and transverse centerlines is enforced. Thus only a quarter of the superstructure need be analyzed.

5.3 Effect of Load Idealization

Since the overload vehicle moves over the birdge, an infinite number of static load configurations are applied to the superstructure. The overload vehicle primarily induced longitudinal bending in the superstructure of Bridge 6A. In the general case the slab may be subjected to both longitudinal and transverse bending while the beams are primarily subjected to longitudinal bending. Construction of a static load configuration to simulate the moment envelope and thus to obtain the maximum possible state of stress at every point in both the slab and the beams is very difficult if not impossible to achieve. Therefore, a vehicular loading that will primarily produce longitudinal bending in both the deck slab and beams is examined. The idealized load configuration used in the analysis approximates the moment envelope for the longitudinal direction only. This moment envelope is produced as the vehicle traverses the superstructure and contains the maximum moment values.

From a user's standpoint, nodal point loads that approximate the maximum static moment diagram may be easier to determine than nodal point loads that approximate the moment envelope produced by the moving vehicle. In order to ascertain if substantial error in the general overload behavior of the bridge superstructure will result if the more simplified procedure in determing the nodal point loads is chosen, the bridge superstructure was analyzed with the following load configurations:

1. Loading A simulates the maximum static moment diagram caused by overload vehicle.
2. Loading B simulates the moment envelope caused by the moving overload vehicle.

Curves A and B in Fig. 66 depict moment diagrams which were produced by loadings A and B (each normalized to a value of unity), respectively. Curve C in Fig. 66 represents the actual moment envelope caused by the overload vehicle used in the experimental test on Bridge 6A. Curve C is also normalized to unity. It can be seen that points On the moment envelope (curves B and C lie above the static moment diagram (curve A). Thus it is expected that for the same midspan moment, loading B will produce higher stress states and correspondingly a larger "damaged" area than loading A.

Figure 67 shows the load-deflection history plots for loading A and B. The midspan moment values were obtained by taking moments about the midspan of the superstructure. The displacement corresponds to the displacement of node 24 shown in Fig. 49. As expected curve B falls below curve A indicating that loading B is a more severe load configuration. The small deviation between the two curves starts at approximately 1000 kip-ft. This deviation can be related to the different rates of cracking in the beams for the two loadings. Figure 68 shows the number of cracked layers in the slab and in the beams for loadings A and B. The difference between the two curves is highlighted by the cross-hatching in the figure. As can be seen the difference in the total number of cracked layers becomes significant at approximately 1000 kip-ft. which corresponds to that mentioned previously for the load-deflection histories.

From a practical point of view the difference between the load-deflection histories can be considered negligible. Furthermore, at 1000 kip-ft. cracking has penetrated through 80% of the depth of the beam. This condition would never be allowed from the serviceability standpoint. Thus the deviation after a load level of 1000 kip-ft. would never be realized. Therefore loading A can be used in the overload analysis rather than the more computationally involved loading B.

5.4 Effect of Material Properties

Quite often the analyst will have values for only the compressive strength of the concrete and yield strength of the steel. Knowledge about the remaining material properties needed for the analysis may be inconclusive or totally lacking. Therefore, acceptable default values for concrete or for steel are automatically assigned when desired by the analyst (Ref. 46). These values are determined using only the prescribed compressive strength or yield strength.

To estimate the error involved when using the default values rather than the actual material properties, analyses were obtained for:

1. Material properties based on the default values reported in Section 5.2 (Ref. 46)
2. Material properties based on test values reported in Refs. 17 and 18.

In the following figures, curves designated by the letter "D" correspond to those obtained using the default values listed under Section 5.2. Curves designated by the letter "A" correspond to those obtained using the actual properties reported in Refs. 17 and 18. The actual properties include:

For the slab concrete;

$f'_c = 5.48$ ksi, $f_t = 0.438$ ksi (assumed), $E_c = 5700$ ksi

For the slab steel;

$f_y = 50.4$ ksi, $E_s = 28800$ ksi, $m_s = 0.70$ (CF),
$n_s = 100.0$ (CF)

For the beam concrete;

$f'_c = 9.11$ ksi, $f_t = 0.71$ ksi, $E_c = 5900$ ksi, $m_c = 0.772$ (CF),
$n_c = 9.0$ (CF)

For the beam steel;

$f_y = 240$ ksi, $E_s = 27600$ ksi, $m_s = 0.75$ (CF),

$n_s = 22.829$ (CF)

Values designated by "CF" have been determined by curve fitting the analytic stress-strain curves to the experimental stress-strain curves reported in Refs. 17 and 18. Figure 69 shows the stress-strain curves for the mild steel reinforcing, the prestressing steel, the beam concrete in compression, and the beam concrete in tension.

Figure 70 shows the resulting load-deflection histories using the default values (D) and the reported values (A). The difference between the two load-deflection curves shown in Fig. 70 is about 4% for both the ultimate and the first cracking loads. The difference between an analysis using the automatically selected default values rather than experimental values, which at best are only estimates, can be considered negligible within practical engineering limits.

5.5 Effect of Load Increment Size and Solution Method

As mentioned in Section 3.9 the user can choose one of two methods used in the overload analysis procedure: (1) the incremental method, or (2) the incremental-iterative method. In the incremental-iterative method load increments are automatically scaled so as to allow only one layer at a time to fail. Iterations within each load step take place so as to obtain a solution which approximately satisfies convergence of the displacement field. In the incremental method fixed load increments are applied to the structure. More than one layer at a time may fail and iterations are not performed. Each successive solution uses stiffness coefficients based on a stress state of the previous load step. If the load increment is too large significant error in the solution may result.

Figure 71 presents results used to evaluate the effect of the load increment size on the overload behavior. These curves correspond to analyses for:

1. The incremental-iterative method (curve B in Fig. 71)
2. The incremental method using a fixed moment increment of 50 kip-ft. (curve C in Fig. 71)
3. The incremental method using a fixed moment increment of 150 kip-ft. (curve D in Fig. 71)

Curve A in Fig. 71 represents the experimental load-deflection curve presented in Ref. 18. The load-deflection curves generated using the incremental method, i.e. curves C and D, tend toward the load-deflection curve generated using the incremental-iterative method, i.e. curve B, as the size of the fixed load increment is reduced. The measured material properties from Refs. 17 and 18, which are presented in Section 5.4, were used in the generation of curves B, C, and D.

Care and judgment must be used when specifying the fixed load increment. It has been found that for prestressed superstructures a fixed load increment size equal to about 10% of the load at first cracking is acceptable. When using the incremental-iterative method the load increment size is automatically selected and the analyst need not be concerned with its value.

5.6 Observations

Several observations can be made with respect to the parametric study:

1. The static load configuration which simulates the overload vehicle need only produce a moment diagram which approximates the shape of the true moment envelope near the midspan region.
2. The shape of the load-deflection curve for prestressed concrete highway bridge superstructures is particularly sensitive to the tensile strength of the concrete and to the shape of the stress-strain curve for the prestress strand.
3. Acceptable results within practical engineering limits can be obtained for the overload behavior by knowing the compressive strength of the concrete and the yield strength of the steel. Additional material properties needed in the analysis are automatically assigned values that are consistent with observed experimental behavior of steel or concrete.
4. The incremental method which employs a fixed load increment uses substantially less computer time than the incremental-iterative method which employs a variable sized load increment. The incremental method of solution can be used to generate the overload behavior of highway bridge superstructures if a sufficiently small load step is specified by the analyst.

6. SUMMARY AND CONCLUSIONS

The research contained herein describes a method for the overload analysis of beam-slab type highway bridge superstructures. Reinforced concrete slabs or beams can be analyzed as a special case of the highway bridge superstructure. Both right bridges and bridges built with a skew can be analyzed. The method gives a solution for the flexural response of the structure including displacements, strains, stresses, and regions of cracking and crushing of the concrete and yielding of the steel. Serviceability criteria at various load levels can also be evaluated (Ref. 46). The solution is applicable up to the flexural collapse of the bridge superstructure.

The finite element method was used as the basic modeling technique. The deck slab and beams are discretized into a series of finite elements interconnected at the node points. These finite elements are further divided into a series of layers through the depth. The elements and layers provide a means to monitor the spread of cracking and crushing of the concrete and yielding of the steel throughout the bridge superstructure. Also this layering enables the consideration of material variations through the depth of the finite element and of nonlinearities inherent in the material stress-strain curves. The following material nonlinearities have been considered in the analysis:

1. Nonlinear and linear stress-strain behavior of slab and beam concrete

2. Nonlinear and linear stress-strain behavior of prestressing steel
3. Elastic-plastic behavior of mild steel reinforcing bars
4. Cracking and crushing of the slab and beam concrete
5. Yielding of the steel

The nonlinearities have been incorporated into the analysis scheme via:

1. Nonlinear/linear uniaxial Ramberg-Osgood stress-strain laws for the beam concrete
2. Nonlinear uniaxial Ramberg-Osgood stress-strain laws for the beam and slab steel
3. Nonlinear/linear biaxial stress-strain laws for the slab concrete
4. Biaxial and uniaxial failure criteria for the slab and beam concrete, respectively

The overload solution is obtained by using a piece-wise linear tangent stiffness solution technique in which solutions are obtained for each load increment up to collapse. The total solution for a particular load level is obtained by adding up the previous solution increments. Two different tangent stiffness solution techniques have been developed: the incremental-iterative method and the incremental method. In the incremental-iterative method iterations and updating of the tangent stiffness matrix take place within each load step until approximate convergence of the solution is obtained. In the incremental method iterations are not performed and a stiffness matrix based on the previous solution is used. The major differences between the two methods are summarized below:

	Incremental-Iterative Method	Incremental Method
Iterations are performed for each load step	Yes	No
Automatic selection of the optimum load step	Yes	No
Load step is variable	Yes	No
Approximate convergence of the solution	Yes	No
Failure criteria may be violated and layers may overstress	No	Yes
Solution time is reduced	No	Yes

The predicted response of five bridges and seven reinforced concrete slabs have been compared with corresponding experimental results (Refs. 43,45). Four of the bridges, which includes two right bridges and two skewed bridges, and two of the slabs have been presented in this study. In all cases adequate agreement was obtained when the primary behavior mode was flexural. Experimental and analytical load-deflection curves were compared for all problems. Crack patterns and strain histories were compared where available. The beam model had been previously developed and was not part of this dissertation. Numerous comparisons between the analytic and experimental results for the beam model can be found in Refs. 27 and 32.

The assumptions in Sections 1.4 and 3.2 are adequate for the inelastic analysis of beam-slab type highway bridges subjected to vehicular overloading. It will be emphasized that:

1. Flexural behavior is adequate to describe the overload response for the cases presented herein
2. Dynamic response phenomena need not be considered for the cases presented herein
3. Shear punch, local buckling, and lateral torsional buckling need not be considered for the cases presented herein

The following conclusions can be made:

1. Concerning beams (From Refs. 27, 32)
    - A. The layer idealizations for the concrete, reinforcing bars, and prestressing steel are adequate.
    - B. The uniaxial Ramberg-Osgood stress-strain laws for concrete, mild steel, and prestressing steel are adequate
    - C. The elastic/inelastic response due to dead loads and/or prestress can be obtained.
    - D. The inelastic flexural behavior up to the collapse of reinforced or prestressed concrete beams or of steel beams can be obtained (due regard to the assumptions of Sections 1.4 and 3.2 must be made).

E. The progression of cracking and crushing of the concrete and yielding of the steel can be monitored throughout the beam.

F. The downward portion of the stress-strain curve for concrete can be used to produce a globally adequate redistribution of stress when modeling the effect of cracking and crushing in a one dimensional space.

G. Transverse shear stresses in the beam caused by flexure can be determined.

2. Concerning Slabs (From Ref. 43)

A. The layer idealizations for the reinforcing bars and concrete are adequate.

B. The uniaxial Ramberg-Osgood stress-strain law is adequate for the steel reinforcing bars.

C. The biaxial stress-strain law for concrete is an adequate idealization.

D. The elastic/inelastic dead load response can be obtained.

E. The inelastic flexural behavior up to collapse of reinforced concrete slabs can be obtained (due regard to the assumptions of Sections 1.4 and 3.2 must be made).

F. The progression of cracking and crushing of the concrete and yielding of the steel can be monitored throughout the slab.

G. The downward portion of the stress-strain curve for concrete can be used to produce a globally adequate redistribution of stress when modeling the effects of cracking and crushing in a two dimensional space.

3. Concerning beam-slab highway bridge superstructures (From Ref. 45)

   A. The elastic/inelastic response of bridge superstructures subjected to dead loads can be obtained.

   B. The inelastic flexural behavior up to collapse of reinforced or prestressed concrete beam-slab highway bridge superstructures built with or without a skew can be predicted (due regard to the assumptions of Sections 1.4 and 3.2 must be made.)

   C. The progression of cracking and crushing of the concrete and yielding of the steel can be monitored throughout the entire bridge superstructure.

   D. The downward portion of the stress-strain curve for concrete can be used to produce a globally adequate redistribution of stress when modeling effects of cracking and crushing.

   E. The interfacial shear between the beam and the deck slab can be approximated.

F. The overload behavior of the superstructure can be compared with the serviceability criteria to define a condition of "failure".

7. FIGURES

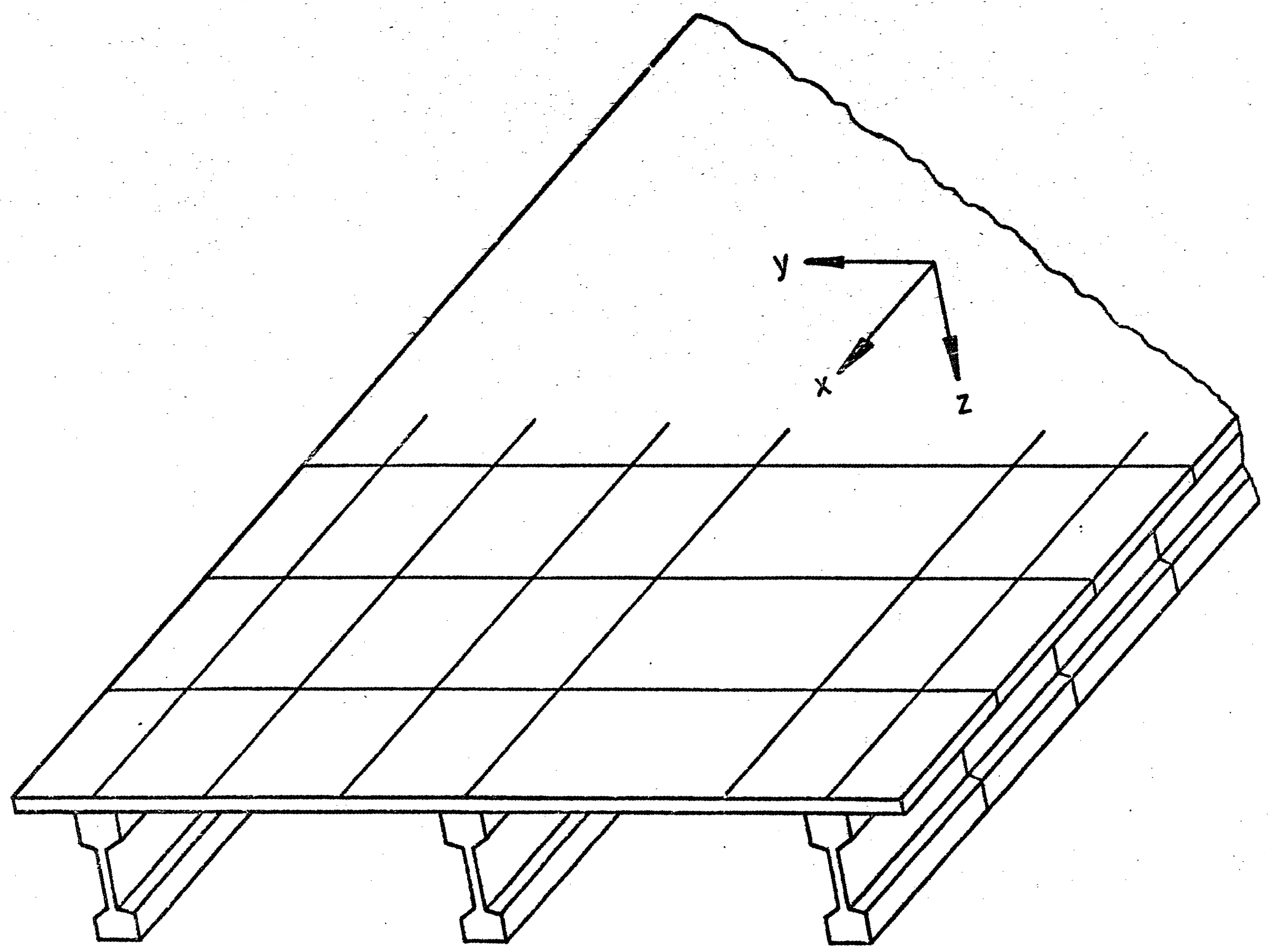

Fig. 1 Typical Beam-Slab Type Bridge and Its Idealization by Beam and Slab Finite Elements

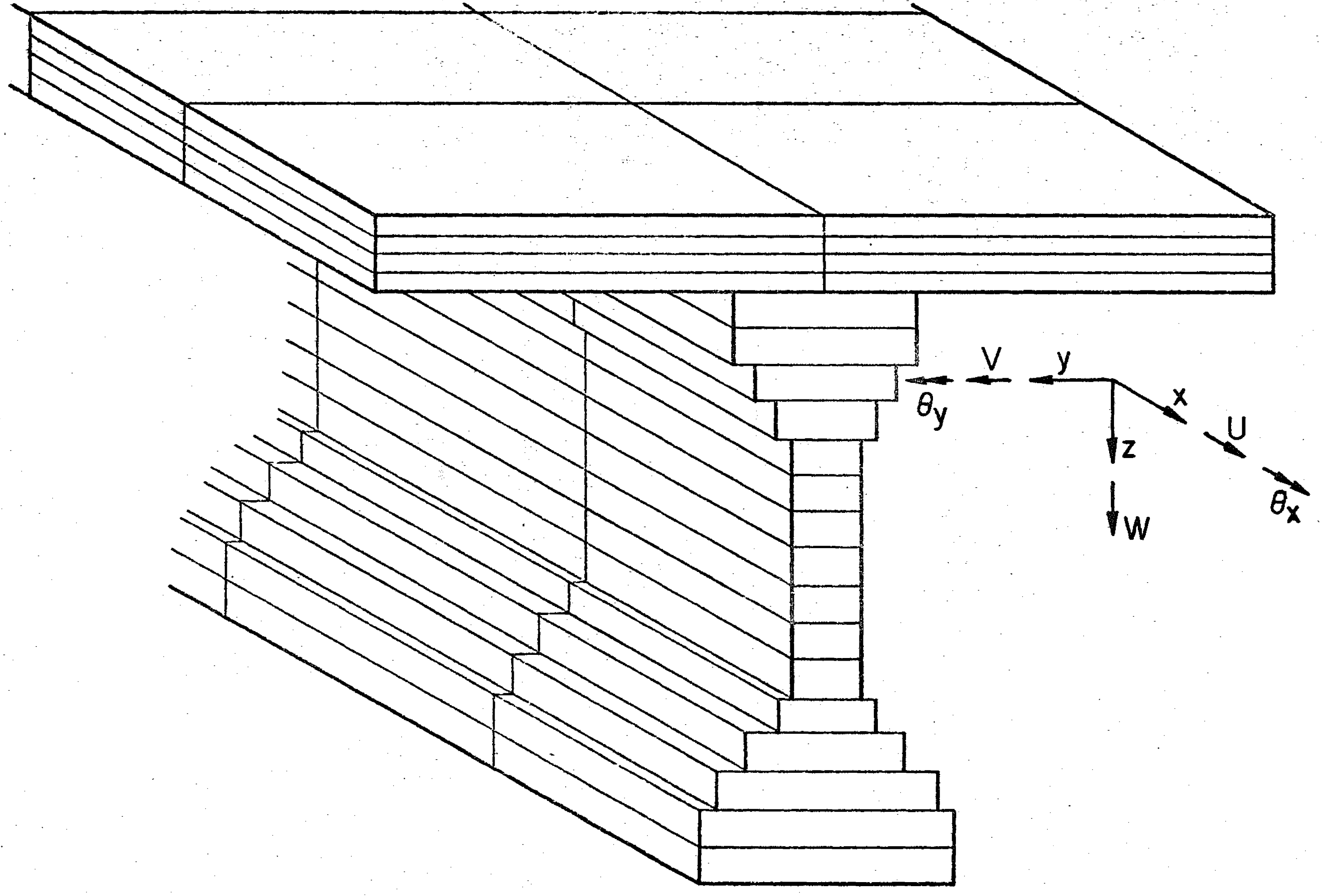

Fig. 2 Beam and Slab Layering

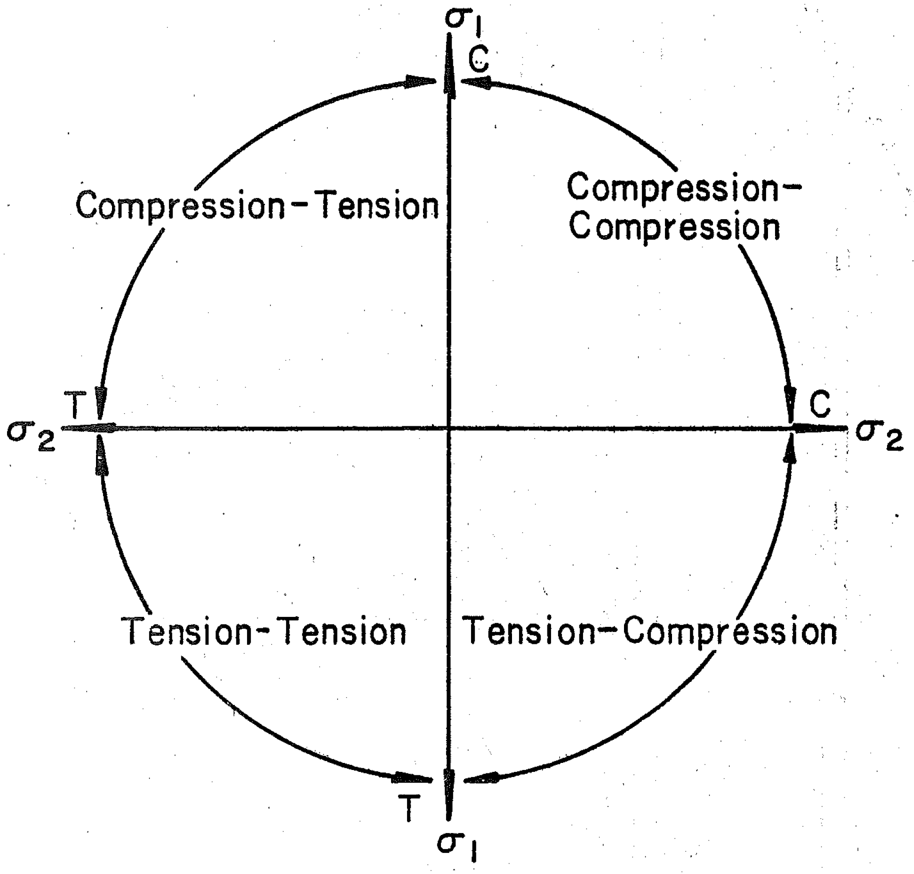

Fig. 3 The Biaxial Principal Stress Space

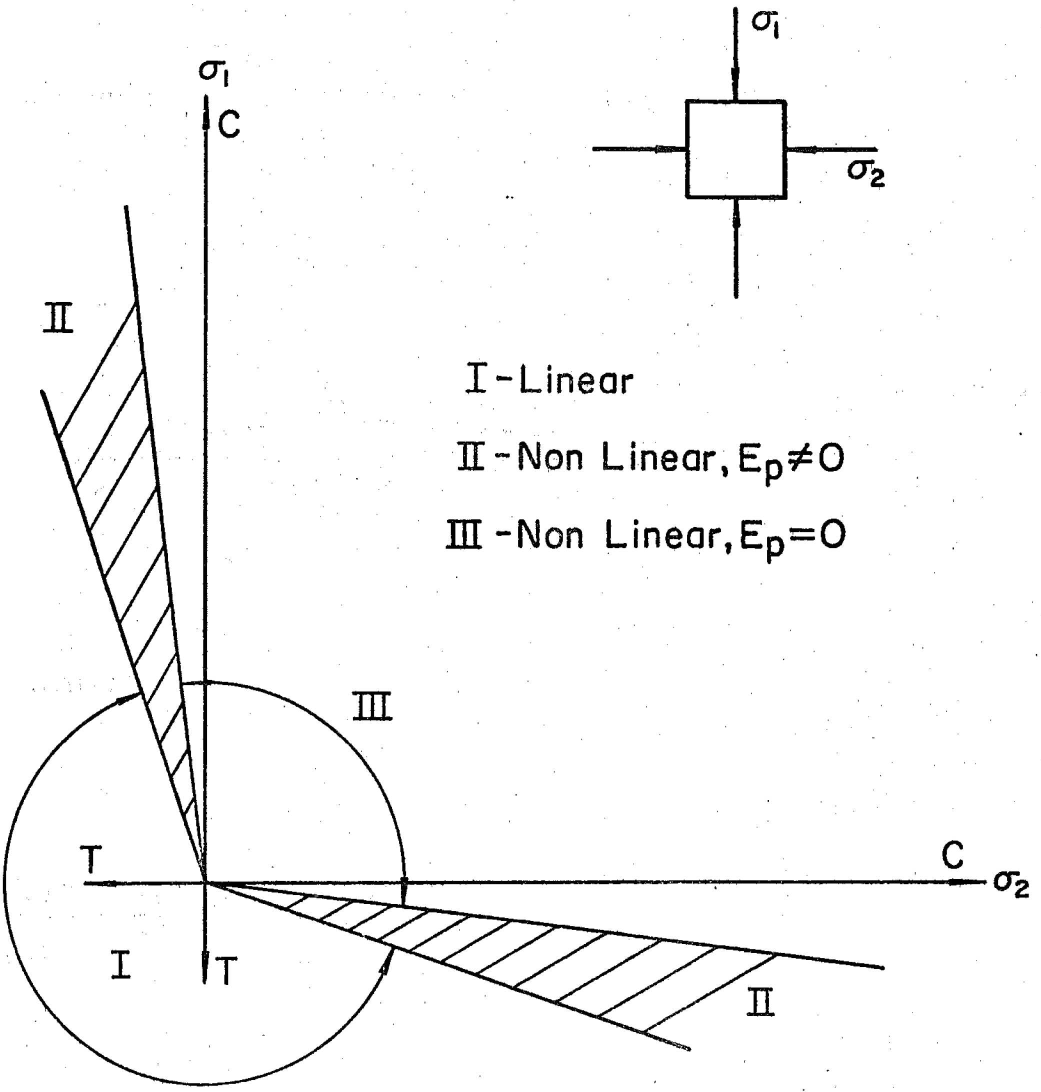

Fig. 4 Linear and Nonlinear Concrete Stress-Strain Curve Regions

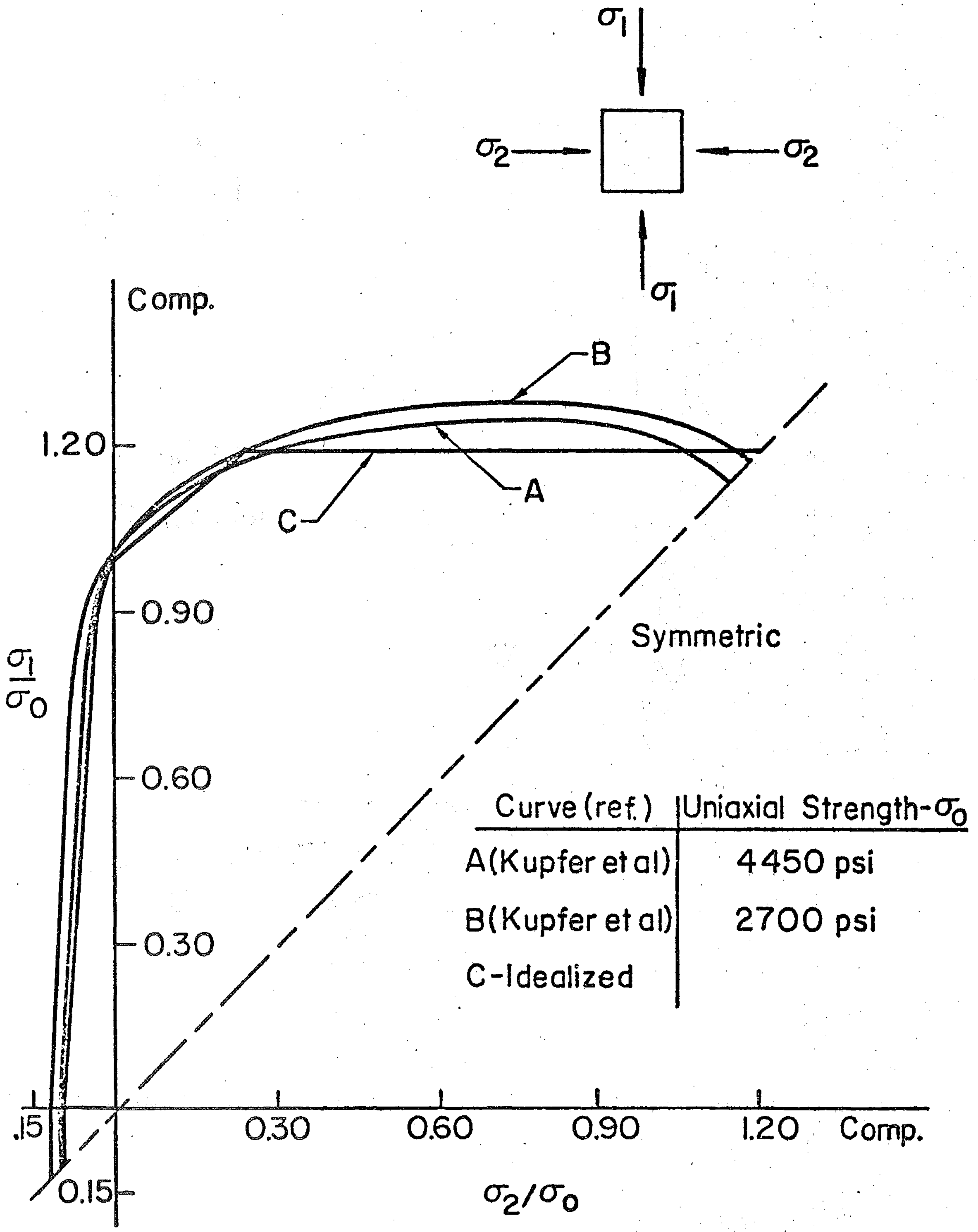

Fig. 5 Actual and Idealized Concrete Failure Envelopes for the Biaxial Stress Space

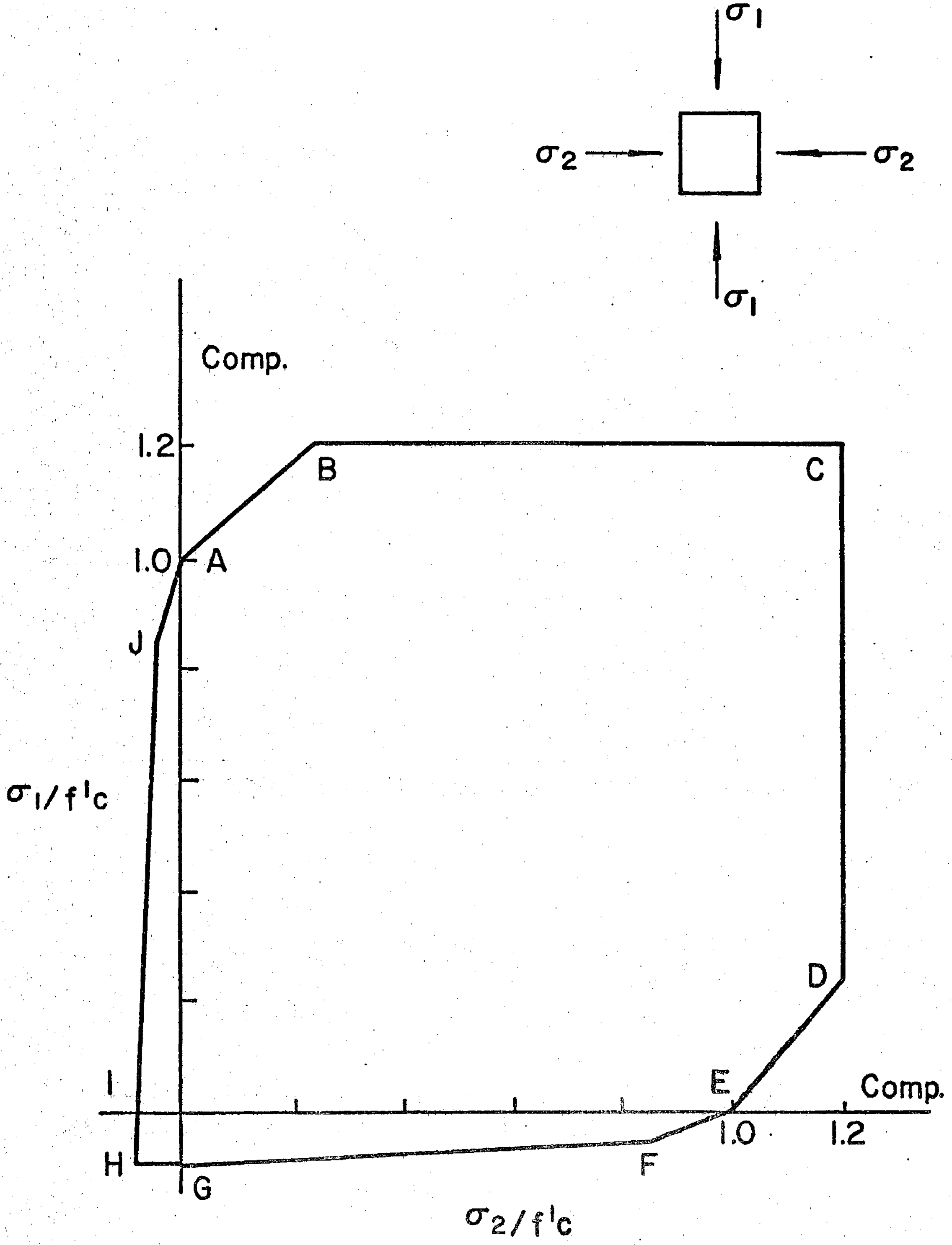

Fig. 6 Idealized Biaxial Failure Envelope with Characteristic Points

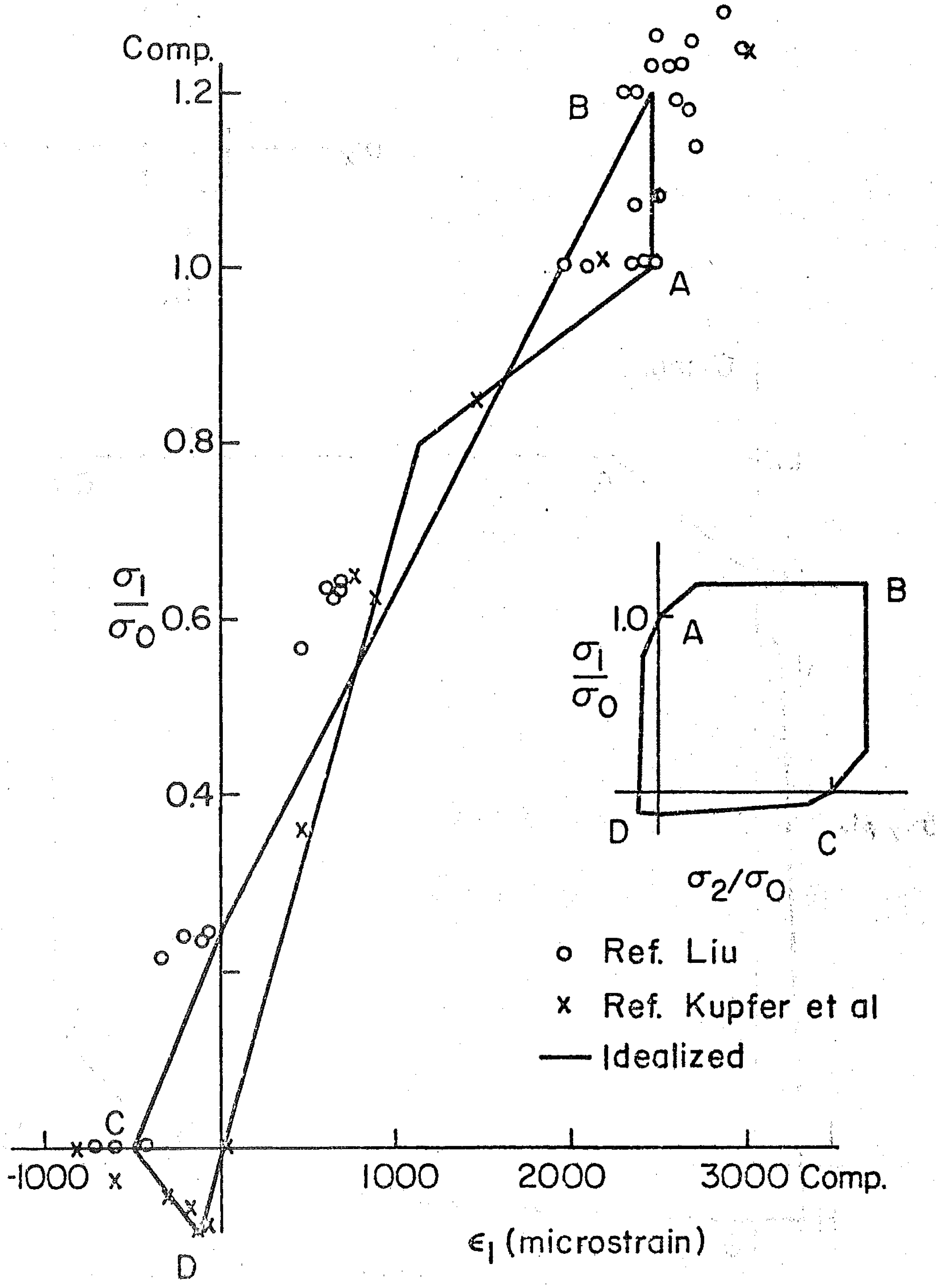

Fig. 7 Peak Strain Envelope

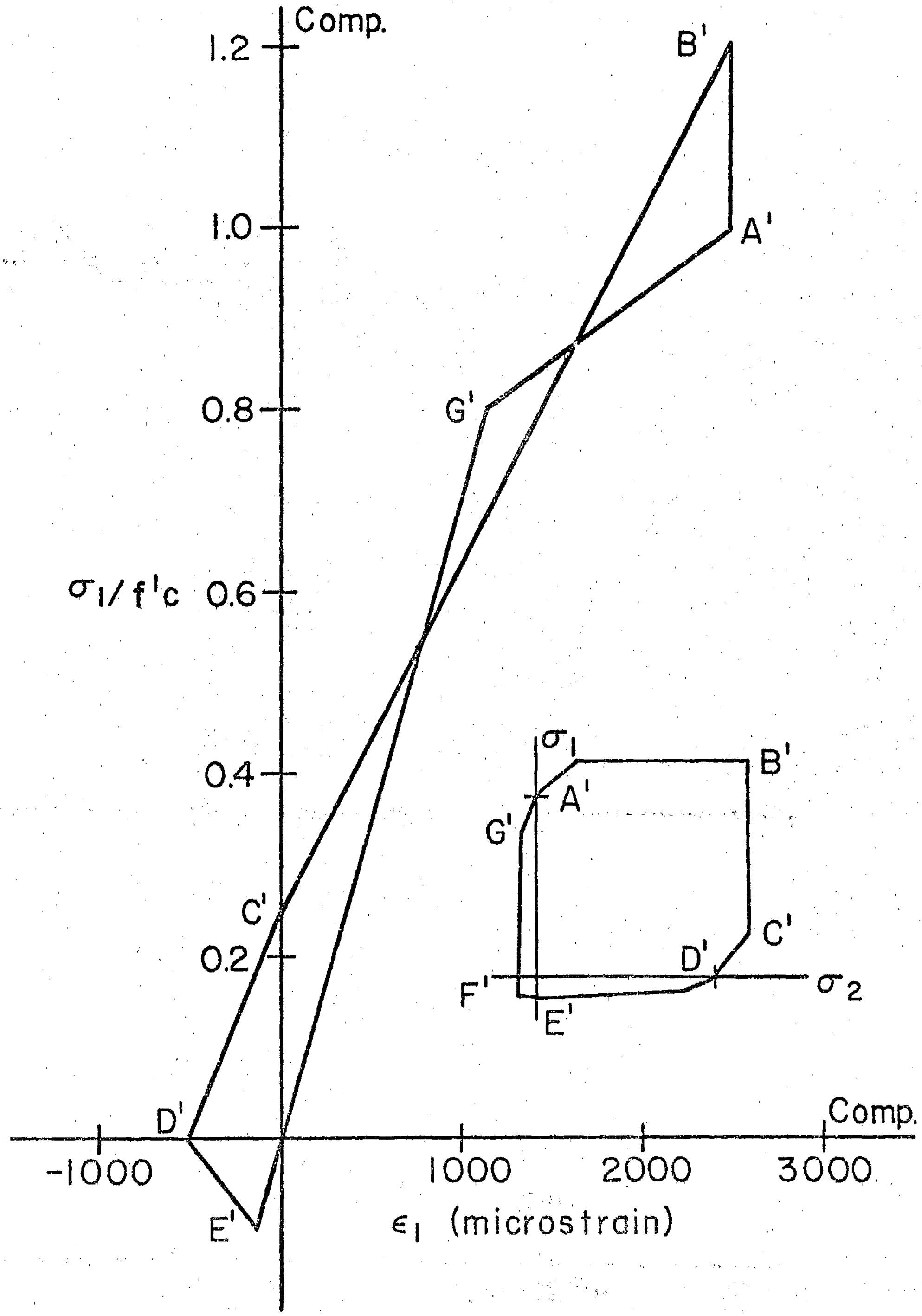

Fig. 8 Peak Strain Envelope with Characteristic Points

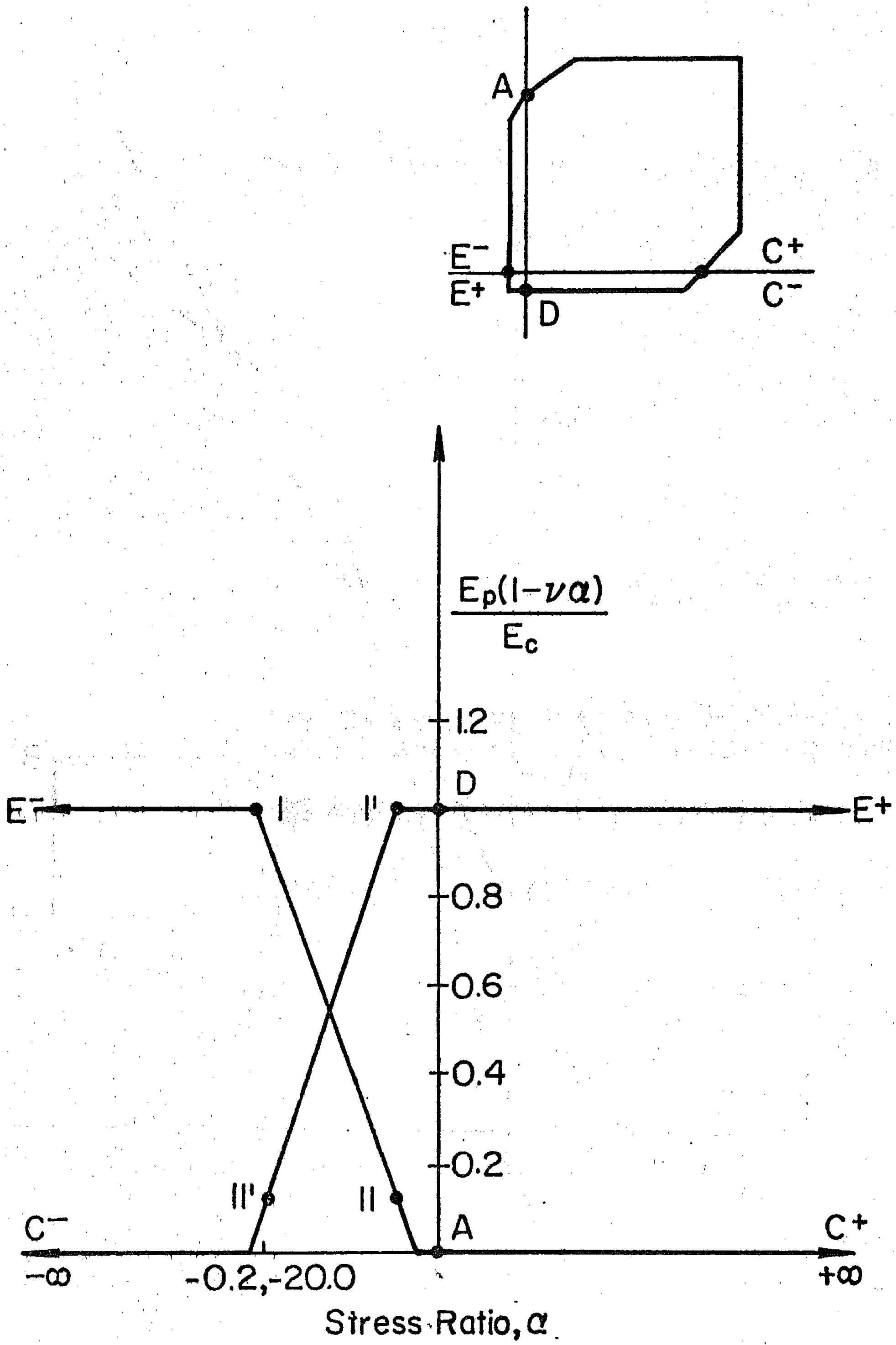

Fig. 9 Ratio of Peak Slope to Initial Slope as a Function of the Stress Ratio

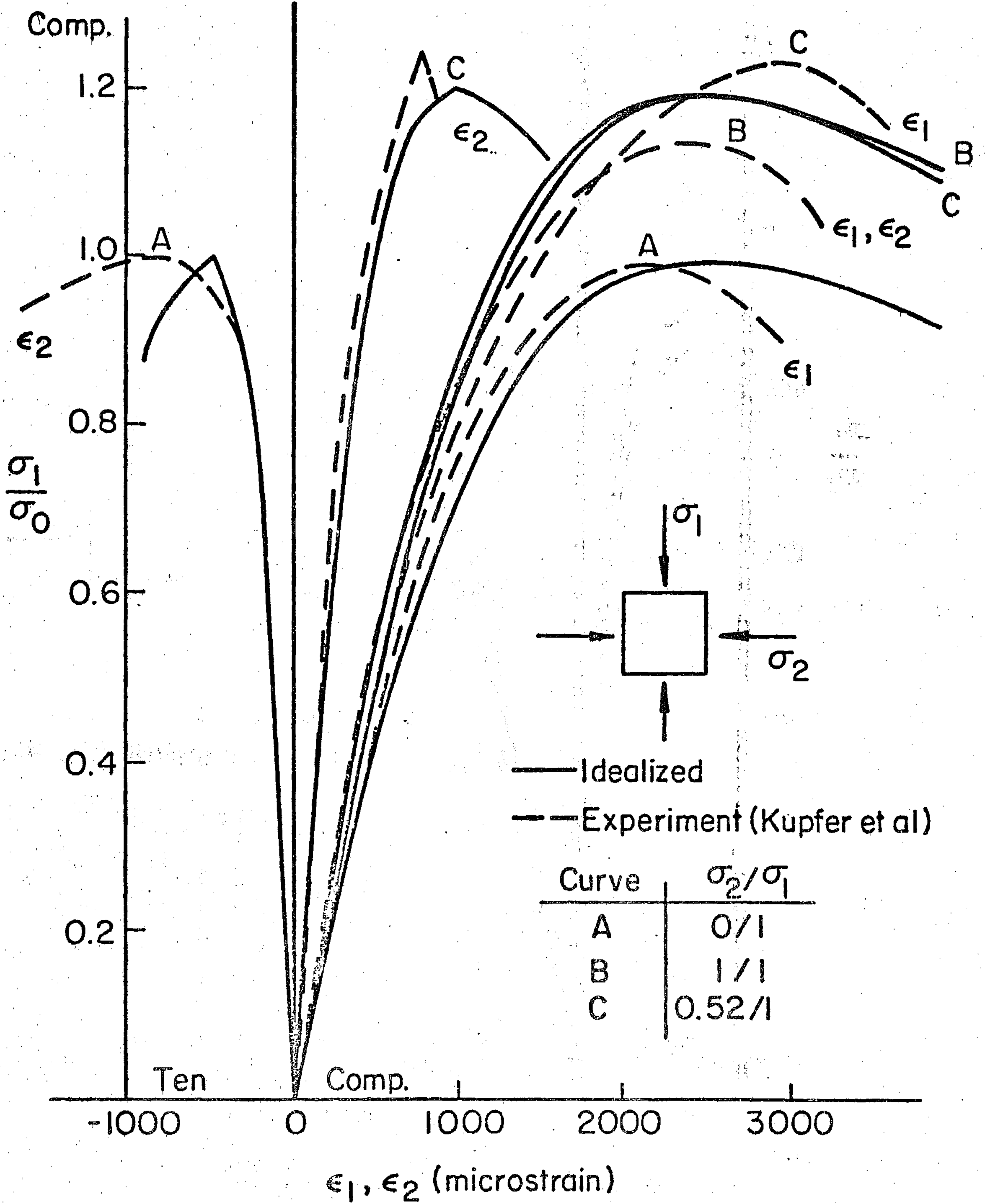

Fig. 10 Concrete Biaxial Stress-Strain Curves: Compression-Compression Region

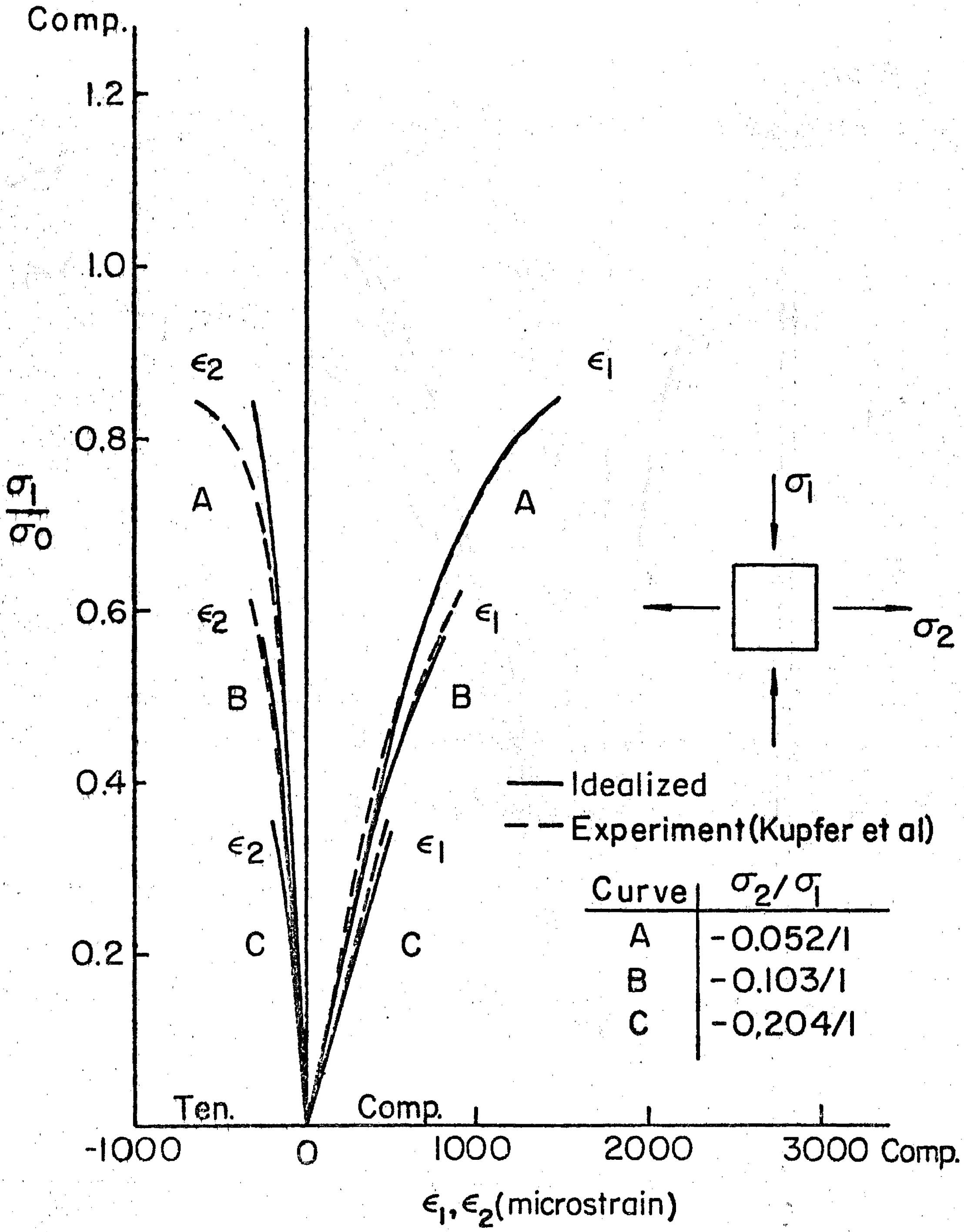

Fig. 11 Concrete Biaxial Stress-Strain Curves: Compression-Tension Region

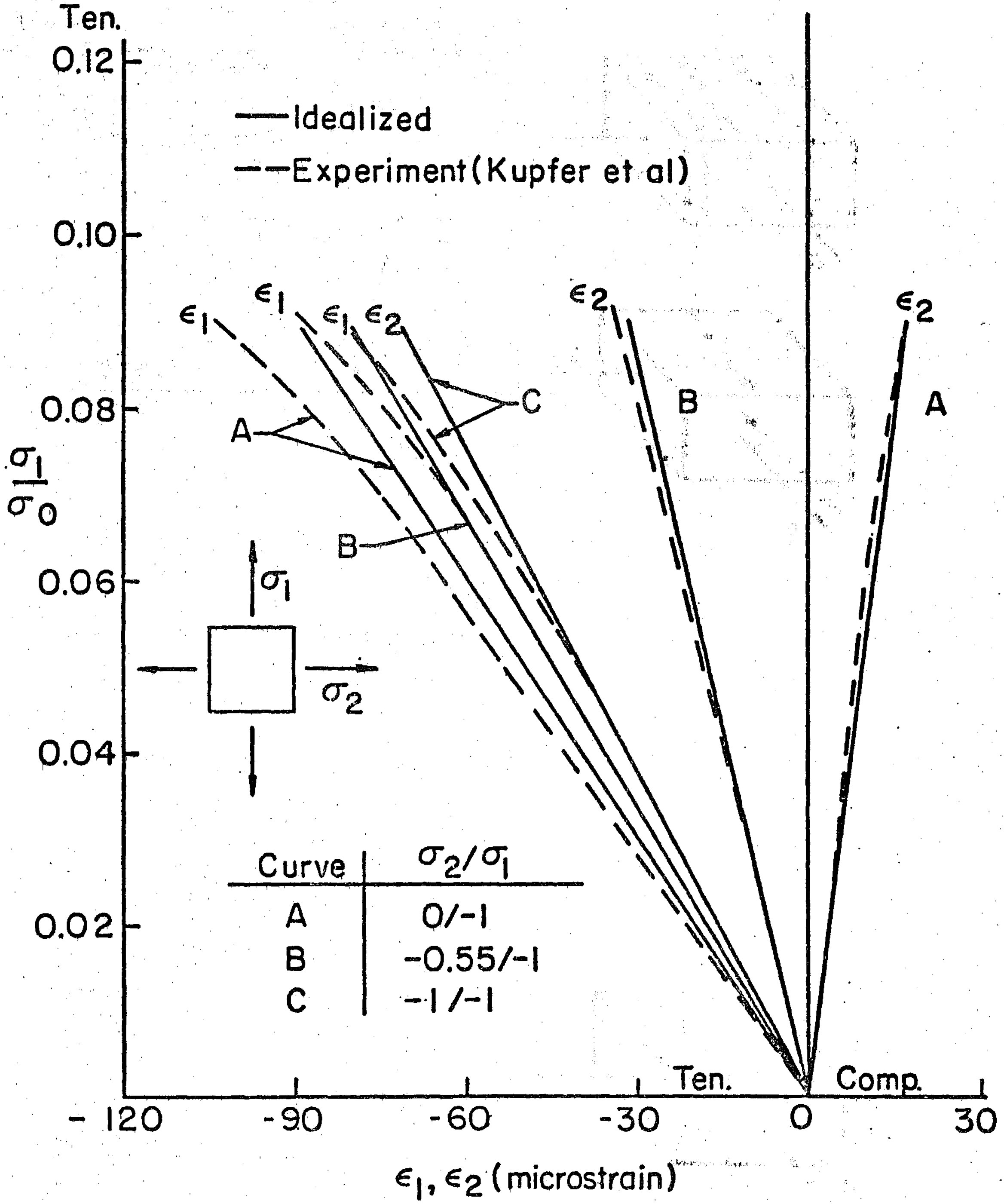

Fig. 12 Concrete Biaxial Stress-Strain Curves: Tension-Tesnion Region

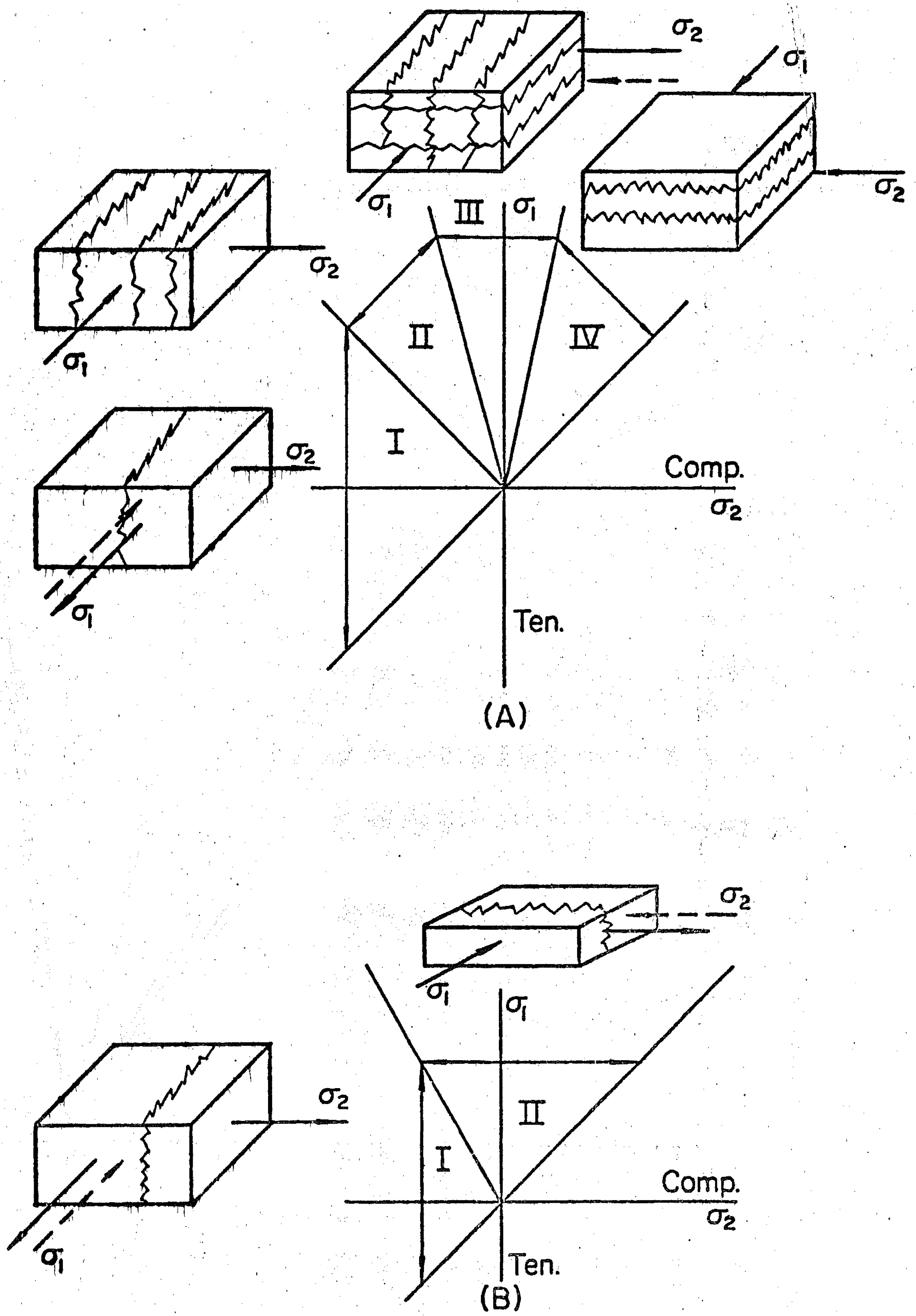

Fig. 13 Actual (A) and Idealized (B) Concrete Failure Modes

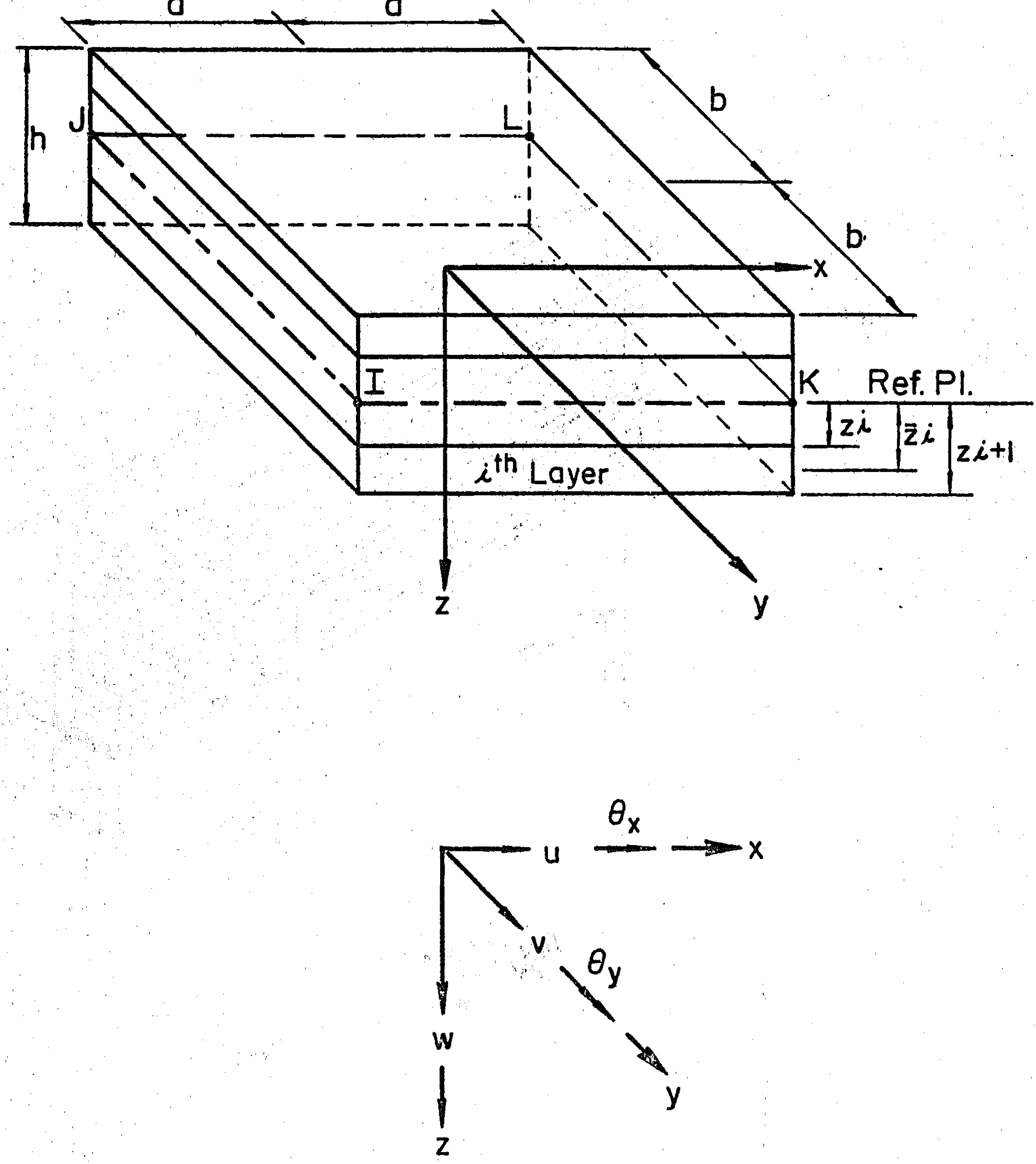

Fig. 14 Rectangular Slab Finite Element: Layering and Co-ordinate System

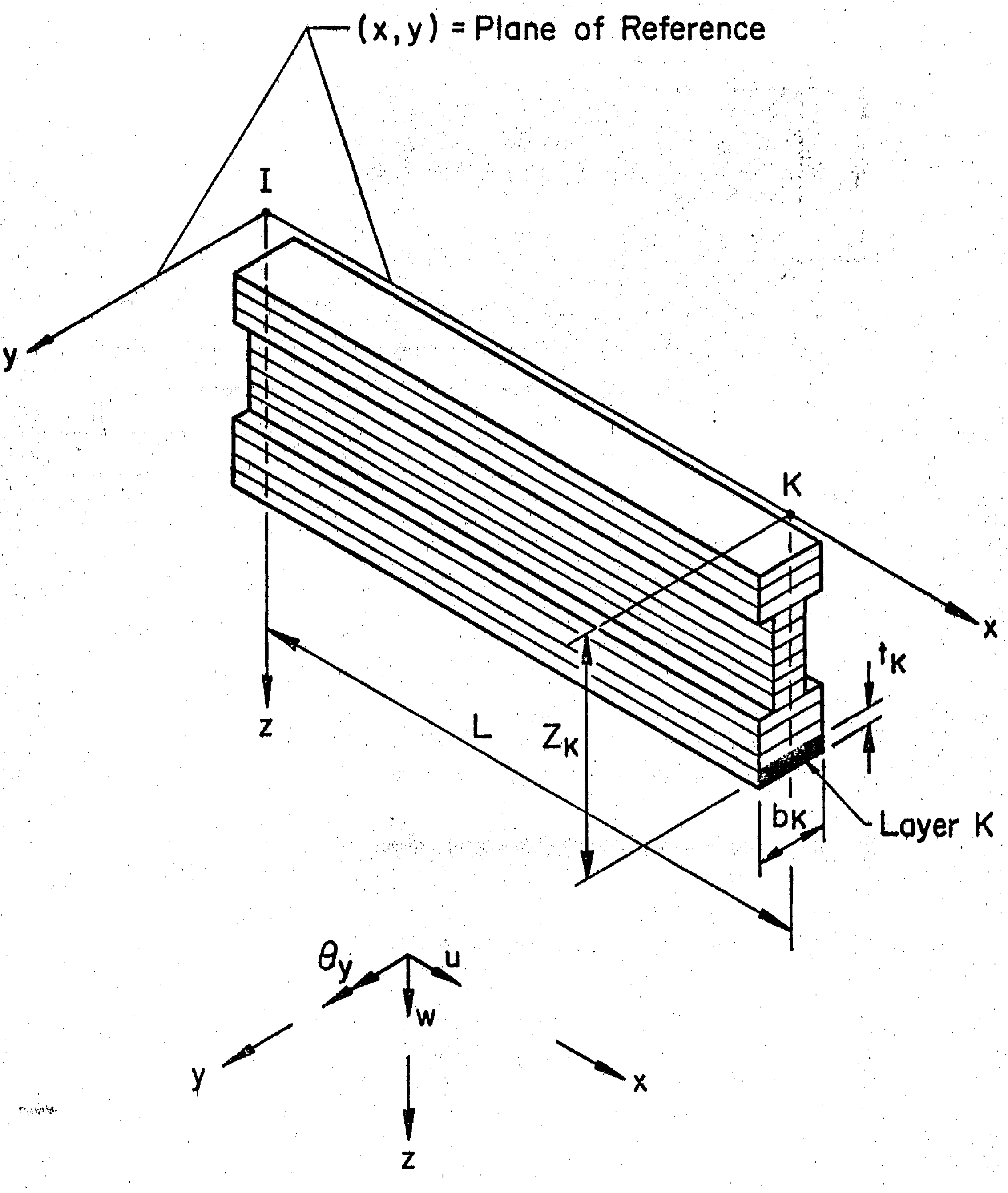

Fig. 15 Beam Finite Element:
Layering and Co-ordinate System

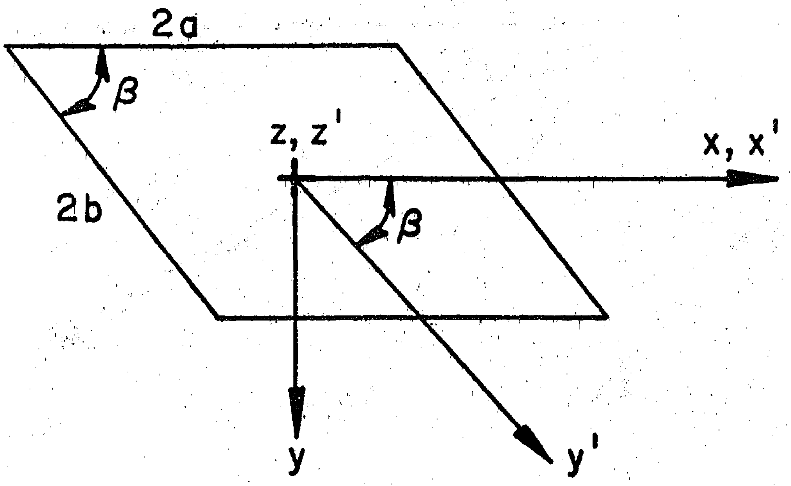

Fig. 16A Parallelogram Finite Element and Skew Co-ordinate System

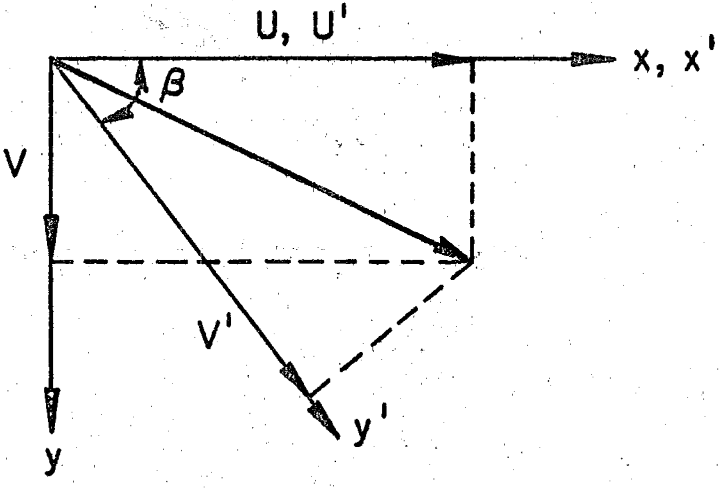

Fig. 16B Covariant Components of an In-plane Displacement Vector

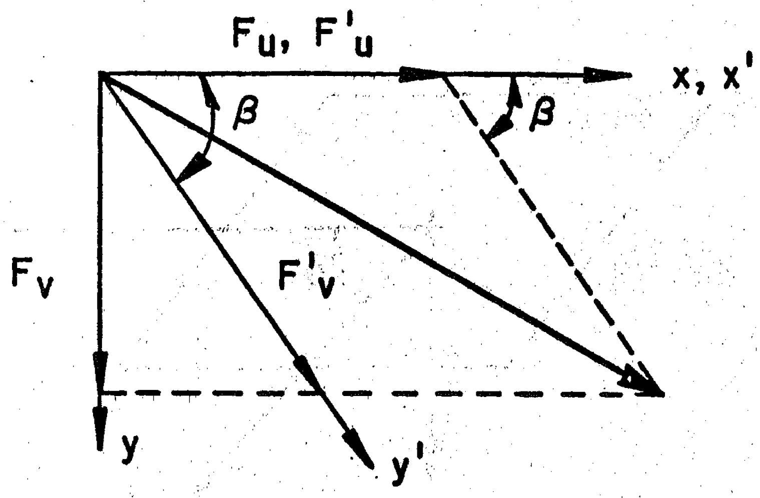

Fig. 17A Contravariant Components of an In-plane Force Vector

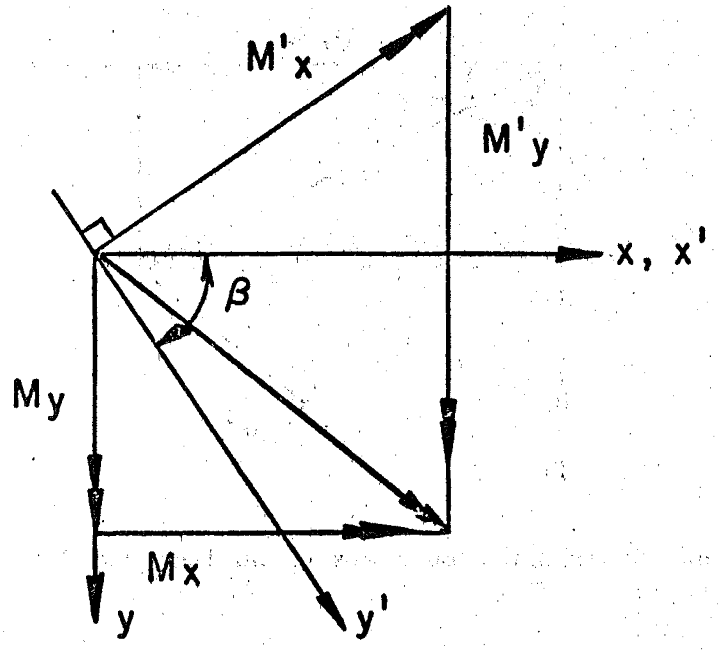

Fig. 17B Contravariant Components of a Moment Vector

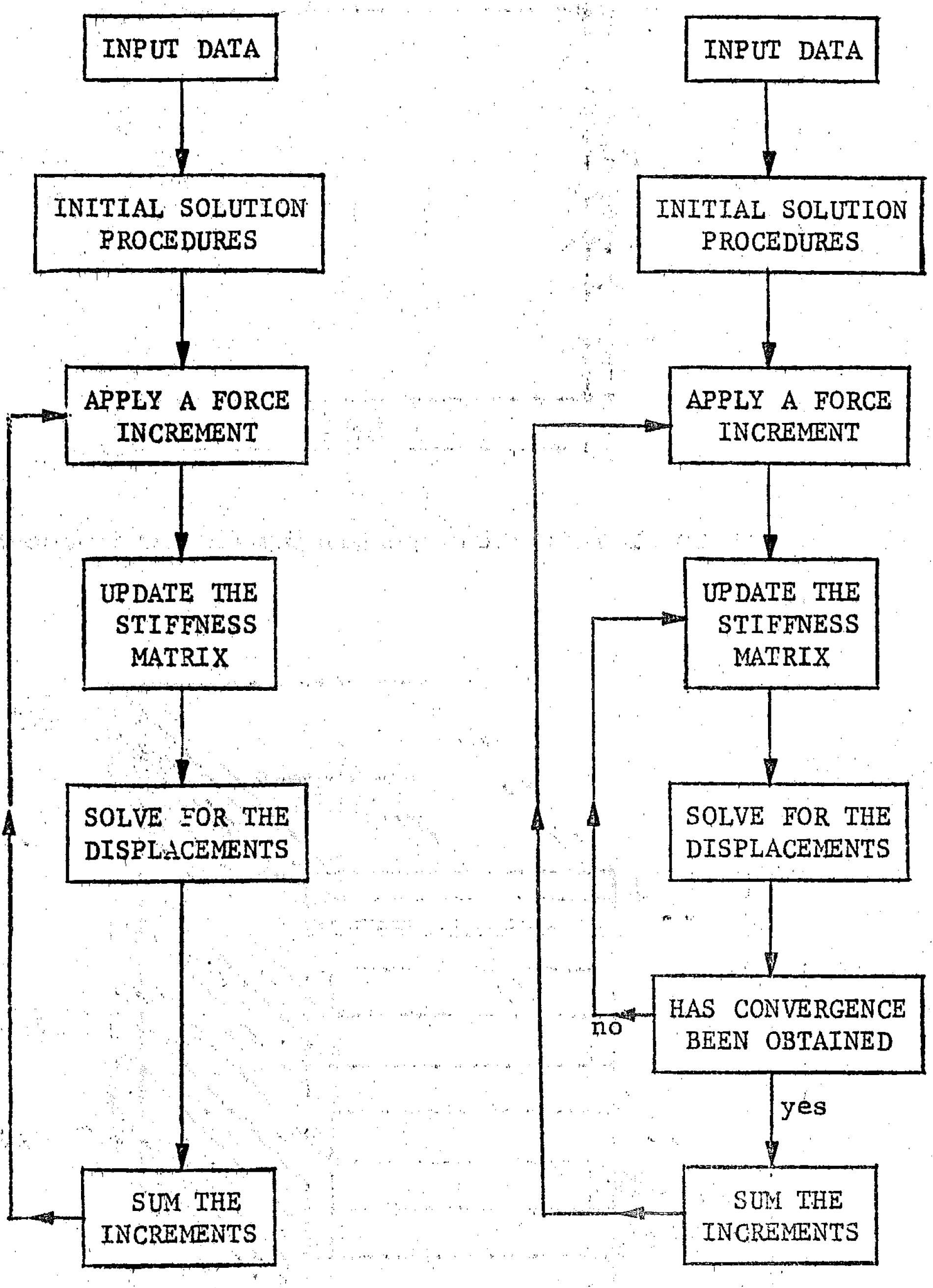

INCREMENTAL METHOD

INCREMENTAL - ITERATIVE METHOD

Fig. 18 Solution Schemes

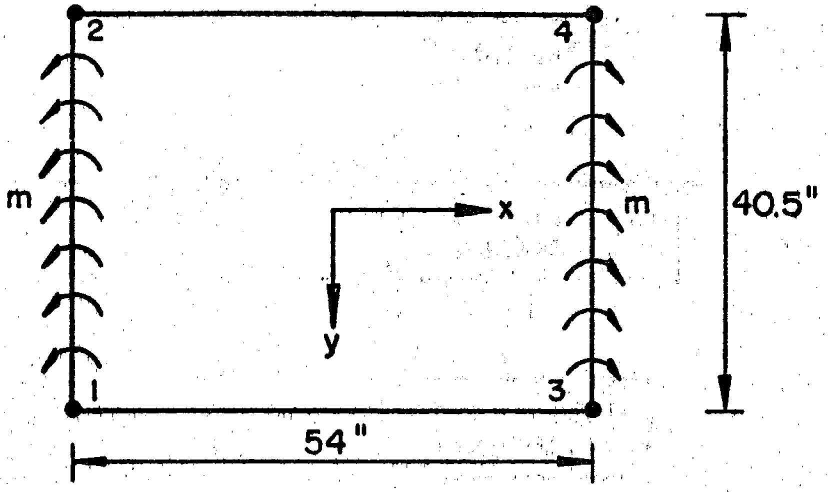

Fig. 19A Discretization and Loading for the Simple-Free Slab

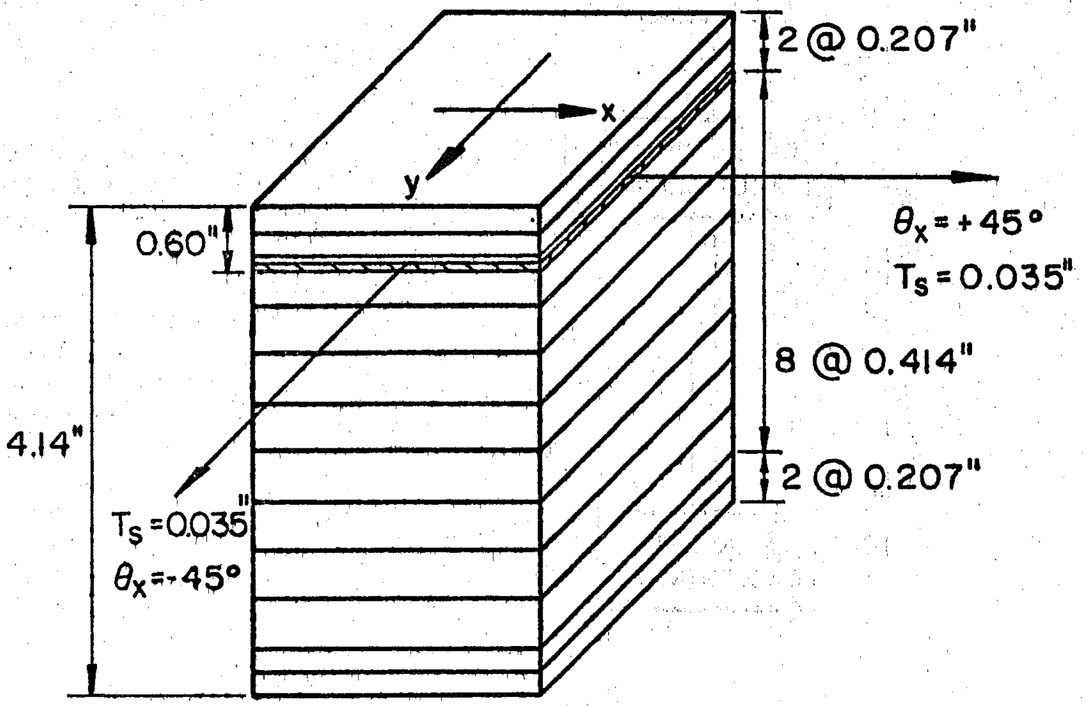

Fig. 19B Layering for the Simple-Free Slab

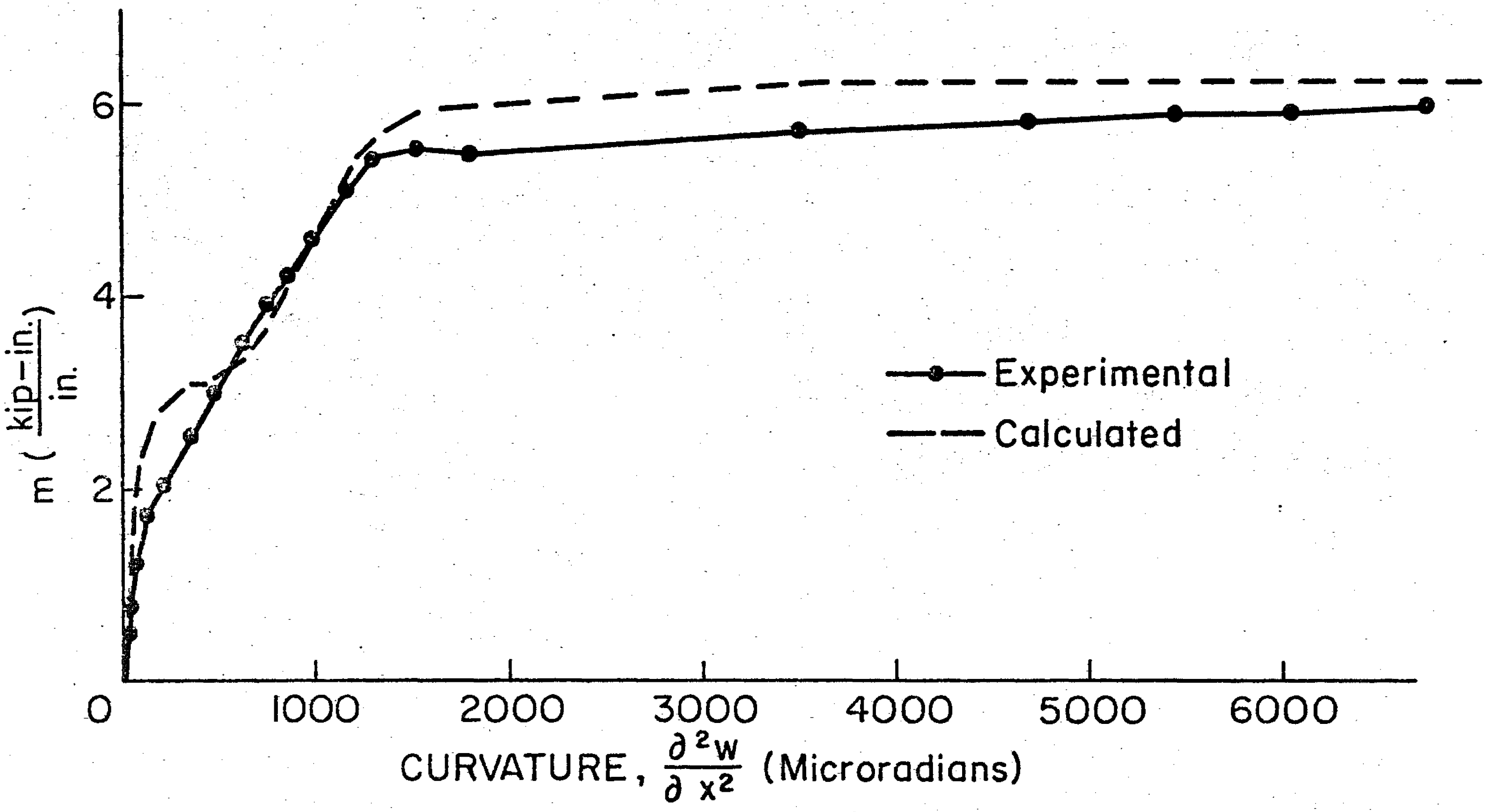

Fig. 20 Moment Versus Curvature History for the Simple-Free Slab

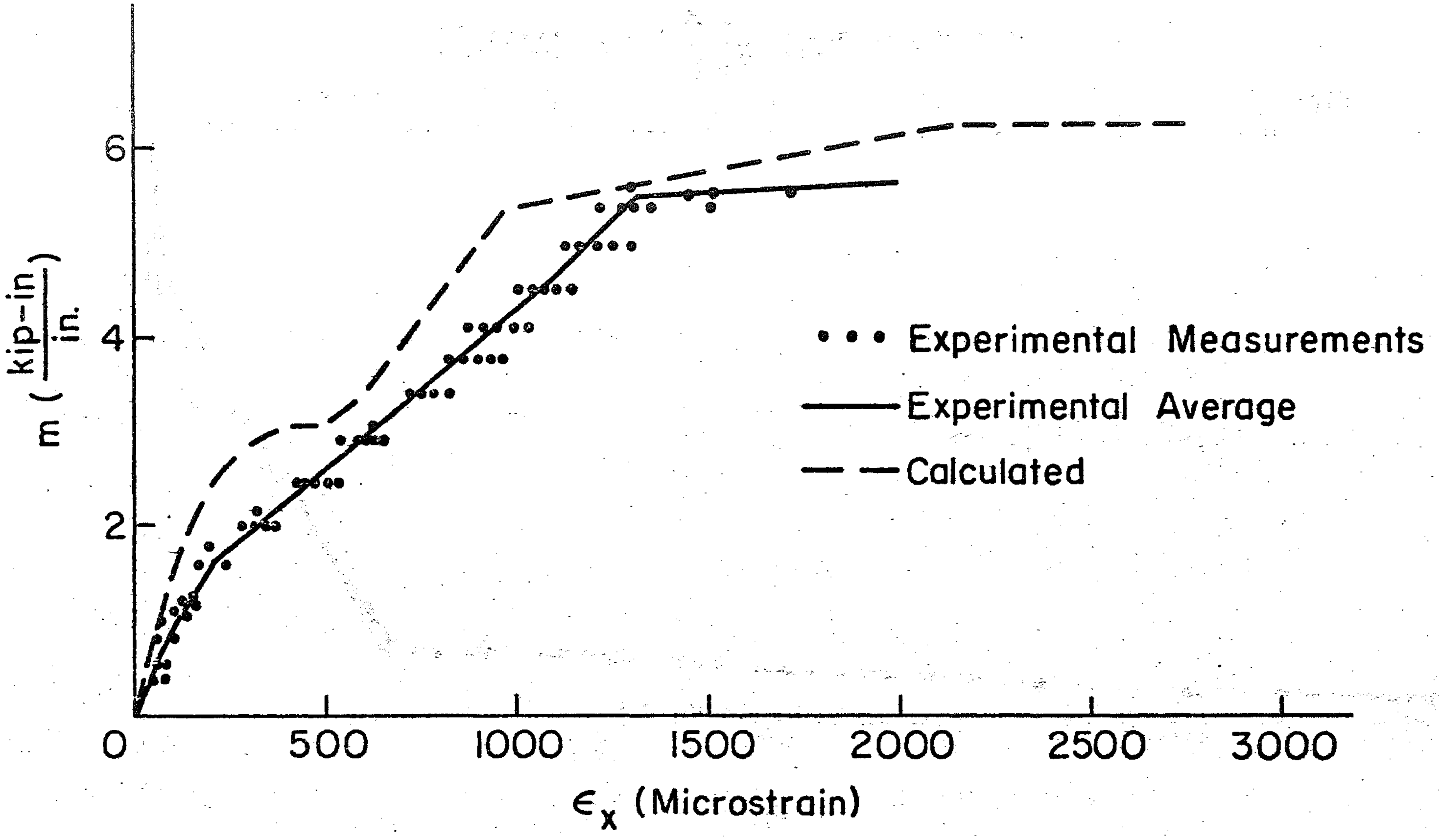

Fig. 21 Moment Versus Concrete Compressive Strain for the Simple-Free Slab

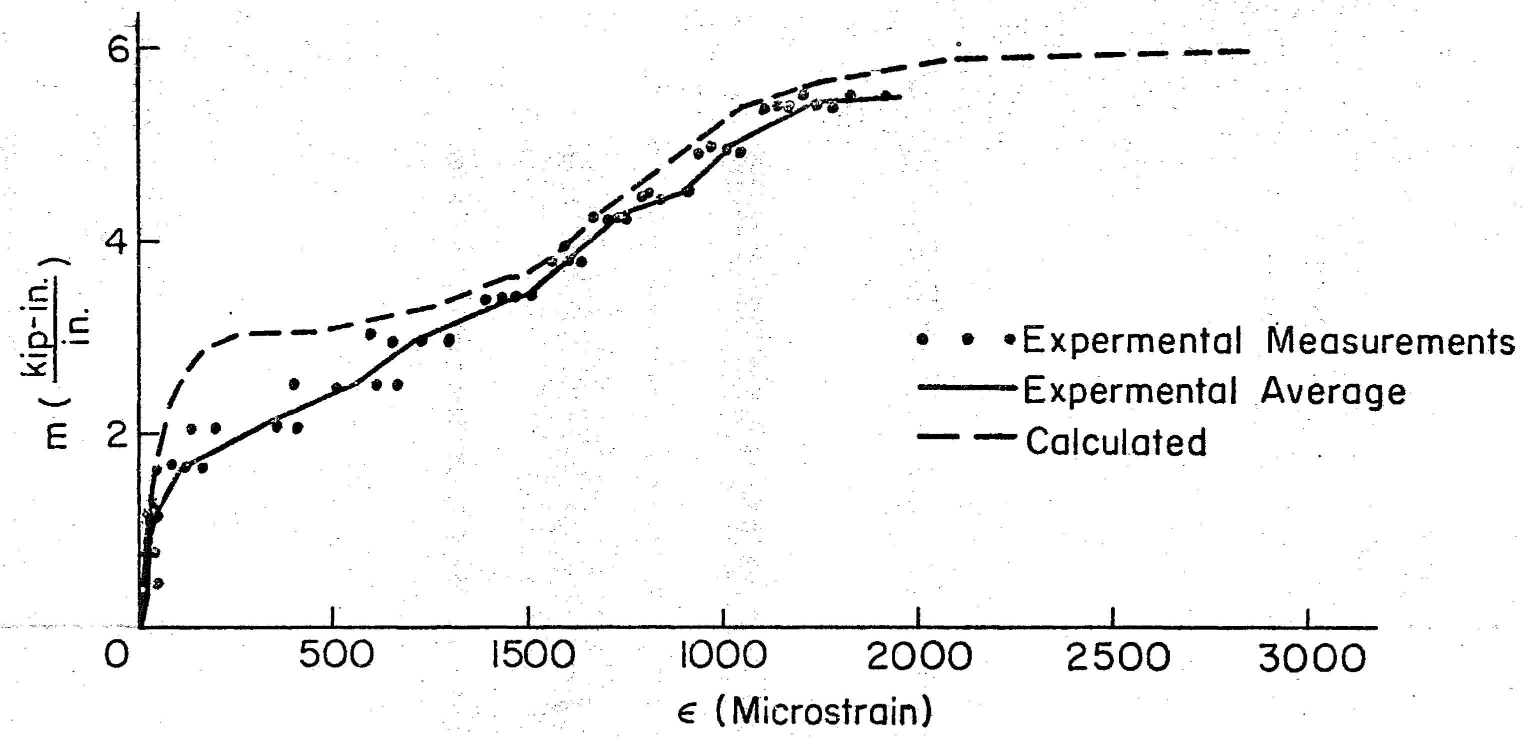

Fig. 22 Moment Versus Average Steel Strain for the Simple-Free Slab

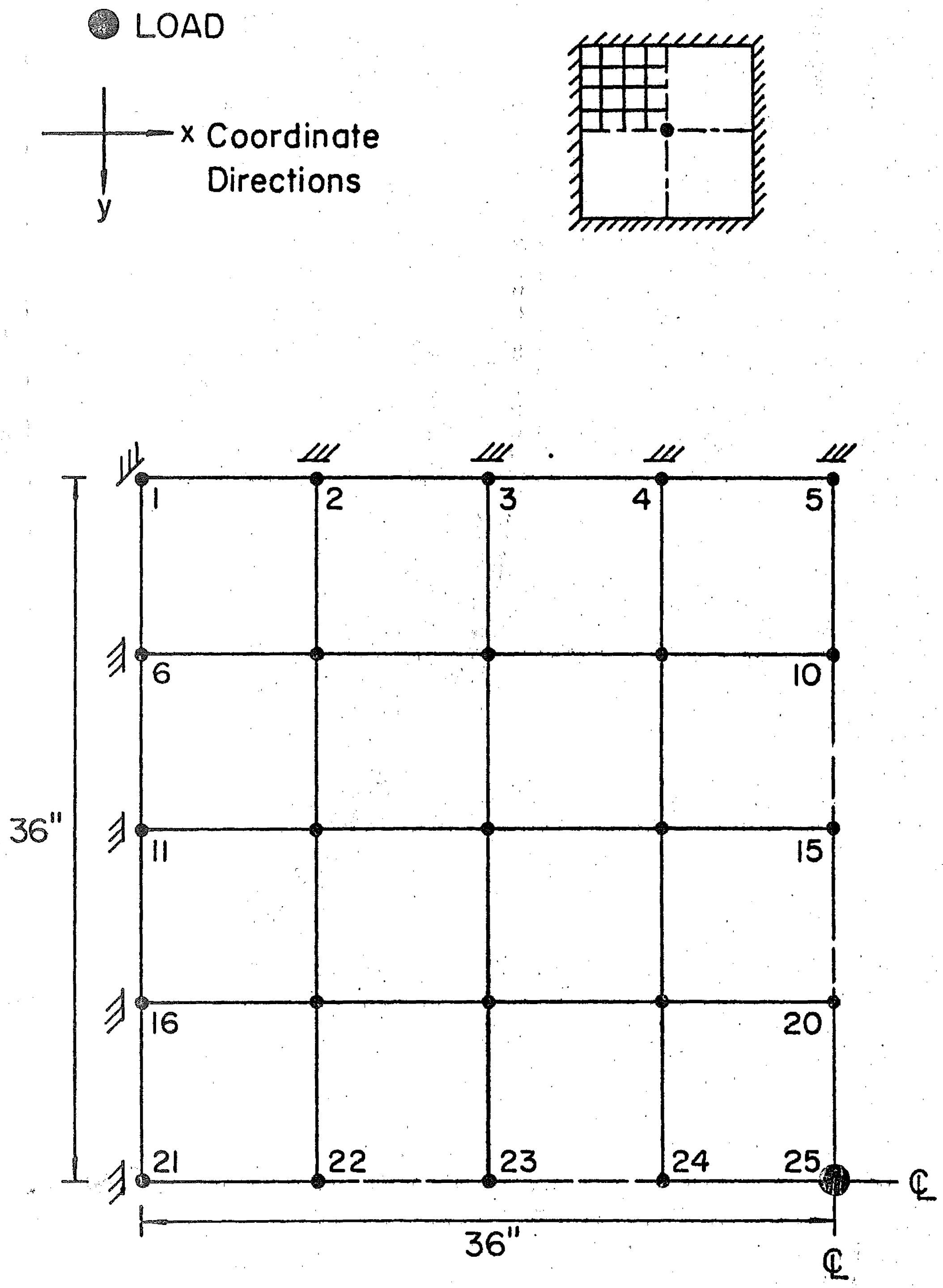

Fig. 23 Discretization and Loading for the Fixed-Fixed Slab

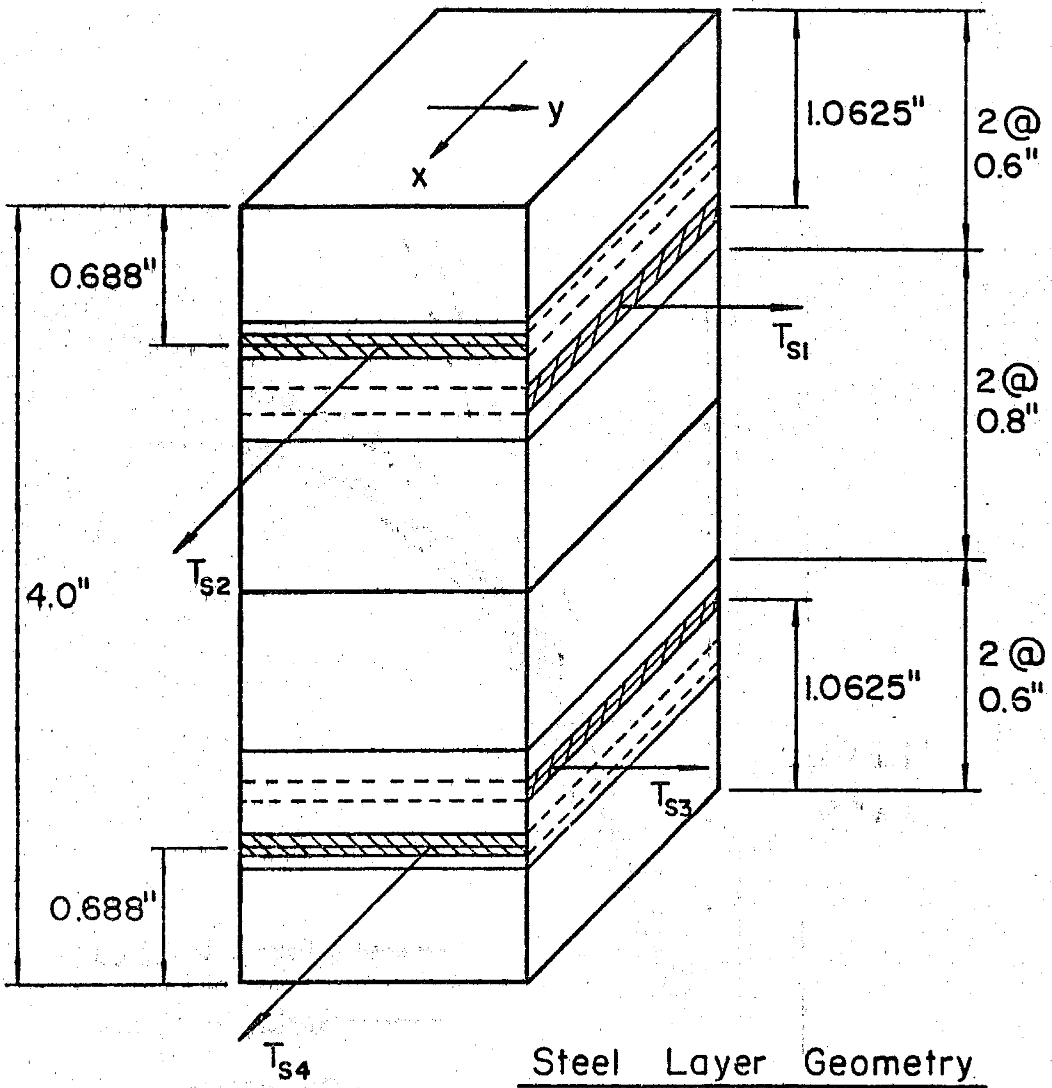

Steel Layer Geometry

	T_S	θ_x
T_{S1}	0.01790"	0°
T_{S2}	0.01646"	-90°
T_{S3}	0.01790"	0°
T_{S4}	0.01646"	-90°

Fig. 24 Layering for the Fixed-Fixed Slab

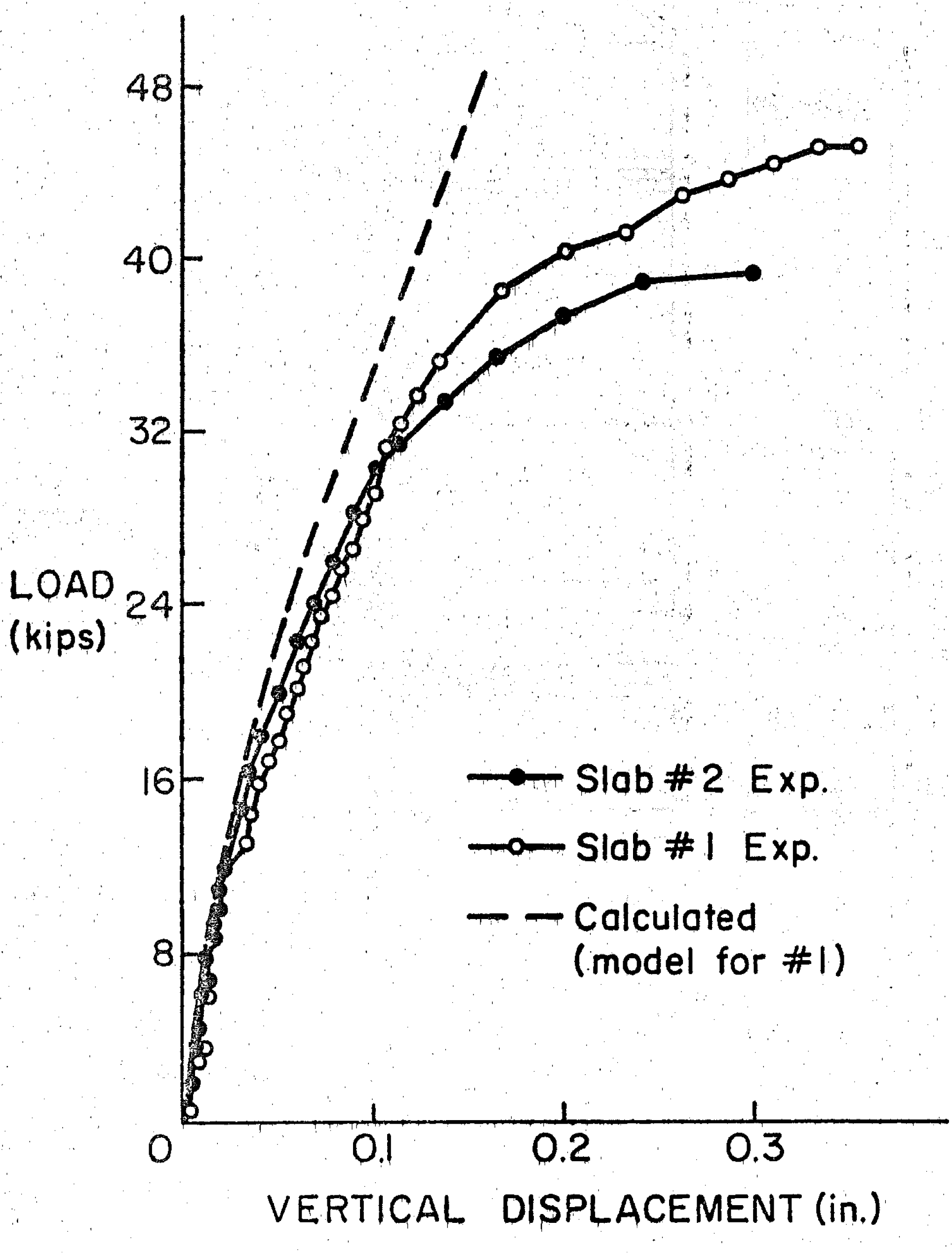

Fig. 25 Load-Deflection History for the Fixed-Fixed Slab

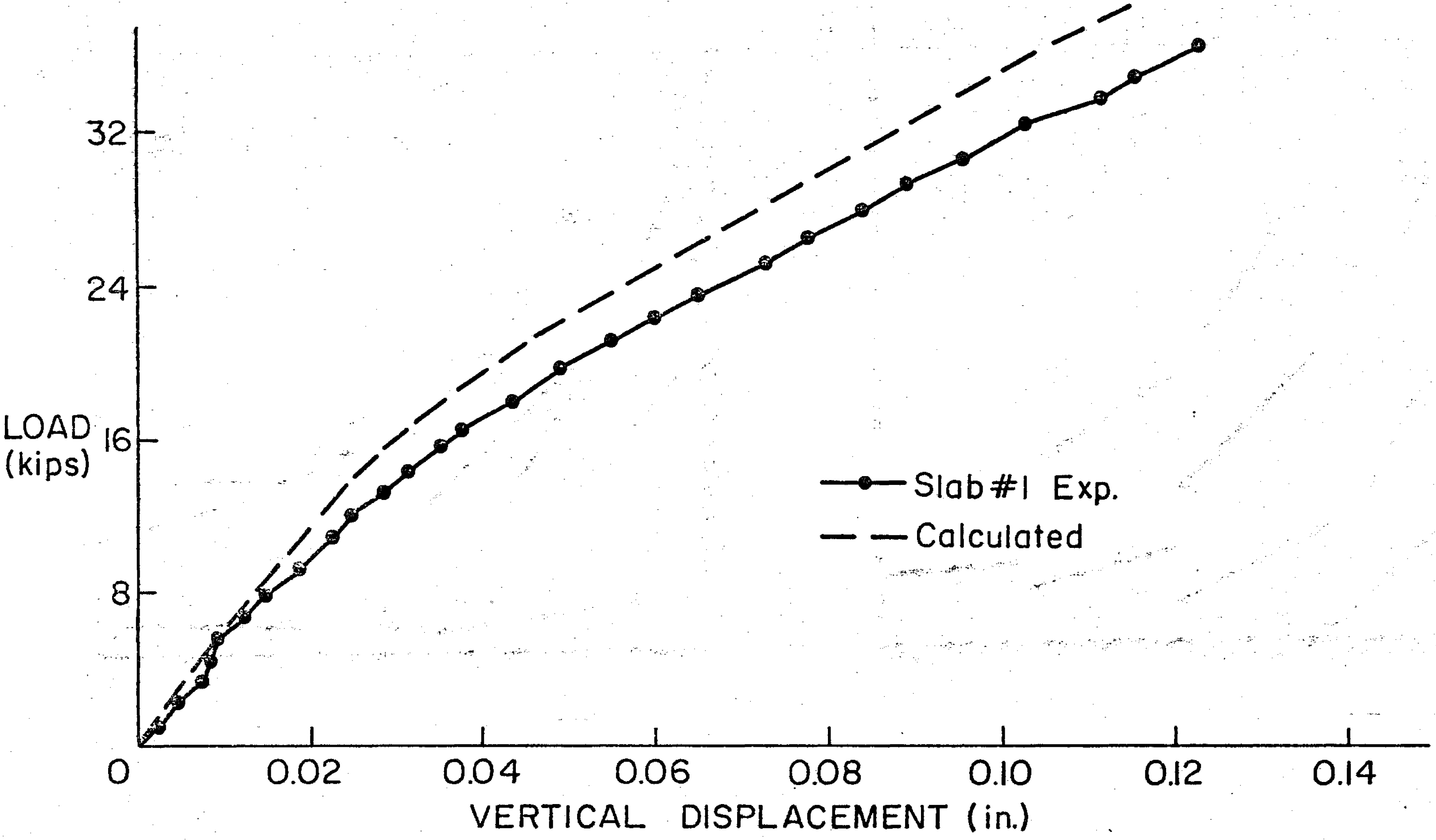

Fig. 26 Load-Deflection History for the Fixed-Fixed Slab

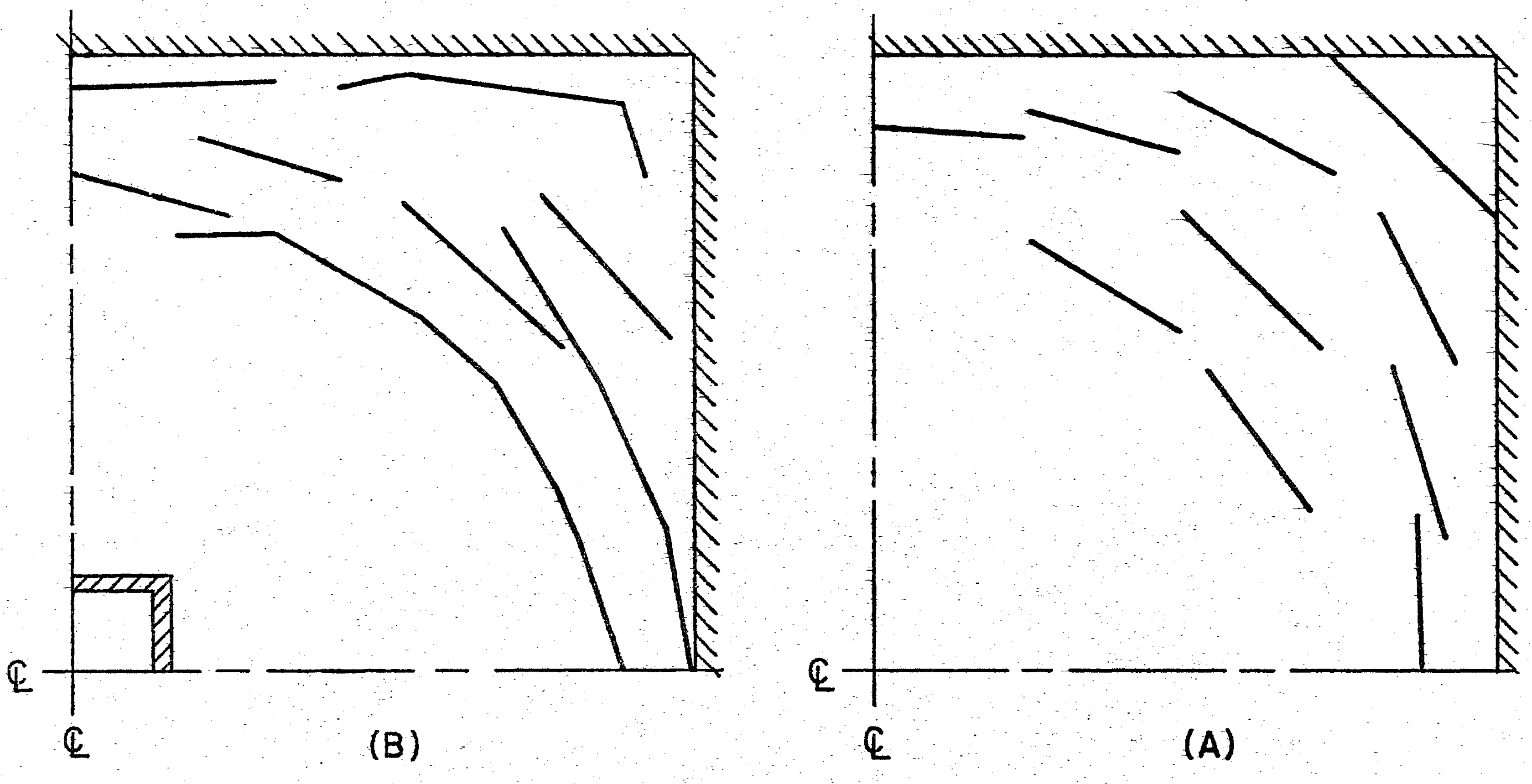

Fig. 27 Analytic (A) and Experimental (B) Top Surface Crack Patterns for the Fixed-Fixed Slab

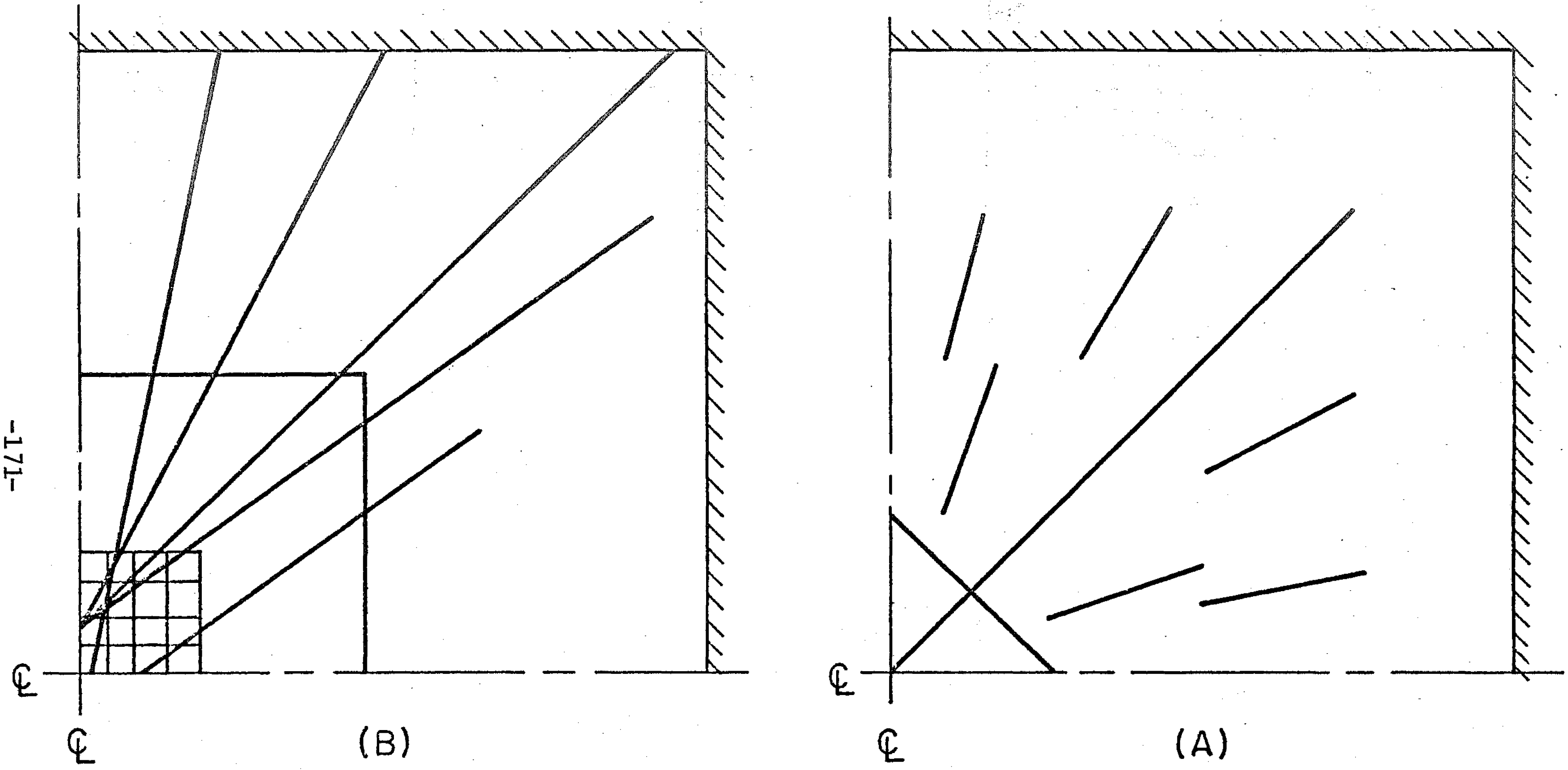

Fig. 28 Analytic (A) and Experimental (B) Bottom Surface Crack Patterns for the Fixed-Fixed Slab

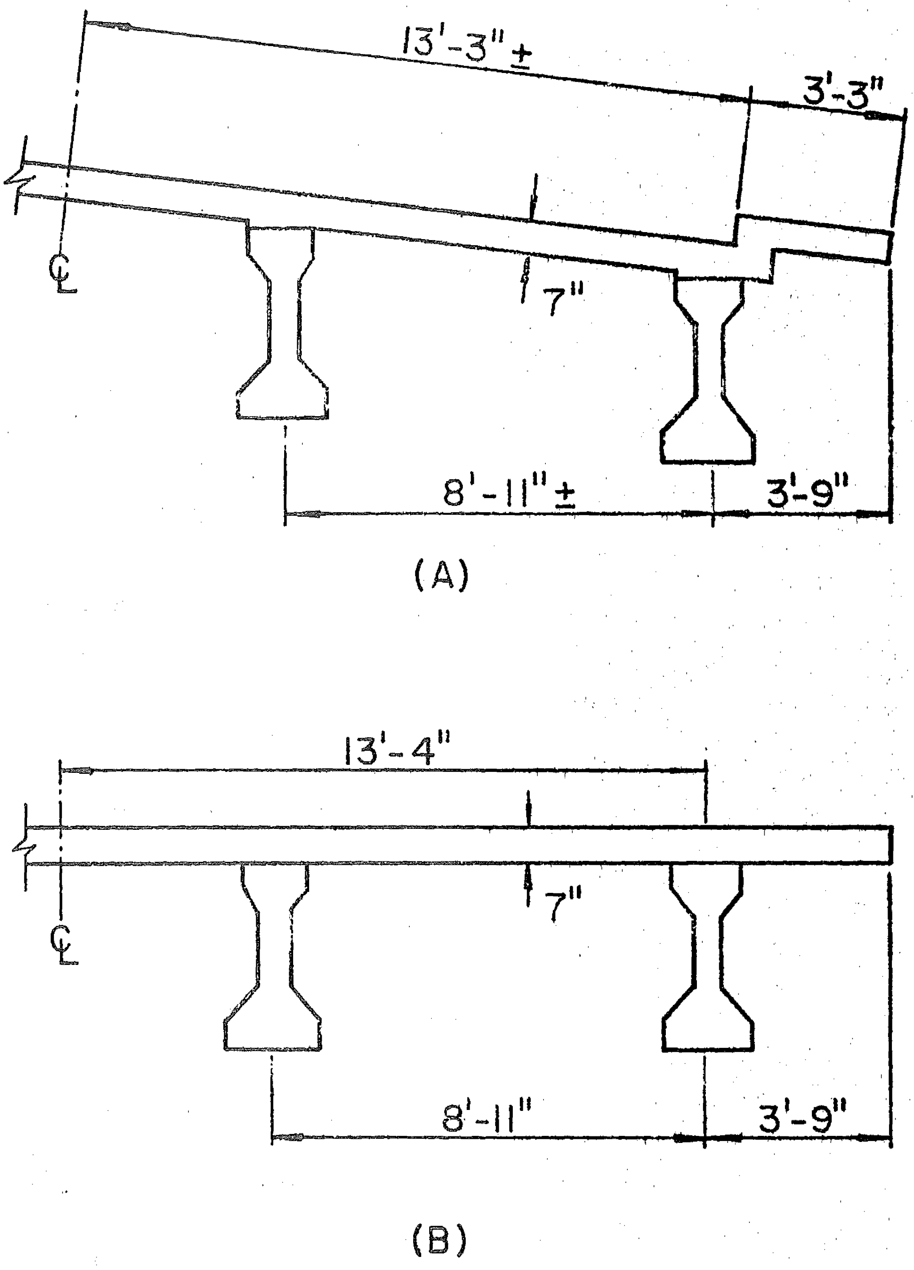

Fig. 29 Example No. 1 (Bridge 2): Actual (A) and Idealized (B) Cross-Sections

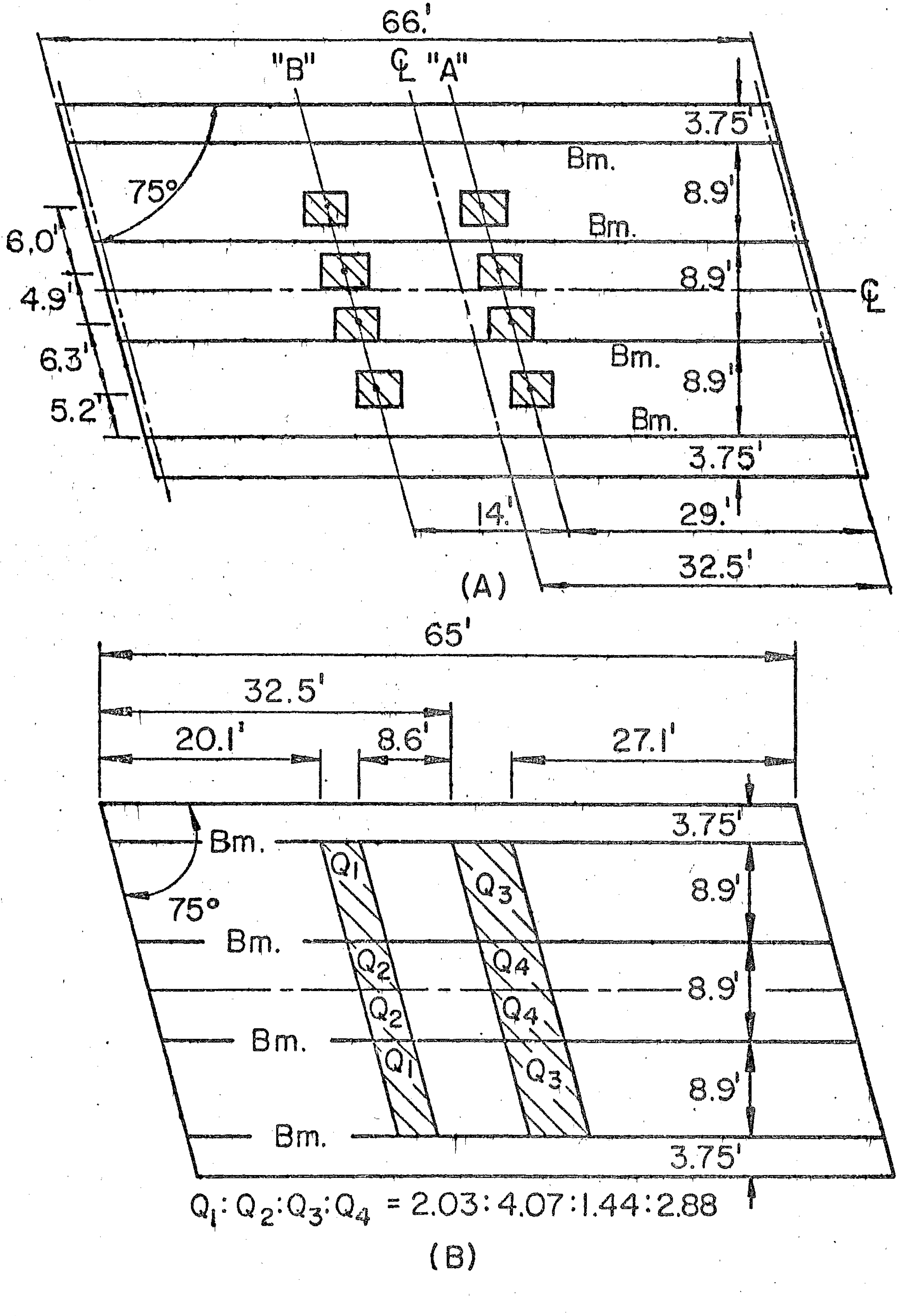

Fig. 30 Example No. 1 (Bridge 2): Actual (A) and Idealized (B) Plan Views

Fig. 31 Photograph of the Loading Devices (through the courtesy of The University of Tennessee)

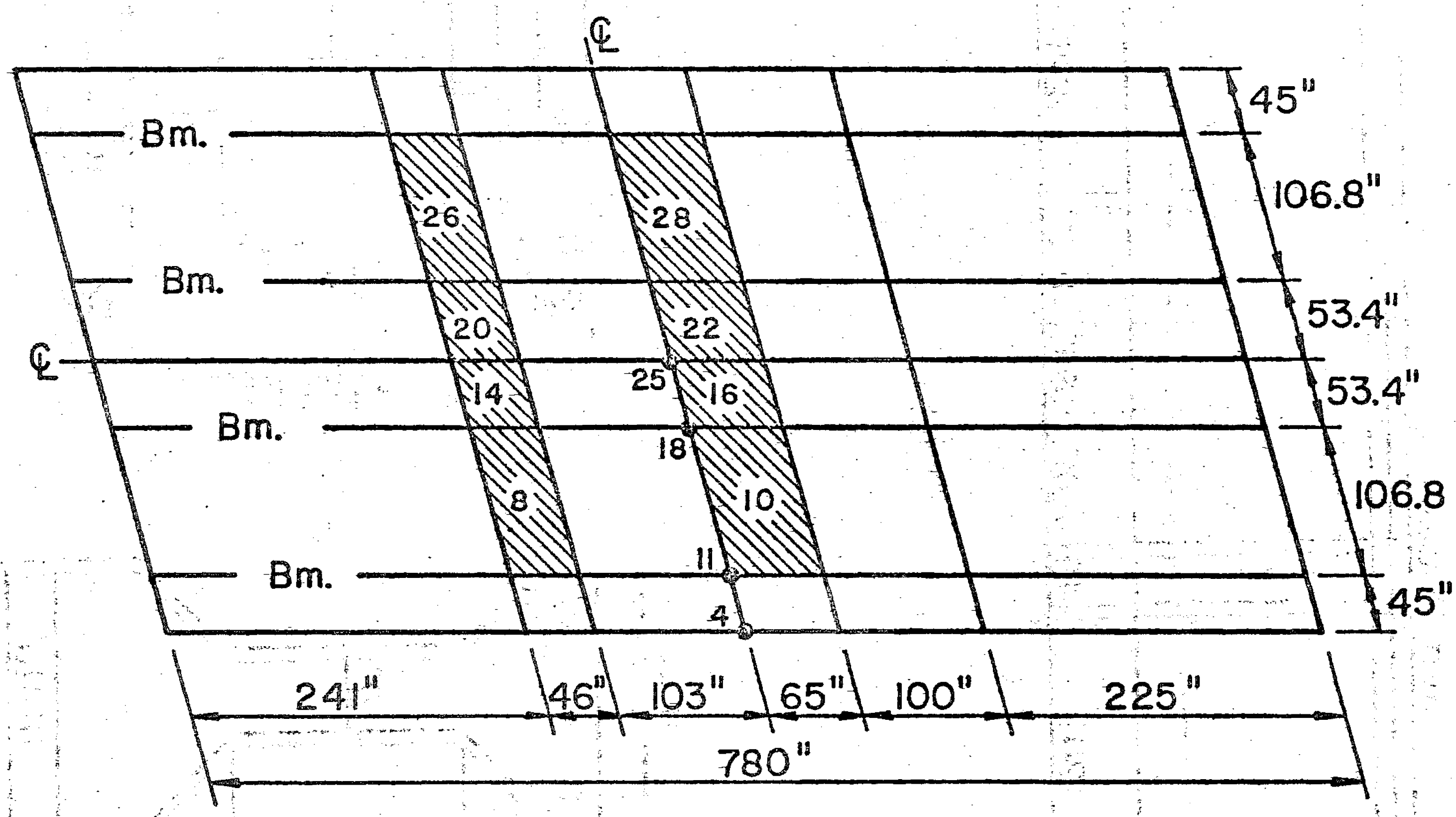

$Q_8 : Q_{14} : Q_{10} : Q_{16} = 2.03 : 4.07 : 1.44 : 2.88$

Fig. 32 Example No. 1 (Bridge 2): Finite Element Discretization and Loading

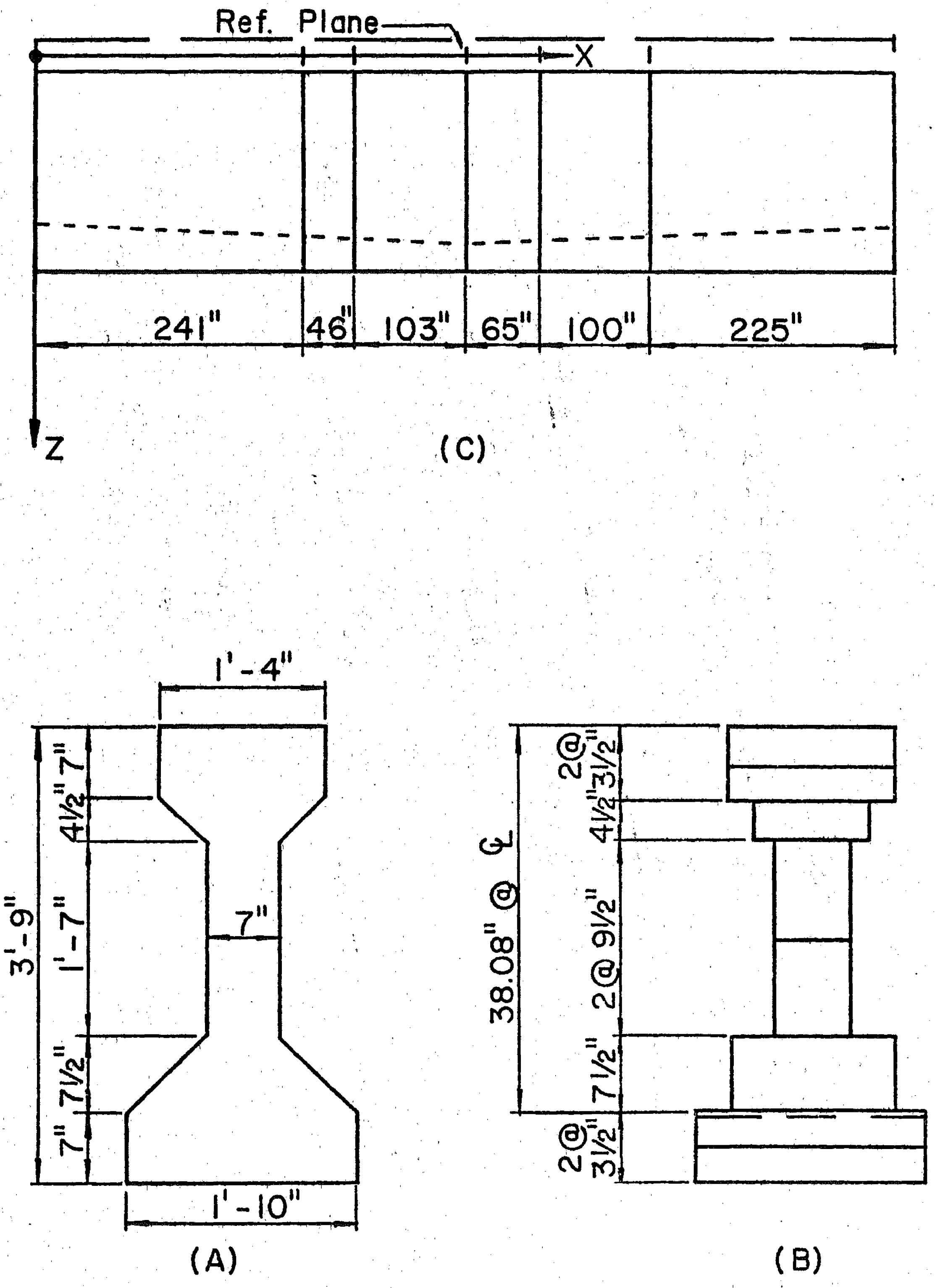

Fig. 33 Example No. 1 (Bridge 2): Beam Layering and Discretization

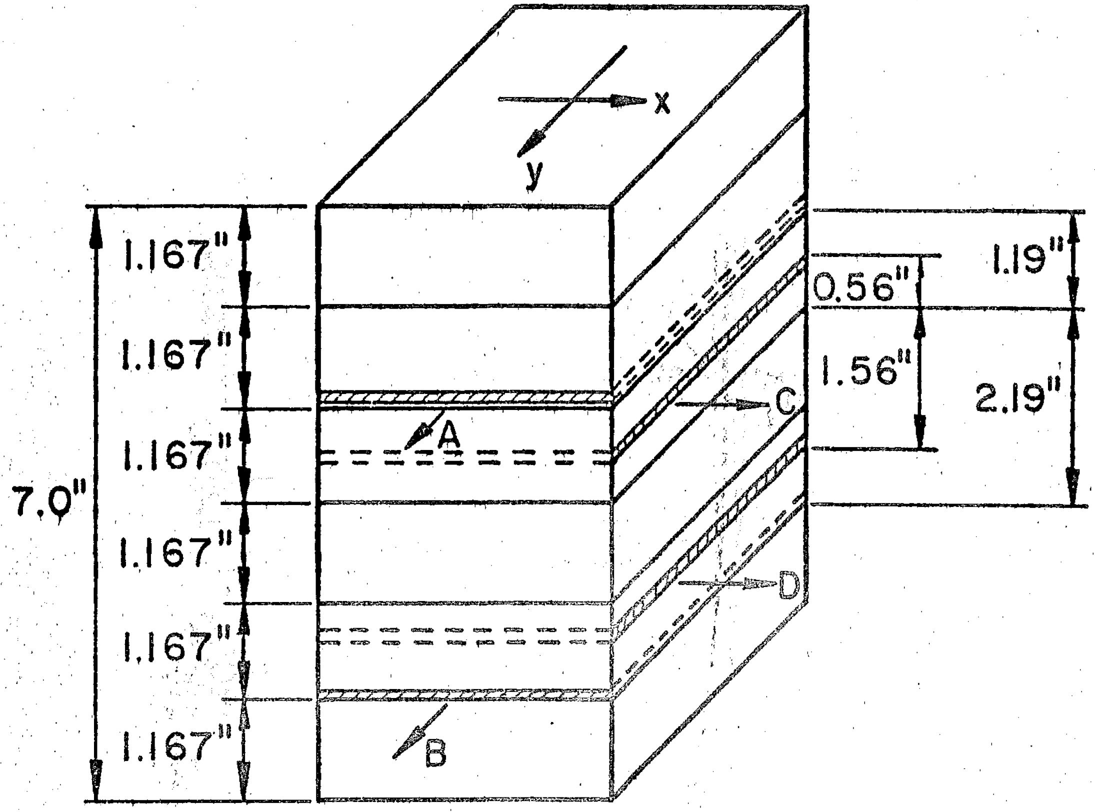

Layer	Ts	θx	Size / Spacing
A	.05667"	-90.0°	#5 At 5.5"
B	.05667"	-90.0°	#5 At 5.5"
C	.03917"	0.0°	#5 At 8.0"
D	.03917"	0.0°	#5 At 8.0"

Fig. 34 Example No. 1 (Bridge 2): Slab Layering

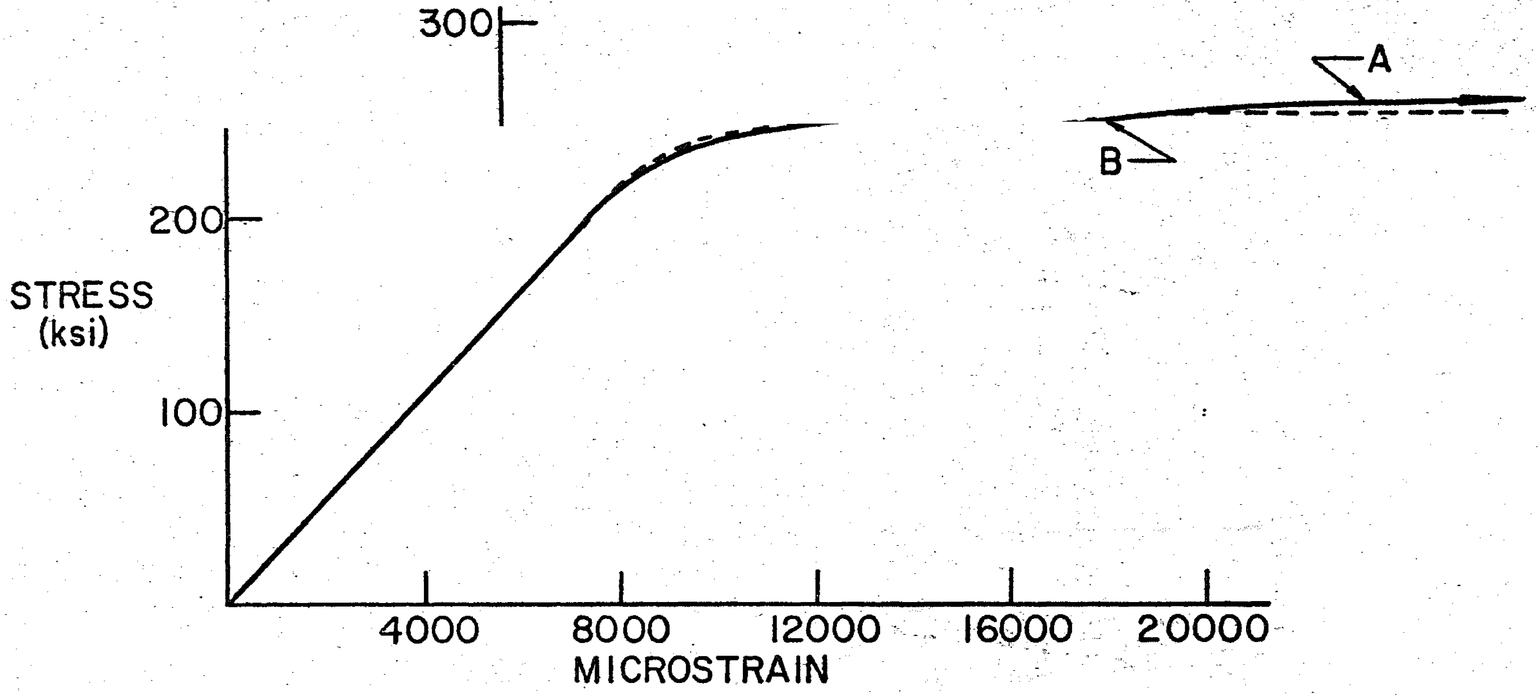

Fig. 35 Example No. 1 (Bridge 2): Idealized (A) and Actual (B) Stress-Strain Curves for the Prestressing Steel

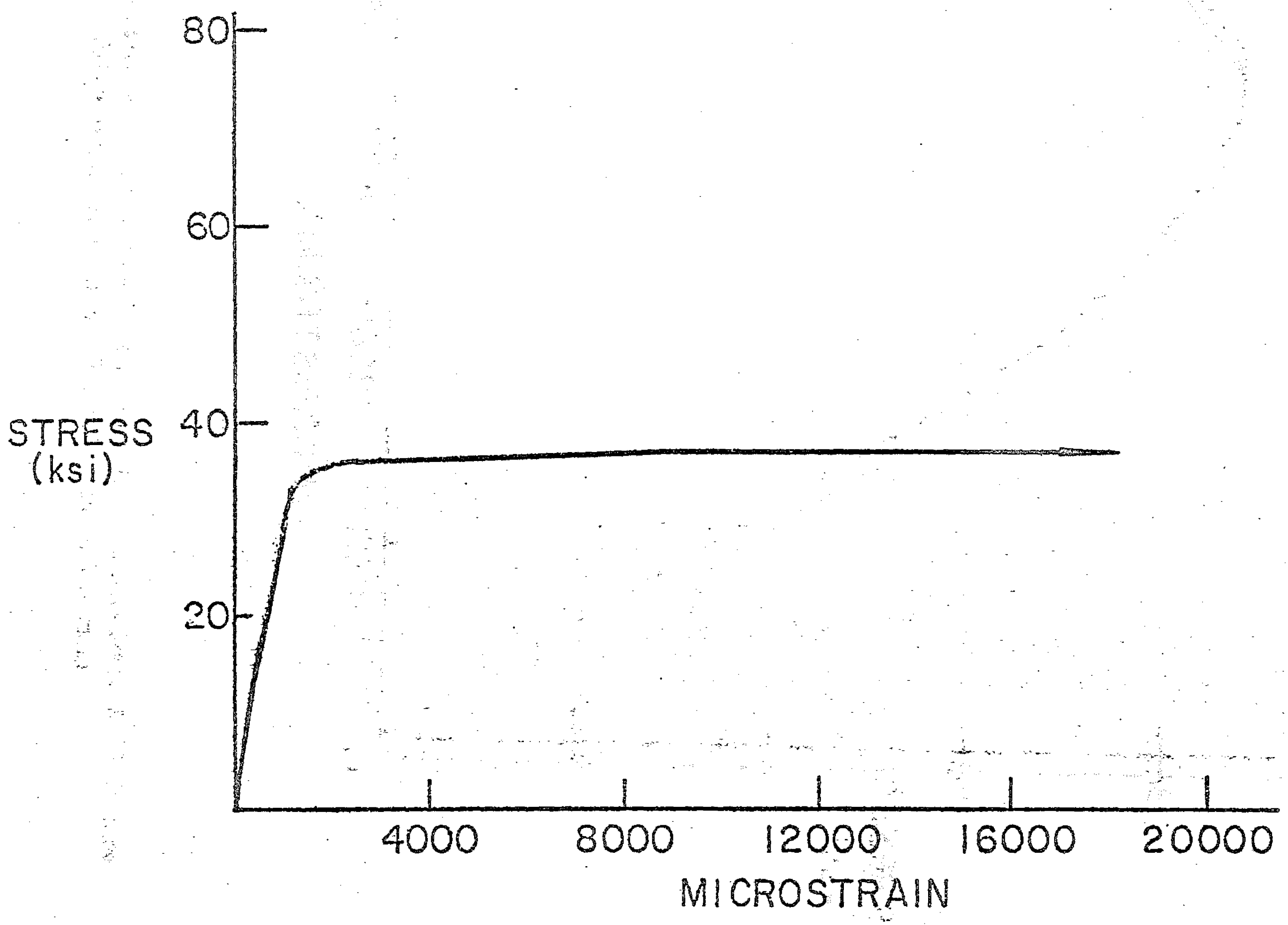

Fig. 36 Example No. 1 (Bridge 2): Analytic Stress-Strain Curve for the Mild Steel Reinforcement

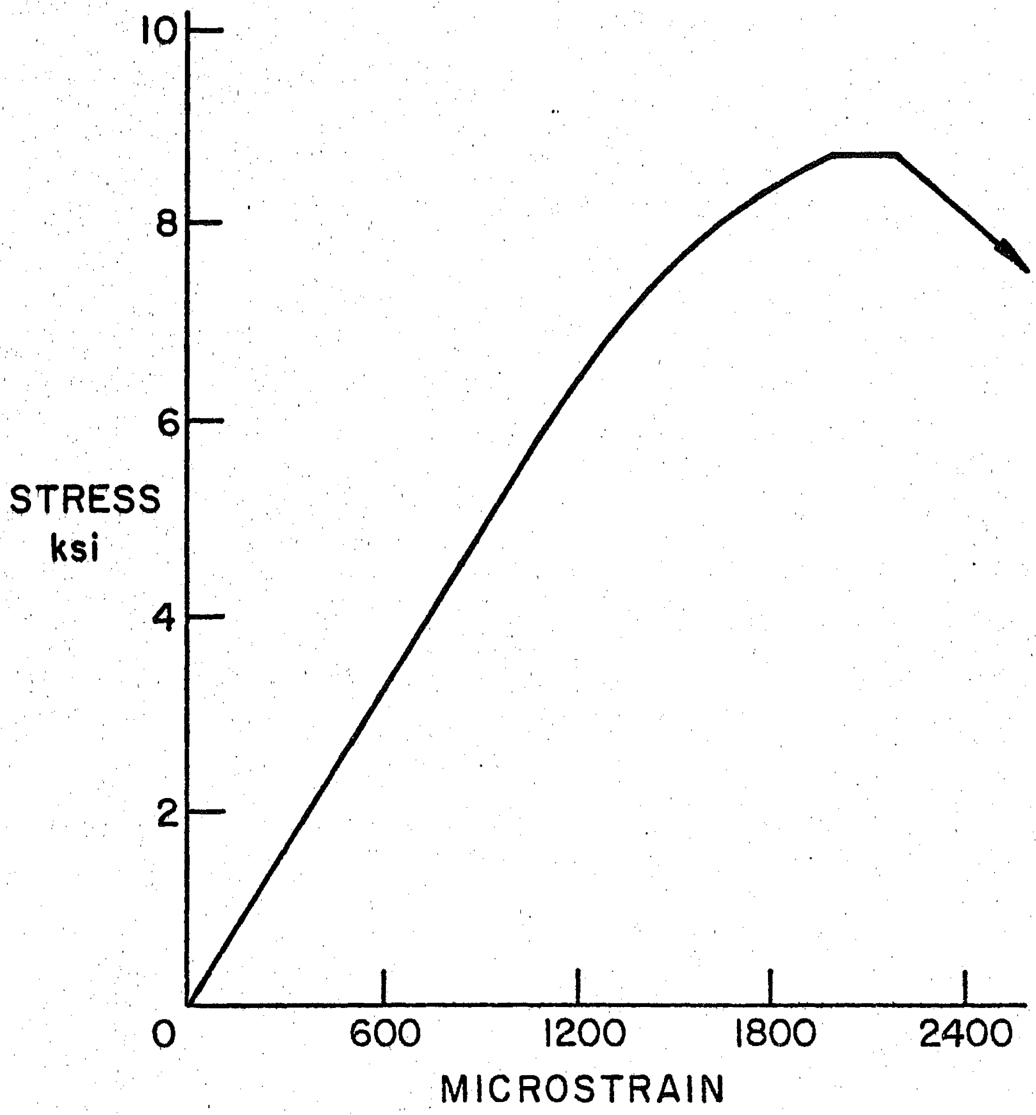

Fig. 37 Example No. 1 (Bridge 2): Analytic Stress-Strain Curve for the Beam Concrete in Compression

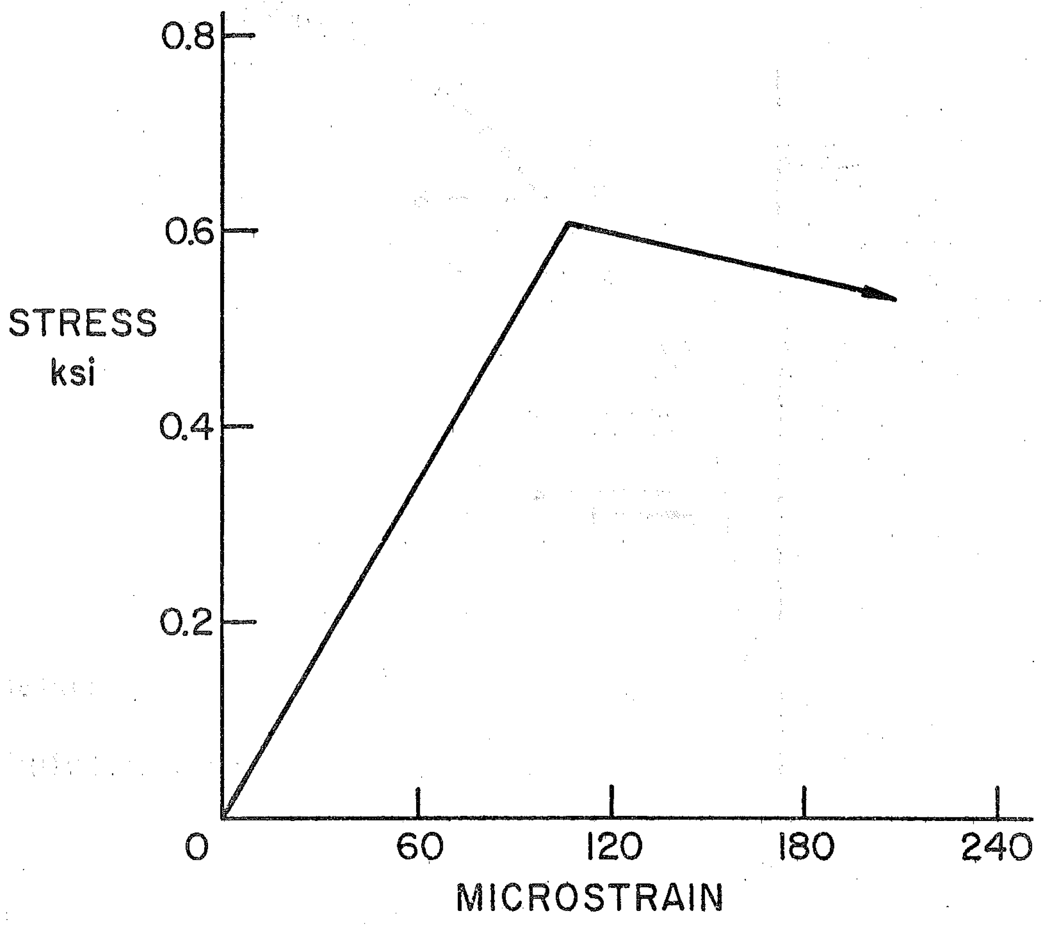

Fig. 38 Example No. 1 (Bridge 2): Analytic Stress-Strain Curve for the Beam Concrete in Tension

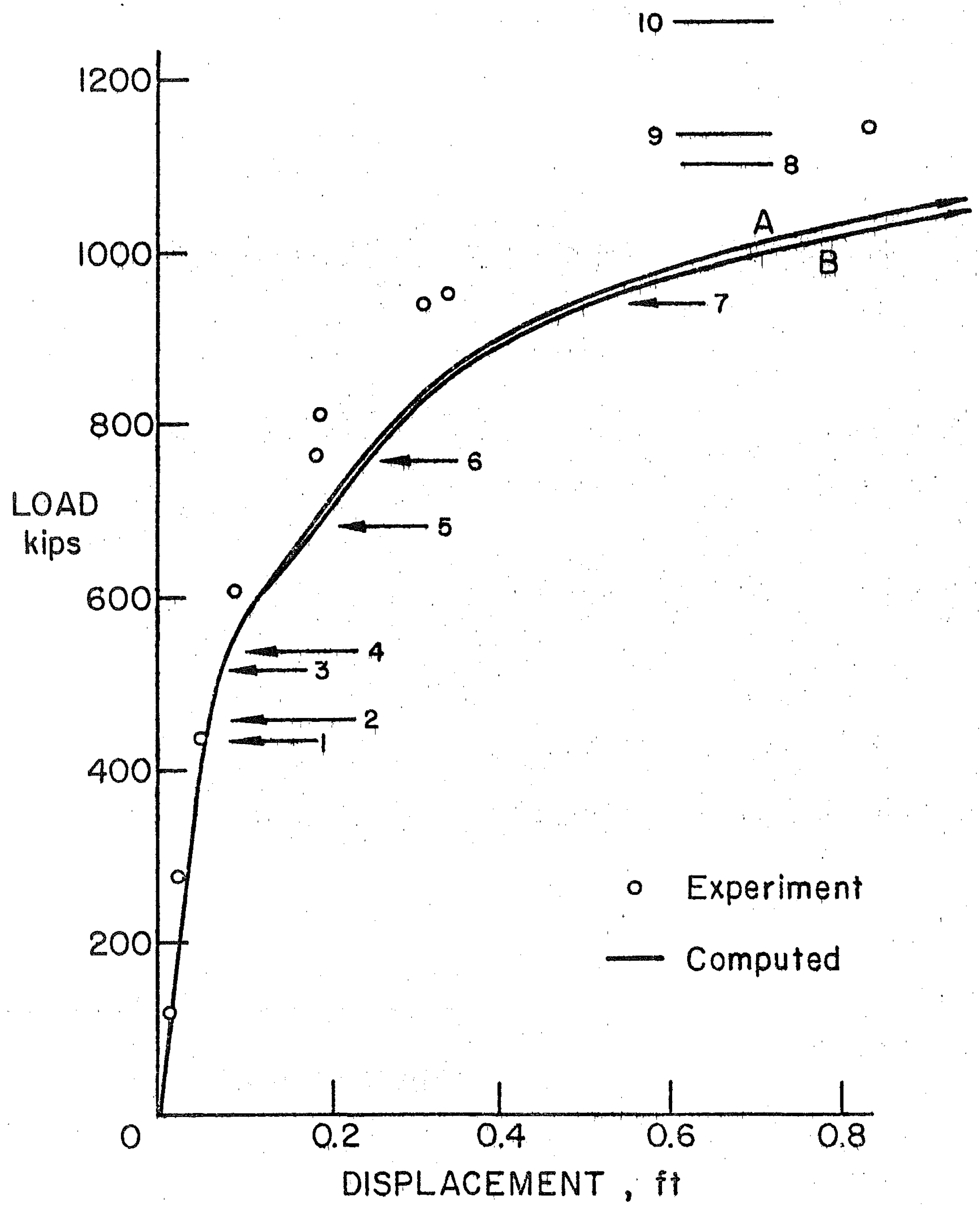

Fig. 39 Example No. 1 (Bridge 2): Load-Deflection Histories for Node 18

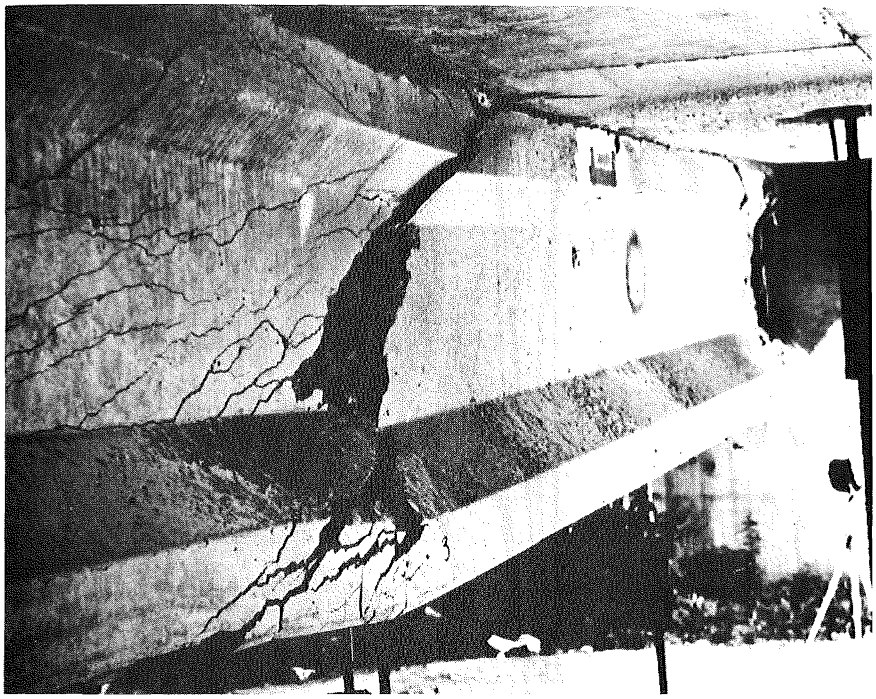

Fig. 40 Photograph of One of the Prestressed Concrete I-Beams of Bridge 2 at Collapse (through the courtesy of The University of Tennessee)

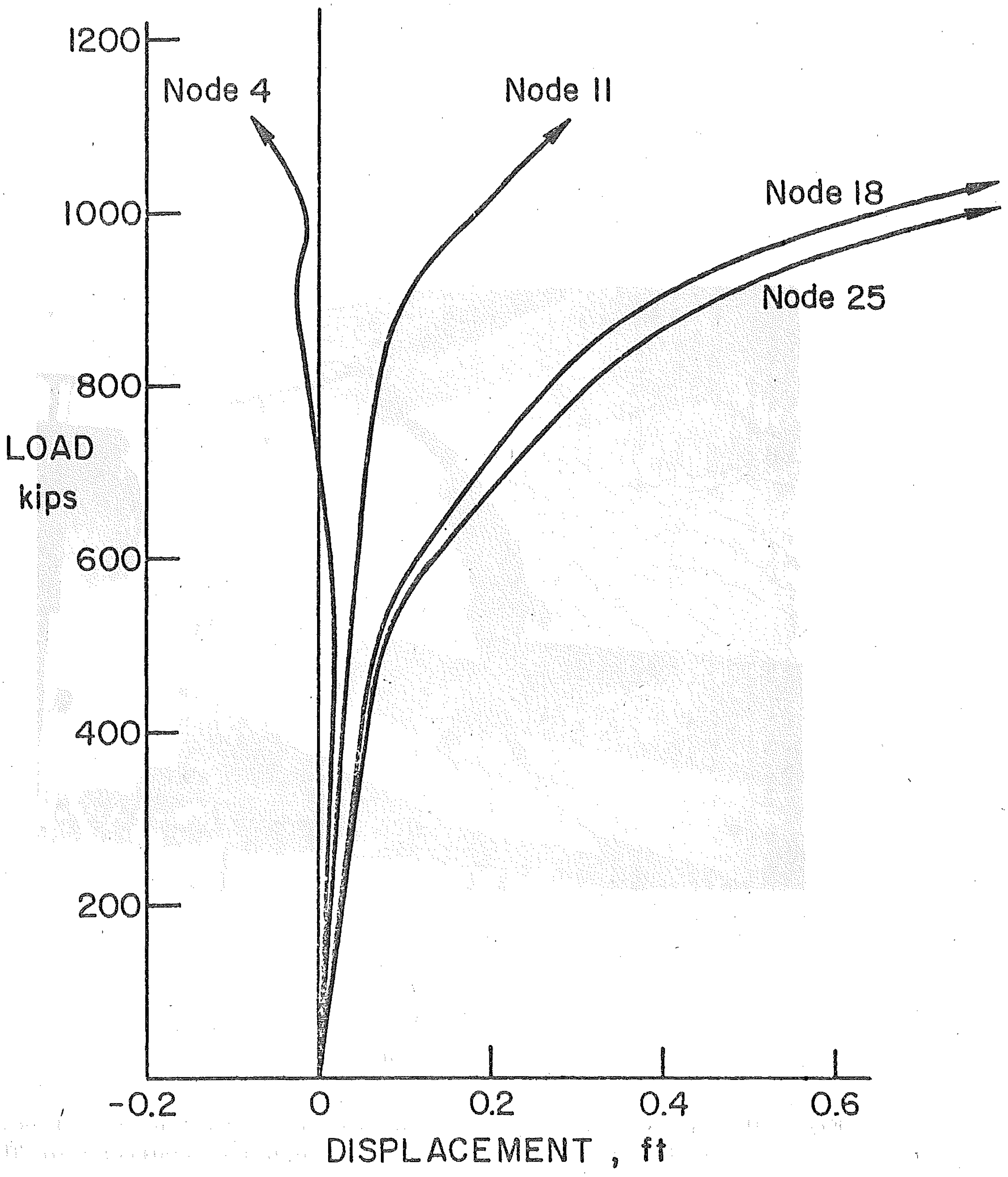

Fig. 41 Example No. 1 (Bridge 2): Load-Deflection Histories for the Midspan Node Line

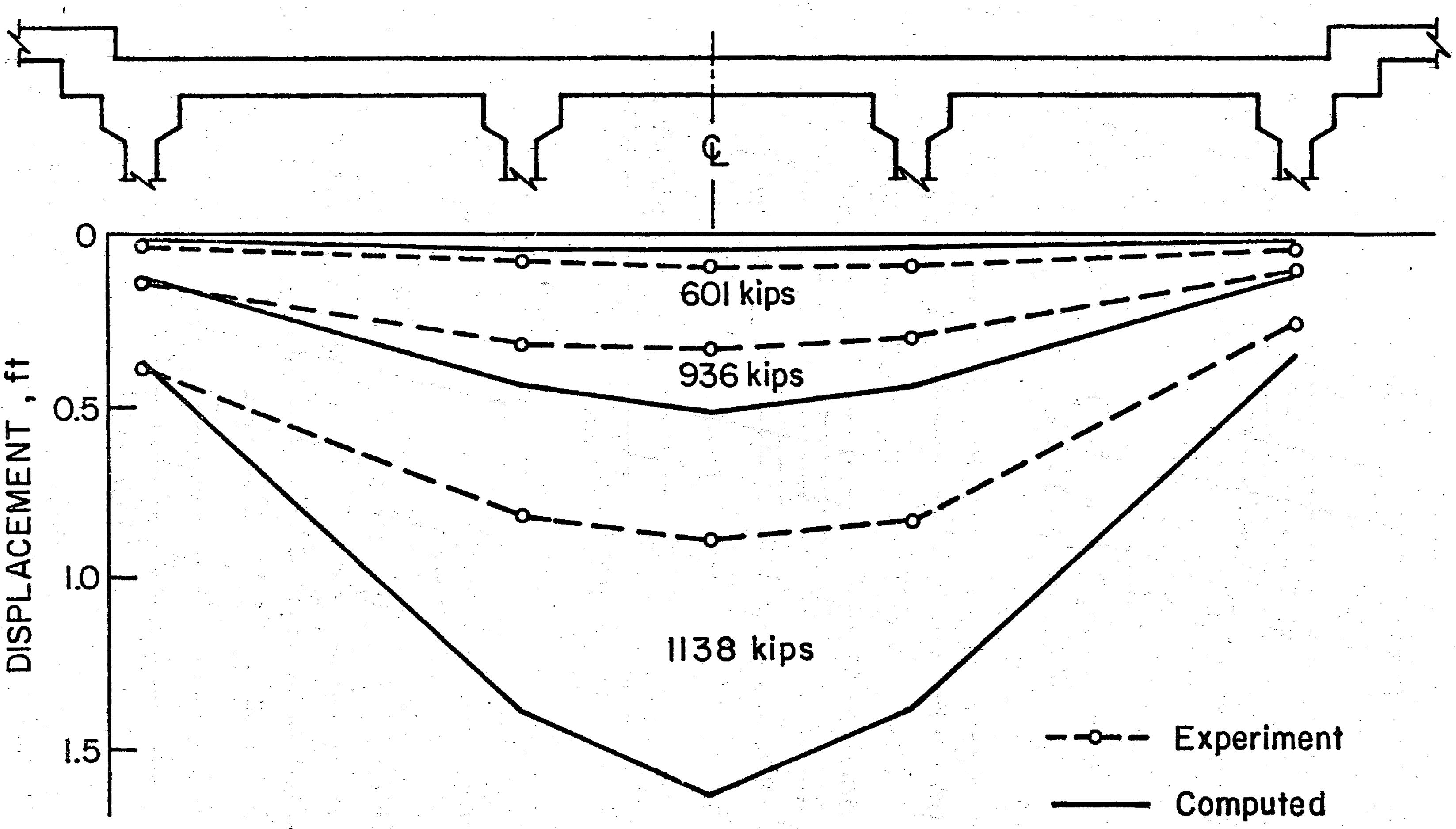

Fig. 42 Example No. 1 (Bridge 2): Load-Deflection Histories for the Midspan Cross-Section

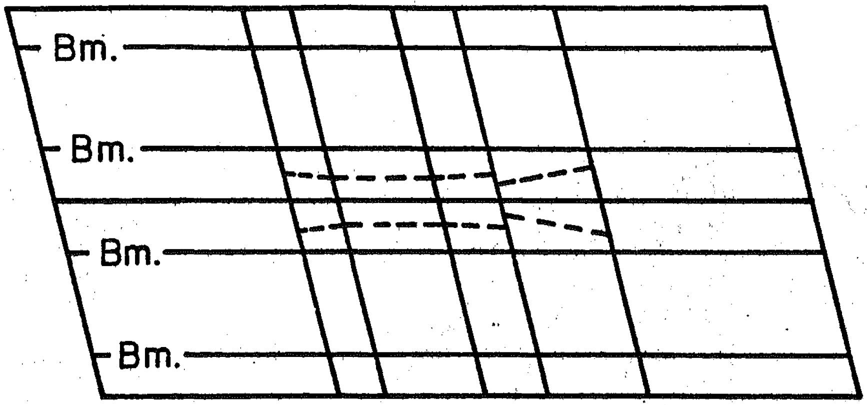

(a) 420 kips

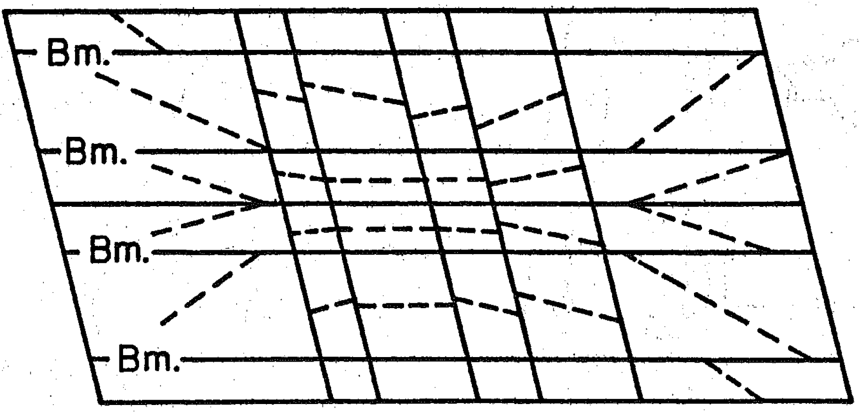

(b) 723 kips

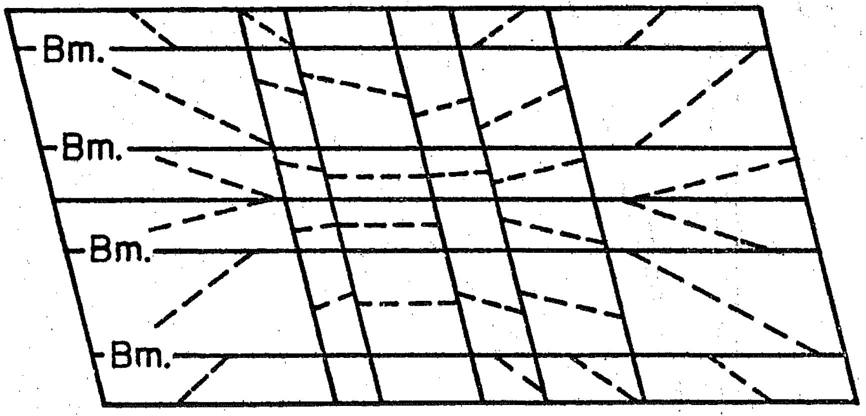

(c) 1108 kips

Fig. 43 Example No. 1 (Bridge 2): Analytic Load-Crack History for the Bottom Surface of the Deck Slab

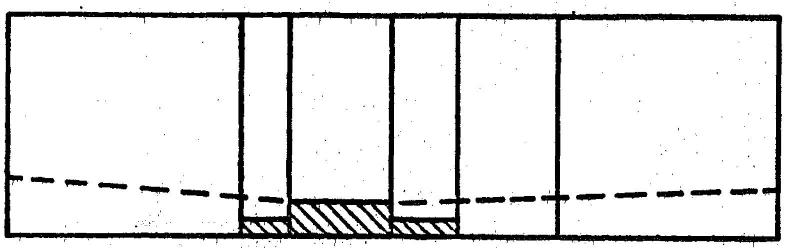

(a) 420 kips

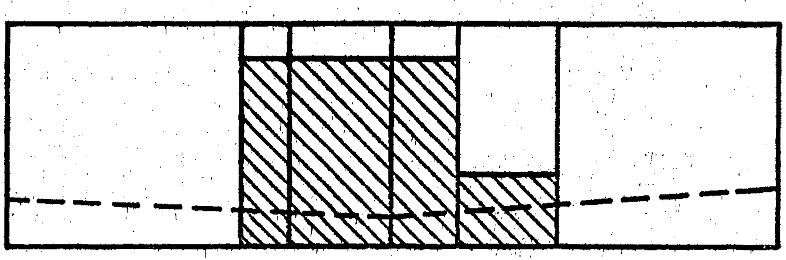

(b) 723 kips

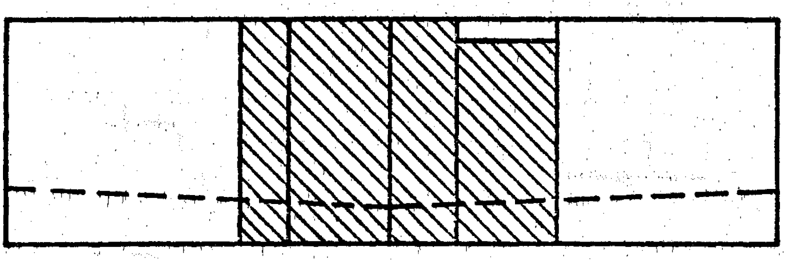

(c) 1108 kips

Fig. 44 Example No. 1 (Bridge 2): Analytic Load-Crack Depth History for the Interior Beam

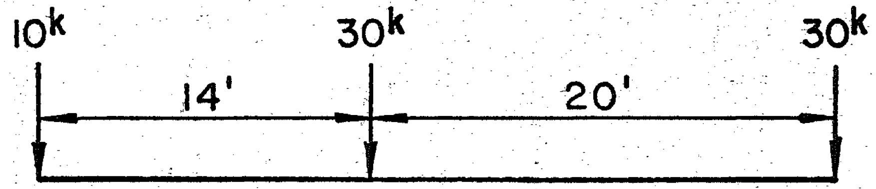

DESIGN LOADING B

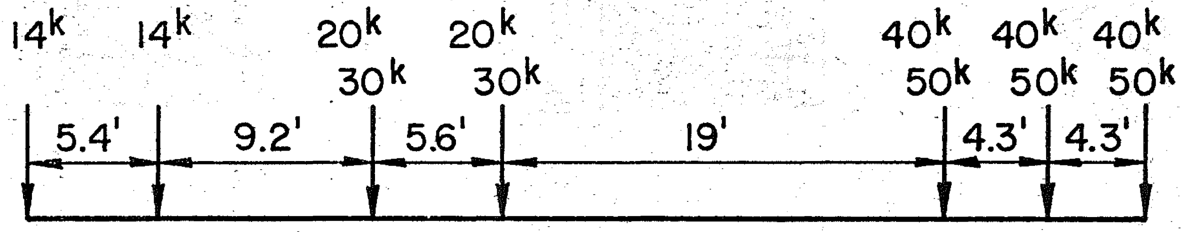

OVERLOAD VEHICLE

Fig. 45 Example No. 2 (Bridge 8B): Axle Loads and Spacing

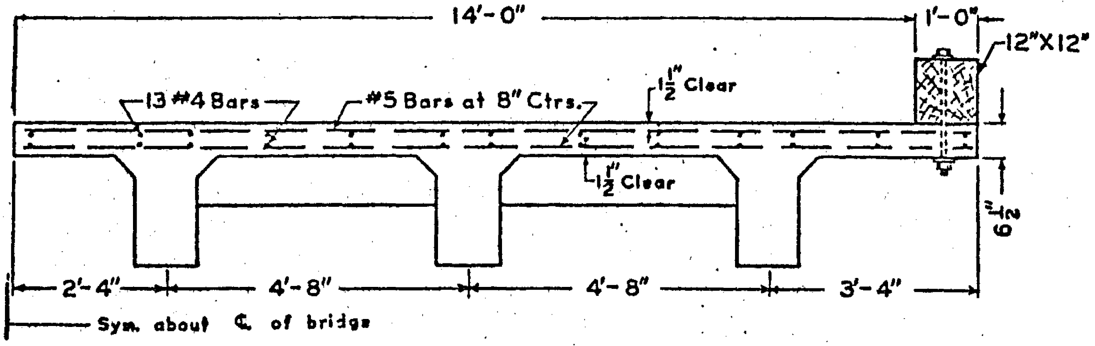

(A) TYPICAL CROSS-SECTION

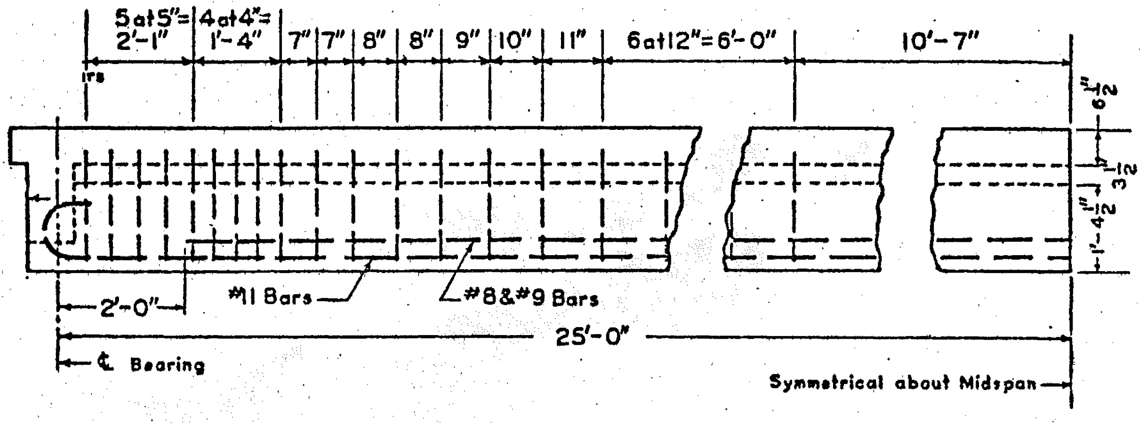

(B) TYPICAL BEAM REINFORCEMENT

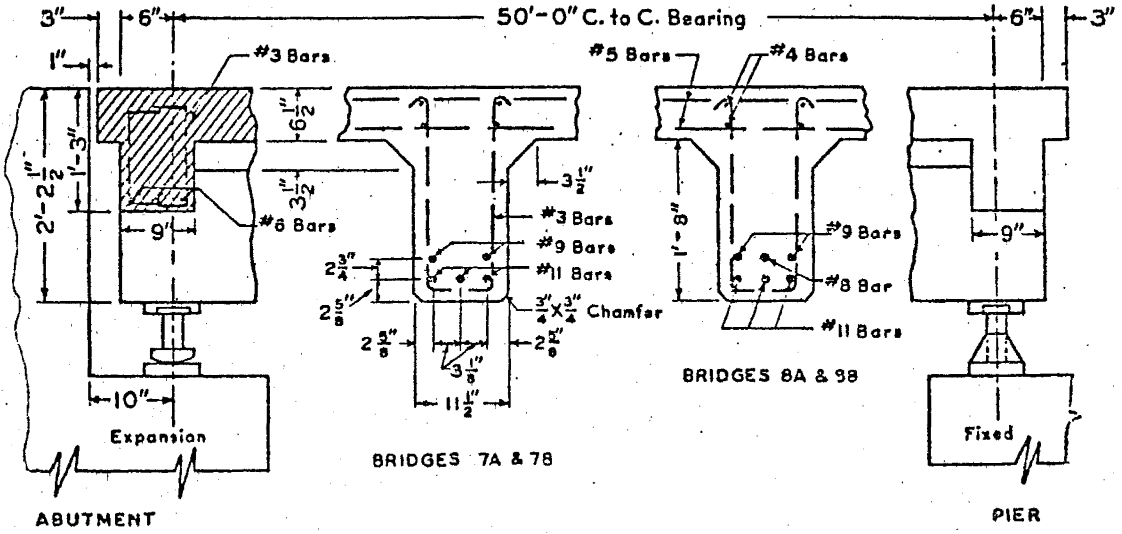

(C) TYPICAL DETAILS

Fig. 46 Example No. 2 (Bridge 8B): Dimensions (taken from Ref. 17)

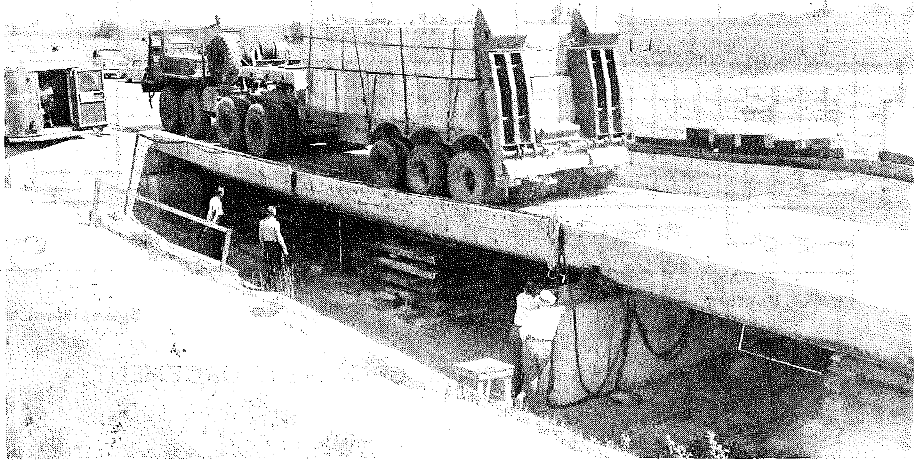

Fig. 47 Photograph of the Overload Vehicle (through the courtesy of the Transportation Research Board)

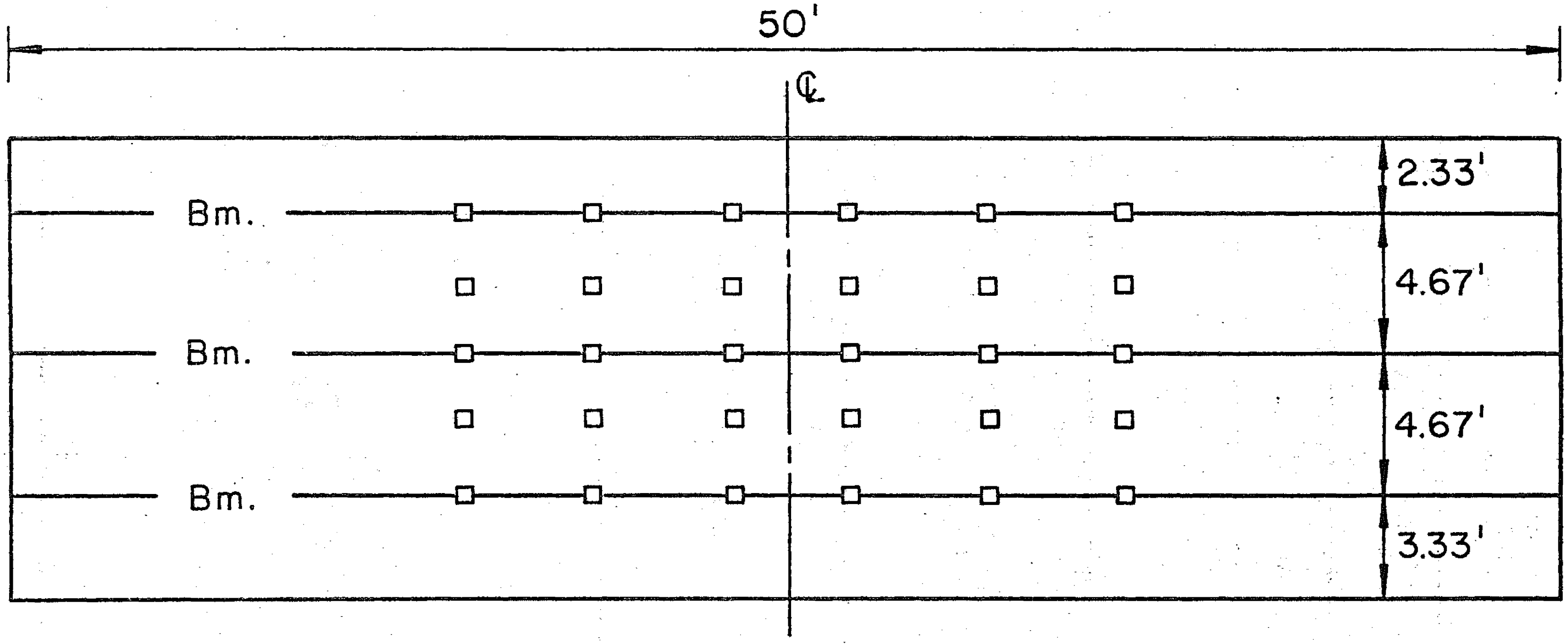

Fig. 48 Example No. 2 (Bridge 8B): Idealized Loading and Plan View

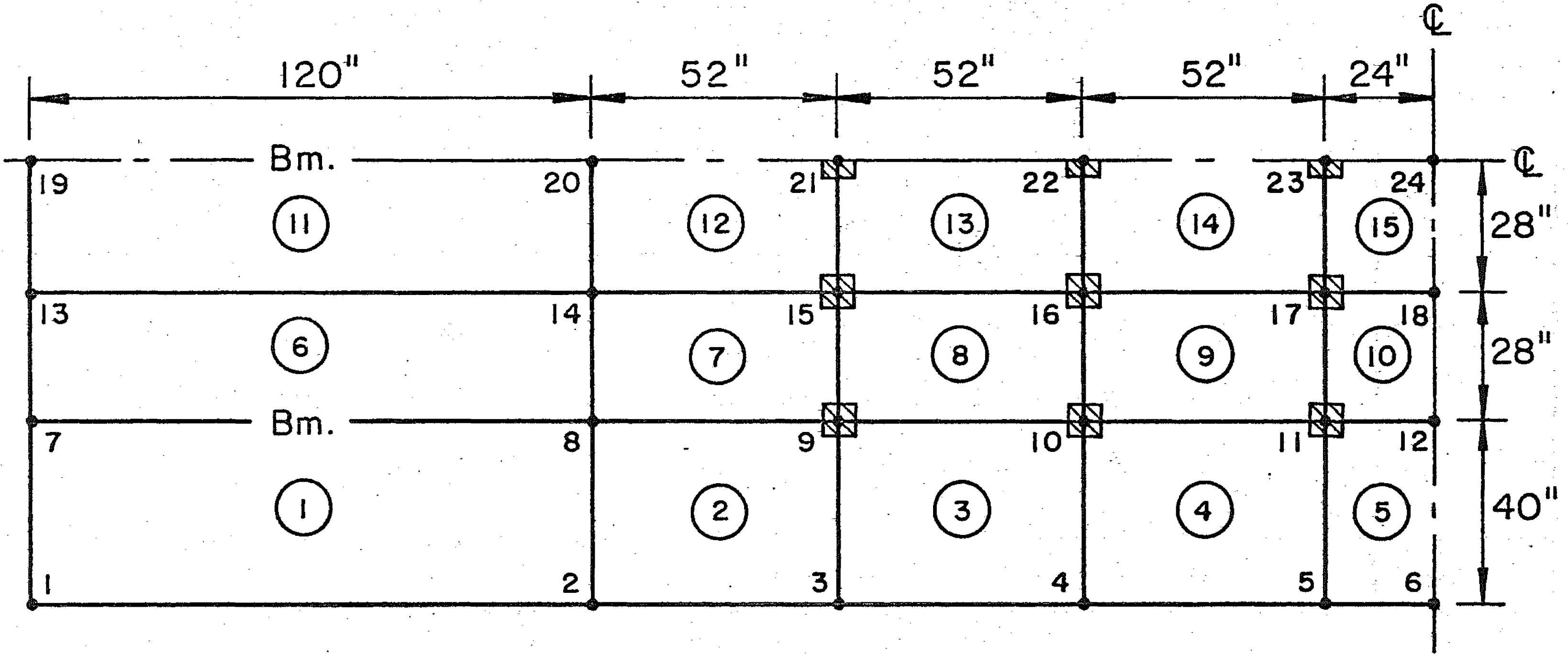

Fig. 49 Example No. 2 (Bridge 8B): Finite Element Discretization and Loading

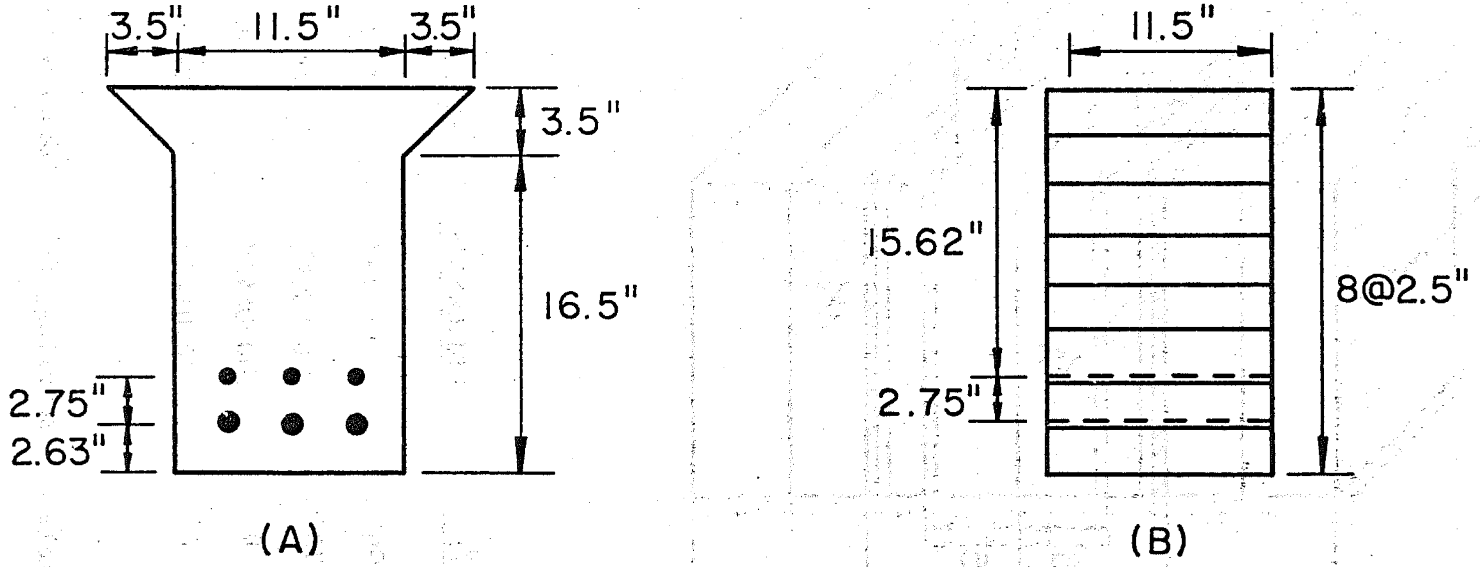

Fig. 50 Example No. 2 (Bridge 8B): Beam Layering

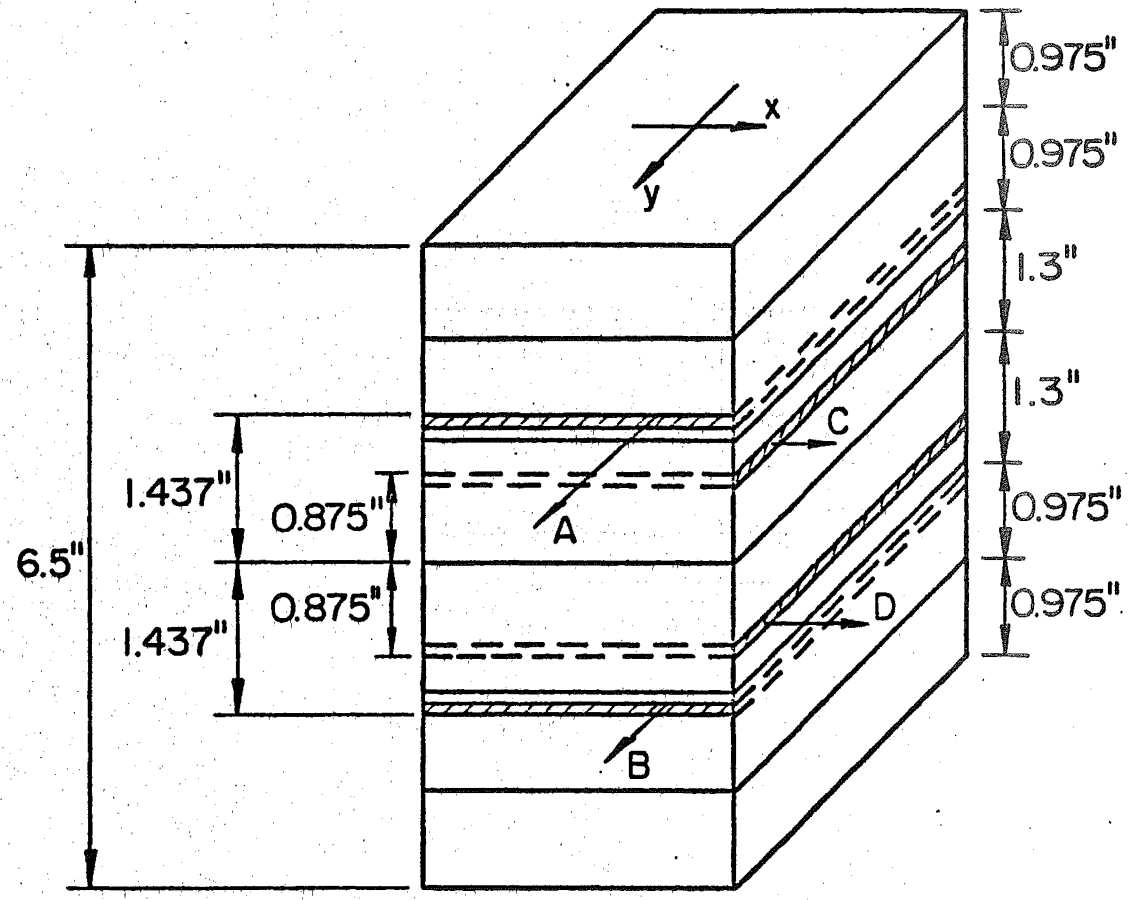

LAYER	θ_x	THICKNESS	SIZE/SPACING
A	90°	0.0379"	#5 @ 8"
B	90°	0.0379"	#5 @ 8"
C	0°	0.0143"	#4 @ 14"
D	0°	0.0143"	#4 @ 14"

Fig. 51 Example No. 2 (Bridge 8B): Slab Layering

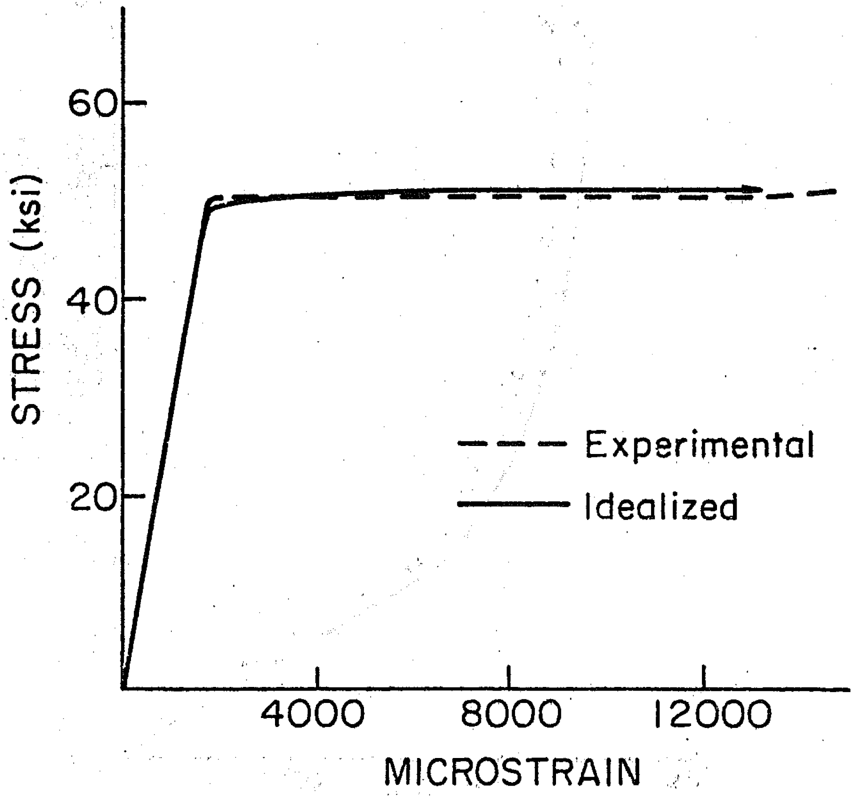

Fig. 52 Example No. 2 (Bridge 8B): Stress-Strain Curve for the Mild Steel Reinforcing

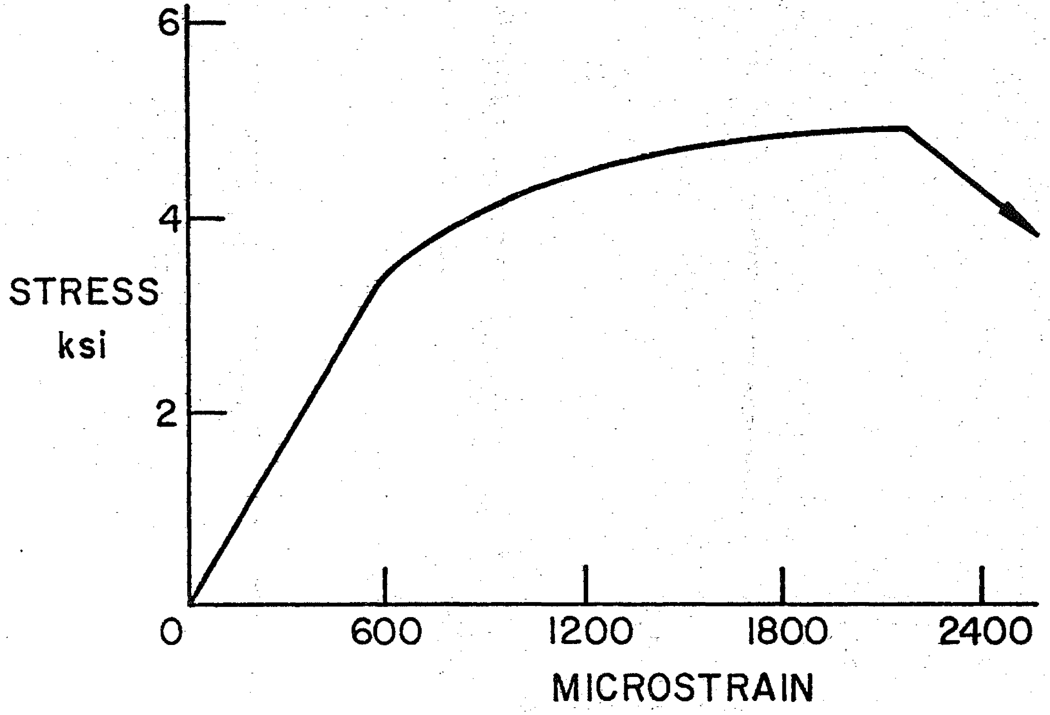

Fig. 53 Example No. 2 (Bridge 8B): Stress-Strain Curve for the Beam Concrete in Compression

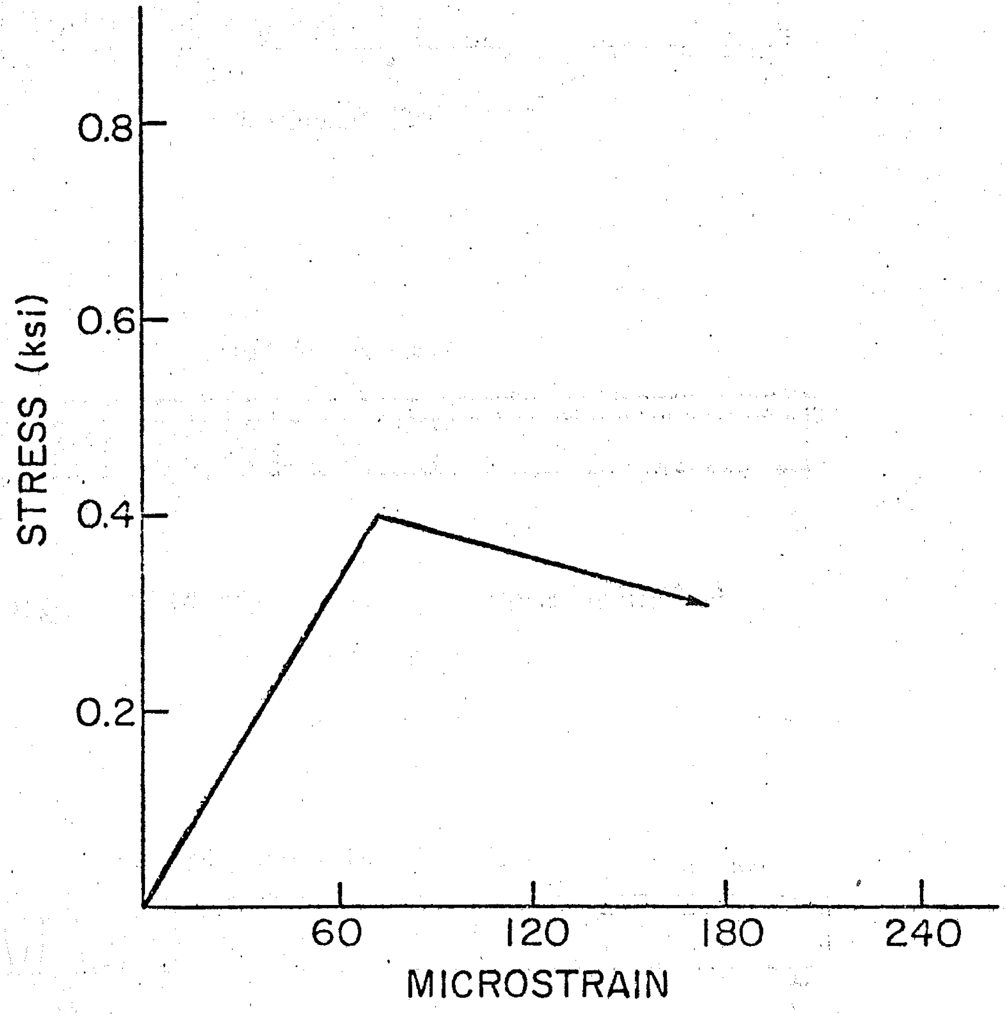

Fig. 54 Example No. 2 (Bridge 8B): Stress-Strain Curve for the Beam Concrete in Tension

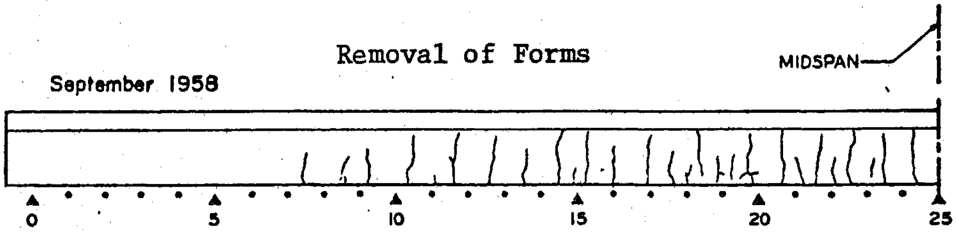
Removal of Forms

September 1958

(A) Measured

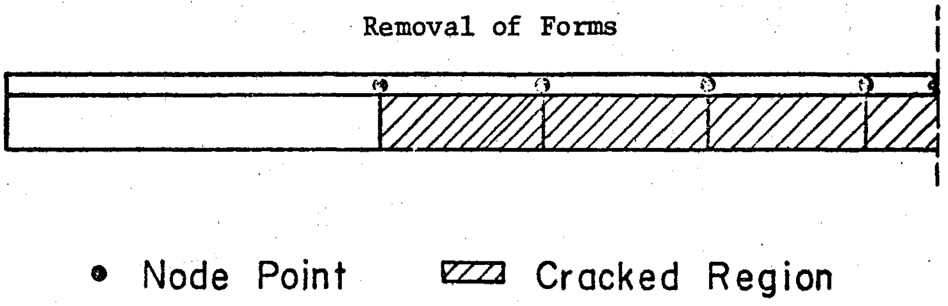
Removal of Forms

● Node Point ▨ Cracked Region

(B) Predicted

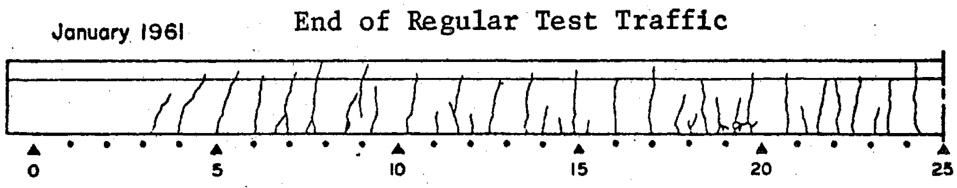
January 1961 End of Regular Test Traffic

(C) Measured

Fig. 55 Example No. 2 (Bridge 8B): Crack Patterns in the Exterior Beam

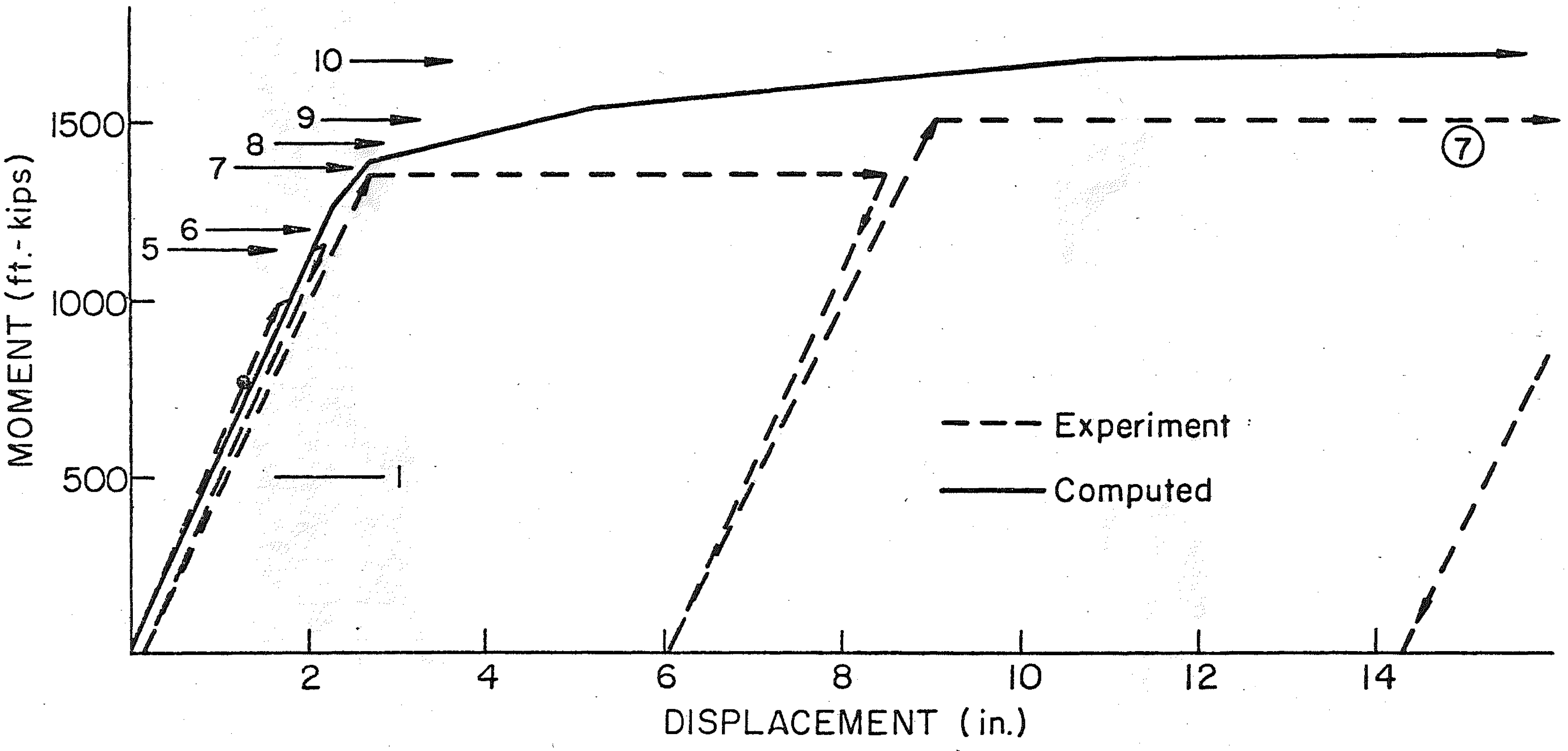

Fig. 56 Example No. 2 (Bridge 8B): Load-Deflection History

Fig. 57A Photograph of the Bridge 8B After Collapse (through the courtesy of the Transportation Research Board)

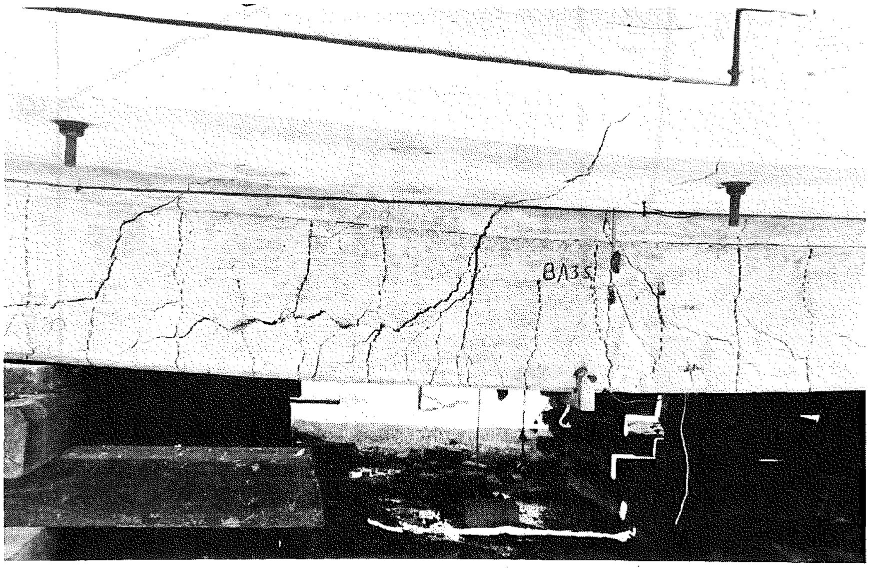

Fig. 57B Photograph of One of the Reinforced Concrete Beams of Bridge 8A After Failure (through the courtesy of the Transportation Research Board)

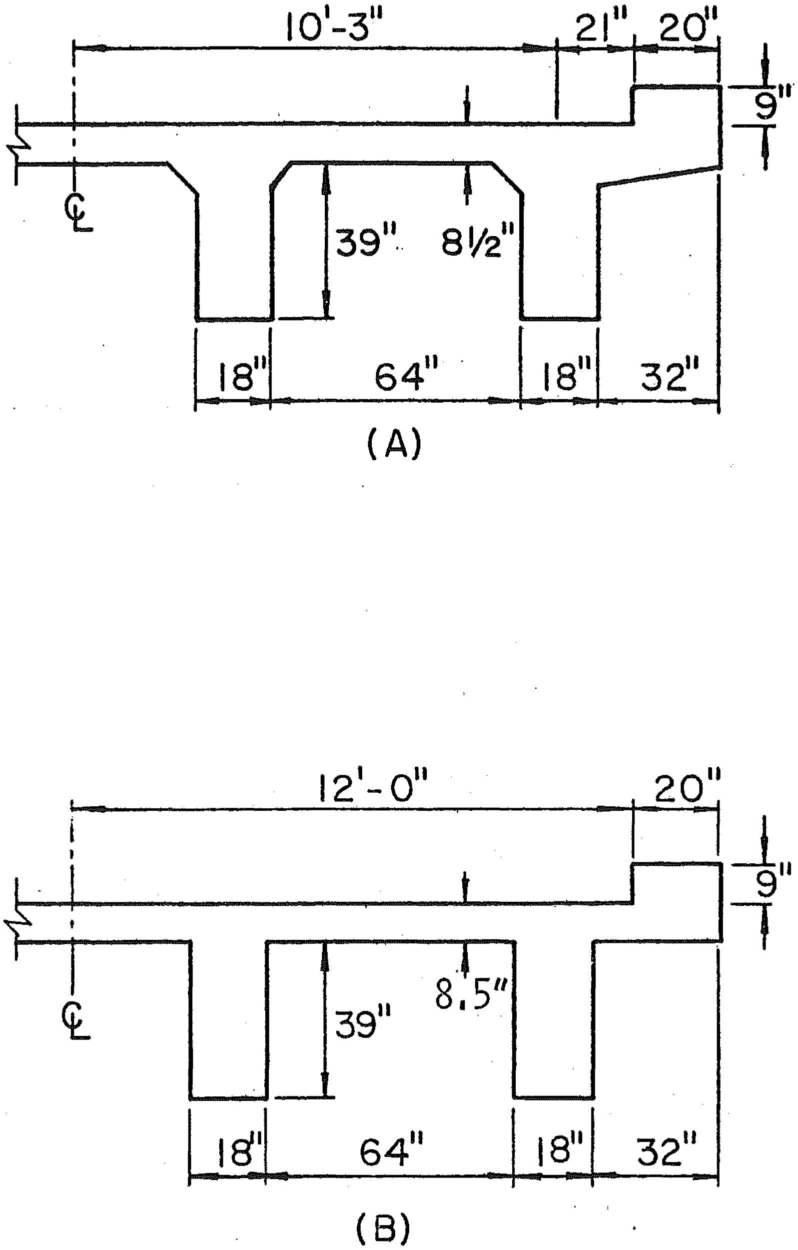

Fig. 58 Example No. 3 (Bridge 3): Actual (A) and Idealized (B) Cross-Sections

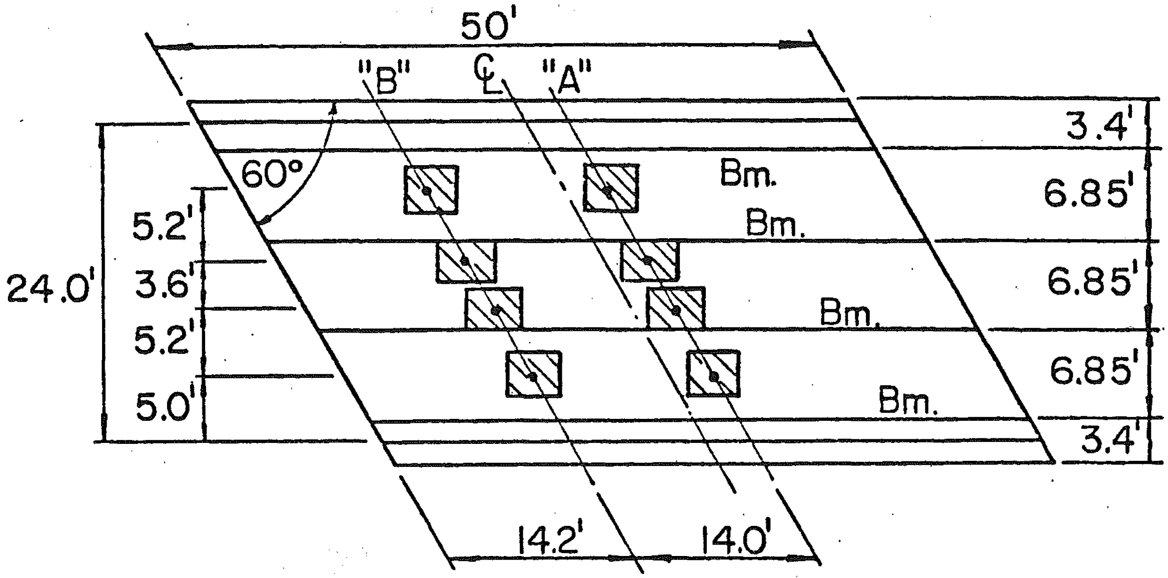

(A)

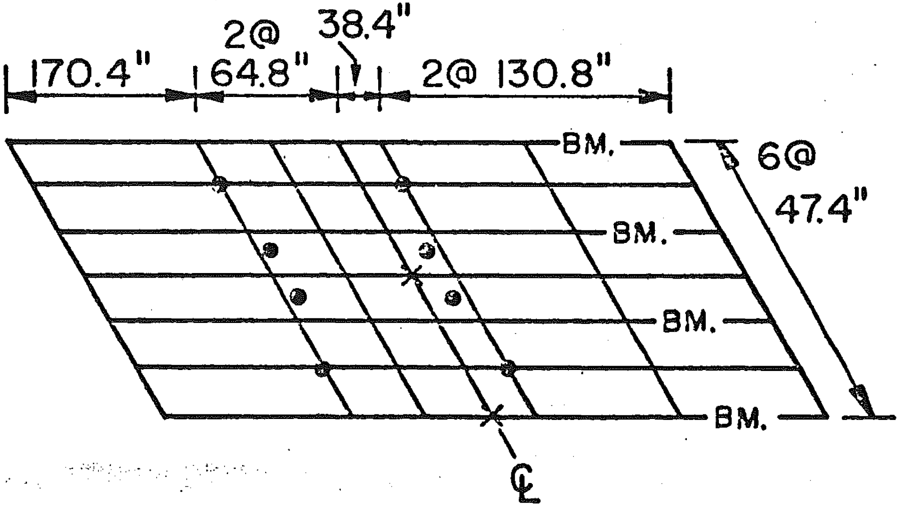

(B)

Fig. 59 Example No. 3 (Bridge 3): Actual (A) and Idealized (B) Plan Views

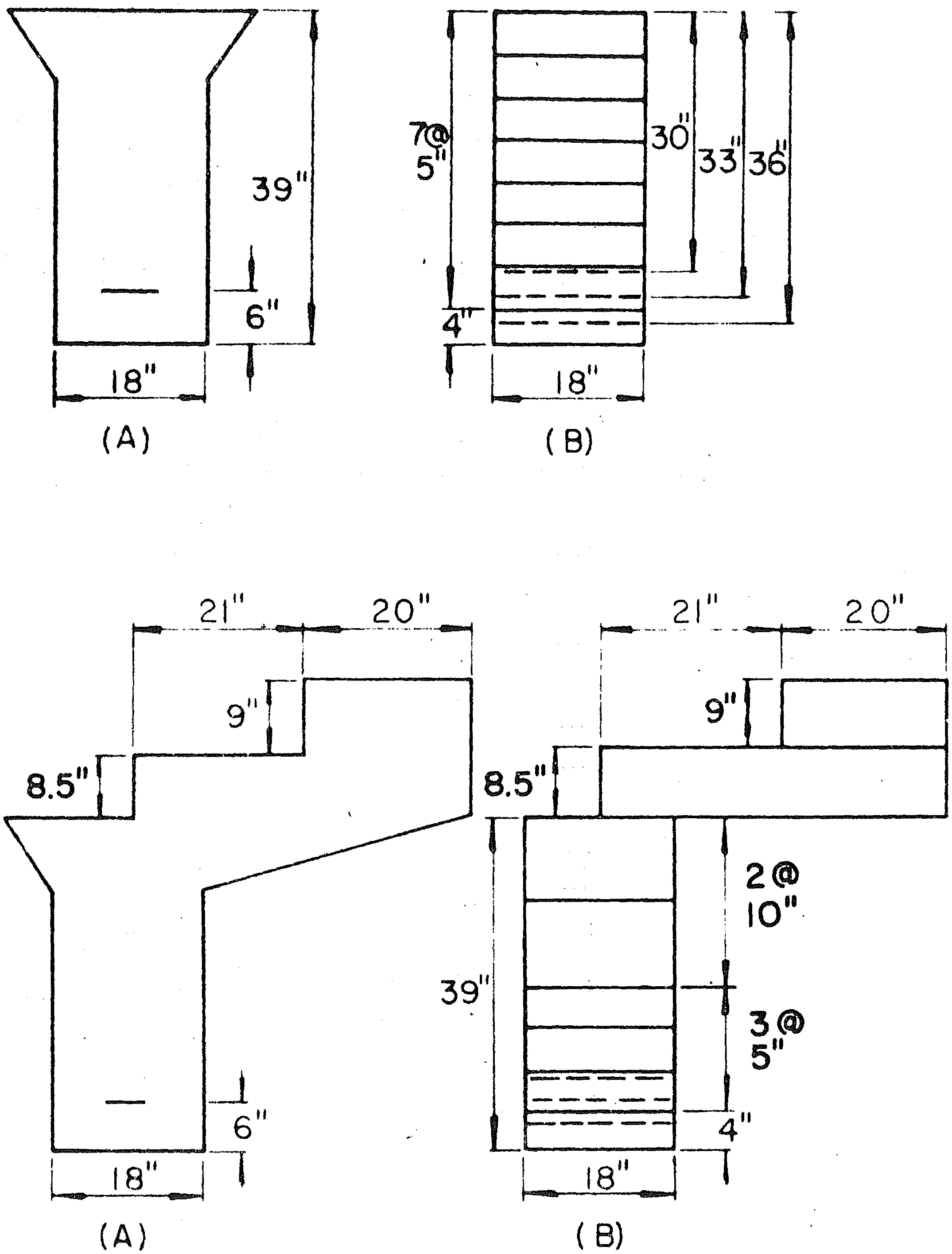

Fig. 60 Example No. 3 (Bridge 3): Actual (A) and Idealized (B) Beam Cross-Sections

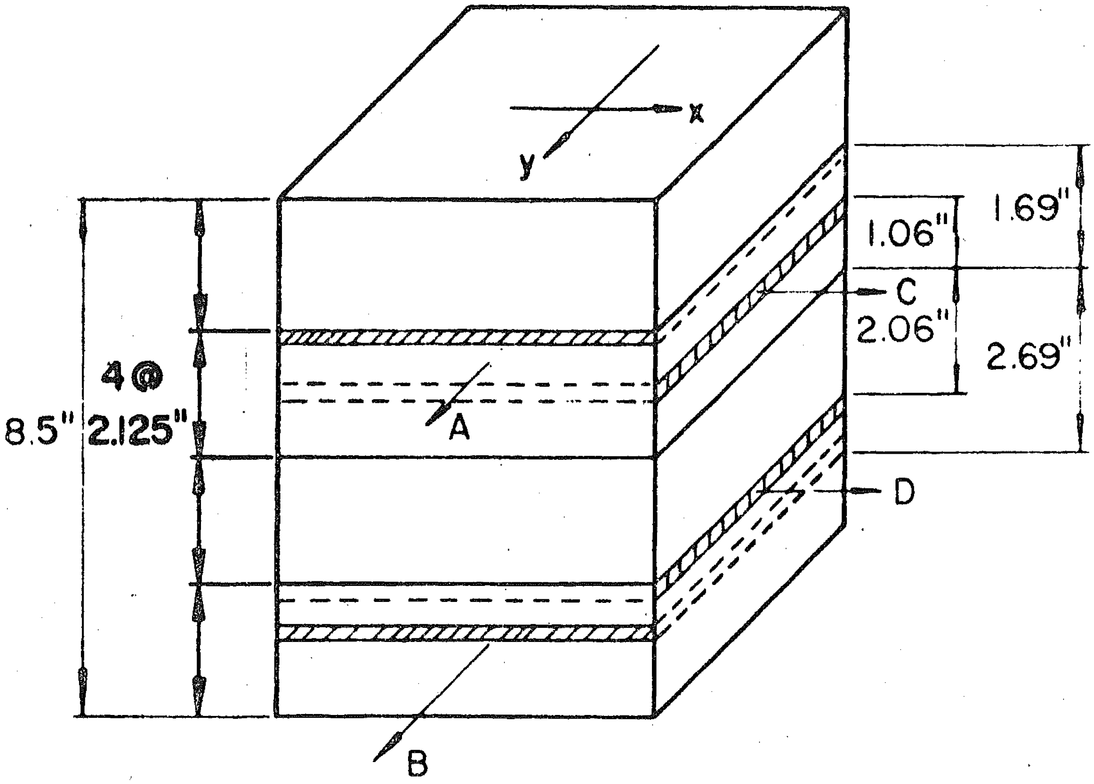

Layer	T s	θx	Size / Spacing
A	.05667"	-90.°	# 5 At 5.5"
B	.05667"	-90.°	# 5 At 5.5"
C	.03917"	0.°	# 5 At 8.0"
D	.03917"	0.°	# 5 At 8.0"

Fig. 61 Example No. 3 (Bridge 3): Slab Layering

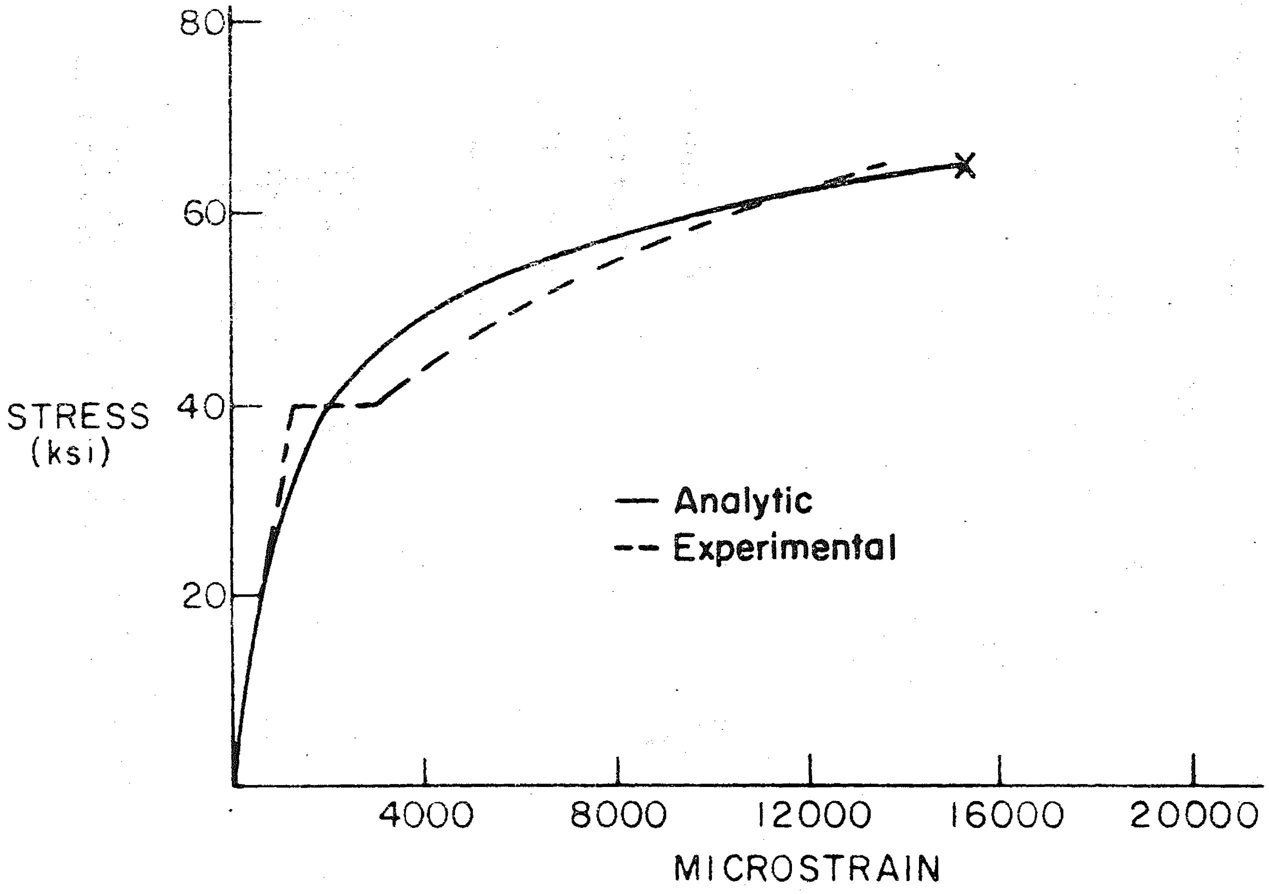

Fig. 62 Example No. 3 (Bridge 3): Stress-Strain Curves for the Steel Reinforcement

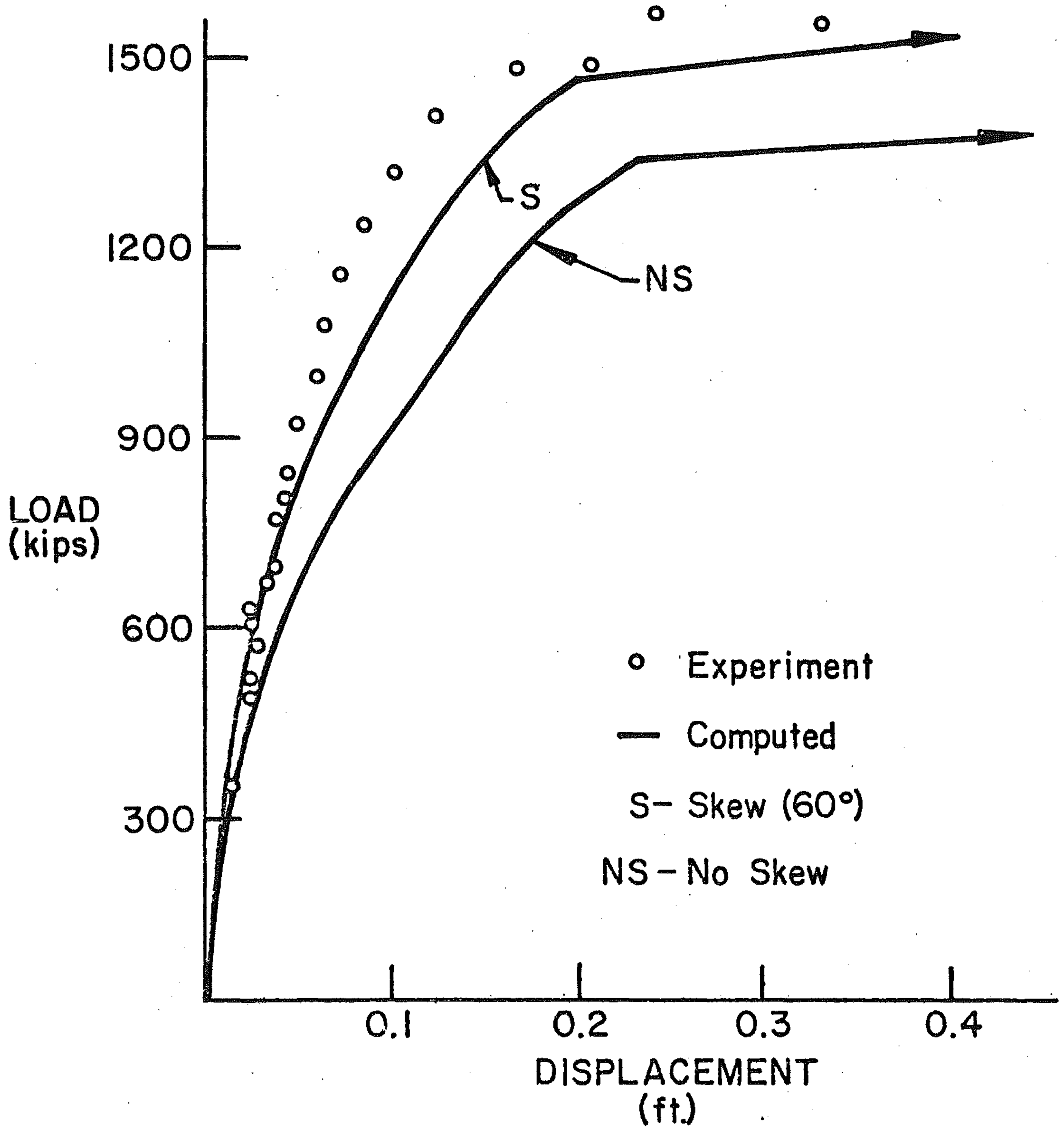

Fig. 63 Example No. 3 (Bridge 3): Load-Deflection Histories for the Midspan of the Exterior Beam

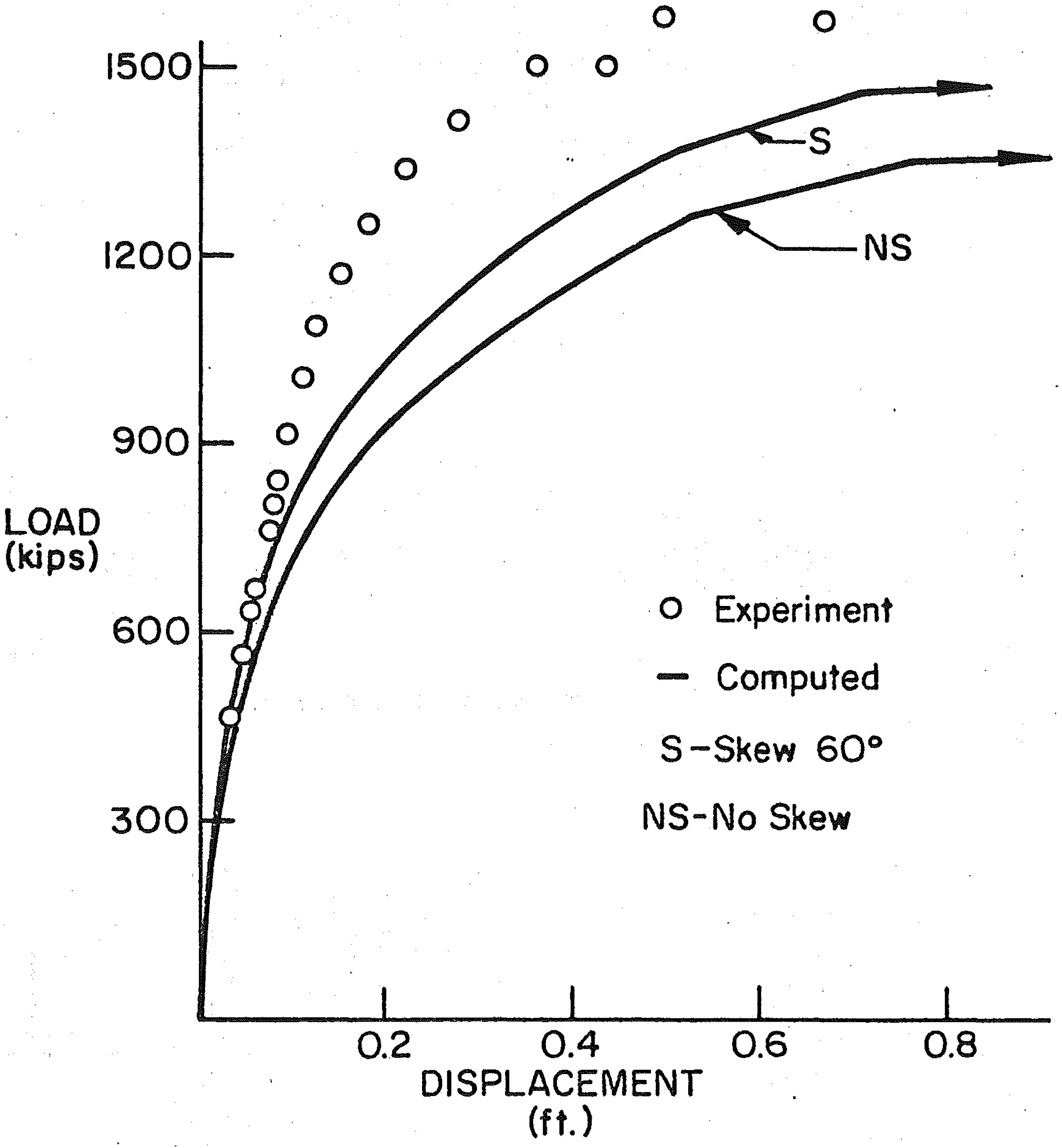

Fig. 64 Example No. 3 (Bridge 3): Load-Deflection Histories for the Center Point of the Superstructure

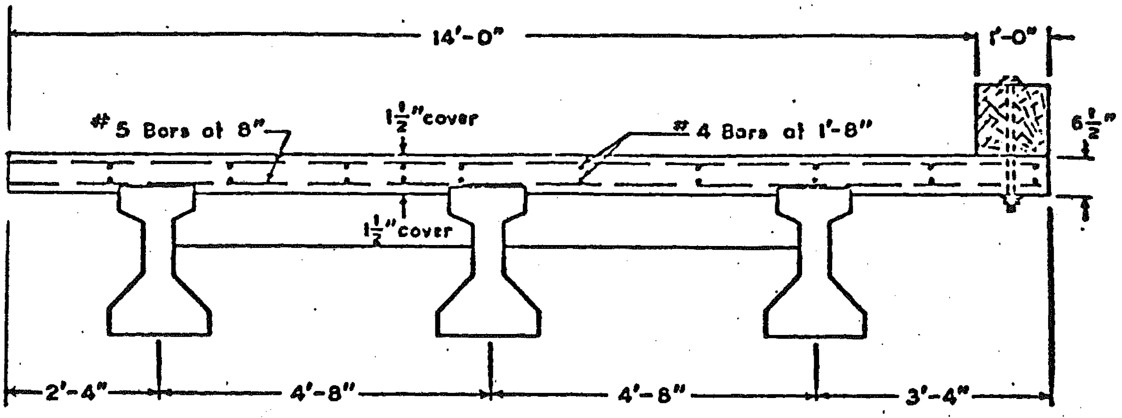

(A) TYPICAL CROSS-SECTION

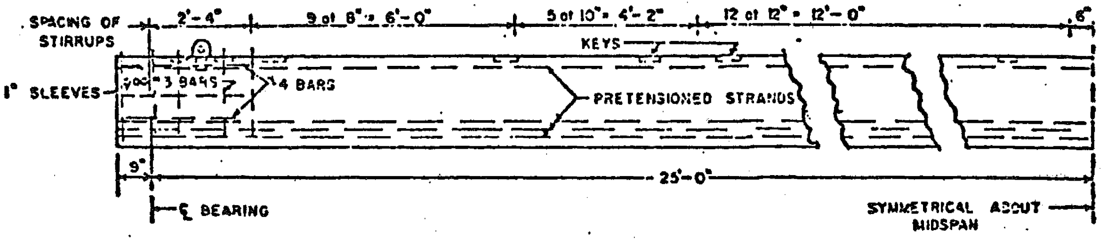

(B) BEAM REINFORCEMENT

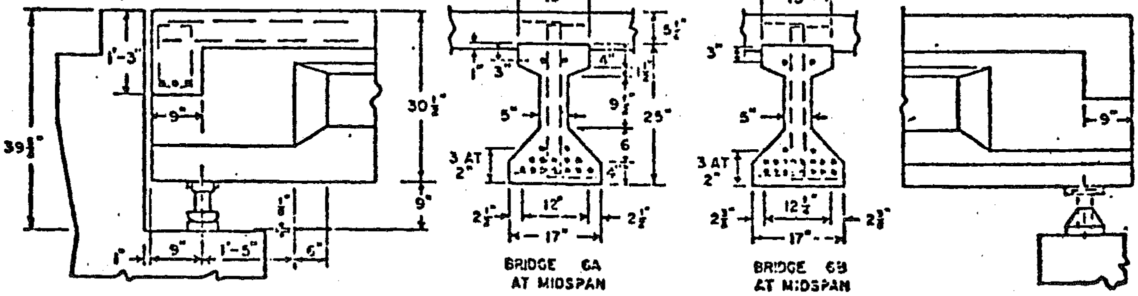

(C) BEAM DETAILS

Fig. 65 Parametric Study (Bridge 6A):
Dimensions (taken from Ref. 17)

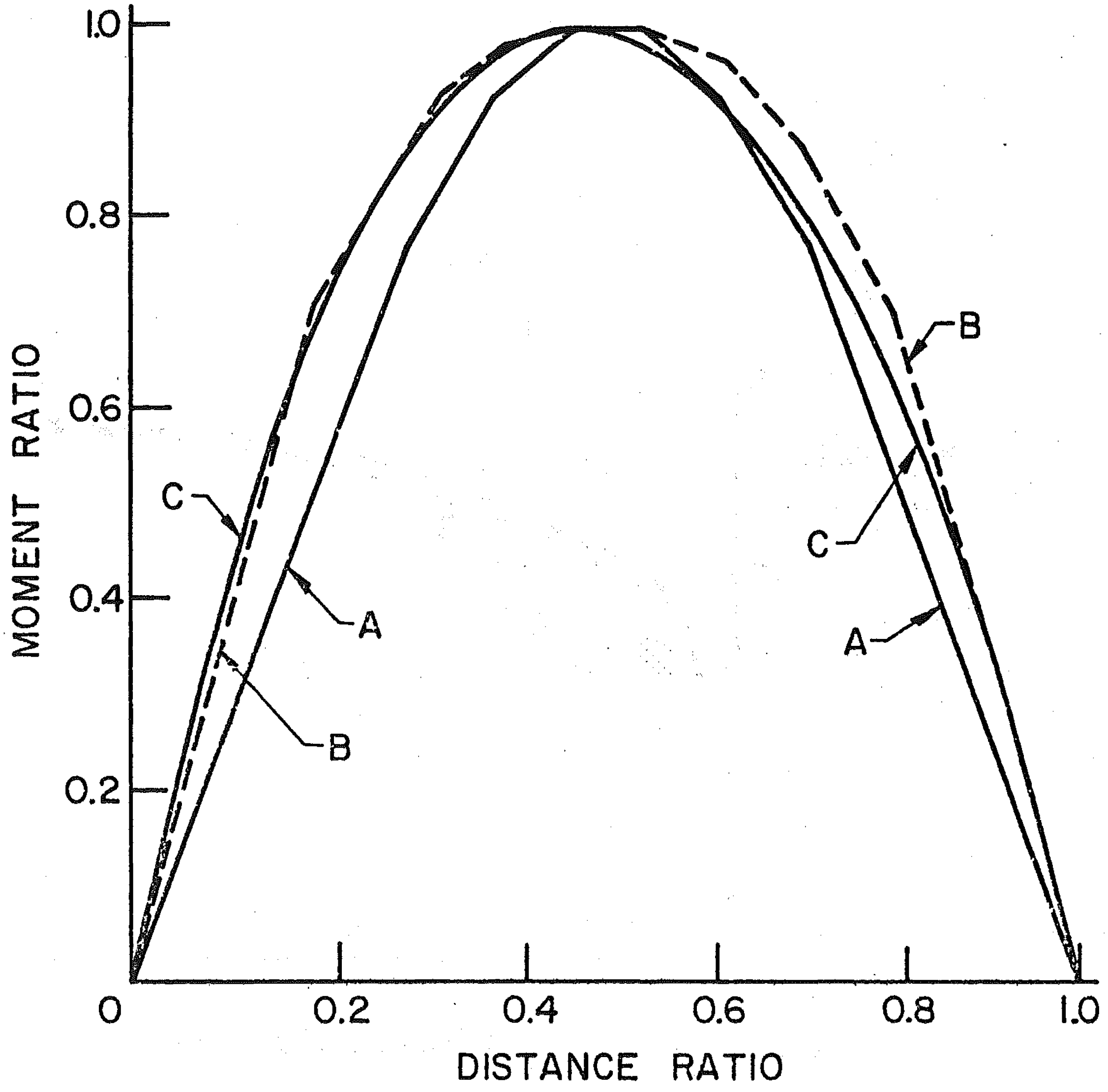

Fig. 66 Moment Ratio Versus Distance Ratio

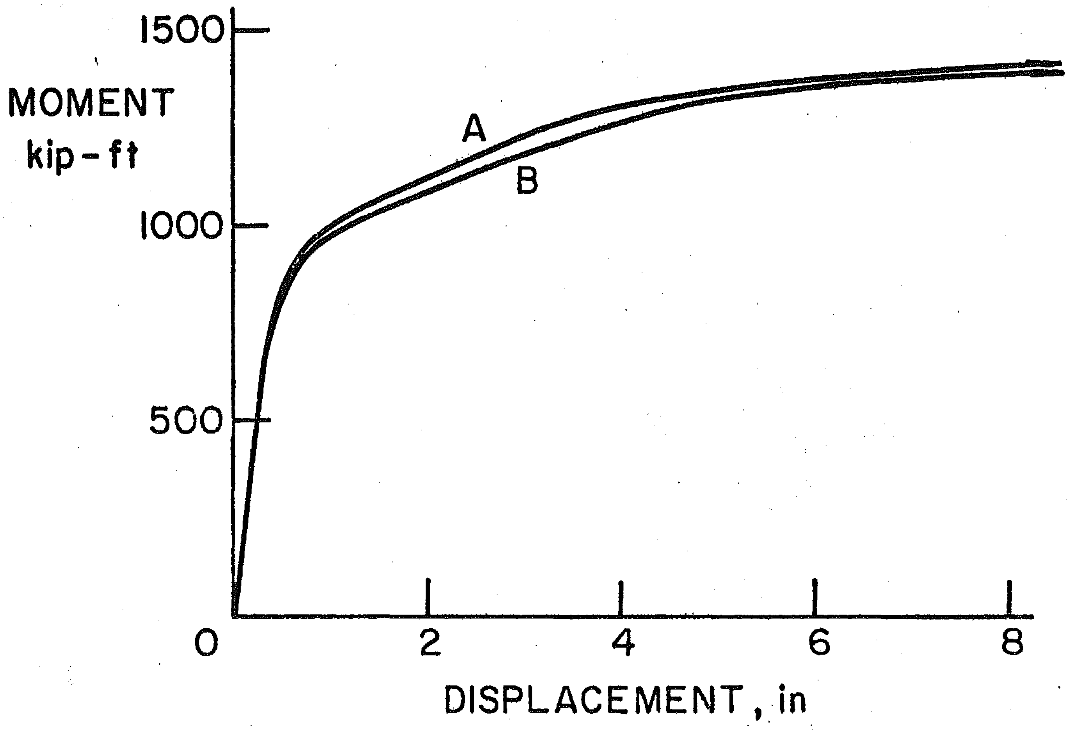

Fig. 67 Midspan Moment Versus Midspan Displacement

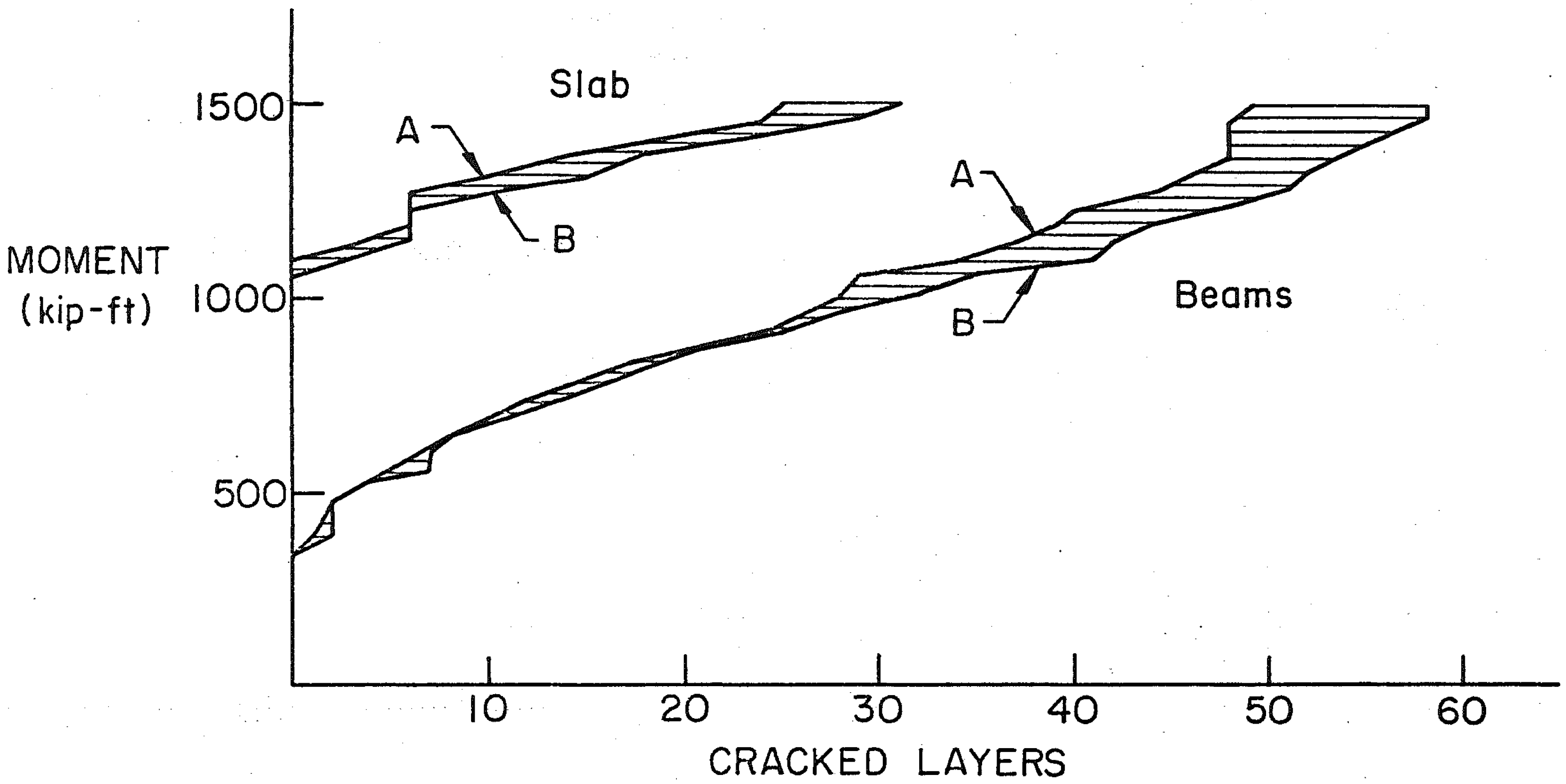

Fig. 68 Midspan Moment Versus Number of Cracked Layers in a Symmetric Quarter of the Superstructure

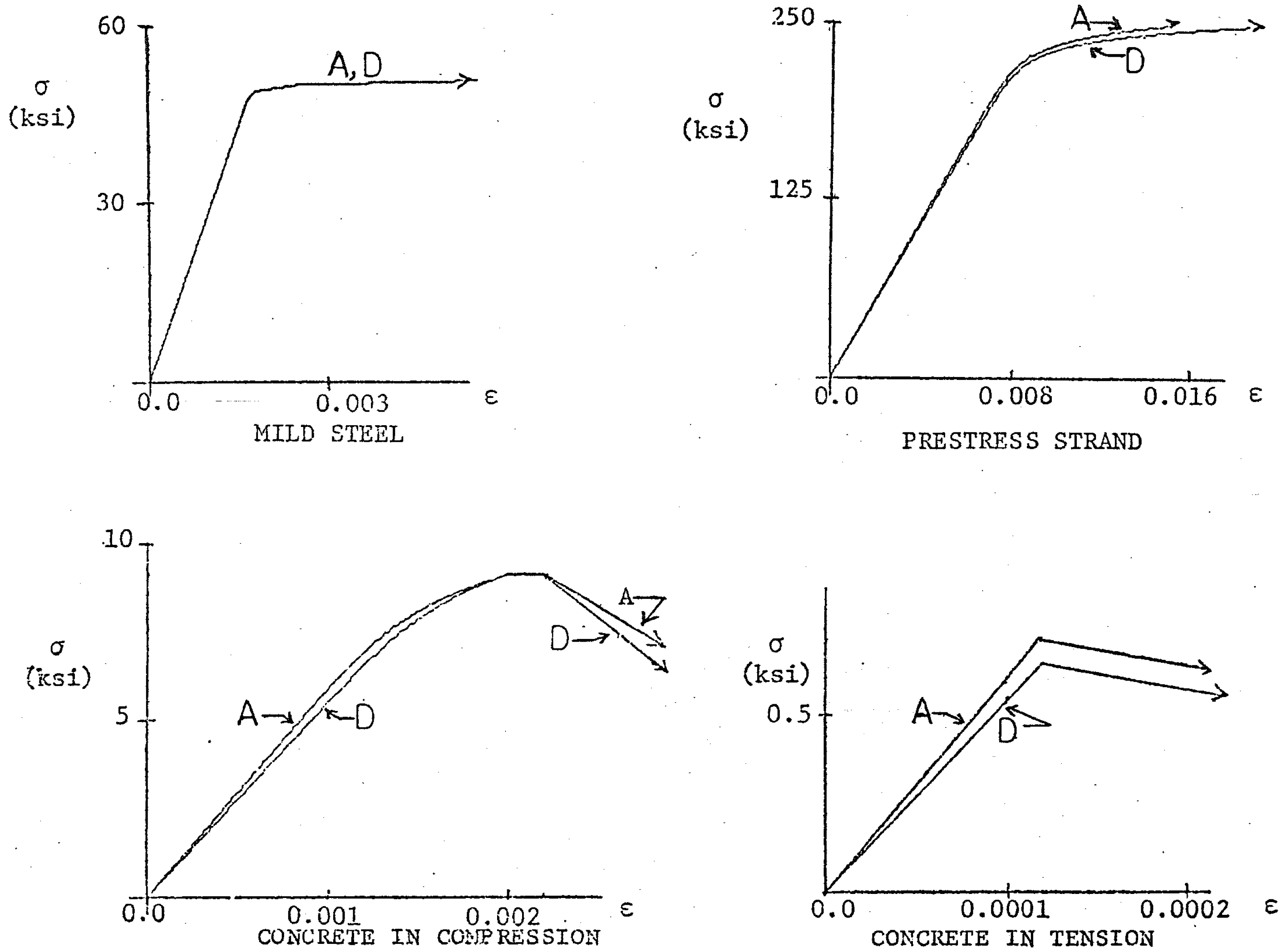

Fig. 69 Actual (A) and Default (D) Material Properties

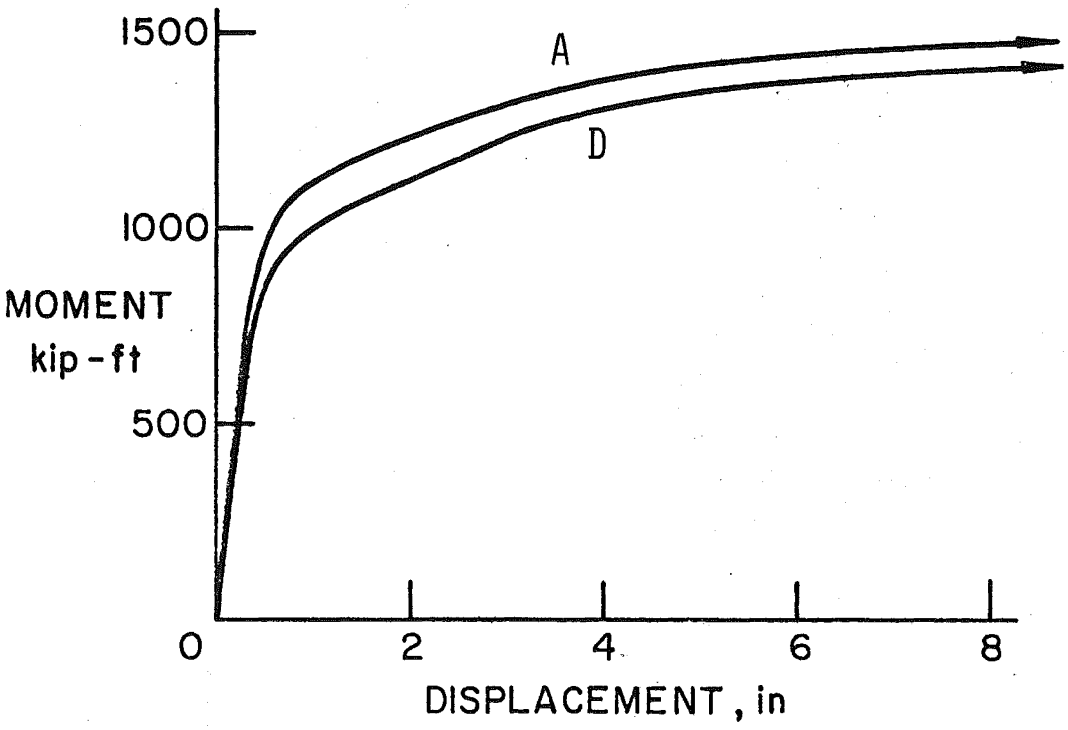

Fig. 70 Midspan Moment Versus Midspan Displacement

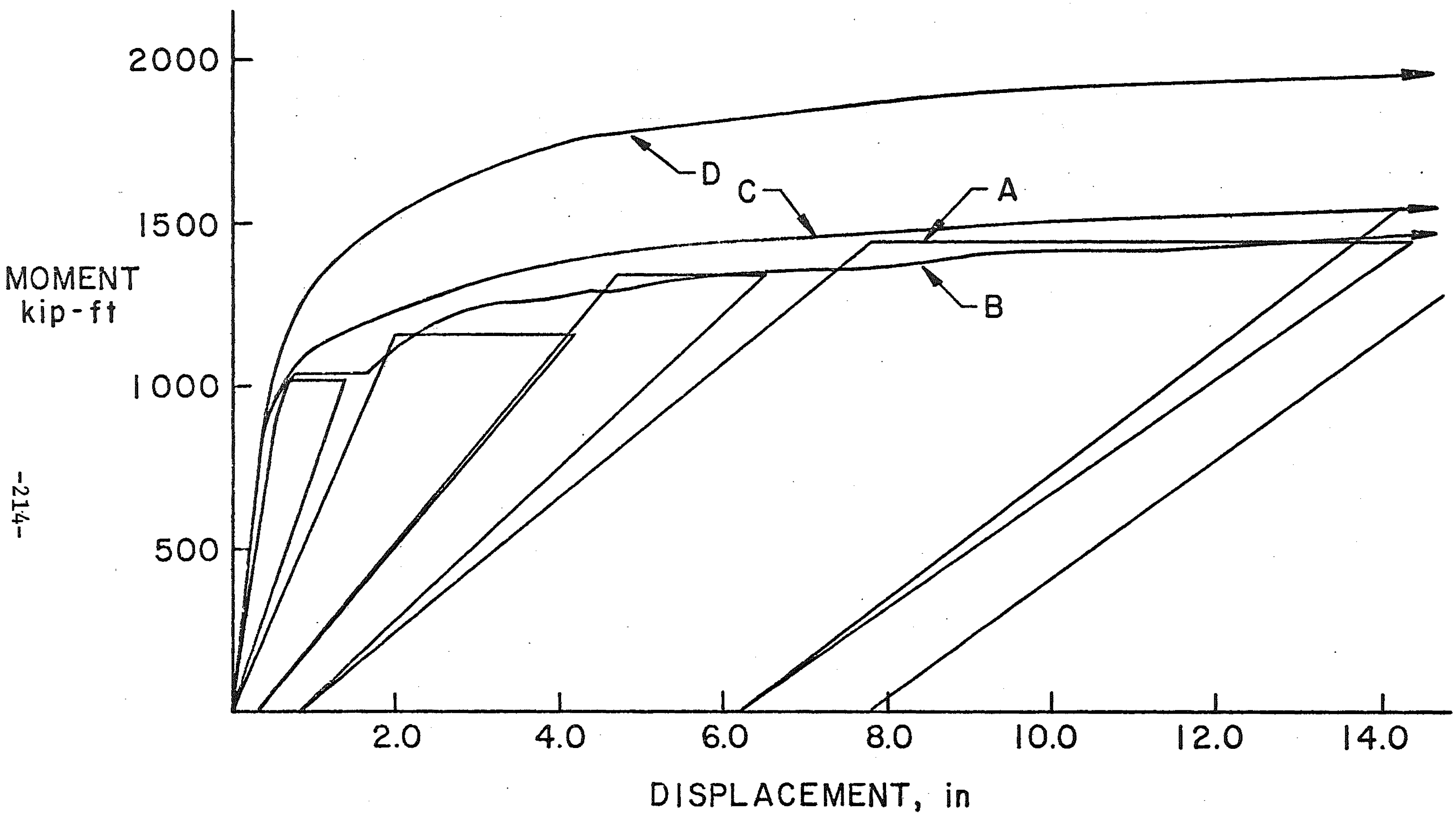

Fig. 71 Midspan Moment Versus Midspan Displacement

8. REFERENCES

1. Adini, A. and Clough, R.W.
ANALYSIS OF PLATE BENDING BY THE FINITED ELEMENT METHOD, Report submitted to the National Science Foundation, Grant G7337, University of California, Berkeley, California, 1960.

2. Argyris, J.H.
CONTINUA AND DISCONTINUA, Matrix methods in Structural Mechanics, Proceedings of the Conference held at Wright-Patterson Air Force Base, J.S. Przemieniecki, et al, editors, October, 1965.

3. Armen, H., Pifko, A. and Levine, H.S.
FINITE ELEMENT ANALYSIS OF STRUCTURES IN THE PLASTIC RANGE, NASA Contractor Report NASA CR-1649, National Aeronautics and Space Administration, Washington, D.C., 1971.

4. Barnard, P.R.
RESEARCHES INTO THE COMPLETE STRESS-STRAIN CURVE FOR CONCRETE, Magazine of Concrete Research, Vol. 16,No. 49, December 1964.

5. Bell, J.C. and Elms, D.G.
NON-LINEAR ANALYSIS OF REINFORCED CONCRETE SLABS, Magazine of Concrete Research, Vol. 24, No. 79, June 1972.

6. Bhaumik, A.K. and Hanley, J.T.
ELASTO-PLASTIC PLATE ANALYSIS BY FINITE DIFFERENCES, Journal of the Structural Division, ASCE, Vol. 93, ST5, October 1967.

7. Burdette, E.G. and Goodpasture, D.W.
FINAL REPORT ON FULL SCALE BRIDGE TESTING -AN EVALUATION OF BRIDGE DESIGN CRITERIA, University of Tennessee, 1971.

8. Cardenas, A. and Sozen, M.A.
STRENTH AND BEHAVIOR OF ISOTROPICALLY AND NONISOTROPICALLY REINFORCED CONCRETE SLABS SUBJECTED TO COMBINATION OF FLEXURAL AND TORSIONAL MOMENTS, Civil Engineering Studies, Structural Research Series No. 336, University of Illinois, Urbana, Illinois, 1968.

9. Clough, R.W.
THE FINITE ELEMENT METHOD IN STRUCTURAL MECHANICS, Chapter 7, of Stress Analysis, edited by O.C. Zienkiewicz and G.S. Hollister, John Wiley and Sons, New York, New York, 1965

10. Clough, R.W. and Tocher, J.L.
FINITE ELEMENT STIFFNESS MATRICES FOR ANALYSIS OF PLATE BENDING, Proceedings of the Conference on Matrix Methods in Structural Mechanics, Wright-Patterson Air Force Base, Ohio, 1965.

11. Dawe, D.J.
PARALLELOGRAMMIC ELEMENTS IN THE SOLUTION OF RHOMBIC CANTILEVER PLATE PROBLEMS, Journal of Strain Analysis, Vol. 1, No. 3, 1966.

12. Doyle, S.K. and Burdette, E.G.
A COMPARISON OF MEASURED AND COMPUTED LOAD DEFLECTION RELATIONSHIPS FOR FOUR HIGHWAY BRIDGES, The University of Tennessee, March 1972.

13. Evans, R.H. and Marathe, M.S.
MICROCRACKING AND STRESS STRAIN CURVES FOR CONCRETE IN TENSION, Materiaux et Constructions, Vol. 1, January-February 1968.

14. Franklin, H.A.
NONLINEAR ANALYSIS OF REINFORCED CONCRETE FRAMES AND PANELS, SESM 70-5, College of Engineering, University of California, Berkeley, March 1970.

15. Hand, F.R., Pecknold, D.A. and Schnobrich, W.C.
A LAYERED FINITE ELEMENT NONLINEAR ANALYSIS OF REINFORCED CONCRETE PLATES AND SHELLS, Civil Engineering Studies, Structural Research Series No. 389, University of Illinois, Urbana, Illinois, August 1972.

16. Hand, F.R., Pechnold, D.A. and Schnobrich, W.C.
NONLINEAR LAYERED ANALYSIS OF RC PLATES AND SHELLS, Journal of the Structural Division, ASCE, Vol. 99, No. ST7, July, 1973.

17. Highway Research Board
THE AASHO ROAD TEST, Report 2, MATERIALS AND CONSTRUCTION, Special Report 61B, 1962.

18. Highway Research Board
THE AASHO ROAD TEST, Report 4, BRIDGE RESEARCH, Special Report 61D, 1962.

19. Hsu, T.T.C., Slate, F.O., Sturman, G.M. and Winter, G.
MICROCRACKING OF PLAIN CONCRETE AND THE SHAPE OF THE STRESS-STRAIN CURVE, Journal of the American Concrete Institute, Vol., 60, No. 2, February 1963.

20. Hughes, B.P. and Chapman, G.P.
THE COMPLETE STRESS-STRAIN CURVE FOR CONCRETE IN DIRECT TENSION, BULLETIN RILEM, No. 30, March 1966.

21. Jensen, V.P.
THE PLASTICITY RATIO OF CONCRETE AND ITS EFFECTS ON THE ULTIMATE STRENGTH OF BEAMS, Journal of the American Concrete Institute, Vol. 14, No. 6, June 1943.

22. Jofreit, J.C. and McNeice, G.M.
FINITE ELEMENT ANALYSIS OF REINFORCED CONCRETE SLABS, Journal of the Structural Division, ASCE, Vol. 97, No. ST3, March 1971.

23. Kostem, C.N.
SHEAR PUNCHING OF BRIDGE DECKS, Fritz Engineering Laboratory Report No. 378B.4, Lehigh University, Bethlehem, Pennsylvania, July 1975.

24. Kostem, C.N.
THE OVERLOADING BEHAVIOR OF BEAM-SLAB TYPE HIGHWAY BRIDGES, Proposal for Initiation of Research Project Submitted to the Pennsylvania Department of Transportation, Lehigh University, Bethlehem, Pennsylvania, September, 1971

25. Kostem, C.N.
ANALYTICAL MODELING OF BEAM-SLAB BRIDGES, Proceedings of the IASS International Symposium on Folded Plates and Spatial Panel Structures, Udine, Italy, 1974.

26. Kulicki, J.M. and Kostem, C.N.
TORSIONAL CONSIDERATIONS IN NONLINEAR BEAM-SLAB BRIDGE SUPERSTRUCTURES, IASS Symposium on Folded Plates and Spatial Panel Structures, Udine, Italy, September 1974.

27. Kulicki, J.M. and Kostem, C.N.
THE INELASTIC ANALYSIS OF REINFORCED AND PRESTRESSED CONCRETE BEAMS, Fritz Engineering Laboratory Report No.378B.1, Lehigh University, Bethlehem, Pennsylvania, November 1972.

28. Kulicki, J.M. and Kostem, C.N.
USER'S MANUAL FOR PROGRAM BEAM, Fritz Engineering Laboratory Report No. 378B.2, Lehigh University, Bethlehem, Pennsylvania, February 1973.

29. Kulicki, J.M. and Kostem, C.N.
THE EFFECT OF DISCRETIZATION ON THE INELASTIC ANALYSIS OF PRESTRESSED CONCRETE BEAMS, Proceedings of the International Symposium on Discrete Methods in Engineering, Milan, Etas Libri, Italy, 1974.

30. Kulicki, J.M. and Kostem, C.N.
FURTHER STUDIES ON THE NONLINEAR FINITE ELEMENT ANALYSIS OF BEAMS, Fritz Engineering Laboratory Report No. 378A.5, Lehigh University, April 1973.

31. Kulicki, J.M. and Kostem, C.N.
NONLINEAR ANALYSIS OF CONCRETE FLEXURAL MEMBERS, Proceedings of the International Conference on Planning and Design of Tall Buildings, Vol. DS, Bethlehem, Pennsylvania, April 1973.

32. Kulicki, J.M. and Kostem, C.N.
THE INELASTIC ANALYSIS OF PRESTRESSED AND REINFORCED CONCRETE BRIDGE BEAMS BY THE FINITE ELEMENT METHOD, Fritz Engineering Laboratory Report No. 378A.6, Lehigh University, Bethlehem, Pennsylvania, September 1973.

33. Kupfer, H., Hilsdorf, H.K. and Rusch, H.
BEHAVIOR OF CONCRETE UNDER BIAXIAL STRESSES, Journal of the American Concrete Institute, Vol. 66, No. 8, August 1969.

34. Lamb, R.S. and Davis, G.
DISCUSSION OF NONLINEAR STRESS ANALYSIS OF REINFORCED CONCRETE, by Valliappan, S. and Doolan, T.F., (Proceedings Paper 8845), Journal of the Structural Division, ASCE, Vol. 99, No. ST3, March 1973.

35. Lin, C.S.
NONLINEAR ANALYSIS OF REINFORCED CONCRETE SLABS AND SHELLS, Ph.D. Dissertation, University of California, Berkeley, California, September 1972.

36. Liu, T.C.
STRESS-STRAIN RESPONSE AND FRACTURE OF CONCRETE IN BIAXIAL COMPRESSION, PH.D. Dissertation, Structural Engineering Department, Cornell University, Ithaca, New York, 1971.

37. Liu, T.C., Nilson, A.H. and Slate, F.O.
BIAXIAL STRESS-STRAIN RELATIONS FOR CONCRETE, Journal of the Structural Division, ASCE, Vol. 98, No. ST5, May 1972.

38. Lopez, L.A. and Ang, A.H.S.
FLEXURAL ANALYSIS OF ELASTIC-PLASTIC RECTANGULAR PLATES, Civil Engineering Studies, Structural Research Series No. 305, University of Illinois, Urbana, Illinois, May 1966.

39. Morley, C.T.
EXPERIMENTS ON THE DISTORTION OF STEEL BARS ACROSS CRACKS IN REINFORCED CONCRETE SLABS, Magazine of Concrete Research, Vol. 18, No. 54, March 1966.

40. Nelissen, L.J.M.
BIAXIAL TESTING OF NORMAL CONCRETE, HERON, Vol. 18, No.1 1972, Stevin-Laboratory of the Department of Civil Engineering of the Technological University and Institute TNO for Building Materials and Building Structures, Delft, The Netherlands.

41. Neville, A.M.
HARDENED CONCRETE: PHYSICAL AND MECHANICAL ASPECTS, American Concrete Institue Monograph No. 6, 1971.

42. Ngo, D. and Scordelis, A.C.
FINITE ELEMENT ANALYSIS OF REINFORCED CONCRETE BEAMS, Journal of the American Concrete Institue, Proceedings, Vol. 64, No. 3, March 1967.

43. Peterson, W.S., Kostem, C.N. and Kulicki, J.M.
THE INELASTIC ANALYSIS OF REINFORCED CONCRETE SLABS, Fritz Laboratory report No. 378B.3, Lehigh University, May, 1974.

44. Peterson, W.S., Kostem, C.N. and Kulicki, J.M.
DISCUSSION OF "FULL RANGE ANALYSIS OF ECCENTRICALLY STIFFENED PLATES", by A.W. Wegmuller, ASCE, Vol. 100, ST9, September 1974.

45. Peterson, W.S. and Kostem, C.N.
THE INELASTIC ANALYSIS OF BEAM-SLAB HIGHWAY BRIDGE SUPERSTRUCTURES, Fritz Laboratory Report No. 378B.5, Lehigh University, Bethlehem, Pennsylvania, March 1975.

46. Peterson, W.S. and Kostem, C.N.
USER'S MANUAL FOR PROGRAM BOVA, Fritz Engineering Laboratory Report No. 378B.6A, Lehigh University, Bethlehem, Pennsylvania, March 1975.

47. Peterson, W.S. and Kostem, C.N.
LISTING OF PROGRAM BOVA, Fritz Engineering Laboratory Report No. 378.6B, April 1975.

48. Peterson, W.S. and Kostem, C.N.
USERS MANUAL FOR PROGRAM MENVLP, Fritz Laboratory Report No. 400.17, Lehigh University, Bethlehem, Pennsylvania, April 1975.

49. Ramberg, W. and Osgood, W.R.
DESCRIPTION OF STRESS-STRAIN CURVES BY THREE PARAMETERS, NACA, TN 902, July 1943.

50. Saenz, L.P.
Discussions of EQUATIONS FOR THE STRESS-STRAIN CURVE OF CONCRETE, by P. Desayi and S. Krishnan, Journal of the American Concrete Institute, Vol. 61, No.9 September 1964.

51. Schnobrich, W.C., Salem, M.H., Pecknold, D.A. and Mohroz, B.
DISCUSSION OF NONLINEAR STRESS ANALYSIS OF REINFORCED CONCRETE by Valliapan, S. and Doolan, T.F. (Proceedings Paper 8845), Journal of the Structural Division, ASCE, Vol. 98, No ST10, October 1972.

52. Smith, G.M. and Young, L.E.
ULTIMATE FLEXURAL ANALYSIS BASED ON STRESS-STRAIN CURVES OF CYLINDERS, Journal of the American Concrete Institute, Vol. 53 No. 6, December 1956.

53. Taylor, R., Maher, D.R.H. and Hayes, B.
EFFECT OF THE ARRANGEMENT OF REINFORCEMENT ON THE BEHAVIOR OF REINFORCED CONCRETE SLABS, Magazine of Concrete Research, Vol. 19, No. 58, March 1967.

54. Thomas, F.G.
THE STRENGTH AND DEFORMATION OF SOME REINFORCED CONCRETE SLABS SUBJECTED TO CONCENTRATED LOADING, From Part VIII of Studies in Reinforced Concrete, Technical Papers, Building Research, Great Britain, 1939.

55. Tottenham, H. and Brebbia, C.
FINITE ELEMENT TECHNIQUES IN STRUCTURAL MECHANICS, Southampton University Press, Southampton, England, 1970.

56. Valliapan, S. and Doolan, T.F.
NONLINEAR STRESS ANALYSIS OF REINFORCED CONCRETE, Journal of the Structural Division, ASCE, ST4, April 1972.

57. Wegmuller, A.W. and Kostem, C.N.
ELASTIC-PLASTIC ANALYSIS OF PLATES, Proceedings of the IASS Symposium on Shell Structures and Climatic Influences, pp. 379-386, Calgary, Canada, July 1972.

58. Wegmuller, A.W. and Kostem, C.N.
FINITE ELEMENT ANALYSIS OF PLATES AND ECCENTRICALLY STIFFENED PLATES, Fritz Engineering Laboratory Report No. 378A.3, Lehigh University, Bethlehem, Pennsylvania, February 1973.

59. Wegmuller, A.W. and Kostem, C.N.
FINITE ELEMENT ANALYSIS OF ELASTIC-PLASTIC PLATES AND ECCENTRICALLY STIFFENED PLATES, Fritz Engineering Laboratory Report No. 378A.4, Lehigh University, Bethlehem, Pennsylvania, February 1973.

60. Wegmuller, A.W. and Kostem, C.N.
EFFECT OF IMPERFECTIONS ON THE STATIC RESPONSE OF BEAM-SLAB TYPE HIGHWAY BRIDGES, Proceedings of the Conference of Finite Element Method in Civil Engineering, McGill University-Engineering Institute of Canada, Montreal, Canada, 1972.

61. Whang, B.
ELASTO-PLASTIC ORTHOTROPIC PLATES AND SHELLS, Proceedings of the Symposium on Application of Finite Element Methods in Civil Engineering, Vanderbilt University, Nashville, Tennessee, November, 1969.

62. Winter, G., Urquhart, L.C., O'Rourke, C.E. and Nilson, A.H.
DESIGN OF CONCRETE STRUCTURES, McGraw Hill, New York, 1964.

63. Zellin, M.A., Kostem, C.N. and VanHorn, D.A.
STRUCTURAL BEHAVIOR OF BEAM-SLAB HIGHWAY BRIDGES, A SUMMARY OF COMPLETED RESEARCH AND BIBLIOGRAPHY, Fritz Engineering Laboratory Report No. 387.1, Lehigh University, Bethlehem, Pennsylvania, May 1973.

64. Zienkiewicz, O.C.
THE FINITE ELEMENT METHOD IN ENGINEERING SCIENCE, McGraw Hill, New York, New York, 1971.

65. American Concrete Institute
BUILDING CODE REQUIREMENTS FOR REINFORCED CONCRETE (ACI 318-63) Detroit, Michigan, 1963.

66. Unpublished Student Report, CE 157, Lehigh University, Group "O", 1970.

67. Peterson, W. S.
THE INELASTIC ANALYSIS OF REINFORCED AND PRESTRESSED CONCRETE BEAM-SLAB HIGHWAY BRIDGE SUPERSTRUCTURES, Ph.D. Dissertation, Civil Engineering Department, Lehigh University, Bethlehem, Pennsylvania, 1975.

9. NOMENCLATURE

Notes: Subscripts u and ϕ refer to in-plane and bending, respectively.

Subscripts uu, uϕ, and $\phi\phi$ refer to in-plane, coupling, and bending, respectively.

Primes, ', refer to quantities expressed in the skew coordinate system.

Bars, $-$, refer to the non-dimensionalized coordinate system.

Scalars

A,B,C,D = Curve parameters

A_i = Layer area

AREA = In-plane area of an element

A_s = Reinforcing bar area for the slab

(a,b) = Slab element half lengths

b_s = Reinforcing bar spacing for the slab

$D_{11}, D_{12}, D_{13}, D_{22}, D_{23}, D_{33}$ = Components of the rigidity matrices where subscripts uu refers to in-plane, uϕ refers to coupling, and $\phi\phi$ refers to bending

E_c = Initial tangent modulus in uniaxial loading for concrete

Ed_c = Downward slope of the concrete stress-strain curve for compression

Ed_t = Downward slope of the concrete stress-strain curve for tension

E_i = Initial modulus of elasticity for the Ramberg-Osgood stress-strain relation

E_p = Tangent modulus at the peak stresss

E_s = Initial modulus of elasticity for steel

E_{1b}, E_{2b} = Tangent moduli for the two principal stress directions

E'_{1b}, E'_{2b} = Tangent moduli for the principal stress directions employed in formulating $[\bar{D}]$

F_i = Term of the assembled force vector

F_i^e = Term of the element force vector

f'_c = Representative uniaxial compressive cylinder strength for concrete

f'_c-4" = 4" x 4" x 4" cube strength

f_t = Direct tensile strength for concrete

f_y = Yield strength for steel

I,K = Nodal points for the beam element

I,J,K,L = Nodal points for the slab element

I_i = Moment of inertia for layer i about its centroid

K_{ij} = Term of the assembled stiffness matrix

k_{ij}^e = Term of the element stiffness matrix

$K_1, K_2, K_3, K_4, K_5, K_6$ = Component matrices of the stiffness matrix

L = Total number of layers

ℓ = Beam element length

m = A dimensionless constant used in the Ramberg-Osgood stress-strain relation

m_c = Ramberg-Osgood "m" parameter for concrete

m_s = Ramberg-Osgood "m" parameter for steel

n = A dimensionless constant used in the Ramberg-Osgood stress-strain relation

n_c = Ramberg-Osgood "n" parameter for concrete

n_s = Ramberg-Osgood "n" parameter for steel

Q = Distributed load

R = Maximum ratio of the concrete strength in biaxial compression to uniaxial compression

T_i = Beam layer (i) width in the y-direction

T_s = Equivalent thickness of a reinforcing bar layer for the slab

$U(x,y), U'$ = In-plane displacement polynomial in the x-direction for the slab

$U(x)$ = In-plane displacement polynomial in the x-direction for the beam

U_z = In-plane displacement in the x-direction at depth z

$V(x,y), V'$ = In-plane displacement polynomial in the y-direction for the slab

V_z = In-plane displacement in the y-direction at depth z

v, v' = Volume of the element

$W(x,y), W'$ = Vertical displacement polynomial for the slab

$W(x)$ = Vertical displacement polynomial for the beam

(x,y) = Local Cartesian coordinates

(x',y') = Skew coordinates

$(\bar{x},\bar{y})$ = Non-dimensionalized coordinates

(x_n,y_n), $(\bar{x}_n,\bar{y}_n)$ = Nodal point coordinates for a slab element

z = Vertical distance from the reference plane

Z_i, Z_{i+1} = Layer boundaries for layer i measured from the reference plane in the vertical direction

$\bar{Z}_i$ = Centroid location of layer i measured from the reference plane in the vertical direction

α = The stress ratio

α_1 = The stress ratio for principal direction 1, σ_2/σ_1

α_2 = The stress ratio for principal direction 2, σ_1/σ_2

α_j = Stress ratio at point j, σ_{2j}/σ_{1j}

β = Skew angle

δ_j = Term of the nodal point displacement vector for the structure

$(\gamma_{xy})_z$ = Shear strain at depth z

$\dot{\gamma}$ = Shear strain increment

ε = A strain in the principal stress direction

ε_c = Peak strain for uniaxial compression of concrete

ε_p = The concrete strain at the peak stress

$\varepsilon_{p1}, \varepsilon_{p2}$ = Concrete strains at the peak stress for the two principal stress directions

ε_t = Peak strain for uniaxial tension of concrete

$\dot{\varepsilon}_x, \dot{\varepsilon}_y, \dot{\gamma}_{xy}$ = Normal and shear strain increments in the x-y coordinate system

$\varepsilon_1, \varepsilon_2$ = Strains in the principal stress directions

$\bar{\varepsilon}$ = Strain at peak stress for the beam concrete

$\bar{\varepsilon}_m$ = Strain at which the downward portion of the stress-strain curve begins for the beam concrete

θ = Angle which defines the principal stress directions

θ_x = Reinforcing bar angle measured from the x-axis

$\theta_x(x,y), \theta'_x$ = Rotations about the x and x' axes for the slab

$\theta_y(x,y), \theta'_y$ = Rotations about the y and y' axes for the slab

$\theta_y(x)$ = Rotation about the y axis for the beam

ν = Poisson's ratio

ν_1, ν_2 = Poisson's ratios in the principal stress directions

σ = A principal stress

$\sigma_{ct}, \varepsilon_{ct}$ = A peak stress-strain value defining point G' on the peak strain envelope

σ_{ij} = Principal stress in direction i at point j on the peak stress envelope

σ_p = The peak stress in a principal direction

σ_{p1}, σ_{p2} = The peak stress for the two principal directions

σ_s = Secant yield strength used in the Ramberg-Osgood stress-strain relation

$\dot{\sigma}_x, \dot{\sigma}_y, \dot{\tau}_{xy}$ = Normal and shear stress increments in the x-y coordinate systems

$\sigma_x, \sigma_y, \tau_{xy}$ = Normal and shear stresses in the x-y coordinate system

σ_0 = Uniaxial compressive strength for concrete

σ_1, σ_2 = Stresses in the principal directions

σ_ν = Peak compressive stress at an $\alpha = 1/\nu$ as obtained from the peak stress envelope

$\dot{\tau}$ = Shear stress increment

Matrices

$\{A\}$ = Constant coefficients for the vertical displacement polynomial

$\{B\}$ = Constant coefficients for the in-plane displacement polynomial

$[B],[B_u],[B_\phi]$ = A connection matrix relating strains within an element to the nodal point displacements of an element

$[C],[C_u],[C_\phi]$ = Matrix relating nodal displacements of the element to the $\{\alpha\}$ constant coefficients

$[D]$ = Elasticity matrix based on the current state of stress which relates the stress increment to the strain increment in the x-y coordinate system

$[D_i]$ = Elasticity matrix for layer i

$[D_{uu}]$ = In-plane rigidity

$[D_{u\phi}]$ = Coupling rigidity

$[D_{\phi\phi}]$ = Bending rigidity

$[\bar{D}]$ = Elasticity matrix in the principal stress space

$\{F\},\{F_u\},\{F_\phi\},\{F'\}$ = Forces applied to the structure at the nodes

$\{\dot{F}\}$ = Force increment applied at the nodes of the structure

$\{F^e\},\{F^e_u\},\{F^e_\phi\}$ = Nodal forces applied to the element

$\{F_c^e\}, \{F_{uc}^e\}, \{F_{\phi c}^e\}$ = Fictitious forces for an element

$[K]$ = The assembled stiffness matrix

$[k^e]$ = Element stiffness matrix

$[k_{uu}^e]$ = In-plane stiffness matrix for an element

$[k_{u\phi}^e]$ = Coupling stiffness matrix for an element

$[k_{\phi\phi}^e]$ = Bending stiffness matrix for an element

$[k_s^e]$ = Element stiffness matrix in the skew coordinate system

$[P(x,y)], [P_u(x,y)], [P_\phi(x,y)]$ = Polynomial functions used to describe the displacement field

$[Q], [Q_u], [Q_\phi]$ = A connection matrix relating strains within an element to the constant coefficients of the displacement field

$[R]$ = Diagonal matrix used in non-dimensionalizing the formulation

$[S]$ = A coordinate transformation for the curvatures

$[t]$ = A coordinate transformation for the displacement field

$[T]$ = Used to transform the elasticity relation from the principal to the x-y coordinate system

$[T\delta]$ = Displacement transformation

$[TF]$ = Force transformation

$[T\varepsilon]$ = Strain transformation

$[T\sigma]$ = Stress transformation

$\{\alpha\}$ = Constant coefficients of the polynomial functions

$\{\dot{\varepsilon}\}$ = The strain increment

$[\Gamma],[\Gamma_u],[\Gamma_\phi]$ = Differential operators used to obtain the strain or curvature fields from the displacement field

$[\bar{\Gamma}_\phi(x,y)]$ = Operators used to obtain the polynomial functions of the displacement field from the vertical displacement function

$[\Delta(x,y)],[\Delta_u(x,y)],[\Delta_\phi(x,y)]$ = General displacement field for coordinate position (x,y)

$\{\delta\},\{\delta'\},\{\delta_u\},\{\delta_\phi\}$ = Node point displacements of the structure

$\{\dot{\delta}\}$ = Displacement increment of the nodal points

$\{\delta^e\},\{\delta^e_u\},\{\delta^e_\phi\}$ = Nodal displacements of the element

$\{\varepsilon\},\{\varepsilon'\}$ = Strain field

$\{\varepsilon\}_z$ = Strain field at depth z

$(\varepsilon_x)_z,(\varepsilon_y)_z,(\gamma_{xy})_z$ = Normal and shear strains at depth z

$\{\varepsilon\}_{\bar{z}_i}$ = Integrated average strain for layer i

$\{\sigma\},\{\sigma'\}$ = Stress field

$\{\dot{\sigma}\}$ = The stress increment

$\{\bar{\sigma}_i\}$ = Integrated average stress for layer i

$\{\dot{\sigma}_r\},\{\dot{\sigma}'_r\}$ = Increment of stress to be redistributed

10. APPENDICES

APPENDIX A

SLAB ELEMENT STIFFNESS FORMULATION

A.1 Introduction

This appendix is a supplement to Sections 3.4 and 3.8. The previous development of stiffness matrices will be expanded upon so that explicit evaluation can be performed. The resulting matrices will be presented as an aid to those who may carry the work further. It will be assumed that the reader has read Chapter 3 in detail.

A.2 Displacement Functions

The displacement functions chosen in this analysis were presented in Eq. 3.11 and Eq. 3.12. Substitution of these equations into Eq. 3.13 yields:

$$[P_u(x,y)] = \begin{bmatrix} 1 & x & y & xy & 0 & 0 & 0 & 0 \\ 0 & 0 & 0 & 0 & 1 & x & y & xy \end{bmatrix} \tag{A.1}$$

$$[P_\phi(x,y)] = \begin{bmatrix} 1 & x & y & x^2 & xy & y^2 & x^3 & x^2y & xy^2 & y^3 & x^3y & xy^3 \\ 0 & 0 & 1 & 0 & x & 2y & 0 & x^2 & 2xy & 3y^2 & x^3 & 3xy^2 \\ 0 & -1 & 0 & -2x & -y & 0 & -3x^2 & -2xy & -y^2 & 0 & -3x^2y & -y \end{bmatrix} \tag{A.2}$$

The W(x,y) displacement function will be non-dimensionalized to facilitate the inversion of the $[C_\phi]$ matrix introduced in Eq. 3.21b and shown inverted in Eq. 3.22a. This is carried out by substituting the non-dimensionalized coordinates $(\bar{x},\bar{y})$ into $W(x,y)$ defined in Eq. 3.11. Thus

$$W(\bar{x},\bar{y}) = [1 \quad \bar{x} \quad \bar{y} \quad \bar{x}^2 \quad \overline{xy} \quad \bar{y}^2 \quad \bar{x}^3 \quad \bar{x}^2\bar{y} \quad \overline{xy}^2 \quad \bar{y}^3 \quad \bar{x}^3\bar{y} \quad \overline{xy}^3] \tag{A.3}$$

$$W(x,y) = [W(\bar{x},\bar{y})] \cdot [R] \cdot \{A\} \tag{A.4}$$

where: $x = a\bar{x}$

$y = b\bar{y}$

[R] is a 12 x 12 diagonal matrix (i.e. all off diagonal elements are zero) where the diagonal terms consist of the following values: 1, a, b, a^2, ab, b^2, a^3, a^2b, ab^2, b^3, a^3b, and ab^3. The quantities a and b are element half lengths in the x-direction and the y-direction, respectively, and are shown in Fig. 14. The three bending displacements are given by Eq. 3.10. The derivatives in Eq. 3.10 may now be obtained for example:

$$\frac{\partial W}{\partial y} = \frac{\partial W(x,y)}{\partial y} = \frac{\partial W(x,y)}{\partial \bar{y}} \frac{\partial \bar{y}}{\partial y} = \frac{\partial}{\partial \bar{y}} [W(\bar{x},\bar{y})] \frac{\partial \bar{y}}{\partial y} [R] \{A\} \tag{A.5}$$

Using Eq. 3.14, it is possible to write

$$\Delta_\phi(x,y) = [\bar{\Gamma}_\phi(x,y)] \; [W(x,y)] \; \{A\} = [P_\phi(x,y)] \; \{A\} \tag{A.6a}$$

$[\bar{\Gamma}_\phi(x,y)]$ is a matrix containing the differential operators indicated in Eq. 3.13. Substitution of Eq. A.4 yields

$$\Delta_\phi(x,y) = [\bar{\Gamma}_\phi(x,y)] \; [W(\bar{x},\bar{y})] \; [R] \; \{A\} \tag{A.6b}$$

Employing the chain rule of differentiation as indicated in Eq. A.5 results in

$$\Delta_\phi(x,y) = [t]\,[\bar{\Gamma}_\phi(\bar{x},\bar{y})]\,[W(\bar{x},\bar{y})]\,[R]\,\{A\} = [t]\,[P_\phi(\bar{x},\bar{y})]\,[R]\,\{A\} \quad (A.7)$$

where:

$$[t] = \begin{bmatrix} 1 & 0 & 0 \\ 0 & \partial\bar{y}/\partial y & 0 \\ 0 & 0 & \partial\bar{x}/\partial x \end{bmatrix} = \begin{bmatrix} 1 & 0 & 0 \\ 0 & 1/b & 0 \\ 0 & 0 & 1/a \end{bmatrix}$$

The $[C_u]$ and $[C_\phi]$ matrices can now be obtained by substituting the nodal point coordinates (x_n,y_n) into Eq. A.1 for $[C_u]$ and $(\bar{x}_n,\bar{y}_n)$ into Eq. A.7 for $[C_\phi]$. (x_n,y_n) consists of the set of I, J, K, and L nodal point coordinates (-a,b), (-a,-b), (a,b), (a,-b). $(\bar{x}_n,\bar{y}_n)$ consists of the set of non-dimensionalized nodal point coordinates (-1,1), (-1,-1), (1,1), and (1,-1). The resulting $[C_\phi]$ and $[C_u]$ matrices are given as:

$$[C_\phi] = \begin{bmatrix} 1 & -1 & 1 & 1 & -1 & 1 & -1 & 1 & -1 & 1 & -1 & -1 \\ 0 & 0 & 1 & 0 & -1 & 2 & 0 & 1 & -2 & 3 & -1 & -3 \\ 0 & -1 & 0 & 2 & -1 & 0 & -3 & 2 & -1 & 0 & -3 & -1 \\ 1 & -1 & -1 & 1 & 1 & 1 & -1 & -1 & -1 & -1 & 1 & 1 \\ 0 & 0 & 1 & 0 & -1 & -2 & 0 & 1 & 2 & 3 & -1 & -3 \\ 0 & -1 & 0 & 2 & 1 & 0 & -3 & -2 & -1 & 0 & 3 & 1 \\ 1 & 1 & 1 & 1 & 1 & 1 & 1 & 1 & 1 & 1 & 1 & 1 \\ 0 & 0 & 1 & 0 & 1 & 2 & 0 & 1 & 2 & 3 & 1 & 3 \\ 0 & -1 & 0 & -2 & -1 & 0 & -3 & -2 & -1 & 0 & -3 & -1 \\ 1 & 1 & -1 & 1 & -1 & 1 & 1 & -1 & 1 & -1 & -1 & -1 \\ 0 & 0 & 1 & 0 & 1 & -2 & 0 & 1 & -2 & 3 & 1 & 3 \\ 0 & -1 & 0 & -2 & 1 & 0 & -3 & 2 & -1 & 0 & 3 & 1 \end{bmatrix}$$

(A.8)

$$[C_u] = \begin{bmatrix} 1 & -a & b & -ab & 0 & 0 & 0 & 0 \\ 0 & 0 & 0 & 0 & 1 & -a & b & -ab \\ 1 & -a & -b & ab & 0 & 0 & 0 & 0 \\ 0 & 0 & 0 & 0 & 1 & -a & -b & ab \\ 1 & a & b & ab & 0 & 0 & 0 & 0 \\ 0 & 0 & 0 & 0 & 1 & a & b & ab \\ 1 & a & -b & -ab & 0 & 0 & 0 & 0 \\ 0 & 0 & 0 & 0 & 1 & a & -b & -ab \end{bmatrix} \qquad \text{(A.9)}$$

Thus the nodal point displacements are:

$$\{\delta_u^e\} = [\Delta_u(x_n, y_n)] = [C_u]\,\{B\} \qquad \text{(A.10)}$$

$$\{\delta_\phi^e\} = [\Delta_\phi(\bar{x}_n, \bar{y}_n)] = [T]\,[C_\phi]\,[R]\,\{A\} \qquad \text{(A.11)}$$

where

$$[T] = \begin{bmatrix} [t] & 0 & 0 & 0 \\ 0 & [t] & 0 & 0 \\ 0 & 0 & [t] & 0 \\ 0 & 0 & 0 & [t] \end{bmatrix} \qquad \text{(A.12)}$$

and [t] is defined in Eq. A.7.

A.3 Strains

Appropriate terms must be included in Eq. 3.18 to reflect the fact that the bending displacement function has been non-dimensionalized. Applying the chain rule results in

$$\begin{Bmatrix} \dfrac{-\partial^2 W}{\partial x^2} \\ \\ \dfrac{-\partial^2 W}{\partial y^2} \\ \\ \dfrac{-2\partial^2 W}{\partial x \partial y} \end{Bmatrix} = [S] \begin{Bmatrix} \dfrac{-\partial^2 W}{\partial \bar{x}^2} \\ \\ \dfrac{-\partial^2 W}{\partial \bar{y}^2} \\ \\ \dfrac{-2\partial^2 W}{\partial \bar{x} \partial \bar{y}} \end{Bmatrix} \tag{A.13}$$

where:

$$[S] = \begin{bmatrix} \dfrac{\partial \bar{x}}{\partial x} \dfrac{\partial \bar{x}}{\partial x} & 0 & 0 \\ 0 & \dfrac{\partial \bar{y}}{\partial y} \dfrac{\partial \bar{y}}{\partial y} & 0 \\ 0 & 0 & \dfrac{\partial \bar{x}}{\partial x} \dfrac{\partial \bar{y}}{\partial y} \end{bmatrix} \tag{A.14a}$$

or:

$$[S] = \begin{bmatrix} \dfrac{1}{a^2} & 0 & 0 \\ 0 & \dfrac{1}{b^2} & 0 \\ 0 & 0 & \dfrac{1}{ab} \end{bmatrix} \tag{A.14b}$$

Thus Eq. 3.18 is modified to reflect the non-dimensionalized coordinates in the following manner: Substitution of Eqs. 3.12, A.4, and A.13 into Eq. 3.18 leads to

$$\{\varepsilon_z\} = [Q_u]\,\{B\} + z\,[S]\,[Q_\phi]\,[R]\,\{A\} \tag{A.15}$$

in which:

$$[Q_u] = \begin{bmatrix} 0 & 1 & 0 & y & 0 & 0 & 0 & 0 \\ 0 & 0 & 0 & 0 & 0 & 0 & 1 & x \\ 0 & 0 & 1 & x & 0 & 1 & 0 & y \end{bmatrix} \tag{A.16}$$

$$[Q_\phi] = \begin{bmatrix} 0 & 0 & 0 & -2 & 0 & 0 & -6\bar{x} & -2\bar{y} & 0 & 0 & -6\overline{xy} & 0 \\ 0 & 0 & 0 & 0 & 0 & -2 & 0 & 0 & -2\bar{x} & -6\bar{y} & 0 & -6\overline{xy} \\ 0 & 0 & 0 & 0 & -2 & 0 & 0 & -4\bar{x} & -4\bar{y} & 0 & -6\bar{x}^2 & -6\bar{y}^2 \end{bmatrix} \tag{A.17}$$

The constants {A} and {B} can be found as indicated in Eqs. 3.22 if care is taken to include the new matrices which result from non-dimensionalizing the bending displacement function.

Thus

$$\{B\} = [C_u^{-1}]\ \{\delta_u^e\} \tag{A.18}$$

$$\{A\} = [R^{-1}]\ [C_\phi^{-1}]\ [T^{-1}]\ \{\delta_\phi^e\} \tag{A.19}$$

Inversion of $[C_u]$ and $[C_\phi]$ results in the following matrices.

$$[C_\phi]^{-1} = \frac{1}{8}\begin{bmatrix} 2 & -1 & -1 & 2 & 1 & -1 & 2 & -1 & 1 & 2 & 1 & 1 \\ -3 & 1 & 1 & -3 & -1 & 1 & 3 & -1 & 1 & 3 & 1 & 1 \\ 3 & -1 & -1 & -3 & -1 & 1 & 3 & -1 & 1 & -3 & -1 & -1 \\ 0 & 0 & 1 & 0 & 0 & 1 & 0 & 0 & -1 & 0 & 0 & -1 \\ -4 & 1 & 1 & 4 & 1 & -1 & 4 & -1 & 1 & -4 & -1 & -1 \\ 0 & 1 & 0 & 0 & -1 & 0 & 0 & 1 & 0 & 0 & -1 & 0 \\ 1 & 0 & -1 & 1 & 0 & -1 & -1 & 0 & -1 & -1 & 0 & -1 \\ 0 & 0 & 1 & 0 & 0 & -1 & 0 & 0 & -1 & 0 & 0 & 1 \\ 0 & -1 & 0 & 0 & 1 & 0 & 0 & 1 & 0 & 0 & -1 & 0 \\ -1 & 1 & 0 & 1 & 1 & 0 & -1 & 1 & 0 & 1 & 1 & 0 \\ 1 & 0 & -1 & -1 & 0 & 1 & -1 & 0 & -1 & 1 & 0 & 1 \\ 1 & -1 & 0 & -1 & -1 & 0 & -1 & 1 & 0 & 1 & 1 & 0 \end{bmatrix} \tag{A.20}$$

$$[C_u]^{-1} = \frac{1}{4}\begin{bmatrix} 1 & 0 & 1 & 0 & 1 & 0 & 1 & 0 \\ -\frac{1}{a} & 0 & -\frac{1}{a} & 0 & \frac{1}{a} & 0 & \frac{1}{a} & 0 \\ \frac{1}{b} & 0 & -\frac{1}{b} & 0 & \frac{1}{b} & 0 & -\frac{1}{b} & 0 \\ -\frac{1}{ab} & 0 & \frac{1}{ab} & 0 & \frac{1}{ab} & 0 & -\frac{1}{ab} & 0 \\ 0 & 1 & 0 & 1 & 0 & 1 & 0 & 1 \\ 0 & -\frac{1}{a} & 0 & -\frac{1}{a} & 0 & \frac{1}{a} & 0 & \frac{1}{a} \\ 0 & \frac{1}{b} & 0 & -\frac{1}{b} & 0 & \frac{1}{b} & 0 & -\frac{1}{b} \\ 0 & -\frac{1}{ab} & 0 & \frac{1}{ab} & 0 & \frac{1}{ab} & 0 & -\frac{1}{ab} \end{bmatrix} \tag{A.21}$$

Substitution of Eqs. A.18 and A.19 into Eq. A.15 defines the strains as a function of the nodal point displacements:

$$\{\varepsilon\}_z = [Q_u]\ [C_u]^{-1}\ \{\delta_u^e\} + z\ [S]\ [Q_\phi]\ [R]\ [R]^{-1}\ [C_\phi]^{-1}\ [T]^{-1}\ \{\delta_\phi^e\} \tag{A.22}$$

After performing the multiplication of the [R] matrices,

$$\{\varepsilon\}_z = [Q_u]\ [C_u]^{-1}\ \{\delta_u^e\} + z\ [S]\ [Q_\phi]\ [C_\phi]^{-1}\ [T]^{-1}\{\delta_\phi^e\} \tag{A.23}$$

Comparison of Eq. A.23 with Eqs. 3.24 shows that the $[B_u]$ and $[B_\phi]$ matrices can be defined as:

$$[B_u] = [Q_u]\ [C_u]^{-1} \tag{A.24a}$$

$$[B_\phi] = [S]\ [Q_\phi]\ [C_\phi]^{-1}\ [T]^{-1} \tag{A.24b}$$

A.4 Element Stiffness Matrices

Evaluation of the inplane, coupling and bending stiffness matrices given in Eqs. 3.33 can now proceed. Substitution of Eqs. A.24a and A.24b into Eqs. 3.33 gives:

$$[k_{uu}^e] = [C_u]^{-1^T} \iint_{yx} [Q_u]^T\ [D_{uu}]\ [Q_u]\ dxdy\ [C_u]^{-1} \tag{A.25}$$

$$[k_{u\phi}^e] = [C_u]^{-1^T} \iint_{yx} [Q_u]^T\ [D_{u\phi}]\ [S]\ [Q_\phi]\ dxdy\ [C_\phi]^{-1}\ [T]^{-1} \tag{A.26}$$

$$[k_{\phi\phi}^e] = [T]^{-1^T}\ [C_\phi]^{-1^T} \iint_{yx} [Q_\phi]^T\ [S]^T\ [D_{\phi\phi}]\ [S]\ [Q_\phi]\ dxdy\ [C_\phi]^{-1}\ [T]^{-1} \tag{A.27}$$

$[D_{uu}]$, $[D_{u\phi}]$, and $[D_{\phi\phi}]$ are the rigidities introduced in Section 3.4.4 and given in Eq. 3.32. The evaluation of the integrals in Eqs. A.25 to A.27 can be simplified by considering only one element of the rigidity matrix to be nonzero at a time. This reduces one very laborious evaluation of each of the three stiffness matrices to six much simpler problems for each one of the stiffness matrices. For each matrix the results are then summed up in the following form:

$$[k^e_{uu}] = [C_u]^{-1^T} \Big[D_{11}\,[K_1] + D_{12}\,[K_2] + D_{13}\,[K_3] + D_{22}\,[K_4] + D_{23}\,[K_5] + D_{33}\,[K_6] \Big]_{uu}\,[C_u]^{-1} \tag{A.28}$$

$$[k^e_{u\phi}] = [C_u]^{-1^T} \Big[D_{11}\,[K_1] + D_{12}\,[K_2] + D_{13}\,[K_3] + D_{22}\,[K_4] + D_{23}\,[K_5] + D_{33}\,[K_6] \Big]_{u\phi}\,[C_\phi]^{-1}\,[T]^{-1} \tag{A.29}$$

$$[k^e_{\phi\phi}] = [T]^{-1^T}\,[C_\phi]^{-1^T} \Big[D_{11}\,[K_1] + D_{12}\,[K_2] + D_{13}\,[K_3] + D_{22}\,[K_4] + D_{23}\,[K_5] + D_{33}\,[K_6] \Big]_{\phi\phi}\,[C_\phi]^{-1}\,[T]^{-1} \tag{A.30}$$

The submatrices pertaining to the inplane stiffness matrix are evaluated by employing Eq. A.28 as follows:

$$\left(D_{11}\ [K_1]\right)_{uu} = \iint_{yx} [Q_u]^T \begin{bmatrix} D_{11} & 0 & 0 \\ 0 & 0 & 0 \\ 0 & 0 & 0 \end{bmatrix}_{uu} [Q_u]\ dxdy \qquad (A.31a)$$

$$\left(D_{12}\ [K_2]\right)_{uu} = \iint_{yx} [Q_u]^T \begin{bmatrix} 0 & D_{12} & 0 \\ D_{21} & 0 & 0 \\ 0 & 0 & 0 \end{bmatrix}_{uu} [Q_u]\ dxdy \qquad (A.31b)$$

$$\left(D_{13}\ [K_3]\right)_{uu} = \iint_{yx} [Q_u]^T \begin{bmatrix} 0 & 0 & D_{13} \\ 0 & 0 & 0 \\ D_{31} & 0 & 0 \end{bmatrix}_{uu} [Q_u]\ dxdy \qquad (A.31c)$$

$$\left(D_{22}\ [K_4]\right)_{uu} = \iint_{yx} [Q_u]^T \begin{bmatrix} 0 & 0 & 0 \\ 0 & D_{22} & 0 \\ 0 & 0 & 0 \end{bmatrix}_{uu} [Q_u]\ dxdy \qquad (A.31d)$$

$$\left(D_{23}\ [K_5]\right)_{uu} = \iint_{yx} [Q_u]^T \begin{bmatrix} 0 & 0 & 0 \\ 0 & 0 & D_{23} \\ 0 & D_{32} & 0 \end{bmatrix}_{uu} [Q_u]\ dxdy \qquad (A.31e)$$

$$\left(D_{33}\ [K_6]\right)_{uu} = \iint_{yx} [Q_u]^T \begin{bmatrix} 0 & 0 & 0 \\ 0 & 0 & 0 \\ 0 & 0 & D_{33} \end{bmatrix}_{uu} [Q_u]\ dxdy \qquad (A.31f)$$

The $(D_{ij})_{uu}$ terms in the above equations correspond to elements of the inplane rigidities given in Eq. 3.32a.. Explicit expressions for Eq. A.31 can be developed by utilizing Eq. A.16. This has been done to generate the following formulae:

$$[K_1]_{uu} = \begin{bmatrix} 0 & & & & & & & \\ 0 & 1 & & & \text{symmetric} & & & \\ 0 & 0 & 0 & & & & & \\ 0 & 0 & 0 & \frac{b^2}{3} & & & & \\ 0 & 0 & 0 & 0 & 0 & & & \\ 0 & 0 & 0 & 0 & 0 & 0 & & \\ 0 & 0 & 0 & 0 & 0 & 0 & 0 & \\ 0 & 0 & 0 & 0 & 0 & 0 & 0 & 0 \end{bmatrix} 4ab \qquad \text{(A.32a)}$$

$$[K_2]_{uu} = \begin{bmatrix} 0 & & & & & & & \\ 0 & 0 & & & \text{symmetric} & & & \\ 0 & 0 & 0 & & & & & \\ 0 & 0 & 0 & 0 & & & & \\ 0 & 0 & 0 & 0 & 0 & & & \\ 0 & 0 & 0 & 0 & 0 & 0 & & \\ 0 & 1 & 0 & 0 & 0 & 0 & 0 & \\ 0 & 0 & 0 & 0 & 0 & 0 & 0 & 0 \end{bmatrix} 4ab \qquad \text{(A.32b)}$$

$$[K_3]_{uu} = \begin{bmatrix} 0 & & & & & & & \\ 0 & 0 & & & \text{symmetric} & & & \\ 0 & 1 & 0 & & & & & \\ 0 & 0 & 0 & 0 & & & & \\ 0 & 0 & 0 & 0 & 0 & & & \\ 0 & 1 & 0 & 0 & 0 & 0 & & \\ 0 & 0 & 0 & 0 & 0 & 0 & 0 & \\ 0 & 0 & 0 & \frac{b^2}{3} & 0 & 0 & 0 & 0 \end{bmatrix} 4ab \qquad \text{(A.32c)}$$

$$[K_4]_{uu} = \begin{bmatrix} 0 & & & & & & & \\ 0 & 0 & & & \text{symmetric} & & & \\ 0 & 0 & 0 & & & & & \\ 0 & 0 & 0 & 0 & & & & \\ 0 & 0 & 0 & 0 & 0 & & & \\ 0 & 0 & 0 & 0 & 0 & 0 & & \\ 0 & 0 & 0 & 0 & 0 & 0 & 1 & \\ 0 & 0 & 0 & 0 & 0 & 0 & 0 & \frac{a^2}{3} \end{bmatrix} 4ab \qquad \text{(A.32d)}$$

$$[K_5]_{uu} = \begin{bmatrix} 0 & & & & & & & \\ 0 & 0 & & & \text{symmetric} & & & \\ 0 & 0 & 0 & & & & & \\ 0 & 0 & 0 & 0 & & & & \\ 0 & 0 & 0 & 0 & 0 & & & \\ 0 & 0 & 0 & 0 & 0 & 0 & & \\ 0 & 0 & 1 & 0 & 0 & 1 & 0 & \\ 0 & 0 & 0 & \frac{a^2}{3} & 0 & 0 & 0 & 0 \end{bmatrix} 4ab \tag{A.32e}$$

$$[K_6]_{uu} = \begin{bmatrix} 0 & & & & & & & \\ 0 & 0 & & & \text{symmetric} & & & \\ 0 & 0 & 1 & & & & & \\ 0 & 0 & 0 & \frac{a^2}{3} & & & & \\ 0 & 0 & 0 & 0 & 0 & & & \\ 0 & 0 & 1 & 0 & 0 & 1 & & \\ 0 & 0 & 0 & 0 & 0 & 0 & 0 & \\ 0 & 0 & 0 & 0 & 0 & 0 & 0 & \frac{b^2}{3} \end{bmatrix} 4ab \tag{A.32f}$$

In a similar manner the submatrices for the coupling and bending element stiffness matrices can be developed from Eqs. A.16 and A.17, Eqs. A.26 and A.27, and Eqs. A.29 and A.30. Care must be exercised to insure that the proper rigidities given in Eqs. 3.32b and 3.32c are employed. The submatrices for the coupling and bending stiffness matrices are presented in Eqs. A.33 and A.34 respectively.

$$[K_1]_{u\phi} = \begin{bmatrix} 0 & 0 & 0 & 0 & 0 & 0 & 0 & 0 & 0 & 0 & 0 & 0 \\ 0 & 0 & 0 & \frac{-8b}{a} & 0 & 0 & 0 & 0 & 0 & 0 & 0 & 0 \\ 0 & 0 & 0 & 0 & 0 & 0 & 0 & 0 & 0 & 0 & 0 & 0 \\ 0 & 0 & 0 & 0 & 0 & 0 & 0 & \frac{-8b^2}{3a} & 0 & 0 & 0 & 0 \\ 0 & 0 & 0 & 0 & 0 & 0 & 0 & 0 & 0 & 0 & 0 & 0 \\ 0 & 0 & 0 & 0 & 0 & 0 & 0 & 0 & 0 & 0 & 0 & 0 \\ 0 & 0 & 0 & 0 & 0 & 0 & 0 & 0 & 0 & 0 & 0 & 0 \\ 0 & 0 & 0 & 0 & 0 & 0 & 0 & 0 & 0 & 0 & 0 & 0 \end{bmatrix} \tag{A.33a}$$

$$[K_2]_{u\phi} = \begin{bmatrix} 0 & 0 & 0 & 0 & 0 & 0 & 0 & 0 & 0 & 0 & 0 & 0 \\ 0 & 0 & 0 & 0 & 0 & \frac{-8a}{b} & 0 & 0 & 0 & 0 & 0 & 0 \\ 0 & 0 & 0 & 0 & 0 & 0 & 0 & 0 & 0 & 0 & 0 & 0 \\ 0 & 0 & 0 & 0 & 0 & 0 & 0 & 0 & 0 & -8a & 0 & 0 \\ 0 & 0 & 0 & 0 & 0 & 0 & 0 & 0 & 0 & 0 & 0 & 0 \\ 0 & 0 & 0 & 0 & 0 & 0 & 0 & 0 & 0 & 0 & 0 & 0 \\ 0 & 0 & 0 & \frac{-8b}{a} & 0 & 0 & 0 & 0 & 0 & 0 & 0 & 0 \\ 0 & 0 & 0 & 0 & 0 & 0 & -8b & 0 & 0 & 0 & 0 & 0 \end{bmatrix} \tag{A.33b}$$

$$[K_3]_{u\phi} = \begin{bmatrix} 0 & 0 & 0 & 0 & 0 & 0 & 0 & 0 & 0 & 0 & 0 & 0 \\ 0 & 0 & 0 & 0 & -8 & 0 & 0 & 0 & 0 & 0 & -8 & -8 \\ 0 & 0 & 0 & \frac{-8b}{a} & 0 & 0 & 0 & 0 & 0 & 0 & 0 & 0 \\ 0 & 0 & 0 & 0 & 0 & 0 & -8b & 0 & \frac{-16b}{3} & 0 & 0 & 0 \\ 0 & 0 & 0 & 0 & 0 & 0 & 0 & 0 & 0 & 0 & 0 & 0 \\ 0 & 0 & 0 & \frac{-8b}{a} & 0 & 0 & 0 & 0 & 0 & 0 & 0 & 0 \\ 0 & 0 & 0 & 0 & 0 & 0 & 0 & 0 & 0 & 0 & 0 & 0 \\ 0 & 0 & 0 & 0 & 0 & 0 & 0 & \frac{-8b^2}{3a} & 0 & 0 & 0 & 0 \end{bmatrix} \tag{A.33c}$$

$$[K_4]_{u\phi} = \begin{bmatrix} 0 & 0 & 0 & 0 & 0 & 0 & 0 & 0 & 0 & 0 & 0 & 0 \\ 0 & 0 & 0 & 0 & 0 & 0 & 0 & 0 & 0 & 0 & 0 & 0 \\ 0 & 0 & 0 & 0 & 0 & 0 & 0 & 0 & 0 & 0 & 0 & 0 \\ 0 & 0 & 0 & 0 & 0 & 0 & 0 & 0 & 0 & 0 & 0 & 0 \\ 0 & 0 & 0 & 0 & 0 & 0 & 0 & 0 & 0 & 0 & 0 & 0 \\ 0 & 0 & 0 & 0 & 0 & 0 & 0 & 0 & 0 & 0 & 0 & 0 \\ 0 & 0 & 0 & 0 & 0 & \frac{-8a}{b} & 0 & 0 & 0 & 0 & 0 & 0 \\ 0 & 0 & 0 & 0 & 0 & 0 & 0 & 0 & \frac{-8a^2}{3b} & 0 & 0 & 0 \end{bmatrix} \tag{A.33d}$$

$$[K_5]_{u\phi} = \begin{bmatrix} 0 & 0 & 0 & 0 & 0 & 0 & 0 & 0 & 0 & 0 & 0 & 0 \\ 0 & 0 & 0 & 0 & 0 & 0 & 0 & 0 & 0 & 0 & 0 & 0 \\ 0 & 0 & 0 & 0 & 0 & \frac{-8a}{b} & 0 & 0 & 0 & 0 & 0 & 0 \\ 0 & 0 & 0 & 0 & 0 & 0 & 0 & 0 & \frac{-8a^2}{3b} & 0 & 0 & 0 \\ 0 & 0 & 0 & 0 & 0 & 0 & 0 & 0 & 0 & 0 & 0 & 0 \\ 0 & 0 & 0 & 0 & 0 & \frac{-8a}{b} & 0 & 0 & 0 & 0 & 0 & 0 \\ 0 & 0 & 0 & 0 & -8 & 0 & 0 & 0 & 0 & 0 & -8 & -8 \\ 0 & 0 & 0 & 0 & 0 & 0 & 0 & \frac{-16a}{3} & 0 & -8a & 0 & 0 \end{bmatrix} \tag{A.33e}$$

$$[K_6]_{u\phi} = \begin{bmatrix} 0 & 0 & 0 & 0 & 0 & 0 & 0 & 0 & 0 & 0 & 0 & 0 \\ 0 & 0 & 0 & 0 & 0 & 0 & 0 & 0 & 0 & 0 & 0 & 0 \\ 0 & 0 & 0 & 0 & -8 & 0 & 0 & 0 & 0 & 0 & -8 & -8 \\ 0 & 0 & 0 & 0 & 0 & 0 & 0 & \frac{-16a}{3} & 0 & 0 & 0 & 0 \\ 0 & 0 & 0 & 0 & 0 & 0 & 0 & 0 & 0 & 0 & 0 & 0 \\ 0 & 0 & 0 & 0 & -8 & 0 & 0 & 0 & 0 & 0 & -8 & -8 \\ 0 & 0 & 0 & 0 & 0 & 0 & 0 & 0 & 0 & 0 & 0 & 0 \\ 0 & 0 & 0 & 0 & 0 & 0 & 0 & 0 & \frac{-16b}{3} & 0 & 0 & 0 \end{bmatrix} \tag{A.33f}$$

$$[K_1]_{\phi\phi} = \frac{16b}{15a^3}\begin{bmatrix}
0 & & & & & & & & & & & \\
0 & 0 & & & & & & & & & & \\
0 & 0 & 0 & & & & & & & & & \\
0 & 0 & 0 & 15 & & & & \text{Symmetric} & & & & \\
0 & 0 & 0 & 0 & 0 & & & & & & & \\
0 & 0 & 0 & 0 & 0 & 0 & & & & & & \\
0 & 0 & 0 & 0 & 0 & 0 & 45 & & & & & \\
0 & 0 & 0 & 0 & 0 & 0 & 0 & 5 & & & & \\
0 & 0 & 0 & 0 & 0 & 0 & 0 & 0 & 0 & & & \\
0 & 0 & 0 & 0 & 0 & 0 & 0 & 0 & 0 & 0 & & \\
0 & 0 & 0 & 0 & 0 & 0 & 0 & 0 & 0 & 0 & 15 & \\
0 & 0 & 0 & 0 & 0 & 0 & 0 & 0 & 0 & 0 & 0 & 0
\end{bmatrix} \tag{A.34a}$$

$$[K_2]_{\phi\phi} = \frac{16}{15ab}\begin{bmatrix}
0 & & & & & & & & & & & \\
0 & 0 & & & & & & & & & & \\
0 & 0 & 0 & & & & & & & & & \\
0 & 0 & 0 & 0 & & & & \text{Symmetric} & & & & \\
0 & 0 & 0 & 0 & 0 & & & & & & & \\
0 & 0 & 0 & 15 & 0 & 0 & & & & & & \\
0 & 0 & 0 & 0 & 0 & 0 & 0 & & & & & \\
0 & 0 & 0 & 0 & 0 & 0 & 0 & 0 & & & & \\
0 & 0 & 0 & 0 & 0 & 0 & 15 & 0 & 0 & & & \\
0 & 0 & 0 & 0 & 0 & 0 & 0 & 15 & 0 & 0 & & \\
0 & 0 & 0 & 0 & 0 & 0 & 0 & 0 & 0 & 0 & 0 & \\
0 & 0 & 0 & 0 & 0 & 0 & 0 & 0 & 0 & 0 & 15 & 0
\end{bmatrix} \tag{A.34b}$$

$$[K_3]_{\phi\phi} = \frac{16}{15a^2} \begin{bmatrix} 0 & & & & & & & & & & & \\ 0 & 0 & & & & & & & & & & \\ 0 & 0 & 0 & & & & & & & & & \\ 0 & 0 & 0 & 0 & & & & \text{Symmetric} & & & & \\ 0 & 0 & 0 & 15 & 0 & & & & & & & \\ 0 & 0 & 0 & 0 & 0 & 0 & & & & & & \\ 0 & 0 & 0 & 0 & 0 & 0 & 0 & & & & & \\ 0 & 0 & 0 & 0 & 0 & 0 & 30 & 0 & & & & \\ 0 & 0 & 0 & 0 & 0 & 0 & 0 & 10 & 0 & & & \\ 0 & 0 & 0 & 0 & 0 & 0 & 0 & 0 & 0 & 0 & & \\ 0 & 0 & 0 & 15 & 0 & 0 & 0 & 0 & 0 & 0 & 0 & \\ 0 & 0 & 0 & 15 & 0 & 0 & 0 & 0 & 0 & 0 & 0 & 0 \end{bmatrix} \tag{A.34c}$$

$$[K_4]_{\phi\phi} = \frac{16a}{15b^3} \begin{bmatrix} 0 & & & & & & & & & & & \\ 0 & 0 & & & & & & & & & & \\ 0 & 0 & 0 & & & & & & & & & \\ 0 & 0 & 0 & 0 & & & & \text{Symmetric} & & & & \\ 0 & 0 & 0 & 0 & 0 & & & & & & & \\ 0 & 0 & 0 & 0 & 0 & 15 & & & & & & \\ 0 & 0 & 0 & 0 & 0 & 0 & 0 & & & & & \\ 0 & 0 & 0 & 0 & 0 & 0 & 0 & 0 & & & & \\ 0 & 0 & 0 & 0 & 0 & 0 & 0 & 0 & 5 & & & \\ 0 & 0 & 0 & 0 & 0 & 0 & 0 & 0 & 0 & 45 & & \\ 0 & 0 & 0 & 0 & 0 & 0 & 0 & 0 & 0 & 0 & 0 & \\ 0 & 0 & 0 & 0 & 0 & 0 & 0 & 0 & 0 & 0 & 0 & 15 \end{bmatrix} \tag{A.34d}$$

$$[K_5]_{\phi\phi} = \frac{16}{15b^2} \begin{bmatrix} 0 & & & & & & & & & & & \\ 0 & 0 & & & & & & & & & & \\ 0 & 0 & 0 & & & & & & & & & \\ 0 & 0 & 0 & 0 & & & & & \text{Symmetric} & & & \\ 0 & 0 & 0 & 0 & 0 & & & & & & & \\ 0 & 0 & 0 & 0 & 15 & 0 & & & & & & \\ 0 & 0 & 0 & 0 & 0 & 0 & 0 & & & & & \\ 0 & 0 & 0 & 0 & 0 & 0 & 0 & 0 & & & & \\ 0 & 0 & 0 & 0 & 0 & 0 & 0 & 10 & 0 & & & \\ 0 & 0 & 0 & 0 & 0 & 0 & 0 & 0 & 30 & 0 & & \\ 0 & 0 & 0 & 0 & 0 & 15 & 0 & 0 & 0 & 0 & 0 & \\ 0 & 0 & 0 & 0 & 0 & 15 & 0 & 0 & 0 & 0 & 0 & 0 \end{bmatrix} \tag{A.34e}$$

$$[K_6]_{\phi\phi} = \frac{16}{15ab} \begin{bmatrix} 0 & & & & & & & & & & & \\ 0 & 0 & & & & & & & & & & \\ 0 & 0 & 0 & & & & & & & & & \\ 0 & 0 & 0 & 0 & & & & & \text{Symmetric} & & & \\ 0 & 0 & 0 & 0 & 15 & & & & & & & \\ 0 & 0 & 0 & 0 & 0 & 0 & & & & & & \\ 0 & 0 & 0 & 0 & 0 & 0 & 0 & & & & & \\ 0 & 0 & 0 & 0 & 0 & 0 & 0 & 20 & & & & \\ 0 & 0 & 0 & 0 & 0 & 0 & 0 & 0 & 20 & & & \\ 0 & 0 & 0 & 0 & 0 & 0 & 0 & 0 & 0 & 0 & & \\ 0 & 0 & 0 & 0 & 15 & 0 & 0 & 0 & 0 & 0 & 27 & \\ 0 & 0 & 0 & 0 & 15 & 0 & 0 & 0 & 0 & 0 & 15 & 27 \end{bmatrix} \tag{A.34f}$$

Addition of the submatrices and multiplication by the $[T]^{-1}$, $[C_{\phi}]^{-1}$, and $[C_u]^{-1}$ matrices shown in Eqs. A.28, A.29 and A.30 are performed in the computer program. The results are the required stiffness matrices.

As mentioned in Section 3.8, when applying the method to superstructures built with a skew it is only necessary to apply a series of transformations so as to obtain the required expressions in the Cartesian coordinate system. The following steps are to be used:

1. Formulate the product $[T_{\varepsilon}]^T$ $[D]$ $[T_{\varepsilon}]$, (see Eq. 3.74).
2. Evaluate the layer rigidities based on the above product (see Eq. 3.32).
3. Evaluate Eqs. A.28, A.29, and A.30 by employing Eqs. A.32, A.33, and A.34.
4. Multiply the results by sin β (see Eq. 3.75).

Steps 1 through 4, listed above, are analogous to the evaluation of Eq. 3.74. To obtain the final stiffness matrix of the skewed slab element in a Cartesian coordinate system it is necessary to carry out the transformation indicated in Eq. 3.73. [TF] in Eq. 3.73 can be evaluated using Eq. 3.59.

Needless to say all of the aforementioned matrix operations are performed by the computer. Also, key matrices, whose terms are constant for the entire analysis, may be evaluated once and then stored for subsequent use.

APPENDIX B

BEAM ELEMENT STIFFNESS FORMULATION

The matrix expressions involved in the layered beam formulation, which was presented in Section 3.5, will be derived in this appendix.

Substitution of the node point coordinates, which are designated by $I(x = 0)$ and $K(x = \ell)$ in Fig. 15, into the prescribed displacement functions (see Eq. 3.35) will give

$$\{\delta_u^e\} = [C_u]\{B\}$$
$$\{\delta_\phi^e\} = [C_\phi]\{A\} \tag{B.1a}$$

where

$$[C_u] = \begin{bmatrix} 1 & 0 \\ 1 & \ell \end{bmatrix} \tag{B.1b}$$

$$[C_\phi] = \begin{bmatrix} 1 & 0 & 0 & 0 \\ 0 & -1 & 0 & 0 \\ 1 & \ell & \ell^2 & \ell^3 \\ 0 & -1 & -2\ell & -3\ell^2 \end{bmatrix} \tag{B.1c}$$

Solving for $\{A\}$ and $\{B\}$ from Eq. B.1a will lead to

$$\{B\} = [C_u]^{-1}\{\delta_u^e\}$$
$$\{A\} = [C_\phi]^{-1}\{\delta_\phi^e\} \tag{B.2a}$$

where $$[C_u]^{-1} = \begin{bmatrix} 1 & 0 \\ -1/\ell & 1/\ell \end{bmatrix} \tag{B.2b}$$

$$[C_\phi]^{-1} = \begin{bmatrix} 1 & 0 & 0 & 0 \\ 0 & -1 & 0 & 0 \\ -3/\ell^2 & 2/\ell & 3/\ell^2 & 1/\ell \\ 2/\ell^3 & -1/\ell^2 & -2/\ell^3 & -1/\ell^2 \end{bmatrix} \tag{B.2c}$$

Substitution of Eq. 3.35 into Eq. 3.38 will give

$$(\varepsilon_x)_z = [Q_u]\ \{B\} + z\ [Q_\phi]\ \{A\} \tag{B.3a}$$

where $$[Q_u] = [0 \quad 1] \tag{B.3b}$$

$$[Q_\phi] = [0 \quad 0 \quad -2 \quad -6x] \tag{B.3c}$$

Thus by employing Eqs. B.2 and B.3, the strain can be expressed in terms of the nodal point displacements

$$(\varepsilon_x)_z = [B_u]\ \{\delta_u^e\} + z\ [B_\phi]\ \{\delta_\phi^e\} \tag{3.39a}$$

whereby employing Eq. 3.39b

$$[B_u] = [-1/\ell \quad 1/\ell] \tag{B.4a}$$

$$[B_\phi] = [(6/\ell^2 - 12x/\ell^3)\ (-4/\ell + 6x/\ell^2)\ (-6/\ell^2 + 12x/\ell^3)\ (-2/\ell + 6x/\ell^2)] \tag{B.4b}$$

Performing the indicated multiplications and integrations of Eq. 3.45 gives the following expressions for the in-plane, bending, and coupling stiffness matrices:

$$[k^e_{uu}] = (D_{uu}) \begin{bmatrix} 1/\ell & -1/\ell \\ -1/\ell & 1/\ell \end{bmatrix} \tag{B.5a}$$

$$[k^e_{\phi\phi}] = (D_{\phi\phi}) \begin{bmatrix} 12/\ell^3 & -6/\ell^2 & -12/\ell^3 & -6/\ell^2 \\ -6/\ell^2 & 4/\ell & 6/\ell^2 & 2/\ell \\ -12/\ell^3 & 6/\ell^2 & 12/\ell^3 & 6/\ell^2 \\ -6/\ell^2 & 2/\ell & 6/\ell^2 & 4/\ell \end{bmatrix} \tag{B.5b}$$

$$[k^e_{u\phi}] = (D_{u\phi}) \begin{bmatrix} 0 & 1/\ell & 0 & -1/\ell \\ 0 & -1/\ell & 0 & 1/\ell \end{bmatrix} \tag{B.5c}$$

The inplane, coupling, and bending rigidities, i.e. (D_{uu}), $(D_{u\phi})$, and $(D_{\phi\phi})$, are defined by Eqs. 3.41a, 3.41b, and 3.41c, respectively.

11. ACKNOWLEDGMENTS

Parts of the reported investigation were sponsored by the Pennsylvania Department of Transportation and the United States Department of Transportation-Federal Highway Administration. Their support is gratefully acknowledged.

The authors extend their gratitude to the Lehigh University Computing Center for making the facilities available for extensive computer based investigations. Thanks are also due to Messrs. Frank Washburn and Vince Slepetz, computer operators at the Lehigh University Computing Center, for their continuous assistance.

Mr. John Kulicki's assistance in different phases of the reported research, and especially his direct contributions on the study of beams, has been instrumental in the successful completion of the investigation.

Grateful appreciation is extended to Mrs. Ruth Grimes who dilligently typed the manuscript, Mesdammes K. Michele Kostem and Dorothy Fielding for their assistance in the preparation of the manuscript and Mrs. Sharon Balogh and Jack Gera for the drafting of the figures contained herein.